

PWSCC Initiation Testing of Ni-base Alloys

Report 2

June 2021

Mychailo B. Toloczko
Ziqing Zhai
Jing Wang
Matthew J. Olszta
Ryan A. Bouffioux

DISCLAIMER

This report was prepared as an account of work sponsored by an agency of the United States Government. Neither the United States Government nor any agency thereof, nor Battelle Memorial Institute, nor any of their employees, makes **any warranty, express or implied, or assumes any legal liability or responsibility for the accuracy, completeness, or usefulness of any information, apparatus, product, or process disclosed, or represents that its use would not infringe privately owned rights.** Reference herein to any specific commercial product, process, or service by trade name, trademark, manufacturer, or otherwise does not necessarily constitute or imply its endorsement, recommendation, or favoring by the United States Government or any agency thereof, or Battelle Memorial Institute. The views and opinions of authors expressed herein do not necessarily state or reflect those of the United States Government or any agency thereof.

PACIFIC NORTHWEST NATIONAL LABORATORY
operated by
BATTELLE
for the
UNITED STATES DEPARTMENT OF ENERGY
under Contract DE-AC05-76RL01830

Printed in the United States of America

Client Distribution

PWSCC Initiation Testing of Ni-base Alloys

Report 2

June 2021

Mychailo B. Toloczko
Ziqing Zhai
Jing Wang
Matthew J. Olszta
Ryan A. Bouffioux

Prepared for
the U.S. Department of Energy
under Contract DE-AC05-76RL01830

and,
the U.S. Nuclear Regulatory Commission
under Agreement No. 31310019N0001

Pacific Northwest National Laboratory
Richland, Washington 99354

Abstract

This is the second progress report on laboratory testing to evaluate stress corrosion crack initiation response of Alloys 600/182 and Alloys 690/152(M)/52(M) in a simulated pressurized water reactor primary water environment. Tensile specimens actively maintained at constant load are being utilized, and time to crack initiation is being measured in-situ using the direct current potential drop technique. The first tests were started in 2016, and a substantial amount of data has been obtained on all alloys of interest. This report has a strong focus on Alloy 182 SCC initiation response that includes a comprehensive analysis of the Alloy 182 stress exponent as well as providing the results of microstructural examinations aimed to provide insight into the very low SCC initiation times that have been observed in the PNNL testing. The Alloy 600 initiation data from this program and the DOE-NE Light Water Reactor Sustainability (LWRS) program task at PNNL were used to determine an SCC initiation stress exponent for comparison to Alloy 182. Alloys 690/152(M)/52(M) results provided here include an updated factor of improvement over Alloys 600/182 and the results of mid-test microstructural examinations performed on selected specimens.

Acknowledgments

The authors would like to acknowledge the assistance of Robert J. Seffens, Ferdinand C. Colon, and Ryley B. Petersen for testing and Anthony Guzman and Michael L. Blazon for specimen preparation.

Acronyms and Abbreviations

ADF	annular darkfield
BF	bright field
BSE	backscattered electron
BWR	boiling water reactor
CDF	cumulative distribution function
CGR	crack growth rate
CF	cold forged
CT	compact tension
DCPD	direct current potential drop
DH	dissolved hydrogen
DIGM	diffusion-induced grain boundary migration
DMW	dissimilar metal weld
DOE	Department of Energy
EBSD	electron back scattering diffraction
EdF	Électricité de France
EDS	energy dispersive spectroscopy
EPRI	Electric Power Research Institute
FEM	finite element model(ing)
FIB	focused ion beam
FOI	factor of improvement
IG	intergranular
IGA	intergranular attack
IGSCC	Intergranular stress corrosion cracking
IPF	inverse pole figure
K	stress intensity
LOF	lack-of-fusion
LWR	light water reactor
LWRS	Light Water Reactor Sustainability (Program)
MLE	maximum likelihood estimation
NRC	Nuclear Regulatory Commission
NWC	normal water chemistry
PNNL	Pacific Northwest National Laboratory
PWR	pressurized water reactor
PWSCC	primary water stress corrosion cracking
SCC	stress corrosion crack(ing)
SCCGR	stress corrosion crack growth rate
SCCI	stress corrosion cracking initiation
SE	secondary electron
SEM	scanning electron microscopy
SGB	solidification grain boundary
SNR	signal-to-noise ratio
STEM	scanning transmission electron microscopy
TEM	transmission electron microscopy
TG	transgranular

xLPR
YS

Extremely Low Probability of Rupture
yield stress

Contents

Abstract	ii
Acknowledgments	iii
Acronyms and Abbreviations	iv
Contents	vi
1.0 Introduction	4
2.0 SCC Initiation Testing Approach	7
2.1 Test Method	7
2.2 Equipment	9
2.3 Equipment Issues and Improvements	10
3.0 Alloy 182 Testing Status	13
3.1 Alloy 182 Tests Conducted at Yield Strength Loading	13
3.2 Effect of Plastic Strain During Loading on SCC Initiation Time	17
3.3 Alloy 182 Tests Conducted at Sub-Yield Strength Loading	20
3.4 Brief Summary of Testing Observations	23
4.0 Alloy 600 Testing Status	25
5.0 Alloy 690/152(M)/52(M) Testing Status	27
5.1 SCC Initiation Behavior	27
5.2 Creep Rate Measurements	31
5.3 Alloy 690/152(M)/52(M) Specimen Microstructure Observations	31
6.0 Statistical Analysis of Alloy 182 and Alloy 600 SCC Initiation	41
6.1 Introduction	41
6.2 Crack Initiation Models	41
6.2.1 Overview	41
6.2.2 Direct Model 1 (Power Law Model)	41
6.2.3 Direct Model 2	42
6.2.4 Weibull Model	42
6.3 Data Source and Pre-Treatment	44
6.4 Analysis of Alloy 182 Initiation Times	45
6.4.1 Analysis Using Direct Model 1	45
6.4.2 Analysis Using Weibull Models	53
6.5 Analysis of Alloy 600 Initiation Times	56
6.5.1 Analysis Using Direct Model 1	56
6.5.2 Analysis using Weibull Models	63
6.6 Complexities in Regression Analysis	66
7.0 SEM Examinations of Low Initiation Time Alloy 182 Specimens	68
7.1 Introduction	68
7.2 Procedures for Microstructural Characterization	68

7.3	Observations	70
7.3.1	15% CF KAPL Alloy 182 Specimens IN166-168.....	70
7.3.2	15% CF Studsvik Alloy 182 Specimens IN170, IN191-93, and IN233.....	74
7.3.3	15% CF Phase 2B Alloy 182 Specimens IN185 and IN216	84
7.3.4	15% CF Flawtech Alloy 182 Specimens IN188-190 and IN221- 223	86
8.0	Detailed Microstructural Comparisons Between a Low and a High Initiation Time Specimen	93
8.1	Overview	93
8.2	SEM Cross-Sectional Analysis	94
8.2.1	Weld Defects in IN233 and IN169	94
8.2.2	Bulk Oxide Inclusions in IN233 and IN169	99
8.2.3	IGA in IN233 and IN169.....	101
8.2.4	SCC Crack Initiation in IN233	105
8.3	EBSD Cross-Sectional Analysis	105
8.4	TEM/STEM Analysis	108
8.4.1	TEM/STEM Analysis of IN233	109
8.4.2	TEM/STEM Analysis of IN169	121
8.5	Summary of Comparisons	131
9.0	Summary	133
9.1	Alloy 182 SCC Initiation Behavior.....	133
9.2	Alloy 600 SCC Initiation Behavior.....	134
9.3	Alloy 690/152 SCC Initiation Behavior	134
10.0	Future Testing and Analysis Recommendations.....	136
10.1	NRC-Expanded Test Matrix.....	136
10.2	Alloy 182 SCC Initiation Evaluation by Dominion Engineering	137
11.0	References.....	139

Figures

Figure 1. Expanded SCC initiation test matrix selected in 2017.	5
Figure 2. Expanded SCC test matrix objectives.	6
Figure 3. Load train for crack initiation testing as installed in PNNL’s small, medium, and large autoclave systems. The interior heights are approximately 33, 60, and 100 cm, respectively.	9
Figure 4. DCPD signal variability for one specimen in a 3-specimen test before and after modifications to the SCC initiation testing software.	11
Figure 5. Servo load, verification load, pull rod tare load, and temperature variation for a PNNL high temperature water SCC test system over a period of ~575 hours.	12
Figure 6. SCC initiation time plotted versus stress for all 36 of the 15% CF Alloy 182 specimens being tested at their YS.	14
Figure 7. Distribution of constant load PWSCC initiation times from PNNL tests of specimens from four 15% CF Alloy 182 welds.	15
Figure 8. Distribution of constant load PWSCC initiation times from EdF tests of Alloy 182 welds with similar applied load to the 15% CF Alloy 182 specimens tested by PNNL.	16
Figure 9. Stress versus strain curve during the initial loading of three 15% CF Phase 2B specimens, IN185-87.	18
Figure 10. Stress versus strain curve during the initial loading of three 15% CF KAPL specimens, IN194-96.	18
Figure 11. SCC initiation time versus initial plastic strain applied to 15% CF Alloy 182 specimens meant to be tested at their YS.	19
Figure 12. SCC initiation time versus total plastic strain applied to 15% CF Alloy 182 specimens meant to be tested at their YS.	19
Figure 13. Stress versus strain response for three 15% CF Studsvik Alloy 182 specimens loaded to 0.2% offset plastic strain yield stress.	20
Figure 14. Stress versus strain response for six 15% CF Studsvik Alloy 182 specimens brought up to 90% YS.	22
Figure 15. Stress versus strain response for six 15% CF KAPL Alloy 182 specimens brought up to 90% YS.	22
Figure 16. Distribution of constant load Alloy 182 PWSCC initiation times as a function of material strength for PNNL tests.	24
Figure 17. DCPD response of the four instrumented Alloy 690 specimens in NRC11. The gray line is the servo displacement. Temporary rapid increases in displacement occur after test restarts.	29
Figure 18. DCPD response of the four instrumented Alloy 52 specimens in NRC11. The gray line is the servo displacement. Temporary rapid increases in displacement occur after test restarts.	30
Figure 19. DCPD response of the four instrumented Alloy 152 specimens in NRC11. The gray line is the servo displacement. Temporary rapid increases in displacement occur after test restarts.	30

Figure 20. SEM-BSE image of the gauge surface of the 15% CF Alloy 690 plate TK-VDM specimen IN108 after 20,659 hours of exposure.33

Figure 21. (a) SEM-BSE image of IN108 showing the location of the FIB trench with an arrow indicating the direction of FIB serial milling, and (b) FIB-SE image showing the starting cross section of the trench in IN108.33

Figure 22. Examples of the FIB-SE images taken of IN108 during the serial FIB milling along the selected portion of a GB identified in Figure 21(a).33

Figure 23. Representative SEM-BSE images of the gauge surface of the 15% CF Alloy 690 CRDM Valinox WP142 specimen IN118 after 20,659 hours of exposure.34

Figure 24. Representative SEM-BSE images of the gauge surface of the 15% CF Alloy 690 CRDM Valinox RE243 specimen IN126 after 20,659 hours of exposure.35

Figure 25. Examples of the FIB-SE images taken of IN126 during the serial FIB milling along the selected portion of a GB identified in Figure 24.35

Figure 26. Representative SEM-BSE images of the gauge surface of the 15% CF Alloy 690 bar Allvac B25K-2 specimen IN137 after 20,659 hours of exposure.36

Figure 27. Representative SEM-BSE images of the gauge surface of the 15% CF Alloy 52M ENSA DPM specimen IN112 after 20,659 hours of exposure.37

Figure 28. (a) SEM-BSE image showing the location of the two FIB trenches in IN112, (b) examples of the FIB-SE images taken during the serial FIB milling along the selected portion of a GB identified in (a), and (c) FIB-SE image showing the cross section of the trench at the location identified in (a).37

Figure 29. SEM-BSE/SE images of the two small cracks identified in the gauge surface of the 15% CF Alloy 152M IHI specimen IN128 after 20,659 hours of exposure.38

Figure 30. (a) SEM-BSE image showing the location of the two FIB trenches in IN128, (b) FIB-SE image showing the cross section of the trench at the location identified in (a), and (c) examples of the FIB-SE images taken during the serial FIB milling along the selected portion of a GB identified in (a).39

Figure 31. Representative SEM-BSE images of the gauge surface of the 15% CF Alloy 52 MHI specimen IN124 after 20,659 hours of exposure.40

Figure 32. Representative SEM-BSE images of the gauge surface of the 15% CF Alloy 152 MHI specimen IN142 after 20,659 hours of exposure.40

Figure 33. Test data for 15% CF, initiated PNNL Alloy 182 samples: a) PWSCC time to initiation vs. true stress; b) PWSCC time to initiation vs. stress ratio.45

Figure 34. Test data for Alloy 182 samples that exhibited SCC initiation obtained at PNNL and other laboratories: a) initiation time vs. true stress; b) initiation time vs. stress ratio.47

Figure 35. Same data and regression curves as in Figure 34 with additional information for prediction bands and confidence bands plotted.49

Figure 36. Test data for Alloy 182 samples with and without SCC initiation obtained at PNNL and other laboratories: a) initiation time vs. true stress; b) initiation time vs. stress ratio.51

Figure 37. Histograms of SCC initiation time for a) PNNL’s test data and other labs’ data in linear and natural log scale; and b) other labs’ data with applied stress range from 350 to 600 MPa in tests. The stress range is selected to roughly match PNNL data and avoid counting low initiated time data at higher stress levels.52

Figure 38. Two-parameter Weibull fittings to Alloy 182: a) tested at PNNL; b) tested at other labs. Note that only data with applied stress ranging within 350-600 MPa were included to match PNNL’s testing condition.53

Figure 39. Weibull analysis on initiated datasets and right-censored datasets for PNNL’s test data, other labs’ data, and the combined of both. The solid lines are the characteristic time θ , as described by the Equation 8, which corresponds to the ~63.2% cumulative probability of SCC initiation at a giving stress ratio.54

Figure 40. PNNL A600 initiation testing result plotted as test time against a) applied stress, and b) stress ratio between applied stress and yield strength of non-cold worked materials at the test temperature.56

Figure 41. Test data for 15% CF, initiated PNNL Alloy 600 samples: a) PWSCC time to initiation vs. true stress; b) PWSCC time to initiation vs. stress ratio.57

Figure 42. Test data for 15% CF, initiated PNNL Alloy 600 samples excluding heat 31907: a) PWSCC time to initiation vs. true stress; b) PWSCC time to initiation vs. stress ratio.58

Figure 43. Test data for Alloy 600 samples that exhibited SCC initiation obtained at PNNL and other laboratories: a) initiation time vs. true stress; b) initiation time vs. stress ratio.59

Figure 44. Re-analysis on several published Alloy 600 datasets using true stress: a) Bandy and van Rooyen 1983 [14], n=2.8; b)Yonezawa 1991 [22], n=1.9; c) Itoh 1994 [21], n=2.4.60

Figure 45. Same data and regression curves as in Figure 43 with additional information for prediction bands and confidence bands plotted.61

Figure 46. Test data for Alloy 600 samples with and without SCC initiation obtained at PNNL and other laboratories: a) initiation time vs. true stress; b) initiation time vs. stress ratio.62

Figure 47. Histograms for SCC initiation time for PNNL’s Alloy 600 test data and other labs’ data in linear and natural log scale.63

Figure 48. Two-parameter Weibull fit to a) Alloy 600 tested at PNNL, and b) Alloy 600 tested at other labs, note the applied stress range is limited to 350-750 MPa, which is the same range as PNNL testing, for comparison.64

Figure 49. Weibull analysis on initiated datasets and right-censored datasets for PNNL’s test data, other labs’ data, and the combined of both. The solid lines are the characteristic time θ , as described by the Equation 8, which corresponds to the ~63.2% cumulative probability of SCC initiation at a giving stress ratio.65

Figure 50. Power law fit to the other labs’ Alloy 182 test data and associated residues: a) linear regression on log-transformed data; b) non-linear regression on raw data.67

Figure 51. Schematic of the surface area of one rotation mapped in SEM for pre-, mid- and post-test examination. The gauge surface mapped in SEM is highlighted in pink and the surface in the fillet region mapped in SEM is highlighted in taupe.69

Figure 52. Referenced strain response for three 15% CF KAPL Alloy 182 specimens, IN166-68.71

Figure 53. Post-test SEM-BSE montage imaging of the entire surface of the gauge and fillet region of the first set of 15%CF KAPL Alloy 182 weld specimens, IN166-168, after initiation was detected. The cracks are highlighted in red.71

Figure 54. Crack evolution on the surface of the 15%CF KAPL Alloy 182 specimen IN168 with SCC initiation detected at 115 hours of exposure. The cracks are highlighted in red with zoom-in images showing the primary crack nucleated from a pre-existing defect on a solidification grain boundary.72

Figure 55. S-L-T nomenclature of cracking orientations relative to weld grain structure.73

Figure 56. The SEM SE (left) and BSE (right) images of the fractured surface of the 15% CF KAPL Alloy 182 specimen with initiation detected at 113 hours. Orange and yellow outlines encompass IG cracking. The position of the precursor crack observed at 33 hours is marked in red along the perimeter of the specimen.73

Figure 57. Referenced strain response during the first 200 hours of the constant load SCC initiation testing for the nine 15% CF Studsvik Alloy 182 specimens.74

Figure 58. Post-test SEM examination of the surface of the 15% CF Studsvik Alloy 182 specimens IN233 and IN170 that initiated at around 30 hours of exposure. Obvious cracks are highlighted in red. The likely primary crack leading to DCPD detection of SCC initiation is also identified in each specimen.75

Figure 59. Post-test SEM examination of the surface of the 15% CF Studsvik Alloy 182 specimens IN191-193 that initiated at 41-83 hours of exposure at yield stress. Obvious cracks are highlighted in red. A zoom-in image was also shown on the primary crack leading to DCPD detection of SCC initiation in each specimen.75

Figure 60. The SEM SE (left) and BSE (right) montage imaging of the fractured surface of the 15%CF Studsvik Alloy 182 specimen with initiation detected at 30 hours of exposure. The area of IG failure was highlighted in orange.76

Figure 61. SEM montage images showing the evolution of the gauge surface of the 15% CF Studsvik Specimen IN233 that initiated within ~30 hours of testing in high temperature water at yield stress. Cracks are highlighted in red.77

Figure 62. SEM montage images showing the evolution of the gauge surface of the 15% CF Studsvik Specimen IN193 that initiated at ~41 hours of testing in high temperature water at yield stress. Defects and cracks are highlighted in red. The zoom-in images of a large dent and a small crack in the fillet region are also presented showing no evolution during the short exposure time.78

Figure 63. SEM montage images showing the evolution of the gauge surface of the 15% CF Studsvik Specimen IN192 that initiated at ~41 hours of testing in high temperature water at yield stress. Defects and cracks are highlighted in

red. The zoom-in image of a small crack in the fillet region is also presented showing no evolution during the short exposure time.....78

Figure 64. SEM montage images showing the evolution of the gauge surface of the 15% CF Studsvik Specimen IN191 that initiated at ~83 hours of testing in high temperature water at yield stress. No pre-existing defects were found prior to testing. Cracks are highlighted in red.....79

Figure 65. Higher magnification SEM-BSE (unless otherwise noted) images acquired prior to test on the pre-existing defects at Site P1 marked in IN192 in Figure 63.80

Figure 66. EDS composition maps of the sites P1-a and b identified in Figure 65. The EDS was conducted using low acceleration voltage (5 kV) for small interaction volume and better detectability of light elements, so that qualitative information of the chemical composition of sub-micrometer size precipitates on the surface can be obtained.80

Figure 67. Crack evolution at Site P1 in Figures 63-66 on the surface of the 15%CF Studsvik Alloy 182 specimen IN192 with SCC initiation detected at 41 hours of exposure. The pre-existing defects are highlighted in blue while the cracks are highlighted in yellow and IG attack along grain boundaries are highlighted in orange. No observable change occurred in the pre-existing defects and new cracks were nucleate at grain boundaries that appear clean of defects.81

Figure 68. SEM examination of the primary crack marked at Site C1 in Figure 62 before and after testing on the surface of the 15% CF Studsvik Specimen IN193 that initiated at ~41 hours of testing in high temperature water at its yield stress.82

Figure 69. SEM examination of the crack marked at Site C1 in Figure 63 before and after testing on the surface of the 15% CF Studsvik Specimen IN192 that initiated at ~41 hours of testing in high temperature water at its yield stress.83

Figure 70. SEM examination of the primary crack marked at Site C2 in Figure 63 before and after testing on the surface of the 15% CF Studsvik Specimen IN192 that initiated at ~41 hours of testing in high temperature water at its yield stress.84

Figure 71. Referenced strain response during the first 300 hours of the constant load SCC initiation testing for the nine 15% CF Phase 2B Alloy 182 specimens.85

Figure 72. Post-test SEM examination of the surface of the 15% CF Phase 2B Alloy 182 specimens IN185 and IN216 that initiated within 150 hours of exposure at yield stress. Obvious cracks are highlighted in red. The primary crack leading to DCPD detection of SCC initiation in each specimen is also shown in a zoom-in image.85

Figure 73. Post-test SEM examination of the primary crack of the 15% CF Phase 2B Alloy 182 specimen IN216 initiated at 132 hours.86

Figure 74. Referenced strain response during constant load SCC initiation testing for the nine 15% CF Flawtech Alloy 182 specimens.87

Figure 75. SEM examination of the surface before and after testing of 15% CF Flawtech Alloy 182 specimens IN188 and IN189 that initiated within 30 hours of

exposure. The pre-existing cracks were observed in these two specimens and are highlighted in the pre-test SEM montage images.88

Figure 76. SEM examination of the surface before and after testing of 15% CF Flawtech Alloy 182 specimens IN223 and IN190 that initiated at ~80-90 hours of exposure. No pre-existing defects are related to the cracks that formed later during exposure.89

Figure 77. SEM examination of the surface before and after testing of 15% CF Flawtech Alloy 182 specimens IN221 and IN222 that initiated at ~100-160 hours of exposure. No pre-existing defects are related to the cracks that formed later during exposure.90

Figure 78. SEM examination of Sites 2 and 3 in Figure 58 before and after SCC initiation testing of the 15% CF Flawtech specimen IN189 that initiated at ≤30 hours of testing in high temperature water at its yield stress.91

Figure 79. SEM examination of Site 5 in Figure 76 after SCC initiation testing of the 15% CF Flawtech specimen IN190 that initiated at ~90 hours in high temperature water at its yield stress.92

Figure 80. Post-test SEM backscatter electron (BSE) montage images of the two 15%CF Studsvik Alloy 182 specimens IN169 (left) and IN233 (right) with obvious cracks highlighted in red. The locations for cross-sectioning and TEM sampling in each specimen are marked in yellow.94

Figure 81. SEM(BSE) of small (micrometers), IG weld defects observed in a cross section of IN233.95

Figure 82. SEM(BSE) of small (micrometers), IG weld defects observed in IN233 that have joined up to form a 20 μm long defect.96

Figure 83. SEM(BSE) of larger (tens to hundreds of micrometers) TG weld defects observed in IN233. Smaller, tight cracks were observed to emanate from these sub-surface defects.97

Figure 84. SEM(BSE) images detailing the void space sub-surface discovered during FIB milling of a TEM lamella from IN233. The TEM lamella was aimed at capturing the identified IGA observed in the trench wall.98

Figure 85. SEM(SE) and EDS elemental maps of the FIB lamella trench showing sub-surface void space.98

Figure 86. SEM(BSE) of micrometer size IG weld defects observed in IN169.99

Figure 87. SEM(BSE) of micrometer, cuboidal oxides observed TG in the sample. Brighter Nb-rich phases were noted to form on the surface. When this oxide intersects the surface, the high temperature water appears to form spinel on top of the matrix oxide.100

Figure 88. SEM(BSE) and EDS of the Cr-, Ti-, Al-, and Mn-rich oxides observed both IG and TG within the bulk of the sample. NbC can be observed nucleating from these larger oxide crystals.100

Figure 89. SEM(BSE) of micrometer, cuboidal oxides observed at TG locations in the sample. Brighter Nb-rich phases were noted to form on the surface.101

Figure 90. SEM(BSE) and EDS of the Cr-, Ti-, Al-, and Mn-rich oxides observed both IG and TG within the bulk of the sample. NbC can be observed nucleating from these larger spinel crystals.101

Figure 91. SEM(BSE) of a number of representative instances of IGA in IN233. The images in the right-hand column are higher magnification conjugates of the lower magnification regions in the left-hand column. The IGA depths were all on the order of hundreds of nanometers.	102
Figure 92. SEM(BSE) and representative EDS of IGA in IN233.	103
Figure 93. SEM(BSE) of a number of representative instances of IGA in IN169. The IGA depths were all greater than 0.5 μm with the longest noted at $\sim 2 \mu\text{m}$	104
Figure 94. SEM(BSE) and representative EDS of IGA in IN169. Note the Ni-rich regions adjacent to the IGA which are indicative of DIGM.	104
Figure 95. SEM(BSE) of one IGSCC crack ($\sim 40 \mu\text{m}$ long) at various magnifications. In this IN233 cross section this was the only crack observed.	105
Figure 96. SEM(BSE) and representative EDS mapping of the leading SCC crack tip in IN233.	105
Figure 97. (a) SE, (b) IPF-X, (c) KAM, and (d) GOS maps of the cross-sectional region in IN233 intersecting the primary crack (Crack 3) and two other cracks found on the surface as shown in Figure 80.	106
Figure 98. (a) SE, (b) IPF-X, (c) KAM, and (d) GOS maps of the cross-sectional region in IN169 intersecting a large, halted crack found on the surface as shown in Figure 80.	107
Figure 99. A closer look at the TEM lift-out sampling location in IN233. In the second image to the left, the cracks are highlighted red while SGBs with IGA are highlighted in yellow.	109
Figure 100. STEM ADF and BF FIB cross section of IN233 showing IGA.	110
Figure 101. STEM ADF and EDS elemental maps of the near-surface IGA of IN233.	111
Figure 102. Higher magnification STEM ADF and EDS elemental images of the near-surface IGA in IN233. The Fe and Cr-rich IGA appears to have increased concentrations of Cl, Ti and S.	111
Figure 103. Higher magnification STEM ADF and EDS elemental maps of the leading IGA of IN233 showing the grain boundary is decorated with Cr carbides and manganese sulfides on the order of tens of nanometers.	112
Figure 104. Subset of the EDS spectrum from a summed region containing Cl signal illustrating that the Cl-K edge is not an artifact. The series of vertical gray lines are the theoretical positions of the Nb-L edge, and hence the identification of the Nb at the Cl-K alpha line is a function of the EDS software labeling and does not indicate Nb (i.e., the Nb line at that energy does not follow the theoretical trend).	112
Figure 105. STEM ADF and BF of the cross section of the second FIB lift-out from IN233 showing IGA as well as a large oxide inclusion micrometers from the surface.	113
Figure 106. STEM ADF and EDS elemental maps of the near-surface IGA of IN233.	114
Figure 107. STEM ADF and EDS elemental images of the near-surface IGA in IN233. The Fe- and Cr-rich IGA appears to have increased concentrations of Cl, Ti and S.	115
Figure 108. STEM ADF and EDS elemental maps of the middle of the IGA of IN233 showing the distribution of the Fe/Cr oxides as well as Ti, Cl and S	

	impurities. A spectrum of the Cl-K edge summed from the region of high Cl is also provided.....	116
Figure 109.	EELS mapping and atomic column imaging of the Ni-rich nodule observed in the middle of the IGA. The atomic column image is flipped from the EELS orientation.	117
Figure 110.	Higher magnification STEM ADF and EDS elemental maps of the leading IGA of IN233 showing the grain boundary is decorated with Cr carbides and manganese sulfides on the order of tens of nanometers. Two line scans were performed across the grain boundary at locations indicated by the arrows in the upper-left figure and the composition variation is shown in the two figures at the bottom.	118
Figure 111.	STEM ADF and EDS elemental maps of the surface oxide indicating the presence of S within the penetrative oxidation and the lack of any Cl signal.	119
Figure 112.	STEM ADF and EDS elemental maps of the sub-surface cuboidal oxide indicating it is rich in Cr, Ti, Mn and Al. MnS and NbC were observed directly adjacent to this large oxide particle.....	120
Figure 113.	Large, buried oxide in the [001] and [114] orientations (spinel type structure). EDS shows it has a core shell of Al-rich oxide. The small Nb-rich and MnS particles around it are oriented to the oxide suggesting that it was in the melt before solidification. It does not have an orientation relationship to either metal grain.	120
Figure 114.	SAD patterns collected from the {001} orientation of the spinel, spinel plus NbC and spinel/NbC/MnS showing that the NbC and MnS are oriented to the spinel.	121
Figure 115.	STEM ADF and BF of the 1 st FIB cross section of IN169 showing IGA of ~500 nm deep from the surface. The IGA is surrounded by penetrative oxidation until last 50 nm of the IGA.	122
Figure 116.	STEM ADF and EDS elemental maps of the near-surface IGA of IN169.	122
Figure 117.	Higher magnification STEM ADF and EDS elemental maps of the near-surface IGA of IN169. Arrows point to regions of DIGM.	123
Figure 118.	STEM ADF and EDS elemental maps of the grain boundary ~1-2 μm ahead of the leading IGA showing minor Cr depletion, Cr and Nb carbides, and no apparent segregation of impurities such as Cl.	124
Figure 119.	Cr-K elemental map of a representative grain boundary micrometers ahead of the IGA showing sensitization.	124
Figure 120.	STEM ADF and BF of the 2 nd FIB cross section of IN169 showing IGA of ~600-700 nm deep from the surface. The IGA is surrounded by penetrative oxidation until last 200 nm of the IGA.....	125
Figure 121.	STEM ADF and EDS elemental maps of the near-surface IGA of IN169.	126
Figure 122.	Higher magnification STEM ADF and EDS elemental maps of the near-surface IGA of IN169 showing the leading IGA front ending near a Cr carbide.....	127
Figure 123.	STEM ADF and BF of the 3 rd FIB cross section of IN169 showing IGA of ~600 nm deep from the surface. The IGA is surrounded by penetrative oxidation until last 200 nm of the IGA.....	128

Figure 124. STEM ADF and EDS elemental maps and line scans of the near-surface IGA of IN169.	129
Figure 125. STEM ADF and BF of a TG inclusion near the IGA intersecting the surface.	130
Figure 126. STEM ADF and EDS elemental maps of the TG inclusion near the surface IGA of IN169.	130
Figure 127. Higher magnification of the Ni-rich portion of the STEM ADF and EDS elemental maps of the TG inclusion near the surface IGA of IN169.	131
Figure 128. Expanded SCC initiation test matrix selected in 2017.	136
Figure 129. NRC-expanded SCC initiation test matrix selected in 2019.	137
Figure 130. SCC initiation behavior of Alloy 600 tested for the DOE LWRS program [3].	138

Tables

Table 1. Candidate heats/welds for each class of material.	4
Table 2. Signal-to-noise ratio improvements for each SCC initiation test system using the modified DCPD scanning method. Values are the average of three of the specimens in the test system.	11
Table 3. SCC initiation times for nine each of four 15% CF A182 welds tested at YS. The combined mean and median initiation times are 1,453 and 735 hours, respectively.	13
Table 4. SCC initiation times for six each of two 7.5% CF Alloy 182 welds tested at YS.	17
Table 5. SCC initiation times for six each of two 15% CF A182 welds tested at 90% YS.	23
Table 6. SCC initiation times of the 15% CF Alloy 600 materials. S# is the string where the specimen resides if it was tested in a 3-string load line. Mean, std. dev., and median of all specimens combined is 858, 683, and 525 hours, respectively.	26
Table 7. Selected information on the Alloy 690/152(M)/52(M) specimens being tested in NRCI-1. The rows correspond to each string, while the yellow highlight indicates specimens with the smallest gauge diameter. The specimens in String-1 (S1) are instrumented for DCPD.	28
Table 8. Current factors of improvement for Alloy 690 relative to Alloy 600 and Alloy 152(M)/52(M) relative to Alloy 182.	29
Table 9. Strain rates measured on Alloy 690, 52, and 152 at ~12,000 hours of exposure in high temperature water (360 °C).	31
Table 10. Alloy 690/152(M)/52(M) specimens examined after 2.4 years of exposure at their YS.	32
Table 11. Estimated parameters for Direct Model 1 defined initiation time-stress relationship for 15% CF Alloy 182.	46
Table 12. Estimated pre-exponential factors and stress exponents for Direct Model 1 for Alloy 182. The pre-exponential factors are expressed with standard error inside the exponential term due to the log transformation.	47
Table 13. Estimated pre-exponential factors and stress exponents for Direct Model 1 for Alloy 182 including non-initiated data. The pre-exponential factors are expressed with standard error inside the exponential term due to the log transformation.	51
Table 14. Parameters for Weibull model analysis in Figure 39.	55
Table 15. Estimated parameters for Direct Model 1 for 15% CF Alloy 182.	57
Table 16. Power law fitting parameters for Alloy 600 SCC initiated data.	60
Table 17. Power law fitting parameters for Alloy 600 SCC initiated and non-initiated data.	63
Table 18. Parameters for Weibull model analysis in Figure 49.	66
Table 19. SCC initiation times for nine each of four 15% CF Alloy 182 welds tested at YS.	68

1.0 Introduction

The goal of this program is to produce stress corrosion crack initiation (SCCI) data on Alloys 690/152(M)/52(M) and Alloys 600/182 in support of a factor of improvement (FOI) determination for Alloys 690/152(M)/52(M) over Alloys 600/182, and to generate temperature, stress, and material strength dependencies for Alloy 182 SCCI times for validation and future refinements of the models that were developed under the Extremely Low Probability of Rupture (xLPR) Program. To accomplish these goals, the U.S. Nuclear Regulatory Commission (NRC) and the Electric Power Research Institute (EPRI) have, through a Memorandum of Understanding Addendum, jointly funded a program at PNNL to perform SCCI testing on these materials. As a first step in this crack initiation testing program, Pacific Northwest National Laboratory (PNNL) proposed a test plan that covered the test method, test matrix, specific materials, and test environment. Revisions to the test plan were made based on reviews by the NRC, EPRI, and experts in the light water reactor (LWR) stress corrosion community. To execute the final, agreed-upon plan, PNNL built two 36-specimen SCCI test systems that utilize in-situ detection of initiation of tensile specimens that are actively held at constant load.

PNNL developed expertise in SCCI testing through an earlier, and still ongoing program to conduct SCCI tests on Alloys 600 and 690 for the U.S. Department of Energy (DOE) Light Water Reactor Sustainability (LWRS) Program. As will be described in Section 2.0, the SCCI test method and equipment are continually being improved to obtain better quality data for all SCCI testing being conducted at PNNL.

The four heats/welds for each class of material, as shown in Table 1, were selected and obtained by PNNL. Many of these materials were obtained from the EPRI material inventory, and the EPRI Alloy 152M U-groove was made specifically to cover the needs of this program. These materials were described in extensive detail in the previous report [1].

Table 1. Candidate heats/welds for each class of material.

Alloy 182 Welds	
NRC/PNNL Phase 2B DMW Mockup Studsvik Buildup	NRC/PNNL Flawtech DMW Mockup KAPL U-Groove
Alloy 600	
Special Materials NX6106XK-11 MA Plate G.O. Carlson 33375-2B MA Plate	ATI 522068 MA Bar WNP5 CRDM Tube
Alloy 152(M)/52(M) Welds	
MHI Alloy 152 U-Groove Mockup ENSA DPM Alloy 52M Butter	MHI Alloy 52 U-Groove Mockup EPRI Alloy 152M U-Groove
Alloy 690	
Valinox RE243 TT CRDM Tube TK-VDM 114092 TT Plate	Valinox WP142 TT CRDM Tube Allvac B25K-2 MA Bar

For the original test plan, two 36-specimen test systems were constructed under NRC and EPRI funding with one test system for Alloy 600/182 tests and the other for Alloy 690/152(M)/52(M) tests. The original test plan was as follows:

Alloy 600/182 autoclave system

- First loading: Four different Alloy 182 welds. For each weld, there were to be six specimens made from 15% cold forged (CF) material and three specimens as-welded material.

- Second loading: Stress effects were to be assessed by loading specimens to specific fractions of their yield stress.
- Third loading: Four heats of Alloy 600. Nine specimens of each heat were to be tested in the 15% CF condition.
- Additional loadings were to be performed based on test results and perceived needs for additional studies.

Alloy 690/152(M)/52(M) autoclave system

- First and only loading: Four heats of Alloy 690 with three specimens per heat and one weld each of Alloys 152, 152M, 52, and 52M with six specimens per weld. All specimens will be in the 15% CF condition.

The use of cold forged materials for much of the test matrix was decided based on a number of factors. The first reason is that cold working was needed as a test accelerant. It was clear from prior SCC initiation tests of Alloy 182 and Alloy 600 by other labs that testing these materials in their as-fabricated (non-cold worked) condition would result in SCC initiation times that are well beyond the available time window to conduct the needed research, even when testing at 360°C. The second primary factor is that SCC initiation of Alloy 182 and Alloy 600 in field components typically occurs in regions of components that have undergone some degree of cold work. This cold work could be in the form of surface damage from grinding or in some cases, due to loose part damage. While cold work in plant components is thought to exist primarily in the near-surface regions of components, for purposes of measuring SCC initiation times, PNNL selected uniformly cold worked specimens because this allows factors such as strength and stress effects to be more directly evaluated. Cold forging in compression was selected because a large fraction of the Alloy 690 SCC growth rate data and some Alloy 152(M)/52(M) SCC growth rate data previously generated at PNNL and other laboratories had been conducted on cold forged materials, thus more readily providing a link between SCC initiation behavior and SCC growth behavior. This topic is covered in greater detail in the prior report [1].

In February 2017, a revised test matrix, as shown in Figure 1, was developed during a meeting between PNNL, NRC, EPRI, Dominion Engineering, and xLPR participants. The matrix includes an increased number of replicate specimens for the originally planned tests, and it includes several additional tests to better identify the effect of temperature, strength, and applied stress on SCC initiation times for Alloy 182 in support of xLPR. The tests that were selected to meet these needs are described in the testing timeline in Figure 2. To aid in completing this expanded test matrix, two 3-specimen test systems and a 6-specimen test system were made available. Efforts toward completing this expanded matrix are underway.

	2016	2017	2018	2019	2020	2021
36-Specimen System #1	<p style="text-align: center;"><u>Alloy 690/52/152 at 100% YS</u> 6 each of 4 welds @ 15% CF + 3 each of four base metals @ 15% CF (F1, F2)</p>					
36-Specimen System #2	<p style="text-align: center;"><u>15% CF A600</u> 6 each of 2 heats (F1)</p>	<p style="text-align: center;"><u>AW A182</u> 6 each of 4 welds (X3)</p>	<p style="text-align: center;"><u>15%CF A182 @ 345°C</u> 12 each of 2 welds (X4)</p>	<p style="text-align: center;"><u>15% CF A182 @ 330°C</u> 12 each of 2 welds (X4)</p>		
3-Spec. System #1	<p style="text-align: center;"><u>15% CF A182</u> 9 each of 4 welds (X1, F2)</p>		<p style="text-align: center;"><u>7.5% CF A182 @ YS</u> 6 each of 2 welds (X3)</p>	<p style="text-align: center;"><u>15% CF A600</u> 6 each of 2 heats (F1)</p>	<p style="text-align: center;"><u>15% CF A182 vs Dissolved Hydrogen</u> (X6)</p>	
3-Spec. System #2					<p style="text-align: center;"><u>15% CF A182 vs Surface Condition</u> (X7)</p>	
6-Spec. System		<p style="text-align: center;"><u>15% CF A182 @ 0.93YS</u> - 6 each of 2 welds (X2)</p>	<p style="text-align: center;"><u>15% CF A182 @ 0.85YS</u> 6 each of 2 welds (X2)</p>	<p style="text-align: center;"><u>7.5% CF A182 @ 0.93YS</u> - 6 each of 2 welds (X3)</p>	<p style="text-align: center;">Other Materials (Interfaces, weld defects)</p>	

Figure 1. Expanded SCC initiation test matrix selected in 2017.

Test Matrix and Timeline Mapping Testing Objectives

Testing Objectives

- xLPR Initiation Model Parameter Objectives (X)
 1. Alloy 182 microstructure / material variability
 2. Stress (or stress ratio = stress/YS)
 3. Yield strength
 4. Temperature
 5. Specimen geometry (tensile vs. bent beam) [bent beam data from NRC peening program]
 6. Hydrogen
 7. Surface condition (tensile and/or bent beam specimens)
- Factors of Improvement Objectives (F)
 1. Ratio of time to initiation for A690 vs. A600
 2. Ratio of time to initiation for A52/152 vs. A182

Test Specimens	2016	2017	2018	2019*	2020*	2021*
15%CF A182 @ YS 4 welds	X1, F2	X1, F2				
AWA182 @ YS 4 welds		X3	X3			
7.5%CF A182 @ YS 2 welds		X3				
15%CF A182 @ 330-345°C 2 welds			X4	X4	X4	
15%CF A182 @ Dh _{var}					X6	X6
15%CF A600 @ YS 4 heats	F1	F1		F1		
15%CF A182 @ 0.93YS 2 welds		X2	X2			
15% CF A182 @ 0.85 YS 2 welds			X2	X2		
7.5% CF A182 @ 0.93 YS 2 welds					X2	
15% CF A182 surface cond.					X7	X7
15% CF A182 4-pt bend		X5	X5			
15%CF A690 @ YS 4 heats	F1	F1	F1	F1	F1	F1
15%CF A52/152 @ YS 4 welds	F2	F2	F2	F2	F2	F2

Figure 2. Expanded SCC test matrix objectives.

To allow the revised test matrix to be completed in a reasonable time frame, four smaller autoclave systems were made available for use, of which, two systems were adapted for testing up to six specimens. Usage of the two 6-specimen test systems is being shared with the DOE LWRS program that owns the systems and co-funded their expansion. In addition, one large system from another NRC program is being used. The same NRC program will be providing two additional large systems in the near future, and another NRC program will be providing three 3-specimen test systems for use in the near future as well.

This report contains a summary of all activities conducted through September 30, 2020 on the NRC/EPRI project. Tables of SCCI times and plots have been updated for the test data obtained as of September 30, 2020. The primary focus of the report is analyzing Alloy 182 response; in particular, first assessments of fitting a stress exponent to the Alloy 182 data are provided. As part of that effort, the stress exponent for Alloy 600 was determined from both literature data and PNNL Alloy 600 data. Another focus area of the report is microstructural investigations aimed at understanding the source of the very low SCC initiation times observed in roughly half of the Alloy 182 specimens tested at their yield stress (YS). Non-destructive microstructural examinations were also performed on selected Alloy 690/152(M)/52(M) initiation specimens after 2.4 years of exposure.

2.0 SCC Initiation Testing Approach

2.1 Test Method

As described in detail in the prior report [1], the test method used for this program was based on a review of known test methods conducted prior to the start of research. Both specimen type and the data provided by the test method were evaluated. Attributes that are highly desirable for SCC initiation testing include:

1. Efficient use of available material. SCC initiation measurements of welds are an important part of this program. Welds are limited in size, especially if the weld is a mockup of an actual plant component, such as a feedwater nozzle dissimilar metal weld.
2. Ability to control material condition. It should be possible to test the material in any desired thermomechanical condition, in particular the level of applied deformation should be controllable because applied deformation can have a substantial effect on SCC initiation time, and some variability of cold work level is expected in plant components.
3. Ability to control specimen surface condition. Plant components may have a range of surface conditions because of the component fabrication method. For instance, welds are often ground smooth, and this process produces a highly cold worked surface layer.
4. Ability to test at a precisely known and controlled stress. Correlation of initiation time to applied stress is an important part of this research effort.
5. Actively maintained stress. This is perhaps most relevant to high temperature water testing where creep is known to occur and will result in stress relaxation if passive loading is used.
6. Ability to test multiple specimens simultaneously. SCC initiation behavior can be highly variable for a given material, and thus multiple tests of each combination of material and test condition need to be conducted to statistically evaluate the data and more clearly understand trends.
7. Ability to readily identify the initiation time.

Several types of specimens partially satisfy this list of attributes. For example, a u-bend specimen can satisfy only attributes 6 and 7 with appropriate testing methodology. A c-ring specimen can satisfy attributes 2, 3, 6, and 7 with appropriate testing methodology. A 4-point bend specimen satisfies all but attributes 4 and 5, although the surface stress can be reasonably well estimated via finite element modeling.

Through tailored experimental approaches, tensile specimens can satisfy all the desired attributes simultaneously. Tensile specimens have often been used for SCC initiation testing, although typically as single specimen tests with SCC initiation defined as the time of specimen failure rather than as the true time of crack initiation. It has been reasonably argued that the time to failure is going to be only slightly higher than the time to form small cracks.

A multi-specimen load line was utilized along with in-situ measurement of crack initiation to attain all the desired attributes. Up to 36 specimens can be tested simultaneously in one large test system, and in-situ measurement of crack initiation response is able to track the initiation behavior of multiple specimens simultaneously.

In-situ measurement of crack initiation is performed by the direct current potential drop (DCPD) method and has several desirable traits:

- The ability to track the initiation of multiple specimens allows for fewer test stops when conducting multi-specimen tests. In contrast, if crack initiation is tracked by specimen failure, then the test has to be stopped and restarted for each specimen failure. For example, when a 12-specimen test is conducted using in-situ identification of crack initiation time, often two or more specimens initiate at similar times, and in most cases, no more than six test stops are needed during the course of the test. However, if time to failure is utilized for a 12-specimen test, then 12 test stops are likely to be required.
- In-situ measurement of crack initiation allows for observation of microstructures directly associated with the initiation response. This can have enormous value for identifying mechanisms controlling SCC initiation.
- The DCPD method allows for specimen strains to be precisely tracked, thus providing detailed information on not only the stress but also the level of strain applied to a specimen when specimens are brought up to test load, making it possible to evaluate the SCC initiation behavior of a material as a function of its complete stress and strain history. As described in Section 3.3, this has been enormously useful for documenting that specimens have been loaded to target stress levels for SCC initiation tests conducted at sub-yield strength stresses.

2.2 Equipment

Test systems were designed and constructed for this program, and some test systems from other programs were made available for extended periods. These test systems are roughly identical with the exception of the autoclave size. Three sizes of autoclaves are being utilized for this research as shown in Figure 3, and the design of the systems was described in detail in the previous report [1]. The small systems can test up to three specimens simultaneously, while the medium size test systems can test up to six specimens. The large test systems can test up to 36 specimens simultaneously.

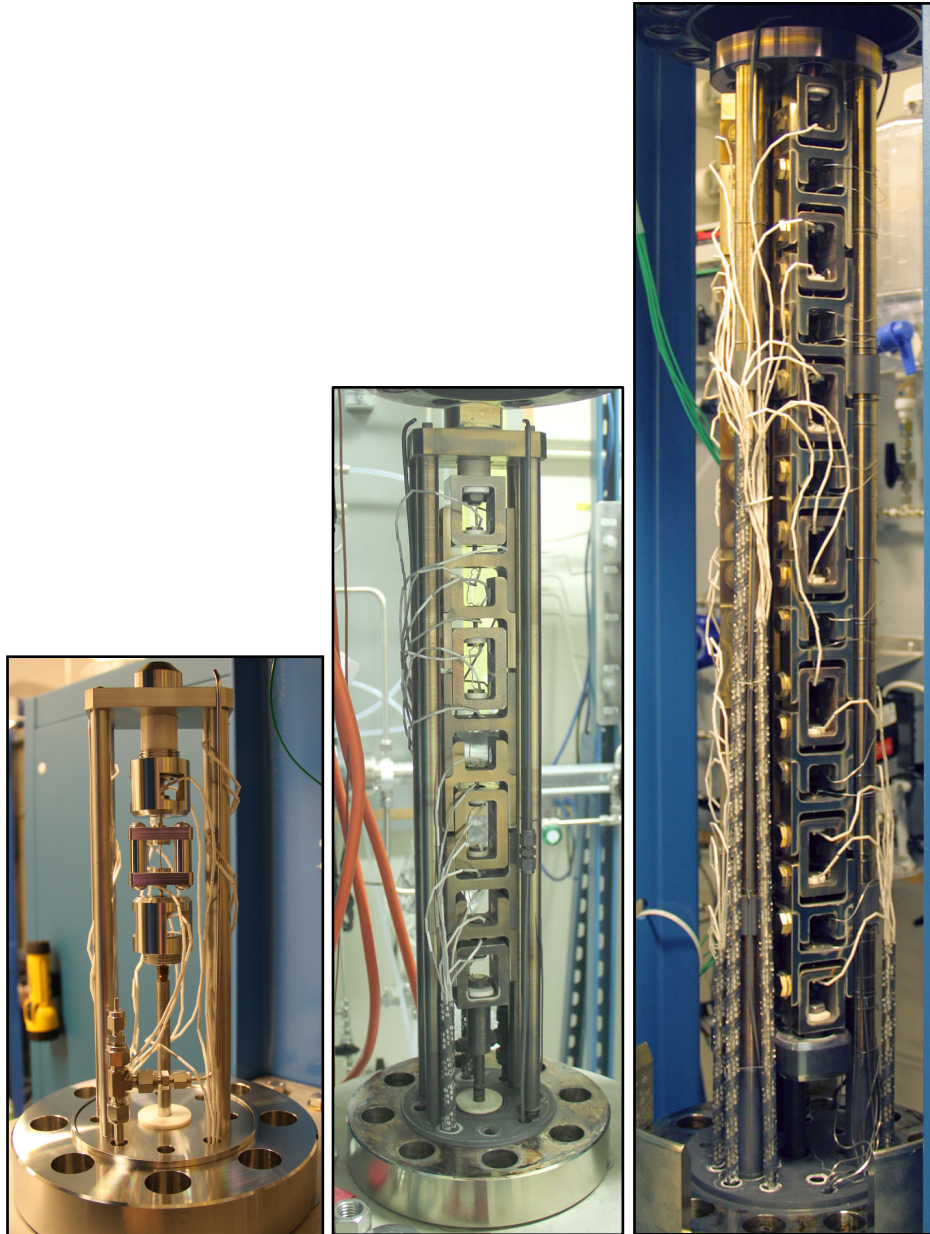


Figure 3. Load train for crack initiation testing as installed in PNNL's small, medium, and large autoclave systems. The interior heights are approximately 33, 60, and 100 cm, respectively.

2.3 Equipment Issues and Improvements

The test systems have generally been running reliably, although two components of the test systems, namely the DCPD system for detecting SCC initiation in-situ and the high pressure pumps for the high pressure water loop, have tended to be problematic areas. Substantial effort has been applied to resolve the issues, as discussed below.

The issue with the high pressure pumps is a suboptimal pump design exacerbated by a steady decline in component quality over the 16 years that PNNL has been purchasing these pumps. A very common issue with these pumps in recent years is that the pump head cover cracks, resulting in a high pressure water leak that cannot be fixed on-the-fly. Either a pump hot swap is required, or the test has to be stopped. Either way, there is undesirable loss of time and high costs associated with this. Another common issue is erratic pumping performance. The manufacturer has made no attempts to resolve quality or design issues despite PNNL presenting these issues numerous times. However, within the last year, the manufacturer has released a new model that appears to be designed to resolve all the issues experienced. New funding from the NRC this year is sufficient to begin purchasing new pumps, but rather than purchase the new model from the current manufacturer, an alternative brand was selected based on discussions with Lucideon on high pressure pumps that they have been evaluating. Swaps to these new pumps began in the fall of 2020.

The issues with the DCPD system were 1) low signal-to-noise ratio (SNR) in some of the systems, and 2) strong sensitivity to changes in laboratory environment, most likely temperature. Disassembly of the DCPD wiring in the problematic systems revealed incorrect assembly of the wiring that allowed for substantial crosstalk among the wiring and to earth ground. Rebuilding the wiring provided substantial improvements in SNR and reduced sensitivity to the laboratory environment. Further improvements in SNR were obtained through more careful grounding of shields and application of other electromagnetic interference (EMI) reduction techniques that had not been previously applied.

Another area where substantial improvement in SNR was obtained was in rewriting the DCPD hardware control algorithm. The record-to-record noise levels were substantially reduced through a change in how the DCPD electronics perform their measurement. Before-and-after examples for the best-case improvement are provided in Figure 4 using plots with the same scale range. The SNR improvement in this best-case example is 4.5x for the gauge section measurement and 10x for the reference region measurement. As shown in Table 2, the level of improvement as characterized by SNR did vary among systems. One system with excellent pre-existing SNR showed no improvement, several test systems exhibited mid-level improvements, and two exhibited very large improvements. Test systems that already had a good SNR tended to show the least amount of improvement. Conversely, there were a few test systems with poor SNR that also showed little improvement. SNR issues with these systems were resolved through repairing the hardware and applying improved EMI reduction methods. The DCPD control algorithm improvements were co-funded by all SCC programs at PNNL because all SCC programs benefited.

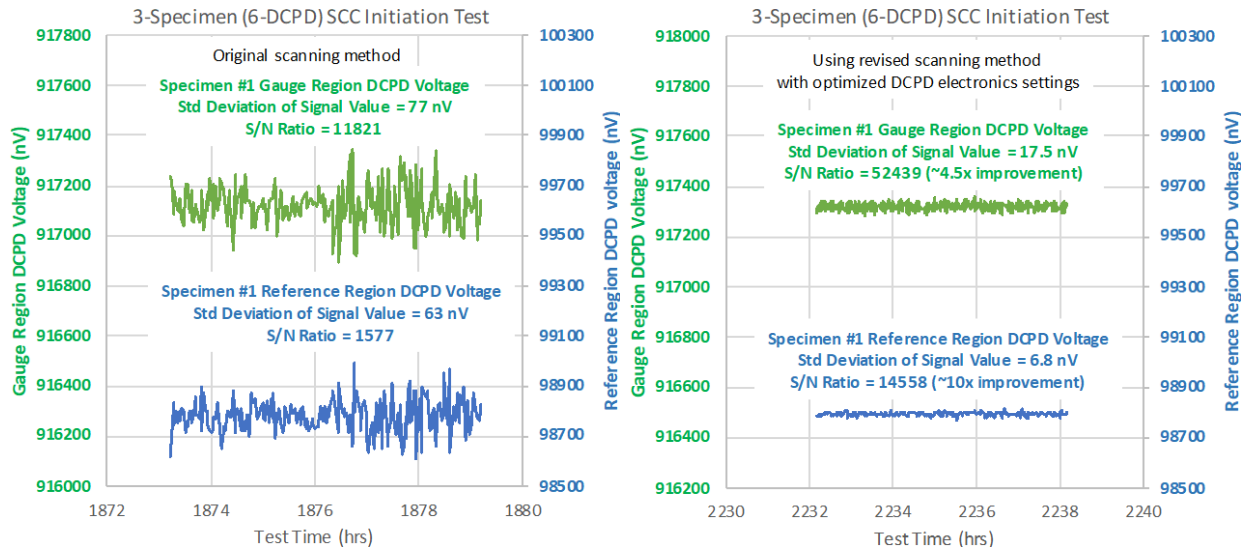


Figure 4. DCPD signal variability for one specimen in a 3-specimen test before and after modifications to the SCC initiation testing software.

Table 2. Signal-to-noise ratio improvements for each SCC initiation test system using the modified DCPD scanning method. Values are the average of three of the specimens in the test system.

Test System	Gauge Region SNR Before	Gauge Region SNR After	Gauge Region DCPD SNR Improvement Factor	Reference Region SNR Before	Reference Region SNR After	Reference Region DCPD SNR Improvement Factor
S1	11,222	17,517	1.6	2,112	3,265	1.5
S2	11,397	56,018	4.9	1,424	21,089	14.8
S3	10,933	45,666	4.2	NA*	NA	NA
S4	20,206	106,803	5.3	2,590	11,393	4.4
S5	18,114	40,961	2.3	3,028	15,962	5.3
S6	5,461	10,028	1.8	NA*	NA	NA
S7	5,662	84,305	14.9	NA*	NA	NA
S8	9,799	10,724	1.1	1,683	1,636	1.0

* This test system was not measuring DCPD across the reference region of any specimens.

The primary value of the SNR improvement is for tests where the reference region DCPD voltage is being monitored and used to estimate the reference-corrected strain because, as shown in Figure 4 and Table 2, the SNR of the reference region is much poorer than for the gauge. The magnitude of the voltage noise is approximately the same for the gauge and reference regions, and the cause of the reduced SNR in the reference region is due to an ~9x lower voltage compared to the gauge region.

In the time since the test systems were built, a second load cell and an electronic pressure sensor for the autoclave were added along with modifying the SCC initiation software to log these measurements. A second load cell was added to the test systems for two reasons. The first reason is that SCC initiation behavior may be highly dependent on small changes in load, in particular, for load variations that drop below the target load, so it was decided that it was important to monitor load as closely as possible. Secondly, in the event that the load measured by the verification load cell exceeds user-configurable upper or lower load limits, it has the

ability to disable the servo loading system. In effect, it is a secondary failsafe on the load control system to help prevent damage to specimens or the test system if a servo system fails in an out-of-control manner. This has happened on three older PNNL test systems for another program when the position feedback hardware on the servo motors failed without warning. There was no damage to the test systems, but specimens were destroyed.

The systems now monitor, and in most cases, control key parameters such as autoclave temperature, autoclave pressure, control load, and verification load to maintain specimen environmental stability. An example of the variability of some of these parameters is provided in Figure 5. As discussed previously, load applied to the specimens is a combination of servo load and pull rod tare load. Servo load in this example is very stable, exhibiting record-to-record variations of no more than ± 0.1 kg that are probably due more to noise in the electronics than an actual variation in load. Verification load (called backup load in the plot) shows some long-term drift, and for this observation, the total span of the drift is no more than 0.3 kg. Tare load that is controlled by water pressure has a nominal value of 147 kg and is stable to within ± 1.5 kg. This results in a total load variability of ± 2 kg and represents a $<0.5\%$ variability in the applied load for the typical target test load of ~ 454 kg. Temperature is extremely stable with a variation within $\pm 0.1^\circ\text{C}$.

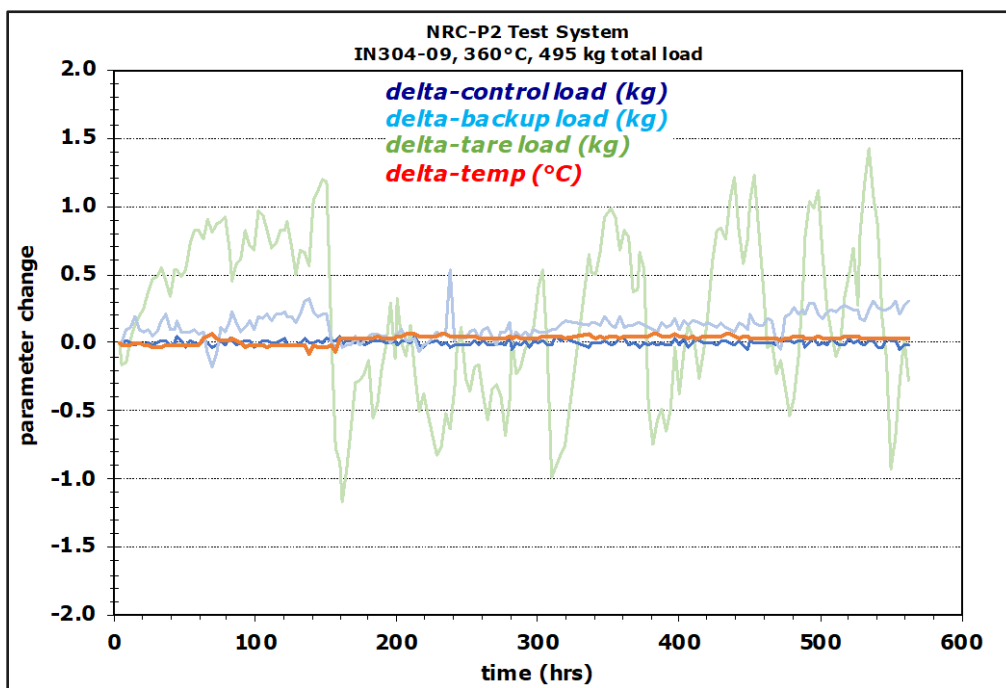


Figure 5. Servo load, verification load, pull rod tare load, and temperature variation for a PNNL high temperature water SCC test system over a period of ~ 575 hours.

One final comment for test system status is that, with the exception of the Alloy 690/152(M)/52(M) specimens, all tests being run in the large test systems are being run in a single string configuration rather than using a 3-string configuration. This decision was made after establishing that precisely measuring the initiation time of Alloy 600/182 specimens is highly important for determining environmental dependencies, and that this would best be done by instrumenting all specimens for DCPD-based observations of SCC initiation. The current limit on DCPD connections in a single system is 12 specimens, which is the capacity of a single string in the large systems.

3.0 Alloy 182 Testing Status

Alloy 182 was or is currently being tested in the 15% and 7.5% CF conditions at the YS (Sections 3.1 and 3.2) and in the 15% CF condition at 90% of YS (Section 3.3).

3.1 Alloy 182 Tests Conducted at Yield Strength Loading

For the Alloy 182 research, the 15% CF specimens tested at their YS represent the baseline condition used to compare SCCI response at other environmental and material conditions. As shown in Table 3, testing is essentially complete on all 36 of these specimens. 30 specimens have undergone SCC initiation, and the remaining 6 specimens have run out to relatively long exposure times without SCC initiation. Mean and median values are provided in the table because such values are commonly considered, but due to the high skew toward low SCC initiation times, these values provide only limited insight into the SCC initiation behavior.

Table 3. SCC initiation times for nine each of four 15% CF A182 welds tested at YS. The combined mean and median initiation times are 1,453 and 735 hours, respectively.

KAPL	YS (MPa)	t _{init} (h)	Studsvik	YS (MPa)	t _{init} (h)
IN166	563	≤30*	IN169	541	>5,126*
IN167	552	≤30	IN170	536	30
IN168	547	113	IN171	534	2,957
IN194	581	1,635	IN191	553	83
IN195	575	1,625	IN192	559	41
IN196	567	1,642	IN193	555	41
IN279	572	>5,554**	IN233	532	≤30
IN280	566	>5,554	IN234	529	725
IN281	576	>5,554	IN235	532	910
Average, Std. Dev.***		2,415; 2,311	Average, Std. Dev.		1,105; 1,680
Median		1,635	Median		83
Phase 2B	YS (MPa)	t _{init} (h)	Flawtech	YS (MPa)	t _{init} (h)
IN185	514	≤105	IN188	518	≤30
IN186	514	>3,173	IN189	518	≤30
IN187	514	409	IN190	518	90
IN197	500	806	IN200	528	825
IN198	506	4,964	IN201	528	746
IN199	506	2,238	IN202	528	900
IN216	462	132	IN221	525	106
IN217	467	>2,971	IN222	525	113
IN218	467	2,908	IN223	525	79
Average, Std. Dev.		1967, 1599	Average, Std. Dev.		324, 356
Median		2,238	Median		106

* Gray highlight indicates no pre-test examination of gauge surface. Red indicates that initiation is associated with an SEM-observable pre-existing defect. Blue indicates that initiation is not associated with any SEM-observable pre-existing defects.

** The ">" indicates not yet initiated. Test plan is to further expose if possible.

*** Statistical values based on exposure time of initiated and non-initiated specimens.

The initiation times for Alloy 182 plotted versus stress are presented in Figure 6. Among the four different welds, the Flawtech weld has the lowest average initiation time while the Phase 2B weld has the highest. However, all four welds had at least two specimens with an initiation time below 150 hours. The distribution of initiation times for these specimens is presented in Figure 7 and shows a strong peak at very low initiation times that is followed by a tail-like distribution out to very high SCC initiation times. While Alloy 182 is known to be more susceptible to SCC crack growth than Alloy 600, and, therefore, may be expected to have a lower SCC initiation time, the <150 hour initiation times for 16 of the 36 specimens tested across four distinctly different weldments was at first unexpected.

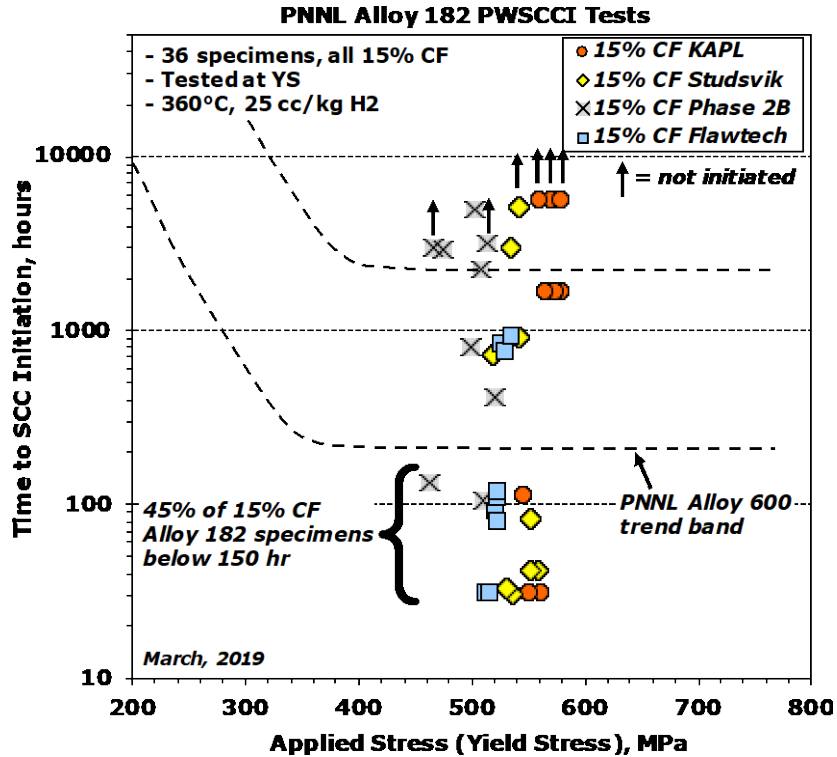


Figure 6. SCC initiation time plotted versus stress for all 36 of the 15% CF Alloy 182 specimens being tested at their YS.

However, a recent analysis of Électricité de France (EdF) Alloy 182 constant load SCC initiation tests [2] (Figure 8) conducted at similar stresses to the PNNL 15% CF Alloy 182 specimens shows very low SCC initiation times in some of those specimens when adjusting the initiation times for test temperature. For the EdF SCCI data scaled to 360°C using their activation energy of 185 kJ/mol, ~50% of the initiations occurred within 350 hours, followed by a tail-like distribution out to higher SCC initiation times like the PNNL tests. The low SCC initiation time values of the EdF tests are approximately double the PNNL, but like with the PNNL results, the EdF results have a large number of low SCC initiation times.

The somewhat higher minimum initiation time for the EdF tests may be due to material, environmental, and test method factors such as the type of cold work applied to the specimens, surface condition, and method for selecting SCC initiation time. PNNL has found that for its tests performed on Alloy 600, any added surface damage increases initiation time compared to polished specimens [3]. This appears to be due to the nano-crystalline grain structure in the

damage layer increasing Cr availability at the specimen surface. Another factor affecting initiation time is the method of measurement. Time to fracture for tensile specimens [2] and time to depressurization [4] for capsules were used by EdF which, based on PNNL experience, will add 24-100 hours compared to DCPD-measured time to initiation. While any one of these factors could be considered to have an inconsequential effect on initiation time, together these could account for the difference in initiation times measured by EdF and PNNL, and can potentially explain the higher minimum initiation time of the EdF tests.

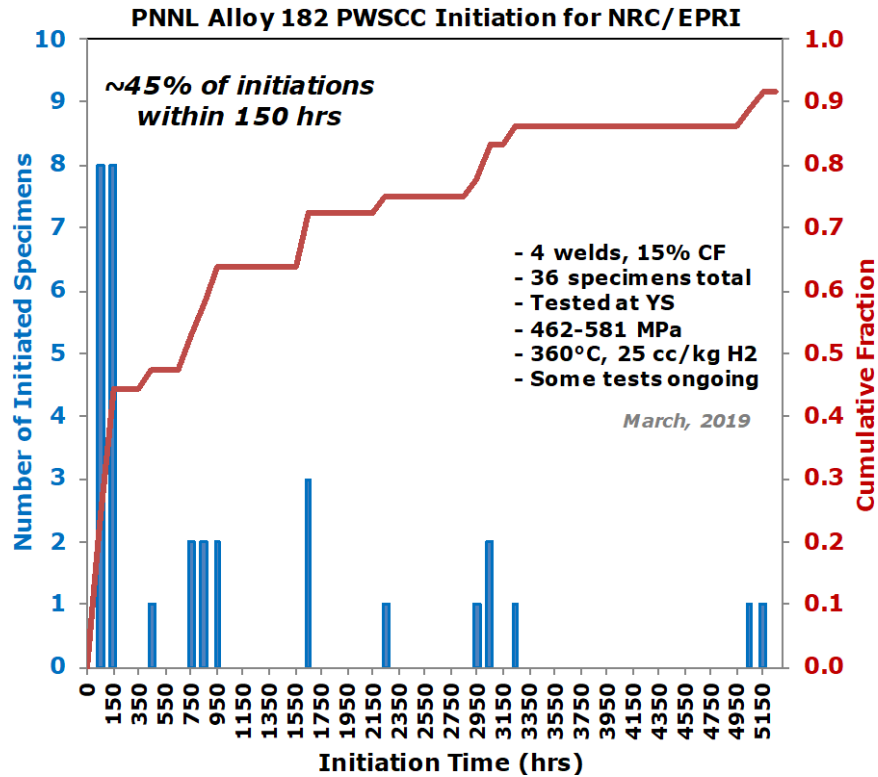


Figure 7. Distribution of constant load PWSCC initiation times from PNNL tests of specimens from four 15% CF Alloy 182 welds.

Physical damage to the specimens such as scratches and dents has been ruled out as being responsible for these low initiation times, and instead it appears that there is either a highly susceptible microstructural feature or a pre-existing weld fabrication defect that intersects the surface of each of these specimens. While a pre-existing weld fabrication defect can be thought of as a susceptible microstructural feature, it is important to differentiate between fabrication defects and inherently susceptible microstructures because they represent a different initiation mechanism. A sufficiently large pre-existing crack can be thought of as an already-initiated crack, while a susceptible microstructure drives initiation through rapid formation of a crack. Detailed SEM examinations of most specimens before and after testing has shown that a few cracks initiated from pre-existing defects (as noted Table 3), but the vast majority of the initiated specimens did not originate from an SEM-observable pre-existing defect. Some of these examinations were shown in the prior report [1], while a detailed comparison of gauge surfaces of the low initiation time specimens is provided in Section 7.0 of this report.

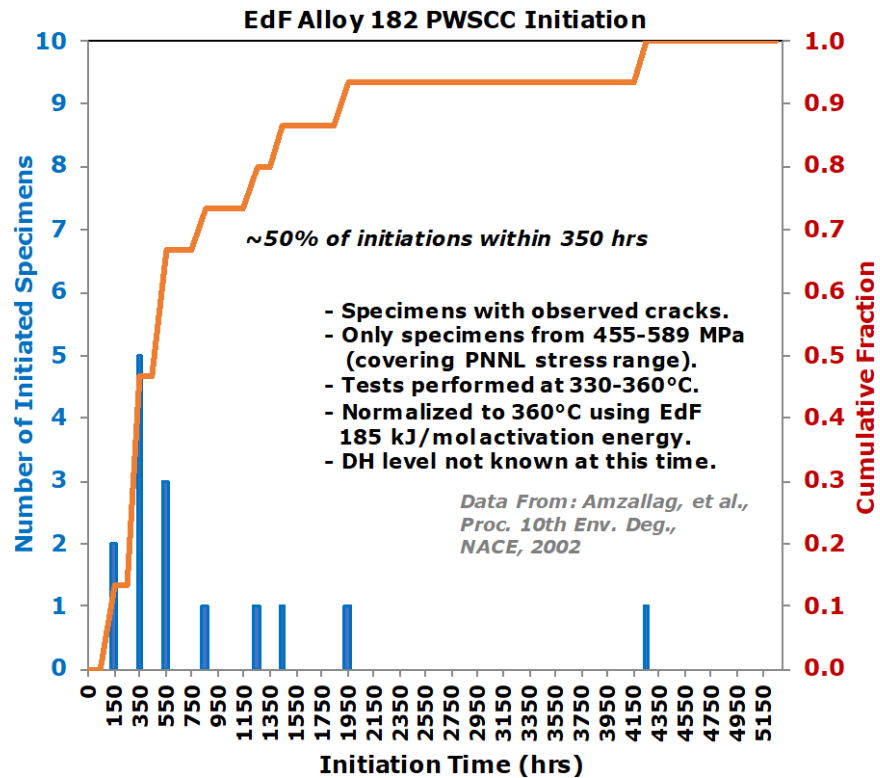


Figure 8. Distribution of constant load PWSCC initiation times from EdF tests of Alloy 182 welds with similar applied load to the 15% CF Alloy 182 specimens tested by PNNL.

Testing is ongoing for the 7.5% CF Alloy 182 at its YS, with summary information presented in Table 4. As was planned, only two of the four original Alloy 182 welds are being tested with six specimens from each of the two welds. The shortest initiation time among the 12 specimens is 602 hours, while several have now exceeded 5,500 hours. The 602-hour initiation time for the KAPL Alloy 182 weld is ~20x higher than the shortest initiation time observed for these two welds in the 15% CF condition (~30 hours). The average initiation time of these two welds at their YS in the 15% CF condition is at least 1,760 hours (accounting for suspended tests), while for the 7.5% CF material, the average is at least 5,407 hours. This is a 3.1x higher SCC initiation time for 7.5% CF compared to 15% CF. These statistics indicate a substantial increase in PWSCC initiation resistance at 7.5% CF compared to 15% CF.

Similarly, the 12 non-cold worked (CW) Alloy 182 specimens have now reached more than 27,800 hours of exposure with no initiations, also suggesting stronger SCC initiation resistance at lower CW levels. The current exposure time is 19x higher than the mean initiation time of the 15% CF material at its YS and 38x higher than the median initiation time. Section 6.0 provides a detailed statistical-based assessment of the stress exponent of Alloy 182 tested at its YS along with a comparison to Alloy 600 response.

Table 4. SCC initiation times for six each of two 7.5% CF Alloy 182 welds tested at YS.

KAPL	YS (MPa)	t _{init} (h)	Studsvik	YS (MPa)	t _{init} (h)
IN236	471	734	IN227	452	>7,734
IN237	472	602	IN228	440	>7,734
IN238	473	1,025	IN229	456	>7,734
IN310	462	>6,590	IN313	442	>6,517
IN311	463	>6,590	IN314	442	>6,517
IN312	463	>6,590	IN315	445	>6,517

† The ">" indicates not yet initiated. Test plan is to expose further if possible.

3.2 Effect of Plastic Strain During Loading on SCC Initiation Time

SCC initiation tests at PNNL are conducted on groups of 3 to 12 specimens, and under ideal circumstances such as shown in Figure 9, all specimens reach the same stress at virtually the same amount of applied plastic strain during loading. However, in some cases such as shown in Figure 10, variability in both the applied stress and applied plastic strain during loading occurs. This is due to the innate variability of the strength of materials, especially welds, and it is also due to small differences in gauge diameter of these specimens that are serially loaded and therefore all see the same load. It is evident from test stresses listed in Table 3 and Table 4 that the variation in final applied stresses is relatively small compared to the actual stresses.

The variations in applied plastic strain are also small but measurable. The PNNL method for bringing the specimens up to test load allows for the stress versus strain response of all specimens in the autoclave to be tracked in real time in high resolution. This is a unique capability absent from historical SCC initiation tests. For SCC initiation specimens meant to be tested at the YS, the load applied to the specimens just prior to the start of the test was intended to be increased until the specimens reached at least 0.2% plastic strain (following the standard definition of the YS of a material). However, not all specimens were loaded to at least 0.2% plastic strain due to specimen-to-specimen variability in the stress versus strain response within a group of specimens in which some specimens exhibited more plastic strain than desired.

To evaluate whether the SCC initiation time of the 15% CF Alloy 182 was substantially affected by the amount of applied plastic strain during loading of the specimens, the initiation data were plotted as function of the amount of initial plastic strain applied to the specimens. Initiation data was also plotted as a function of the cumulative plastic strain that results when specimens undergo small amounts of plastic strain during reloading to their test stress after a test is stopped to remove initiated specimens. These plots are shown in Figure 11 and Figure 12, respectively. Whether the initial plastic strain or cumulative plastic strain are considered, there appears to be a general trend for lower initiation times for higher amounts plastic strain applied during loading, but more careful inspection of the data, especially on a weld by weld basis, reveals that the variability is predominantly random for <0.3% plastic strain. However, as applied plastic strain surpasses 0.3%, there may be a very slight trend toward lower SCC initiation times. This is accentuated by the specimen loaded to 0.76% plastic strain.

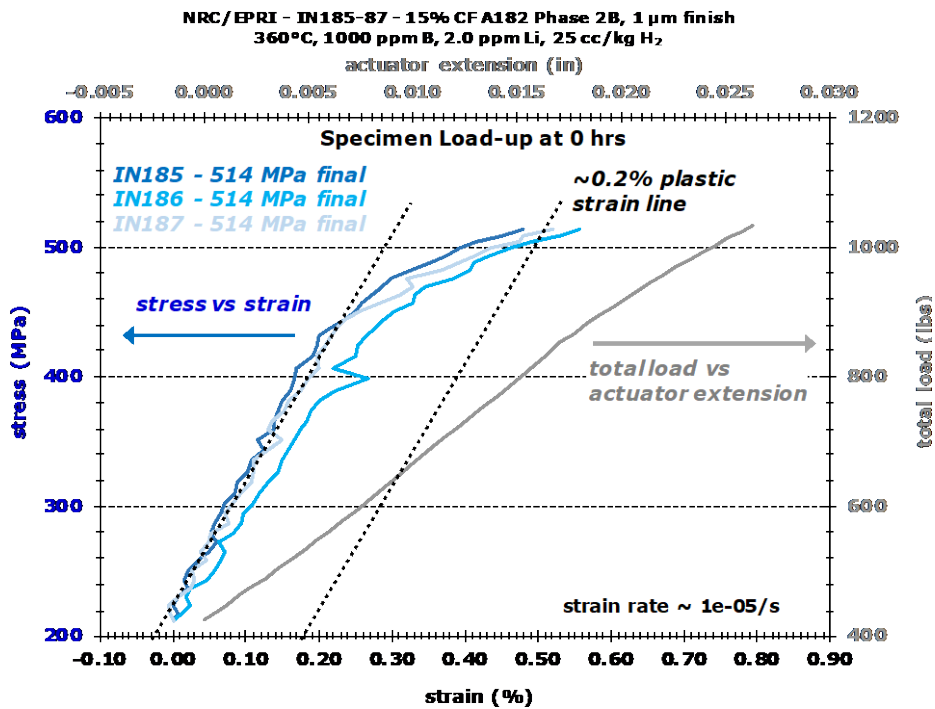


Figure 9. Stress versus strain curve during the initial loading of three 15% CF Phase 2B specimens, IN185-87.

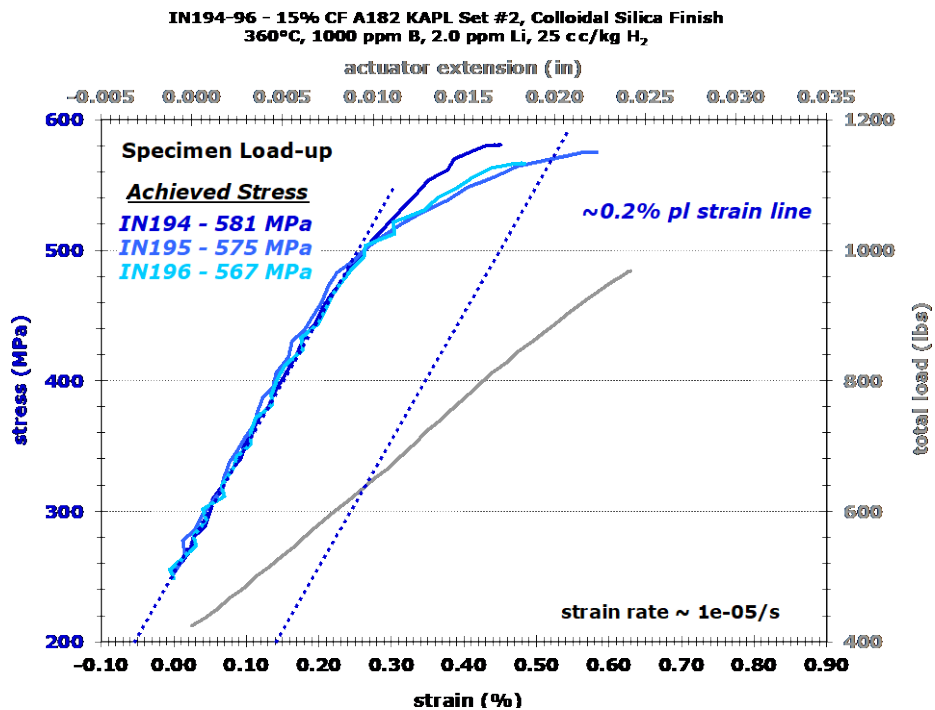


Figure 10. Stress versus strain curve during the initial loading of three 15% CF KAPL specimens, IN194-96.

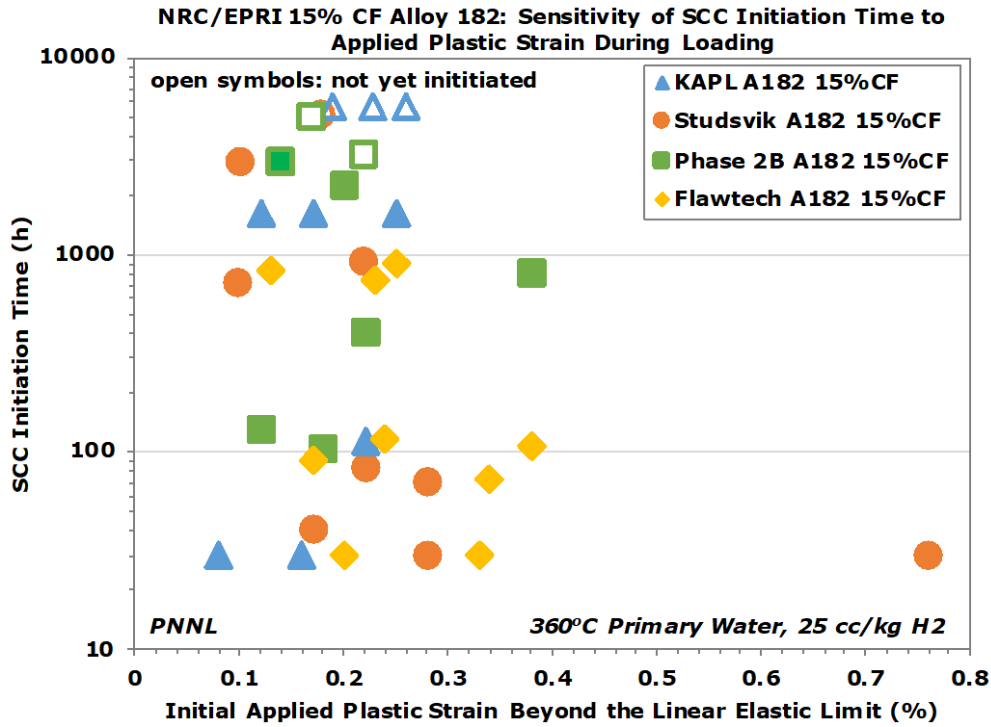


Figure 11. SCC initiation time versus initial plastic strain applied to 15% CF Alloy 182 specimens meant to be tested at their YS.

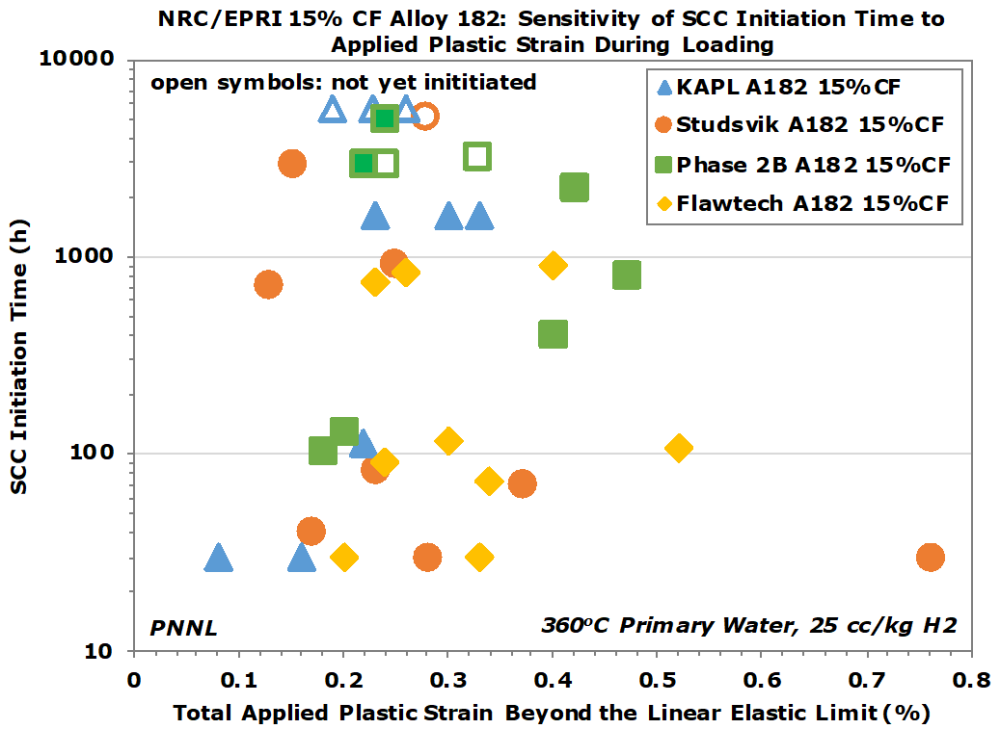


Figure 12. SCC initiation time versus total plastic strain applied to 15% CF Alloy 182 specimens meant to be tested at their YS.

3.3 Alloy 182 Tests Conducted at Sub-Yield Strength Loading

SCCI tests were conducted to assess the effect of sub-yield strength loading on SCC initiation time. Six specimens each of the KAPL and Studsvik Alloy 182 welds in the 15% CF condition were tested at 90% YS. The PNNL SCC initiation test systems are unique from any other previous SCC initiation test capability because the ability to precisely track elastic and plastic strains with a resolution of 0.02% strain during specimen loading.

This capability caused some careful reconsideration of the notion of what it means to be at or below the yield stress for an SCC initiation test. The idea of yield stress generally invokes the notion of a deviation from the linear elastic response. However, the engineering definition of yield stress is the stress that is observed at 0.2% plastic strain applied to a specimen. This method for measuring yield stress exists because there is less uncertainty in determining this value than there is in attempting to determine the stress at the deviation from the linear elastic limit. All specimens tested at the yield strength for this program were intended to be loaded to the 0.2% offset yield stress rather than at the elastic limit. The 0.2% offset yield stress is often well above the stress at the elastic limit, and as shown in Figure 13, it is ~20% above the elastic limit for the 15% CF Alloy 182 materials tested at PNNL.

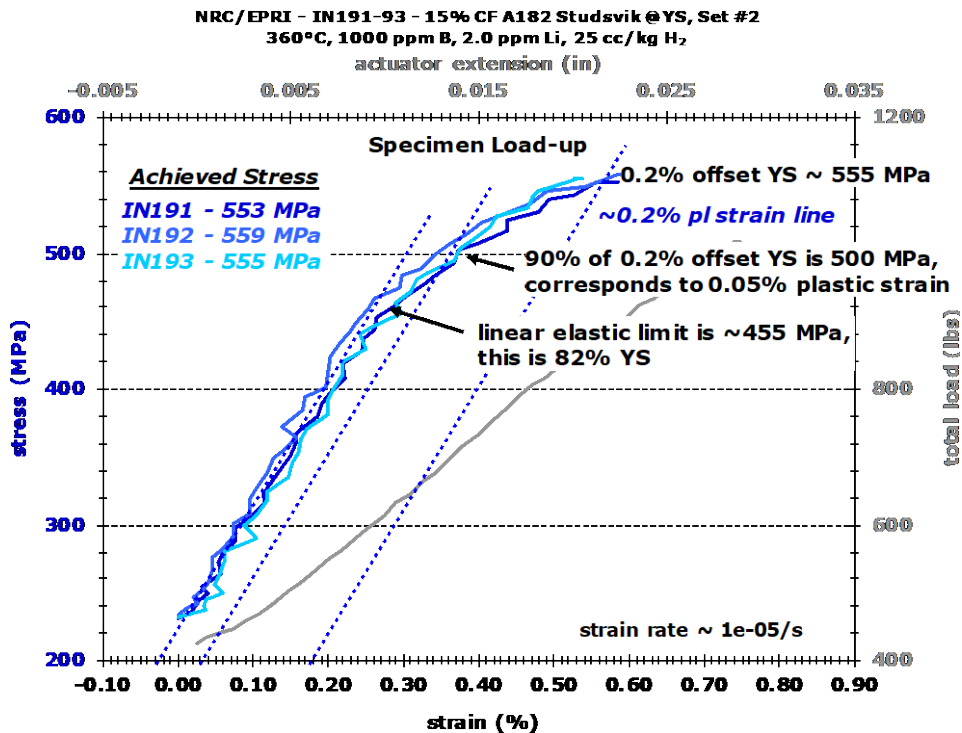


Figure 13. Stress versus strain response for three 15% CF Studsvik Alloy 182 specimens loaded to 0.2% offset plastic strain yield stress.

During the February 2017 meeting between the NRC, EPRI, PNNL, Dominion Engineering, and xLPR project members where the revised test matrix was devised, sub-YS loads of 93% and 85% YS were selected based on the level of knowledge that had been accumulated at that time about the SCC initiation response of Alloy 182 and Alloy 600. The current level of experience

showing little difference in initiation time for 5% variation in applied stress and applied plastic strains during loading as low as 0.1% (Section 3.2) suggests that if a clear trend of the effect of sub-YS loading is to be observed, the selected fraction of YS should be less than 93% YS. A variety of values could be selected depending on the needs. A strong need for this program is to keep SCC initiation times as short as possible while still providing the needed information. Based on these criterion, 90% YS was selected as the higher of the two sub-YS stresses. As shown in Figure 13, this stress is more than 10% above the linear elastic limit and will produce ~0.05% plastic strain, so it was thought to still be relatively aggressive. The choice for the lower sub-YS stress value has been reduced to 80%. This value is should be approximately equal to the linear elastic limit, and thus, it may be useful in providing data that can better clarify the role of sub-YS loading and small yielding strains on SCC initiation.

Another aspect for consideration when performing a sub-YS SCC initiation test is the choice of load path, i.e., whether the test is monotonically increased to the sub-YS value, or whether the load is first brought up to the 0.2% offset YS and then reduced to the sub-YS value. It was decided that monotonic loading was the most appropriate approach because raising a specimen up to 100% YS and then dropping below would complicate interpretation of the results.

With the sub-YS loading target stress and strain values selected for the two weld metals, testing was started using a displacement-based strain rate of $\sim 1 \times 10^{-5}$ /sec. The specimens were brought up to the test load as shown in Figure 14 for the Studsvik weld and Figure 15 for the KAPL weld. Note that the KAPL and Studsvik materials were tested in different systems. Noise levels in the DCPD-based strain measurement were low, and all specimens behaved almost identically, allowing the linear elastic limit to be easily detected. The final stress was based on a combination of the expected linear elastic limit, the expected 0.2% offset YS, and the expected amount of plastic strain (0.05%) to reach 90% YS. For the Studsvik weld, based on the available information from prior tests, the linear elastic limit was expected to be at 455-460 MPa, but instead these specimens exhibited a lower than expected elastic limit of ~420-430 MPa. The prior data also showed that the ratio of the stress at the linear elastic limit to the 0.2% offset yield stress was consistently 81-83%. Therefore, the predicted 90% YS was recalculated using the applied stress relative to the linear elastic limit and the extent of plastic strain to determine a value of 465-472 MPa. When the test load reached this value, the observed plastic strain was ~0.05% as predicted, so the load was held at this point. Thus, both the previously established elastic-limit-to-YS ratio and the plastic strain at 90% YS were used to establish that the specimens were at 90% YS. The ability to approach the testing with this degree of understanding of the testing conditions is a method that has not been used before and provides an assurance of the testing conditions that strengthens the certainty of the observed test results.

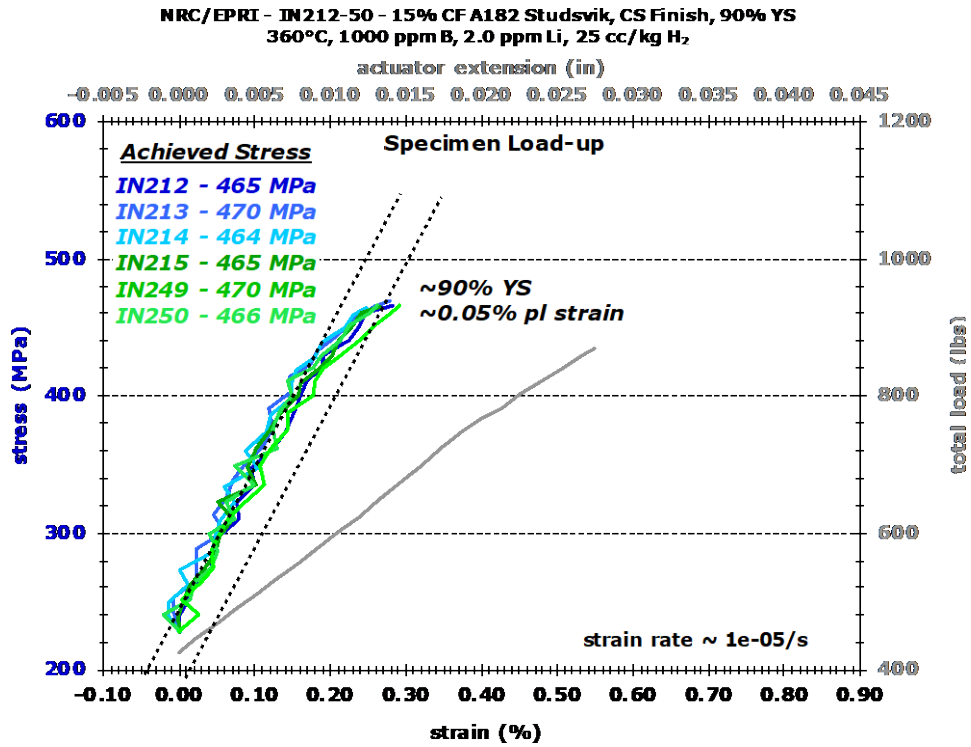


Figure 14. Stress versus strain response for six 15% CF Studsvik Alloy 182 specimens brought up to 90% YS.

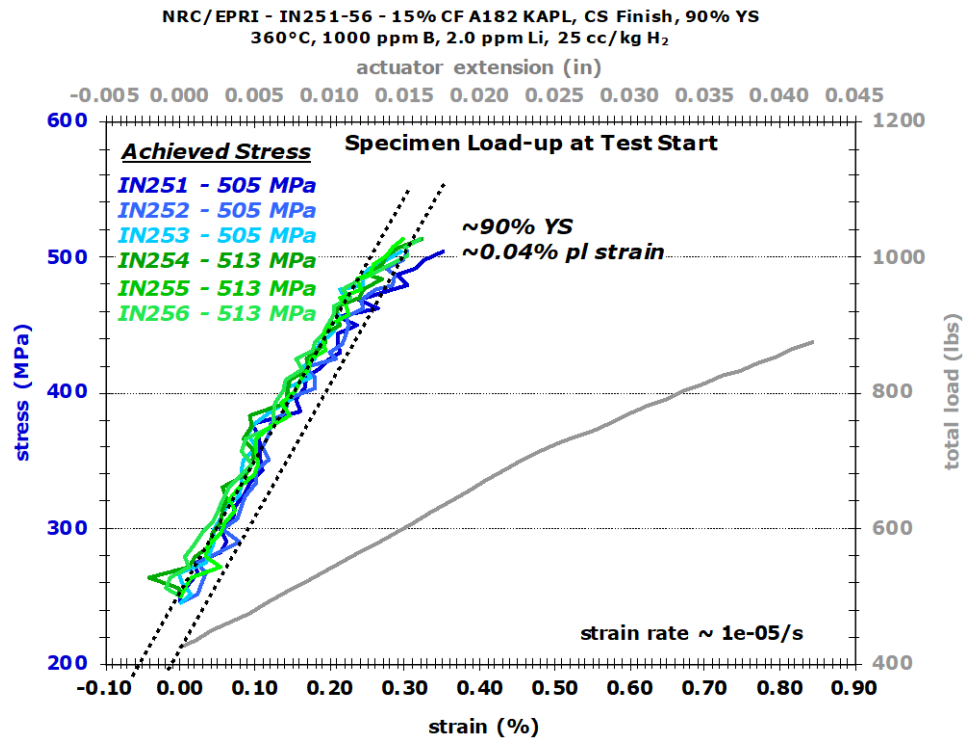


Figure 15. Stress versus strain response for six 15% CF KAPL Alloy 182 specimens brought up to 90% YS.

Table 5 shows the SCCI testing results obtained for the KAPL and Studsvik Alloy 182 specimens. One specimen made from the KAPL Alloy 182 initiated at ~500 hours, while the remaining specimens initiated after 9,200 hours. Notably, the KAPL specimen that initiated at 500 hours had one of the lowest amounts of applied plastic strain during loading.

The one 500-hour initiation at 90% YS compared to the lowest initiation time (~30 hours) for 45% of the specimens tested at their YS suggests at least a ~17x increase in SCC initiation resistance at 90% YS. The average initiation time of all 12 specimens is at least 9,100 hours which is 5.2x higher than the average of these welds at their YS in the 15% CF condition (1,760 hours).

Table 5. SCC initiation times for six each of two 15% CF A182 welds tested at 90% YS.

KAPL	90% YS (MPa)	t _{init} (h)	Studsvik	90% YS (MPa)	t _{init} (h)
IN251	505	9,205	IN212	465	10,437
IN252	505	9,312	IN213	479	10,437
IN253	505	9,284	IN214	464	>10,467
IN254	513	9,178	IN215	465	10,437
IN255	513	9,312	IN249	470	10,446
IN256	513	500	IN250	466	10,264

† The ">" indicates not yet initiated. Will expose further if possible.

3.4 Brief Summary of Testing Observations

When viewing the PNNL data set as a whole, some trends in Alloy 182 behavior are apparent:

- PWSCC initiation of Alloy 182 is highly dependent on material strength and/or the degree of cold work. For tests conducted at the yield strength, reducing the cold work and corresponding YS from the baseline condition of 15% CF with a YS of 500-560 MPa to 7.5% CF with a YS of 440-475 MPa or to as-welded material with a YS of 350-415 MPa is resulting in much higher SCC initiation times. When comparing the lowest initiation times among the different CW levels, the 7.5% CF is currently 20x higher than 15% CF Alloy 182, and the as-welded Alloy 182 is currently >900x higher than 15% CF Alloy 182. The current SCC initiation time data as a function of material strength is shown in Figure 16. A more detailed analysis of stress dependence is presented in Section 6.0.
- PWSCC initiation times of Alloy 182 appear to be greatly extended for sub-YS loading. The increase in SCC initiation time is well beyond what was expected, and there may be value in conducting additional sub-YS tests at 90% loading to further confirm these results because these results could have substantial impact on SCC initiation models. The long initiation times also provide insight into SCC initiation times indicated by other test methods where constant load is not necessarily obtained. For example, u-bend tests are known to undergo stress relaxation on the tensile-loaded outer surface even when using spring-loaded specimens, so initiation times for that test type could be much higher than for constant load SCC initiation tests of Alloy 182.

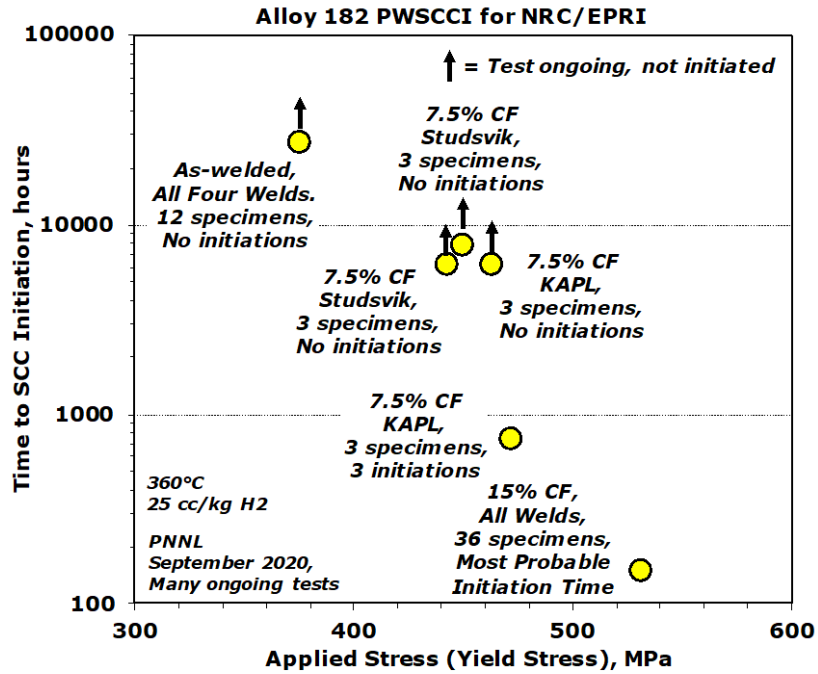


Figure 16. Distribution of constant load Alloy 182 PWSCC initiation times as a function of material strength for PNNL tests.

4.0 Alloy 600 Testing Status

This task is being conducted as part of the effort to determine a FOI in initiation time for Alloy 690 over Alloy 600. In addition, Alloy 600 SCC initiation time measurements also provide a point of comparison for Alloy 182 SCC initiation behavior. To this end, nine specimens each of four heats of 15% CF Alloy 600 are being SCC initiation tested. The initiation times are summarized in Table 6.

Initiation times for all four heats, as a whole, are somewhat lower than expected based on PNNL's prior experience. During early testing at PNNL on 15-20% cold rolled and 15-20% tensile strained NX6106XK-11 for the DOE-NE LWRS program, initiation times were 1,500-2,000 hours. However, the 15% CF materials tested for EPRI/NRC program are generally exhibiting initiation times below 1,000 hours including some 15% CF NX6106XK-11 specimens, suggesting that the method of application of cold work may have a substantial effect on SCC initiation susceptibility. This could be a potential topic for future work.

Two of the 33375-2B specimens and six of the NX6106XK-11 specimens with higher initiation times were tested under less than ideal conditions resulting in higher initiation times that are not likely to be representative. These eight specimens along with four other specimens were tested together as IN154-IN165. IN163 that initiated at 1,062 lbs was accidentally allowed to fail in-situ at full load, and as a result, the remaining six specimens in the autoclave - IN154-57, IN160, 61, 64, and 65 - were subjected to a brief (millisecond time frame) overload that produced ~0.05-0.5% plastic strain in most of these specimens as observed by DCPD. After the failed specimen was removed, testing was resumed at the original load, but because these specimens had been overloaded, the original load was no longer the current YS of the specimens. After a time span of 1,772 hours at the original load, the load was slowly increased until the majority of the eight remaining specimens yielded. The remaining eight specimens began to initiate shortly thereafter. Additional SCC initiation tests are planned to make up for these likely non-representative initiation times. The very low SCC initiation time of 120 hours for 33375-2B IN158 specimen was determined to be caused by a surface-breaking defect in the gauge section. Additional details on this test are available in the 2017 report [1].

Table 6. SCC initiation times of the 15% CF Alloy 600 materials. S# is the string where the specimen resides if it was tested in a 3-string load line. Mean, std. dev., and median of all specimens combined is 858, 683, and 525 hours, respectively.

33375-2B	S#	YS (MPa)	t_{init} (h)	NX6106XK-11	S#	YS (MPa)	t_{init} (h)
IN154	1	528	†3,026/1,254	IN156	1	544	†4,600/2,828
IN155	1	537	†3,250/1,478	IN157	1	547	†4,591/2,819
IN158	2	558	120	IN160	2	544	†3,000/1,228
IN159	2	551	1,025	IN161	2	547	†3,205/1,433
IN162	3	547	830	IN164	3	544	†3,250/1,478
IN163	3	558	1,062	IN165	3	547	†4,100/2,328
TBD				IN291	NA	516	252
TBD				IN292	NA	515	247
TBD				IN293	NA	521	221
Mean, SD			962; 427	Mean, SD			1,426; 999
Median			1,044				1,433
522068	S#	YS (MPa)	t_{init} (h)	WNP5 CRDM	S#	YS (MPa)	t_{init} (h)
IN224	NA	450	880	IN288	NA	497	475
IN225	NA	450	890	IN289	NA	494	242
IN226	NA	450	840	IN290	NA	501	420
IN304	NA	472	508	IN298	NA	509	478
IN305	NA	472	550	IN299	NA	514	430
IN306	NA	473	725	IN300	NA	509	467
IN307	NA	474	477	IN301	NA	509	457
IN308	NA	475	525	IN302	NA	512	415
IN309	NA	474	483	IN303	NA	511	460
Mean, SD			653;169	Mean, SD			427; 69
Median			550	Median			457

† These specimens spent 1,772 hours at ~90-96% of their YS. The lower number listed is the initiation time minus 1,772 hours.

5.0 Alloy 690/152(M)/52(M) Testing Status

5.1 SCC Initiation Behavior

This test on 36 specimens was started in January 2016 and consists of four heats of Alloy 690 and one weld each of Alloy 152, Alloy 152M, Alloy 52, and Alloy 52M. There are three specimens each of the Alloy 690 heats and six specimens each of the Alloy 152(M)/52(M) welds. One specimen of each Alloy 690 heat and two of each Alloy 152(M)/52(M) weld (12 specimens total among all the materials) have been instrumented for DCPD detection of initiation while the other 24 specimens have been instrumented for detection of failure. Dimensional measurements and selected details on each specimen are given in Table 7. The specimens were arranged in the autoclave so that for each material, the smallest gauge diameter was instrumented for DCPD. This arrangement was selected to enable the best chance of observing the highest strains that might occur during loading, and if any initiations were to occur, it would most likely happen in the smallest gauge diameter specimens that are being monitored. This test is planned to run the entire duration of the project, and testing will only be stopped for test system maintenance, building power outages that affect required services, and for occasional specimen examinations.

Testing was stopped at 20,659 hours (2.4 years) to perform planned midterm examination of the specimens. Due to the formation of a nearly continuous spinel oxide on the surface, no useful surface observations were possible however selected focused ion beam trenching was performed to reveal the grain boundaries in cross section to a depth of $\sim 10 \mu\text{m}$ on one each of the Valinox Alloy 690 (IN126), TK-VDM Alloy 690 (IN108), ENSA DPM Alloy 52M (IN112), and IHI Alloy 152M (IN128) specimens. These Alloy 690 materials were selected for examination because their fine, high density grain boundary (GB) carbide distribution promotes GB cavity formation in more highly cold worked materials. Details of these examinations are provided in Section 5.3.

While the test was stopped at the 2.4 year mark, analysis of the DCPD wiring was performed to try to identify the source of DCPD noise that occurred in the months prior to the test stoppage (see Figure 17 to Figure 19). No issues were found with the wiring itself or its routing within the autoclave, however, several of the current wire spot weld attachments to the specimens were found to be very weak. It was assumed that the weakened spot welds were the cause of the DCPD noise, and the decision was made to keep the existing DCPD wiring. The available data since restart show minimal noise levels suggesting that the cause of the DCPD noise was fixed.

Table 7. Selected information on the Alloy 690/152(M)/52(M) specimens being tested in NRCI-1. The rows correspond to each string, while the yellow highlight indicates specimens with the smallest gauge diameter. The specimens in String-1 (S1) are instrumented for DCPD.

	1 A	2 B	3 C	4 D	5 E	6 F
S1	IN107, A690 TK-VDM HT# 114092, B#1, S#2 1 um Finish, 460 MPa 30.51, 12.26, 3.54 MUX1	IN110, A52M ENSA DPM B#4, S#1 1 um Finish, 430 MPa 30.52, 12.20, 3.65 MUX2	IN113, A52M ENSA DPM B#3, S#4 1 um Finish, 430 MPa 30.48, 12.29, 3.66 MUX3	IN116, A690 Valinox HT# WP142, B#3, S#3 1 um Finish, 450 MPa 30.46, 12.26, 3.57 MUX4	IN119, A52 MHI B#1, S#1 1 um Finish, 470 MPa 30.44, 12.37, 3.44 MUX5	IN122, A52 MHI B#2, S#4 1 um Finish, 485 MPa 30.48, 12.22, 3.47 MUX6
	IN108, A690 TK-VDM HT# 114092, B#1, S#1 1 um Finish, 460 MPa 30.52, 12.25, 3.55 FC1	IN111, A52M ENSA DPM B#3 S#1 1 um Finish, 430 MPa 30.52, 12.22, 3.67 FC2	IN114, A52M ENSA DPM B#4 S#2 1 um Finish, 430 MPa 30.46, 12.23, 3.67 FC3	IN117, A690 Valinox HT# WP142, B#3, S#1 1 um Finish, 450 MPa 30.48, 12.21, 3.59 FC4	IN120, A52 MHI B#2, S#2 1 um Finish, 470 MPa 30.50, 12.25, 3.47 FC5	IN123, A52 MHI B#2, S#5 1 um Finish, 485 MPa 30.52, 12.26, 3.47 FC6
	IN109, A690 TK-VDM HT# 114092, B#1, S#3 1 um Finish, 460 MPa 30.44, 12.29, 3.56 FC13	IN112, A52M ENSA DPM B#3 S#2 1 um Finish, 430 MPa 30.49, 12.24, 3.67 FC14	IN115, ENSA DPM A52M B#4 S#4 1 um Finish, 430 MPa 30.52, 12.21, 3.67 FC15	IN118, A690 Valinox HT# WP142, B#3, S#2 1 um Finish, 450 MPa 30.50, 12.21, 3.58 FC16	IN121, A52 MHI B#2, S#3 1 um Finish, 470 MPa 30.45, 12.31, 3.47 FC17	IN124, A52 MHI B#2, S#6 1 um Finish, 485 MPa 30.47, 12.13, 3.47 FC18
	7 G	8 H	9 I	10 J	11 K	12 L
S1	IN125, A690 Valinox HT# RE243, B#1, S#1 1 um Finish, 415 MPa 30.31, 12.15, 3.72 MUX7	IN128, A152M IHI B#1, S#1 1 um Finish, 555 MPa 30.45, 12.73, 3.22 MUX8	IN131, A152M IHI B#1, S#4 1 um Finish, 555 MPa 30.49, 12.45, 3.24 MUX9	IN134, A152 MHI B#1, S#2 1 um Finish, 500 MPa 30.48, 12.35, 3.37 MUX10	IN137, A690 Allvac HT# B25K-2, S#1 1 um Finish, 515 MPa 30.45, 12.35, 3.32 MUX11	IN140, A152 MHI B#1, S#4 1 um Finish, 500 MPa 30.47, 12.40, 3.37 MUX12
	IN126, A690 Valinox HT# RE243, B#1, S#2 1 um Finish, 415 MPa 30.50, 12.24, 3.72 FC7	IN129, A152M IHI B#1, S#2 1 um Finish, 555 MPa 0.48, 12.60, 3.22 FC8	IN132, A152M IHI B#1, S#5 1 um Finish, 555 MPa 30.50, 12.55, 3.26 FC9	IN135, A152 MHI B#1, S#3 1 um Finish, 500 MPa 30.49, 12.40, 3.37 FC10	IN138, A690 Allvac HT# B25K-2, S#1 1 um Finish, 515 MPa 30.54, 12.49, 3.34 FC11	IN141, A152 MHI B#1, S#5 1 um Finish, 500 MPa 30.43, 12.31, 3.37 FC12
	IN127, A690 Valinox HT# RE243, B#1, S#3 1 um Finish, 415 MPa 30.45, 12.20, 3.72 FC19	IN130, A152M IHI B#1, S#3 1 um Finish, 555 MPa 30.49, 12.77, 3.22 FC20	IN133, A152M IHI B#1, S#6 1 um Finish, 555 MPa 30.50, 12.46, 3.26 FC21	IN136, A52M ENSA DPM, B#3, S#3 1 um Finish, 430 MPa 30.46, 12.15, 3.67 FC22	IN139, A690 Allvac HT# B25K-2, S#2 1 um Finish, 515 MPa 30.53, 12.44, 3.34 FC23	IN142, A152 MHI B#1, S#1 1 um Finish, 500 MPa 30.43, 12.40, 3.39 FC24

- smallest gauge diameter
- blue text = instrumented
- Surface exams at 2.4 yrs
- Surface and FIB trench GB exams at 2.4 yrs

The responses of the 12 DCPD-instrumented specimens are presented in Figure 17 through Figure 19 up to the test time of 35,414 hours (4.05 years) which corresponds to a test stop to perform system maintenance. Actuator displacement is provided in these plots to assess servo system behavior and provide further information on the possible creep response of the specimens. All specimens have exhibited a non-referenced strain response that is primarily due to resistivity evolution and creep of the materials and are not indicative of SCC initiation.

The current FOI for the Alloy 690 compared to the Alloy 600 is 41x when considering the average initiation time of the Alloy 600 and 67x when considering the median initiation time. Assuming that the remaining Alloy 600 initiation tests do not substantially change the Alloy 600 initiation time statistics, reaching five years of exposure on the Alloy 690 without initiation will give FOIs of 51x and 83x for average and median times, respectively. For Alloy 152(M)/52(M),

the current FOIs are 24x and 48x for average and median relative to Alloy 182 initiation times, respectively. These will increase to 30x and 60x if no initiations occur before 5 years. These values are summarized in Table 8.

Table 8. Current factors of improvement for Alloy 690 relative to Alloy 600 and Alloy 152(M)/52(M) relative to Alloy 182.

	Alloy 690	Alloy 152(M)/52(M)
Current FOI based on average SCCI time	41x	24x
Current FOI based on median SCCI time	67x	48x
FOI after 5 years of testing based on average SCCI time	51x	30x
FOI after 5 years of testing based on median SCCI time	83x	60x

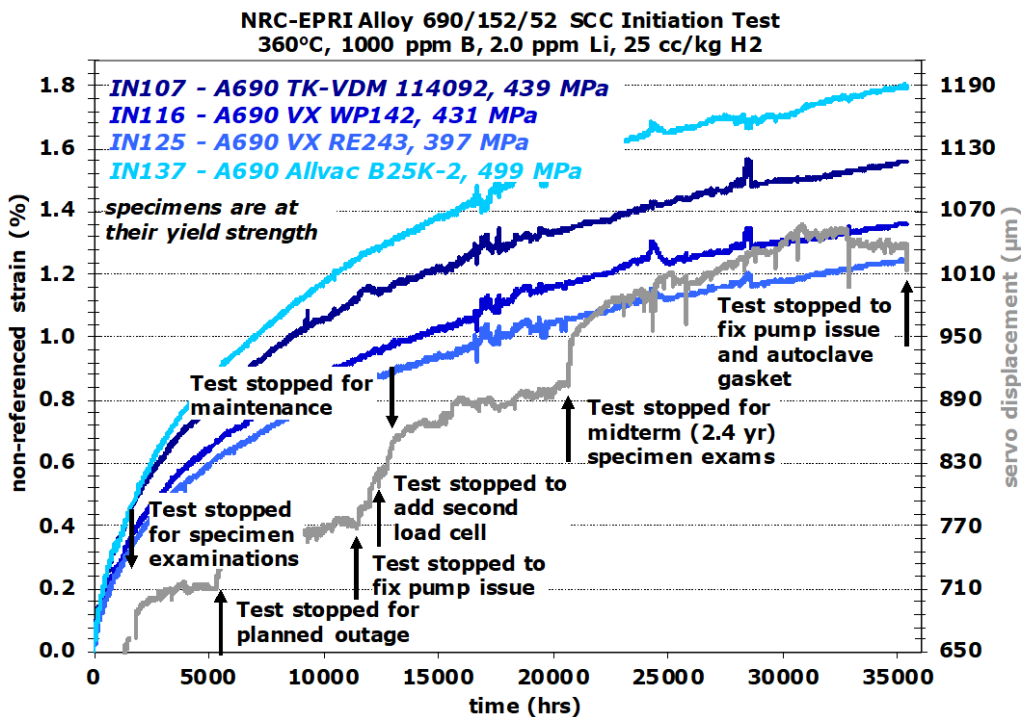


Figure 17. DCPD response of the four instrumented Alloy 690 specimens in NRC11. The gray line is the servo displacement. Temporary rapid increases in displacement occur after test restarts.

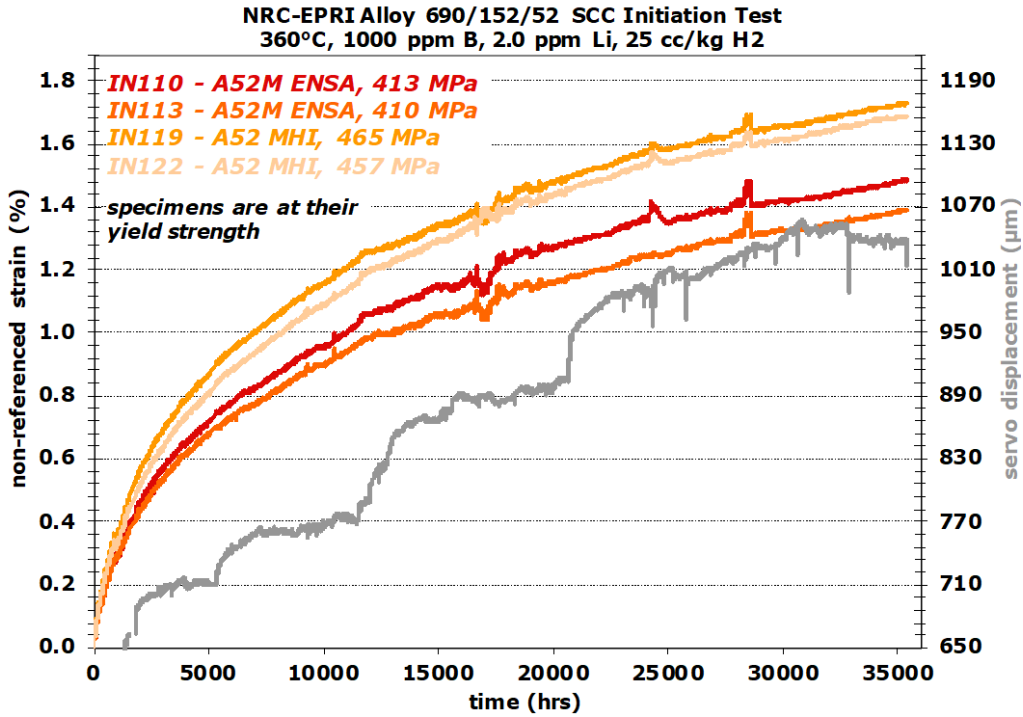


Figure 18. DCPD response of the four instrumented Alloy 52 specimens in NRC11. The gray line is the servo displacement. Temporary rapid increases in displacement occur after test restarts.

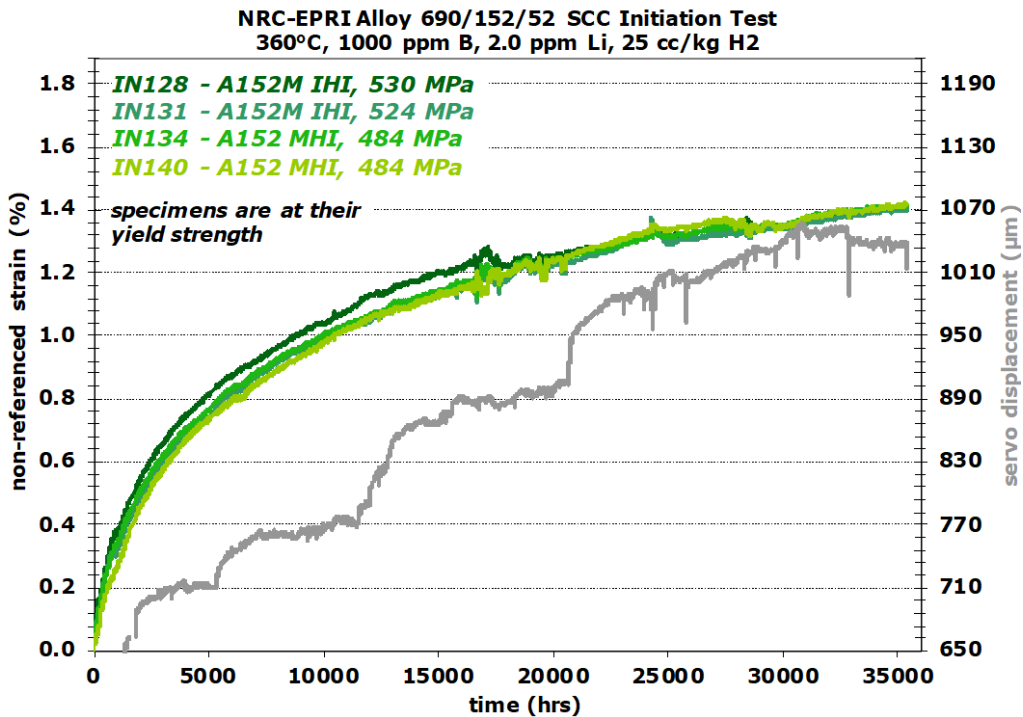


Figure 19. DCPD response of the four instrumented Alloy 152 specimens in NRC11. The gray line is the servo displacement. Temporary rapid increases in displacement occur after test restarts.

5.2 Creep Rate Measurements

Because the specimens are not exhibiting any cracking, the recorded DCPD-based strain rate is due only to a combination of specimen creep and resistivity evolution of the material. The resistivity evolution contribution can be measured by performing a DCPD observation at low load where creep is expected to be much lower. This resistivity contribution is then subtracted from the DCPD response at full load. At approximately 12,000 hours of test time, the test was stopped to perform system maintenance. After maintenance, the test system was brought back up to test temperature, and the DCPD response of the specimens was observed with just the tare load due to water pressure on the pullrod. The tare load loads the specimens to ~45% of their YS.

Creep strain rate estimates at 12,000 hours of exposure for all 12 DCPD-instrumented specimens are presented in Table 9. The strain rates at YS range from 2.8×10^{-9} to 11×10^{-9} %/sec, representing 0.09-0.35% strain per year. It appears that the Alloy 152 and 152M materials have the highest average creep rate, likely due to the higher average applied stresses on these specimens. There is limited data in the literature for comparison, but a creep strain rate study published by Attanasio [5] shows a similar creep strain rate for Alloy 690 in high temperature water.

Table 9. Strain rates measured on Alloy 690, 52, and 152 at ~12,000 hours of exposure in high temperature water (360 °C).

ID	Material	Heat	Full Load Stress (MPa)	Total Strain Rate (%/sec)	Material Resistivity Contribution (%/sec)	Creep Strain Rate (%/sec)
IN107	690	TK-VDM 114092	439	1.4×10^{-8}	6.9×10^{-9}	7.1×10^{-9}
IN116	690	Valinox WP142	431	7.3×10^{-9}	2.4×10^{-9}	4.9×10^{-9}
IN125	690	Valinox RE243	397	7.3×10^{-9}	4.5×10^{-9}	2.8×10^{-9}
IN137	690	Allvac B25K-2	499	1.3×10^{-8}	7.3×10^{-9}	5.7×10^{-9}
IN110	52M	ENSA	413	1.1×10^{-8}	8.3×10^{-9}	2.7×10^{-9}
IN113	52M	ENSA	410	9.7×10^{-9}	6.9×10^{-9}	2.8×10^{-9}
IN119	52	MHI	465	9.7×10^{-9}	6.9×10^{-9}	2.8×10^{-9}
IN122	52	MHI	457	9.9×10^{-9}	7.1×10^{-9}	2.8×10^{-9}
IN128	152M	IHI	530	1.1×10^{-8}	3.5×10^{-9}	7.5×10^{-9}
IN131	152M	IHI	524	1.1×10^{-8}	5×10^{-10}	1.1×10^{-8}
IN134	152	MHI	484	1.1×10^{-8}	7×10^{-10}	1.0×10^{-8}
IN140	152	MHI	484	1.1×10^{-8}	3.5×10^{-9}	7.5×10^{-9}

5.3 Alloy 690/152(M)/52(M) Specimen Microstructure Observations

During the test stop at the 2.4-year mark (20,659 hours), selected specimens were removed from the load line for examinations. Examinations of more highly cold worked Alloy 690 SCC initiation specimens under the DOE LWRS Ni-base alloy SCC initiation task at PNNL revealed creep cavity formation along GBs of 30% CW Alloy 690 and to a much lesser extent in 20% CW Alloy 690 [6]. This mechanism has been observed to be responsible for SCC initiation in a small number of 30% CW Alloy 690 specimens. Because of these observations, there was strong interest in examining the NRC/ERPI 15% CF Alloy 690 specimens that had been exposed to a similar length of time as the DOE LWRS program specimens. Specimen surface

observations and focused ion beam (FIB) trench cross-section examinations were performed by scanning electron microscopy (SEM) to look for indications of creep cavities.

Exposure of these specimens to 360°C simulated PWR primary water for 2.4 years led to the formation of a thick Fe-rich spinel oxide layer on the surface of most specimens, making it difficult to observe the GBs intersecting the gauge surface of the specimens. Nevertheless, areas with thinner surface oxide coverage were found in some of the specimens. A list of the specimens that were examined is provided in Table 10. FIB trenching to view GBs in cross section to shallow depths (<10 µm) into the specimens was performed on one specimen each of the TK-VDM Alloy 690, Valinox Alloy 690, ENSA DPM Alloy 52M, and IHI Alloy 152M specimens. These particular Alloy 690 specimens were selected because these materials are most likely to have GB cavity formation based on long-term testing of these materials in a more highly CW condition in the DOE LWRS program. A summary of the examinations of the NRC/EPRI program specimens is presented here.

Table 10. Alloy 690/152(M)/52(M) specimens examined after 2.4 years of exposure at their YS.

ID	Material	Heat	YS (MPa)	Gauge Surface Exam	FIB Trench Cross Section of GBs	Notes
IN108	690	TK-VDM 114092	460	Yes	Yes	Surface cavities only
IN118	690	Valinox WP142	450	Yes		Surface cavities only
IN126	690	Valinox RE243	415	Yes	Yes	Surface cavities only
IN137	690	Allvac B25K-2	515	Yes		Surface cavities only
IN112	52M	ENSA DPM	430	Yes	Yes	Surface cavities only
IN124	52	MHI	485	Yes		Difficult to observe
IN128	152M	IHI	555	Yes	Yes	Cracks ≤1 µm deep
IN142	152	MHI	500	Yes		Difficult to observe

15% CF Alloy 690TT plate TK-VDM specimen IN108

No cracks were observed on the surface of this specimen. However, as shown in Figure 20, similar to 20% CW specimens of this material tested for the DOE-NE LWRS program, some GBs at the surface are decorated with what appear to be nano-sized, discrete holes or cavities. PNNL describes this as a “postage stamp” border appearance. To better understand the nature of these features, in particular to determine whether cavities exist on the GBs in the interior of the specimen, FIB trenching was performed (Figure 21) to expose a selected GB in cross section to view the sub-surface morphology of the “postage stamp” features. Multiple different serial observations of the GB were obtained by trenching further along the grain boundary providing additional information. Serial FIB milling was conducted over a distance of ~10 µm and a total of ~100 images were taken with examples shown in Figure 22. Small cavities were only found on the surface where the GB exhibits the “postage stamp” features, but no cavities were found on GBs below the surface. This same heat of material in the 21% CF condition was examined after approximately the same exposure duration and found to contain not only surface voids but also a very limited number of nano-sized cavities in cross section.

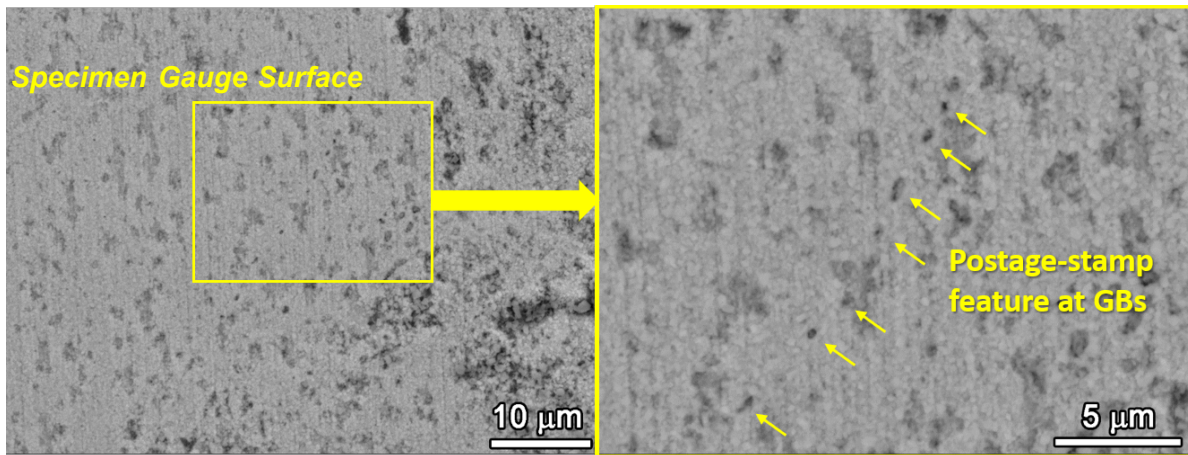


Figure 20. SEM-BSE image of the gauge surface of the 15% CF Alloy 690 plate TK-VDM specimen IN108 after 20,659 hours of exposure.

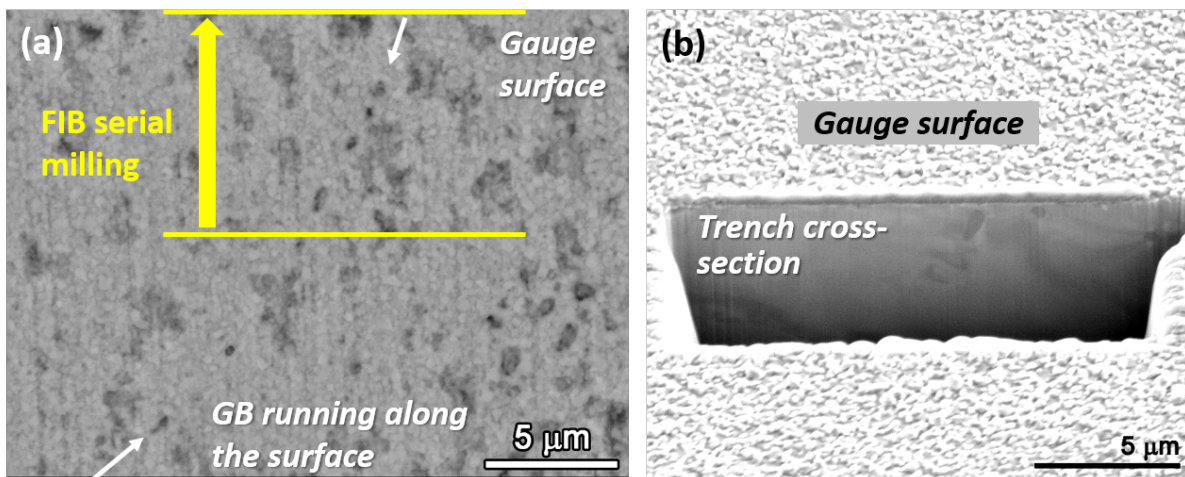


Figure 21. (a) SEM-BSE image of IN108 showing the location of the FIB trench with an arrow indicating the direction of FIB serial milling, and (b) FIB-SE image showing the starting cross section of the trench in IN108.

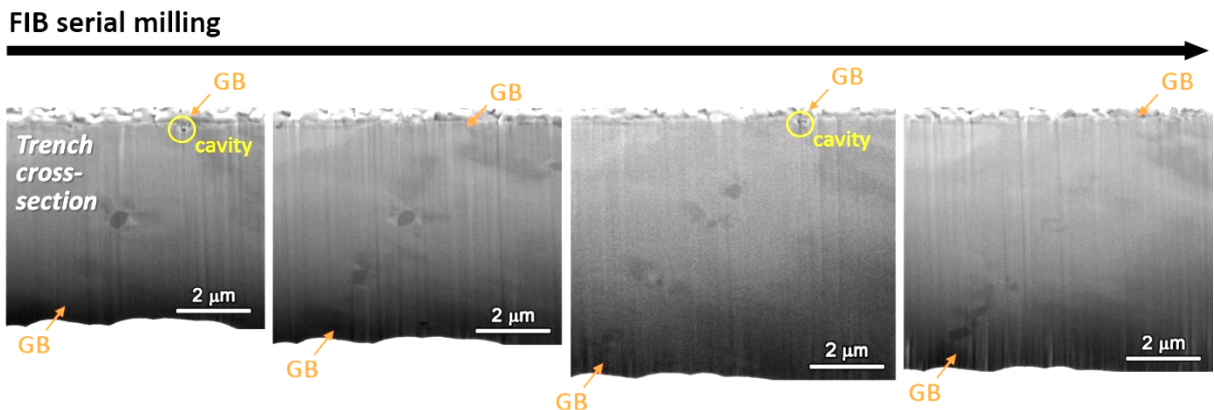


Figure 22. Examples of the FIB-SE images taken of IN108 during the serial FIB milling along the selected portion of a GB identified in Figure 21(a).

15% CF Alloy 690TT CRDM Valinox WP142 specimen IN118

The 15% CF Valinox heat WP142 specimen IN118 also exhibited extensive “postage stamp” features at GBs in the gauge surface (Figure 23). On some GBs, a darker continuous contrast was observed as shown in Site 1, indicative of slight IG damage. However, since the damage is believed to be very shallow (nanometer depth), no FIB trenching or serial milling was performed on this specimen.

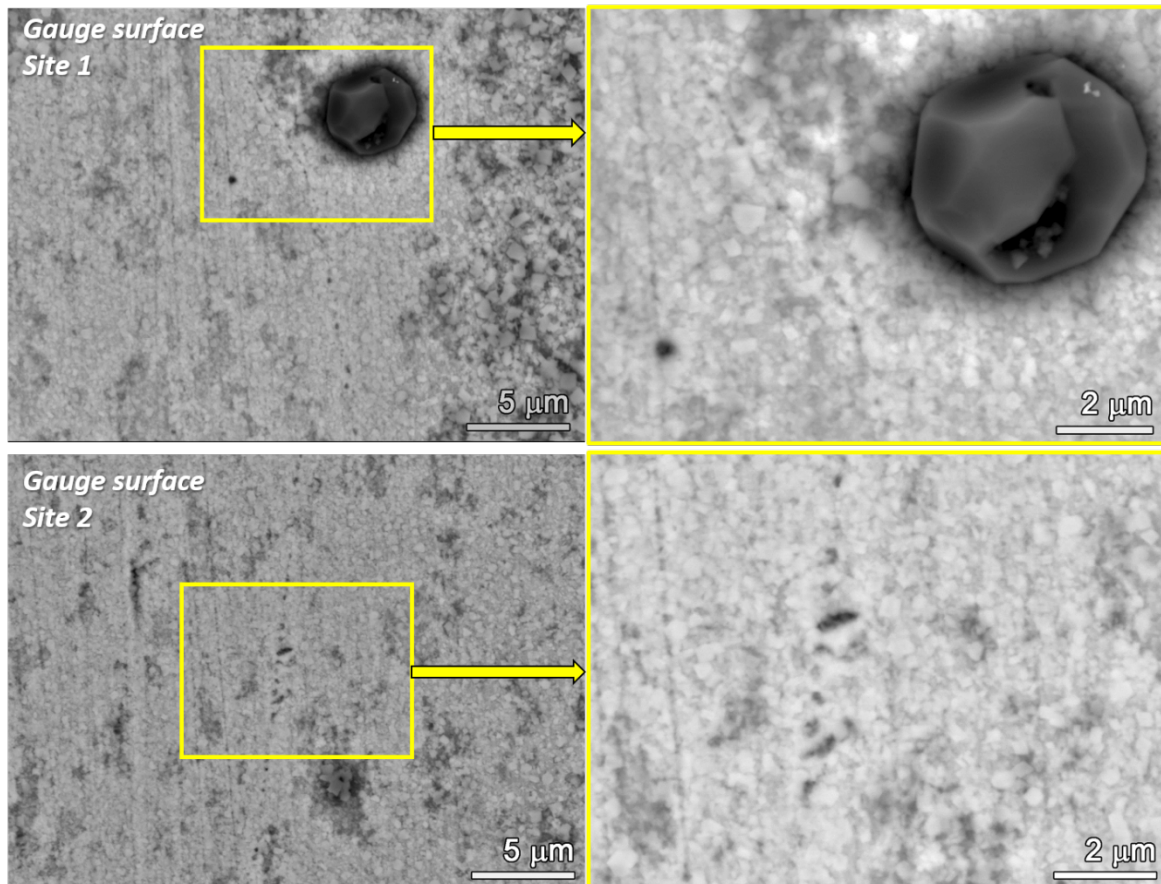


Figure 23. Representative SEM-BSE images of the gauge surface of the 15% CF Alloy 690 CRDM Valinox WP142 specimen IN118 after 20,659 hours of exposure.

15% CF Alloy 690TT CRDM Valinox RE243 specimen IN126

Coupled surface and FIB-trench cross-section examinations were also performed on one specimen of this heat of material in a region on the surface where “postage stamp” features at GBs were observed (Figure 24). Serial FIB milling was performed along the GB over a distance of ~18 μm with examples showing the cross-section morphology in Figure 25. The cavities observed on the surface were found to be no more than 100 nm in depth, and as with the RE243 specimen, no GB cavities were found below the surface.

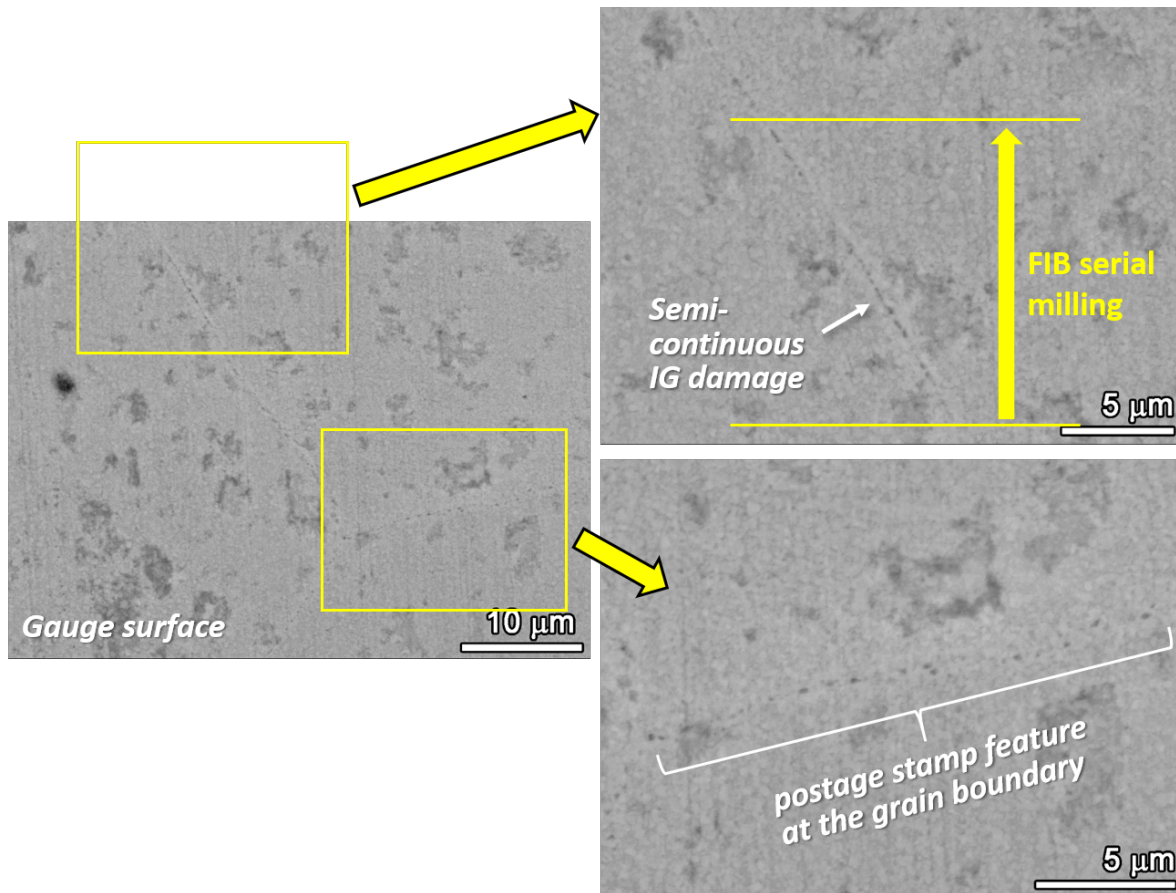


Figure 24. Representative SEM-BSE images of the gauge surface of the 15% CF Alloy 690 CRDM Valinox RE243 specimen IN126 after 20,659 hours of exposure.

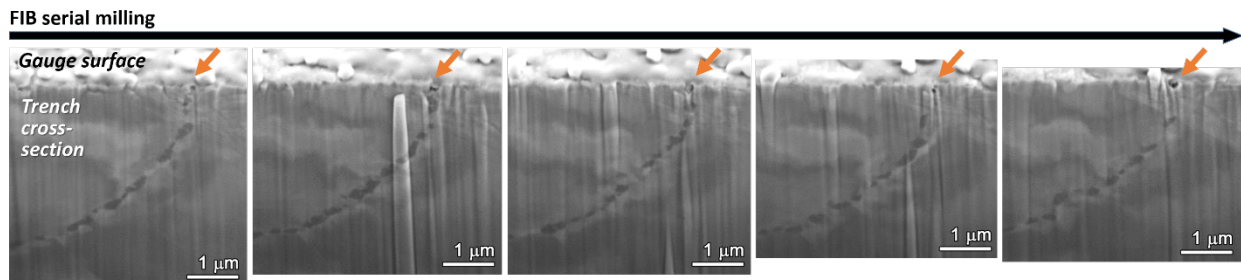


Figure 25. Examples of the FIB-SE images taken of IN126 during the serial FIB milling along the selected portion of a GB identified in Figure 24.

15% CF Alloy 690MA bar Allvac B25K-2 specimen IN137

As shown in Figure 26, the 15%CF Allvac heat B25K-2 specimen IN137 exhibited a thicker spinel oxide layer on the gauge surface obscuring a clear examination of GB features. Pre-test microstructure examination revealed primarily micrometer-sized, transgranular (TG) carbides in this material. Based on our previous experience, such microstructures are much less susceptible to cavity formation as compared to materials featuring a semi-continuous distribution of nanometer-sized GB carbides. As a result, no further FIB trenching or serial milling were performed on this specimen during the test interruption.

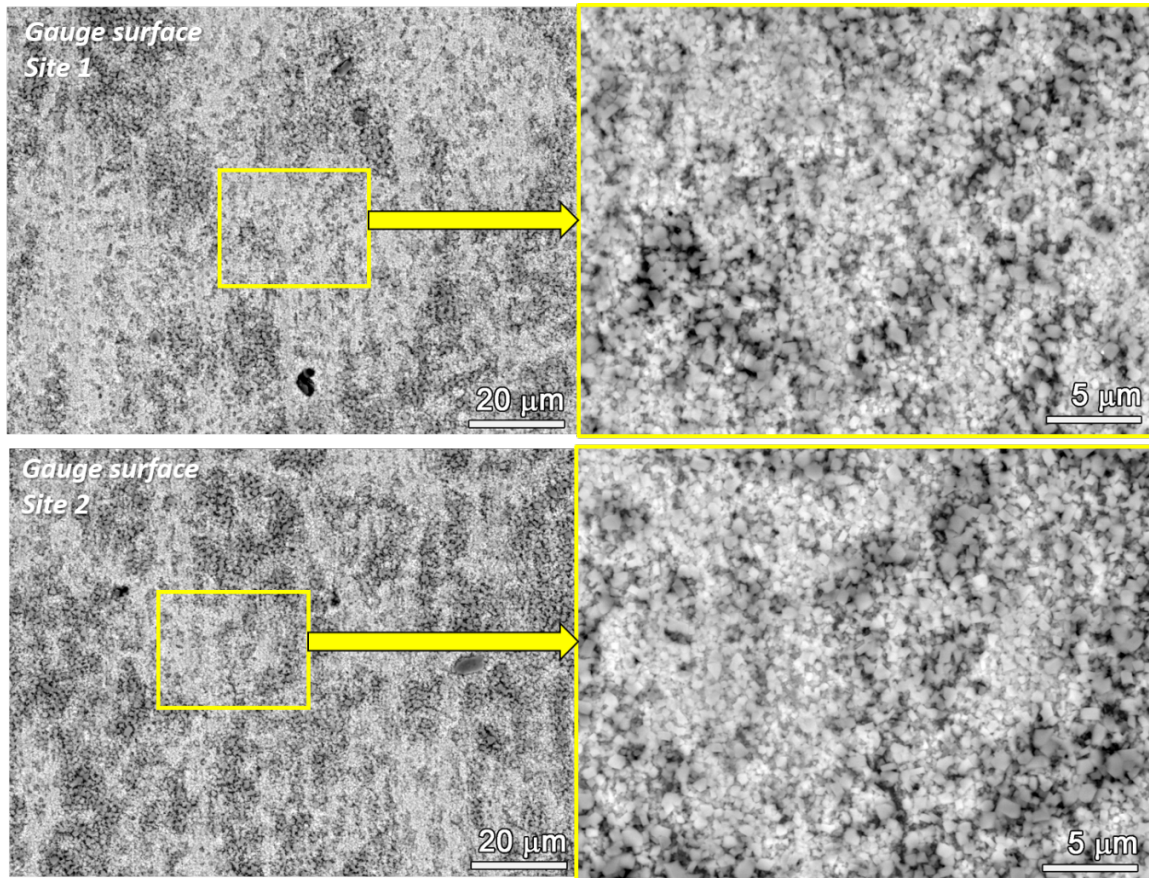


Figure 26. Representative SEM-BSE images of the gauge surface of the 15% CF Alloy 690 bar Allvac B25K-2 specimen IN137 after 20,659 hours of exposure.

15% CF Alloy 52M ENSA DPM specimen IN112

Similar to the three examined Alloy 690TT specimens from different heats, solidification grain boundaries (SGBs) in the 15%CF Alloy 52M ENSA DPM specimen IN112 also partially featured some “postage stamp” features as demonstrated in Figure 27, but not as extensive as seen in the Alloy 690 specimens. Two FIB trenches were made on a selected grain boundary without clear indication of postage stamp features. Serial milling of a short distance of $\sim 5 \mu\text{m}$ was performed in one of the trenches as illustrated in Figure 28b, and the other trench was made for a quick examination of cross-section morphology of the investigated grain boundary. A high density of IG precipitates was revealed in both locations, but no IG defects were observed in either of them.

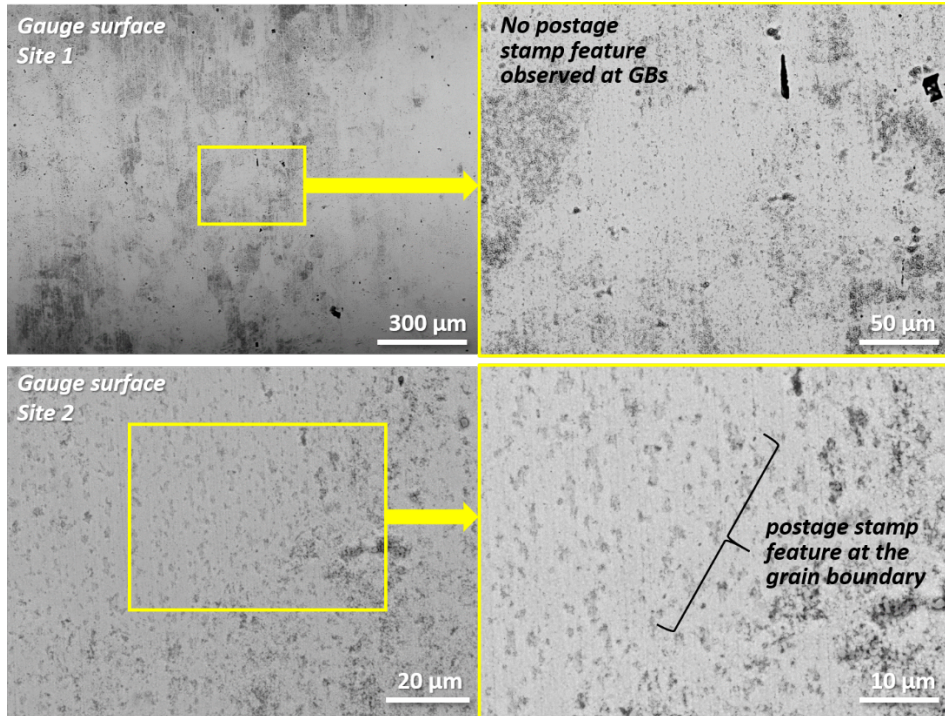


Figure 27. Representative SEM-BSE images of the gauge surface of the 15% CF Alloy 52M ENSA DPM specimen IN112 after 20,659 hours of exposure.

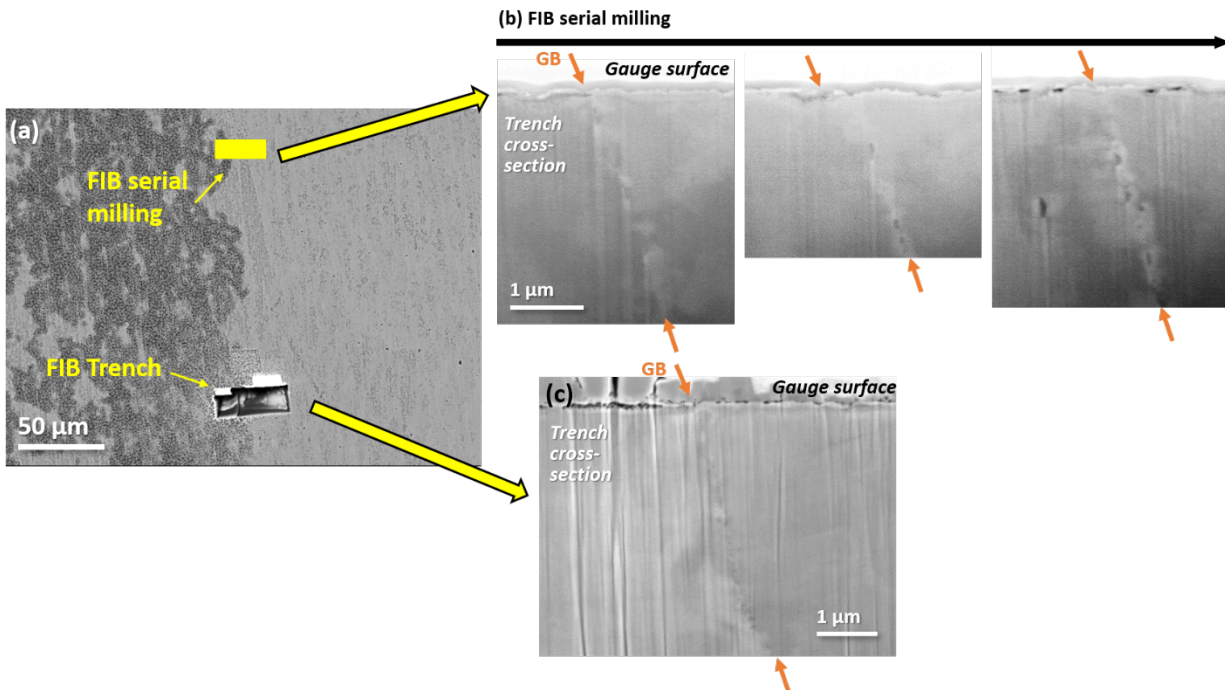


Figure 28. (a) SEM-BSE image showing the location of the two FIB trenches in IN112, (b) examples of the FIB-SE images taken during the serial FIB milling along the selected portion of a GB identified in (a), and (c) FIB-SE image showing the cross section of the trench at the location identified in (a).

15% CF Alloy 152M IHI specimen IN128

A crack-like feature was found in the low-magnification SEM-BSE montage of the 15%CF Alloy 152M IHI specimen IN128, therefore higher resolution SEM examination was performed in the vicinity of this feature (labeled Crack 1 in Figure 29). Details of this crack can be seen in the SEM-BSE and SE images of this crack presented in the bottom right of Figure 29. The BSE image revealed a total crack length on the surface of $\sim 25\ \mu\text{m}$, but in the SE image only the more widely opened middle-section of this crack is visible because of a smaller interaction volume associated with the secondary electrons. Another smaller, $\sim 15\ \mu\text{m}$ long crack-like feature was spotted to the left of Crack 1 (denoted as Crack 2 in Figure 29) during the higher resolution SEM examination. This crack had not been observable in the low-magnification SEM-BSE montage image. The detailed morphology of this crack is presented in the bottom left of Figure 29. It appears to be an IG crack since slip bands (denoted by slightly varying bands of darker and brighter contrast almost orthogonal to the crack) can be seen in the BSE image.

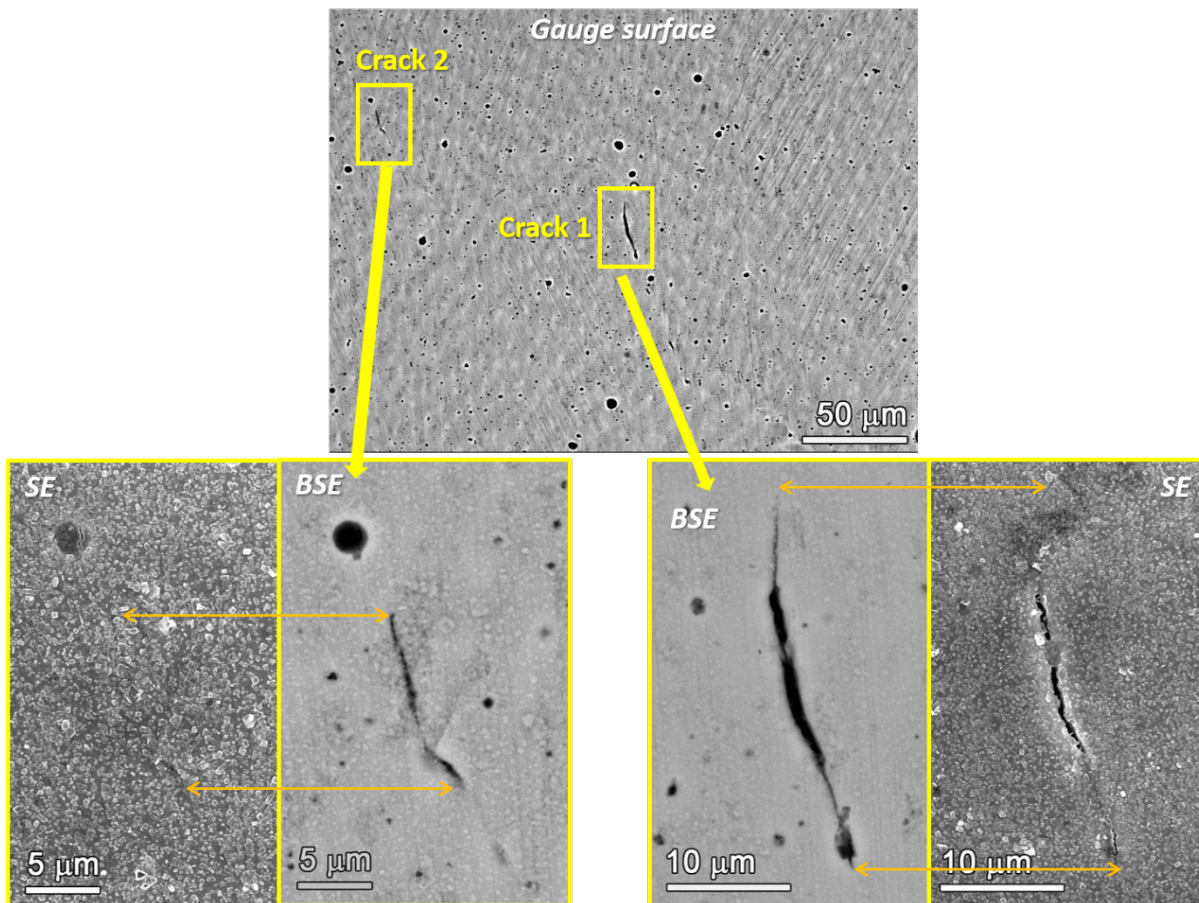


Figure 29. SEM-BSE/SE images of the two small cracks identified in the gauge surface of the 15% CF Alloy 152M IHI specimen IN128 after 20,659 hours of exposure.

To better understand these IG cracks, FIB was employed to make shallow trenches of $\sim 6\ \mu\text{m}$ in depth at two locations on Crack 1 as shown in Figure 30a. The first trench was made at the lower tip of Crack 1 for examination of the cross-section morphology of the crack. As shown in Figure 30b, no crack opening was observed, and instead only a shallow but wide IG oxidation with a penetration depth of $\sim 500\ \text{nm}$ from the surface was found. No other IG defects such as

cavities were observed in the near-surface region. To preserve this feature for future exposure and documentation of its evolution over time, a second trench was made $\sim 10 \mu\text{m}$ away from the lower tip of the crack, where serial milling across a span of $\sim 5 \mu\text{m}$ on the surface was performed. Interestingly, a lack-of-fusion defect was revealed during the serial milling at $\sim 2 \mu\text{m}$ below the surface along the same GB where the crack is observed $\sim 10 \mu\text{m}$ away (Figure 30c). This indicates that the surface crack may be associated with the sub-surface welding defect and is likely a pre-existing crack rather than a new crack formed during the long-term exposure. However, more examinations are needed to confirm this deduction.

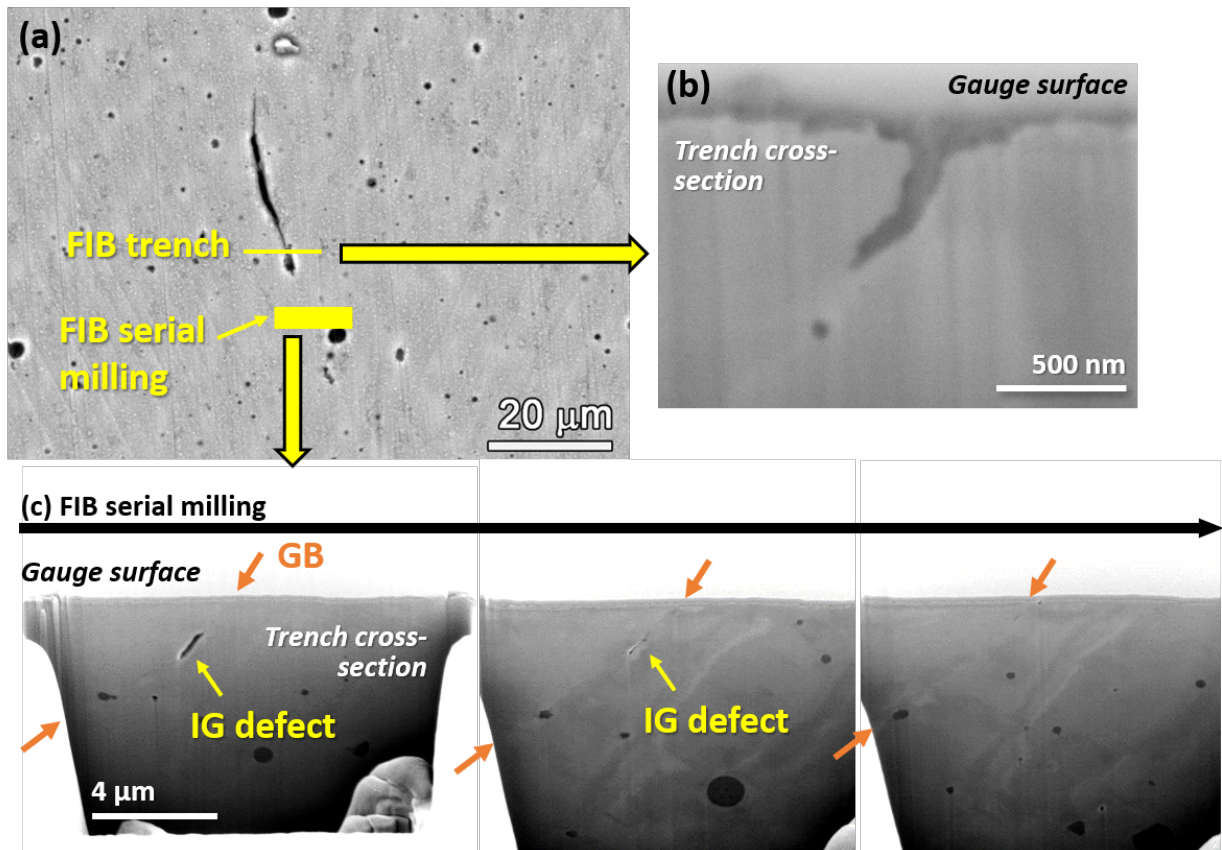


Figure 30. (a) SEM-BSE image showing the location of the two FIB trenches in IN128, (b) FIB-SE image showing the cross section of the trench at the location identified in (a), and (c) examples of the FIB-SE images taken during the serial FIB milling along the selected portion of a GB identified in (a).

15% CF MHI Alloy 52 specimen IN124 and Alloy 152 specimen IN142

The other two specimens that were observed under SEM are the Alloy 52 specimen IN124 and Alloy 152 specimen IN142, both from MHI. As shown in Figures 31 and 32 for IN124 and IN142 respectively, grains were partially revealed on the gauge surface of both specimens possibly due to orientation-dependent formation of spinel oxides. However, the oxides had grown so thick that the grain boundaries are not observable even knowing that the change in surface appearance likely represented the location of GBs.

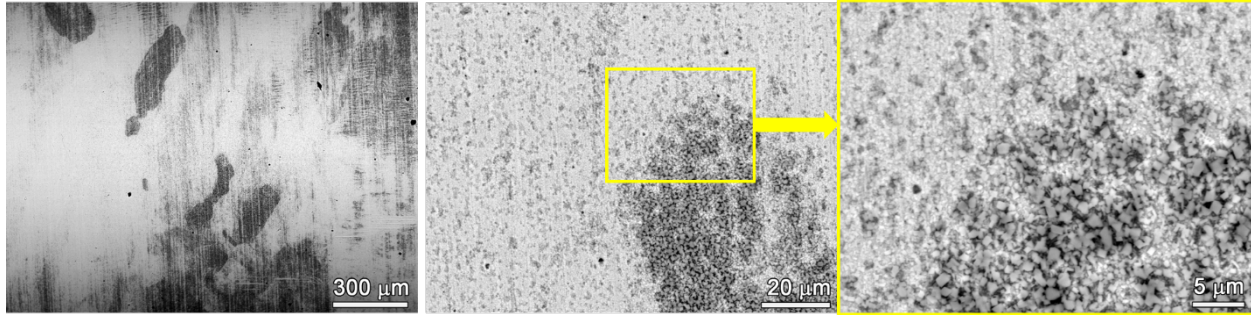


Figure 31. Representative SEM-BSE images of the gauge surface of the 15% CF Alloy 52 MHI specimen IN124 after 20,659 hours of exposure.

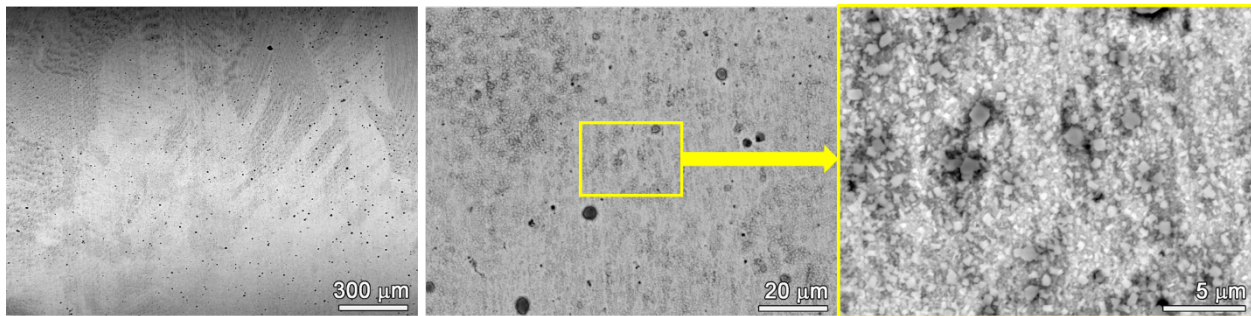


Figure 32. Representative SEM-BSE images of the gauge surface of the 15% CF Alloy 152 MHI specimen IN142 after 20,659 hours of exposure.

Summary of Observations

The lack of GB creep cavity formation in the 15% CF Alloy 690 specimens is consistent with a previously observed strong reduction in GB cavity formation when dropping from 30% CW to 20% CW for SCCI tests conducted under the DOE-NE LWRs program, and it is suggestive that the 15% CF Alloy 690/152(M)/52(M) specimens in the NRC/EPRI program will reach five years of exposure without any significant GB cavity formation and without crack initiation.

The likelihood for GB cavity formation and crack initiation in 15% CF Alloy 690/152(M)/52(M) after very long times, e.g., 10+ years, is unclear. Arioka and Staehle have predicted that GB cavity formation would be the most likely long-term degradation mechanism in Alloy 690 [7, 8]. Among the four examined weld metal specimens, crack-like features at the surface of the specimens and having a depth of less than 1 μm were only identified in the IHI A152M specimen IN128 after 2.4 years of exposure. The features were IG and may be associated with pre-existing weld defects in the material rather than GB cavity formation or intergranular oxidation driven SCC crack formation, but further analysis is needed to confirm this hypothesis. While a thick layer of spinel oxide was found on the surface of several specimens that obscured a clear examination of surface IG damage, it is believed that any open crack will be readily identifiable even with a high degree of surface oxide coverage.

6.0 Statistical Analysis of Alloy 182 and Alloy 600 SCC Initiation

6.1 Introduction

One goal for this program is to obtain Alloy 182 crack initiation data that can be used to verify, supplement, or replace data from the literature that is being used by the xLPR program to calibrate Alloy 182 crack initiation models. These models, as will be described here, focus on stress and temperature dependences of Alloy 182 crack initiation. The data currently being used by xLPR are based on a variety of sources but comes mainly from researchers in France [2, 4, 9, 10]. Sufficient data have now been obtained by PNNL to allow for the determination and comparison of a stress exponent to the body of literature on Alloy 182 initiation.

For this program, an in-depth statistical analysis was performed to fully assess the stress dependence of SCC initiation of Alloy 182, both from literature and PNNL data. In particular, the analysis was expanded to include exposure times for non-initiated specimens. This was previously performed by Park [11] for some of the literature data, but in analyzing their results, it was determined that some errors existed in their approach. The corrected approach is provided here. As often occurs, some of the literature studies were missing important pieces of information, in this case the YS of the as-fabricated material and the true stress of the test specimen were typically not provided. When needed, these were estimated following methods developed by Troyer [12] to provide consistency with the literature.

As will be shown, the stress exponent based on PNNL data is somewhat higher than the value estimated from the literature. As a means to evaluate whether this is due to PNNL test methods, the stress exponent for crack initiation of Alloy 600 from PNNL tests and the literature was estimated. It was found that the Alloy 600 stress exponent from PNNL data and literature data were slightly different, but considering the large variety of test methods that have been used for crack initiation studies, the values were very close, thus lending further credibility to the PNNL SCC initiation test method for determining stress exponent.

6.2 Crack Initiation Models

6.2.1 Overview

Currently, three models [13], namely Direct Model 1 [14, 15], Direct Model 2 [16, 17], and a modified Weibull model that considers applied stress [13, 18], are included in the xLPR module codes to predict PWSCC initiation. The initiation testing program at PNNL is intended to provide data to validate, and if needed, calibrate parameters in these models that are affected by environmental variations such as stress and temperature.

6.2.2 Direct Model 1 (Power Law Model)

Direct Model 1 is the simplest model. It describes a power law relationship between the initiation time, t , and the applied stress, σ , on a control load sample, as described in Equation 1. The model was initially proposed by Bandy and van Rooyen [14] from their observation of Alloy 600 SCC initiation testing under constant load in deaerated water. Then it was included in a methodology for stress corrosion life estimation for Alloy 600 components by Amzallag [15]. Because SCC initiation in Alloy 600 is a thermally activated process, an Arrhenius temperature dependence was proposed and added to the stress dependence based on laboratory and field

service data [15]. Various activation energy values are reported in different studies. Bandy and van Rooyen studied Alloy 600 U-bend samples and estimated the activation energies were in the range from ~125 kJ/mol to ~293 kJ/mol for carbon level variations from 0.01% to 0.05% [14]. PNNL has not yet performed the tests necessary to estimate Alloy 182 activation energy, but an estimated value of 185 kJ/mol, which is the activation energy recommended for Alloy 600 SCC initiation, is recommended in the literature [12] and is used here when needed to normalize initiation times from various sources where initiation tests were performed at different temperatures.

$$\frac{1}{t_{ini}} = A e^{-Q/RT} \sigma^n, \sigma > \sigma_{th} \quad \text{Equation 1}$$

t_{ini} = initiation time under fixed set of conditions (hours)

T = temperature (Kelvin)

σ_{th} = stress threshold parameter (MPa)

A = Direct Model 1 proportionality constant (hours/MPa⁻ⁿ)

n = stress exponent (unitless)

Q = activation energy for initiation (kJ/mol)

R = universal gas constant (kJ/(mol•K))

6.2.3 Direct Model 2

Direct Model 2 has multiple dependencies, including YS and ultimate strength dependencies, that can potentially better align responses from multiple welds. It has thus far not been applied by anyone to a large body of the available Alloy 182 literature data, so it is not covered in this report. If application of Direct Model 2 to PNNL data is of interest to EPRI or the NRC, the PNNL data will be applied to it.

6.2.4 Weibull Model

Weibull models are widely used in reliability engineering and failure analysis for predicting and forecasting product/component lifetime. It has various forms and parameterizations. One common model contains two parameters, and the corresponding probability density function and cumulative distribution function for this variant are shown in Equation 2 and Equation 3. In the two-parameter Weibull distribution, the shape parameter β is related to the failure rate, where $\beta < 1$ indicates the failure rate decreases over time, $\beta = 1$ indicates a constant failure rate, and $\beta > 1$ indicates increasing failure rate over time; and θ implies a characteristic time at which the Weibull cumulative distribution function (CDF) reaches a value of roughly 0.632 ($F = 1 - e^{-1}$ when $t = \theta$). In the xLPR framework, the scale parameter θ is expanded as a term to include the effects of applied stress σ and test temperature T , as shown in the Equation 4. Directly applying this equation for the Weibull analysis may cause some issues, such as difficulties in parameter estimation, since non-scaled stress data could cause data overflow in the optimization process.

$$f(t; \beta, \theta) = \frac{\beta}{\theta} \left(\frac{t}{\theta} \right)^{\beta-1} \exp \left(- \left(\frac{t}{\theta} \right)^{\beta} \right)$$

Equation 2

$$F(t; \beta, \theta) = 1 - \exp \left(- \left(\frac{t}{\theta} \right)^{\beta} \right)$$

Equation 3

$$\theta = C \exp(-Q / RT) \sigma^{-n}$$

Equation 4

t = initiation time under fixed set of conditions (hours)

β = shape parameter (unitless)

θ = scale parameter (hours)

C = a proportionality constant (hours/MPa⁻ⁿ)

Q = activation energy for initiation (kJ/mol)

R = universal gas constant (kJ/(mol•K))

T = temperature (Kelvin)

σ = surface stress (MPa)

n = stress exponent (unitless)

Standard two-parameter Weibull analysis can be applied to test data using a Weibull probability plot, which is a graph where the horizontal axis (x-axis) is the initiation time in log scale, and the vertical axis (y-axis) is the cumulative probability plotted in a double log scale. The corresponding input variable is $\log(t)$, and the dependent variable is $\log(-\ln(1-F(t)))$, as described in the Equation 5. The empirical cumulative probability F is approximated by applying Equation 6 on an ordered ascending sequence of initiation time. The Weibull probability plot approach was intended only for initiated data (called ‘complete data’ here).

$$\log(-\ln(1 - F(t))) = \beta \log t - \beta \log \theta$$

Equation 5

$$\hat{F} = \frac{i - 0.3}{n + 0.4}$$

Equation 6

i = the rank of data in the ordered sequence

n = the number of data points

SCC testing is a time-consuming process and thus laboratory data are limited and valuable. There are around 150 SCC initiation test data points (initiated and non-initiated combined) available in the open literature, for Alloy 182 (~50 obtained by PNNL and ~100 obtained by other labs). About half of the tests were stopped before initiation occurred. However, many analyses use only initiated data. Incorporating non-initiated data into an analysis would almost double the data utilization. A dataset containing both initiated and non-initiated test data is commonly referred to as “right-censored”. This name is used because for non-initiated data, the test stop time is the lower bound for actual SCC initiation time. Right-censored data is commonly seen in survival analysis and reliability engineering. The methodology for incorporating censored data in Weibull models is well-established. It utilizes the maximum likelihood estimation (MLE) approach, and the modification of the likelihood function to include both initiated and non-initiated cases is described in Equation 7. An application of this approach has been reported by Park [11] for Alloy182/132/82 data. In addition to the MLE, the scale

parameter is modified to follow a power law relationship with respect to the ratio of applied stress and yield stress, as described in Equation 8.

$$\text{LogLikelihood}(\beta, \theta) = \sum_{i=1}^n \ln f(t_i) + m \ln(1 - F(t)) \quad \text{Equation 7}$$

$$\theta = \eta_r r^{-n_r} \quad \text{Equation 8}$$

m = number of specimens not failed (unitless)

r = ratio between applied true stress and yield stress at test temperature (unitless)

n_r = stress ratio exponent (unitless)

η_r = scale parameter of the Weibull distribution when stress ratio is 1 (hours)

6.3 Data Source and Pre-Treatment

Alloy 182 and Alloy 600 initiation data generated at PNNL are included in this analysis. The literature data on SCC initiation that was used to establish a baseline to which the PNNL data were compared was acquired mainly from the following publications: Vaillant et al. [9], Scott et al. [4], and Couvant et al. [10] for Alloy 182; and Boursier et al. [19], Richey et al. [20], Itoh et al. [21], Yonezawa et al. [22], and Bandy et al. [14] for Alloy 600. Other major sources containing Alloy 182 data are Amzallag et al. [2] and Troyer et al. [12], where the Amzallag-reported data has large overlap with Scott and Vaillant (suggested by Couvant and Troyer, as well as our own visual inspection of various figures), and Troyer summarized some Alloy 182 initiation data together with Alloy 82 and Alloy 132. One data point from Amzallag was discarded because its adjusted true stress is 1,200 MPa [2] which is unrealistically high for Alloy 182. Troyer et al. [12] also did not use this data point in their analysis.

Because SCC initiation tests were conducted at different environmental conditions, it was necessary to normalize the data to a common baseline for comparison of stress effects. It is commonly agreed that the influence of testing temperature on SCC initiation time follows an Arrhenius relationship. Therefore, all SCC initiation times were adjusted to a nominal test temperature of 325°C assuming an activation energy of 185 kJ/mol for both Alloy 182 and Alloy 600. Unlike Alloy 600, the activation energy of Alloy 182 has only been limitedly explored. Troyer et al. suggested following the EdF-proposed value of 185 kJ/mol that is borrowed from the widely adopted activation energy for Alloy 600.

Since true stress is used in the xLPR models, true stress is used in this analysis. Any reported engineering stresses were converted to true stress using an exponential relationship proposed by Troyer [12]. The stresses reported in PNNL tests are all true stress.

The stress dependence as a function of stress ratio, which is the ratio between applied true stress and the YS of as-received (as-welded) samples at the test temperature, was also explored. The stress ratio acts to normalize the response of different materials based on their as-fabricated YS. This normalization may be helpful to data interpretation and exploration. If only room temperature YS was available for data from other labs, YS at test temperature is estimated by multiplying a factor of ~0.87, as described in [12]. Evaluation of initiation data as a function of stress ratio was also performed by Troyer [12] and Park [11] in their compilations. A unique aspect of the PNNL initiation specimens is that the strength of the materials was increased by cold forging in compression whereas the data covered by Troyer and Park were obtained from specimens that were either uniaxially tensile strained (tensile specimens) or biaxially tension strained (capsules). PNNL believes that no matter what the mode of deformation, the use of stress ratio relative to as-fabricated (or as-welded) YS of a material is fully relevant to xLPR due to reactor structures undergoing various modes of deformation.

Comparing SCC initiation times as a function of stress ratio will be a valuable tool in understanding how deformation mode may affect SCC initiation behavior.

When applying a curve fit to data that are expected to have a power law dependence, it is common to apply a log transformation to the data and then apply a least squares linear regression to the log-transformed data as a function of the independent variable. This method was selected because it appears to be the method used by previous researchers of Alloy 182 initiation data. However, as will be shown in Section 6.6, at least one other fitting method exists that may produce a more representative curve fit to the data.

6.4 Analysis of Alloy 182 Initiation Times

6.4.1 Analysis Using Direct Model 1

The first analysis focused on PNNL-tested 15% CF Alloy 182 samples with detected SCC initiation. The initiation times are plotted against true stress and against stress ratio in Figure 33. All samples were tested within a relatively narrow true stress range of 450 to 600 MPa, and the corresponding stress ratios were around 1.2-1.6. The time to SCC initiation in this dataset varied by around two orders of magnitude, where some samples initiated as early as ~10² hours (when normalized to a test temperature of 325°C), while other samples did not initiate until close to 100,000 hours. The estimated parameters for Direct Model 1 are listed in Table 11, and the corresponding curves are plotted as solid lines in Figure 33. The estimated stress exponent, *n*, is 5.2 and 8.9 for datasets using true stress and stress ratio, respectively. Although stress is commonly used as the input variable (independent variable) to estimate a stress exponent, stress ratio is an alternative input variable to evaluate the stress dependence of SCC initiation. In particular, the Weibull model uses stress ratio rather than applied stress. For the PNNL Alloy 182 data presented here, no obvious improvement in data fit is apparent when stress ratio is used in a power law fit.

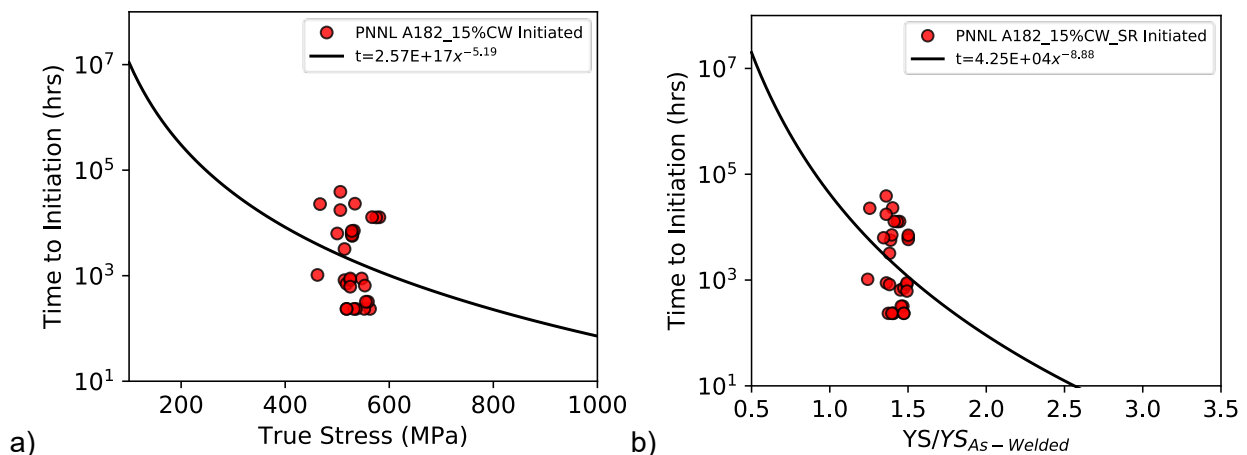


Figure 33. Test data for 15% CF, initiated PNNL Alloy 182 samples: a) PWSCC time to initiation vs. true stress; b) PWSCC time to initiation vs. stress ratio.

Table 11. Estimated parameters for Direct Model 1 defined initiation time-stress relationship for 15% CF Alloy 182.

Dataset	Input Variable	Number of Data	Pre-exponential factor	Stress Exponent	R-squared
PNNL 15% CF Initiated	True Stress	30	$\exp(40.1 \pm 38.4)$	5.2 ± 6.1	0.025
PNNL 15% CF Initiated	Stress Ratio	30	$\exp(10.7 \pm 2.3)$	8.9 ± 6.4	0.064

Next, the analysis was expanded to all PNNL-tested Alloy 182 samples that exhibited SCC initiation, namely initiated 15% and 7.5% CF samples. None of the PNNL as-welded specimens have initiated. All available initiation data from other labs were also analyzed for comparison. The time to SCC initiation versus true stress and stress ratio for PNNL and other labs initiation data along with the corresponding regression curves are shown in Figure 34, while the estimated parameters are listed in Table 12. For PNNL-initiated data, the estimated stress exponents are 6.6 as a function of true stress and 7.3 as a function of stress ratio. The addition of the several 7.5% CF data points causes the difference between using true stress and stress ratio to be reduced. The regression analysis on the comparison data from other labs produced stress exponents of 5.7 and 5.8 for true stress and stress ratio datasets, respectively. These values are only slightly higher than the value of 5.2 determined by Troyer. Merging both PNNL's

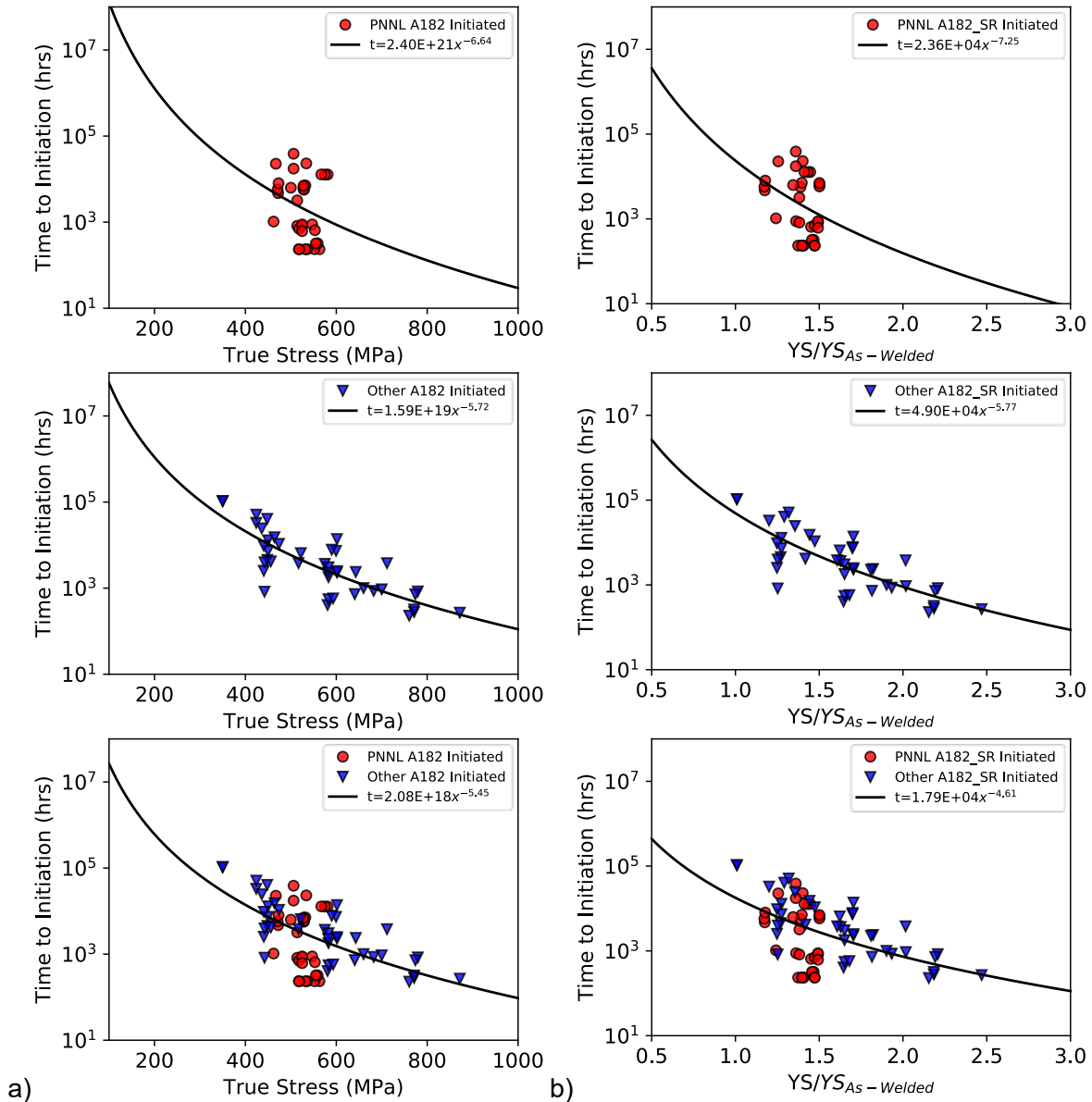


Figure 34. Test data for Alloy 182 samples that exhibited SCC initiation obtained at PNNL and other laboratories: a) initiation time vs. true stress; b) initiation time vs. stress ratio.

Table 12. Estimated pre-exponential factors and stress exponents for Direct Model 1 for Alloy 182. The pre-exponential factors are expressed with standard error inside the exponential term due to the log transformation.

	Input Variable	Number of Data	Pre-exponential factor	Stress Exponent	R-squared
PNNL Initiated	True Stress	33	$\exp(49.2 \pm 30.4)$	6.6 ± 4.9	0.057
Others Initiated		41	$\exp(44.2 \pm 4.3)$	5.7 ± 0.7	0.648
PNNL+ Others Initiated		74	$\exp(42.2 \pm 5.6)$	5.4 ± 0.9	0.333
PNNL Initiated	Stress Ratio	33	$\exp(10.1 \pm 1.4)$	7.3 ± 4.1	0.096
Others Initiated		41	$\exp(10.8 \pm 0.4)$	5.8 ± 0.7	0.605
PNNL + Others Initiated		74	$\exp(9.8 \pm 0.4)$	4.6 ± 0.9	0.264

and other labs' Alloy 182 data gives estimated stress exponents of 5.5 for true stress and 4.6 for stress ratio. A comparison of the stress range covered by PNNL data and literature data show that the PNNL data cover a much narrower stress range, and this is partially responsible for its relatively large R-squared value. In this regard, it can be considered coincidental that the PNNL data produce stress exponents that are relatively similar to the literature data that covers a much wider stress range. The PNNL data also have a relatively large amount of scatter of initiation times, covering approximately two orders of magnitude over a relatively narrow stress range. It has been suggested that this is uniquely higher than the literature data, however a review of the initiation time data reported by Troyer reveals that some of the Valliant data at 400 MPa covers almost two orders of magnitude. And when non-initiated specimens are included for the literature data (as will be shown a little later), the stress range for literature data at a particular stress level grows beyond two orders of magnitude.

In the scale of initiation times, PNNL Alloy 182 data is visually in good agreement with the data from other labs. A closer look at data within the 400-600 MPa stress range suggests that the PNNL data contains several samples that initiated at a lower time than data from other labs. As discussed earlier, this could be due to the use of DCPD detection of initiation at PNNL. It is more sensitive to early-stage SCC initiation than intermittent visual inspection and the test-until-rupture approaches that were used in the studies reported in the literature.

Figure 35 is a reproduction of Figure 34 with the addition of 95% prediction bands and 95% confidence bands plotted for each dataset. The prediction band establishes the range within which new data is expected to fall given a fixed probability. The confidence band can be interpreted as the confidence that the real regression line exists in the bounds. Both are based on the error assumptions for the regression, which is generally assumed to be normally distributed. For a power law fit, the error term was assumed to be normally distributed in the log space.

The standard errors and confidence bands suggest that parameter estimation based on PNNL-only Alloy 182 with SCC initiation data produces larger uncertainties compared with the other labs' data and when compare to the combined data of PNNL and other labs. However, the larger standard error and lower R-squared does not undermine the meaningfulness and the value of the data. Instead, it means that relying solely on PNNL data for parameter estimation may not be the best choice, likely because of the relatively narrow true stress and stress ratio range associated with the PNNL-only data.

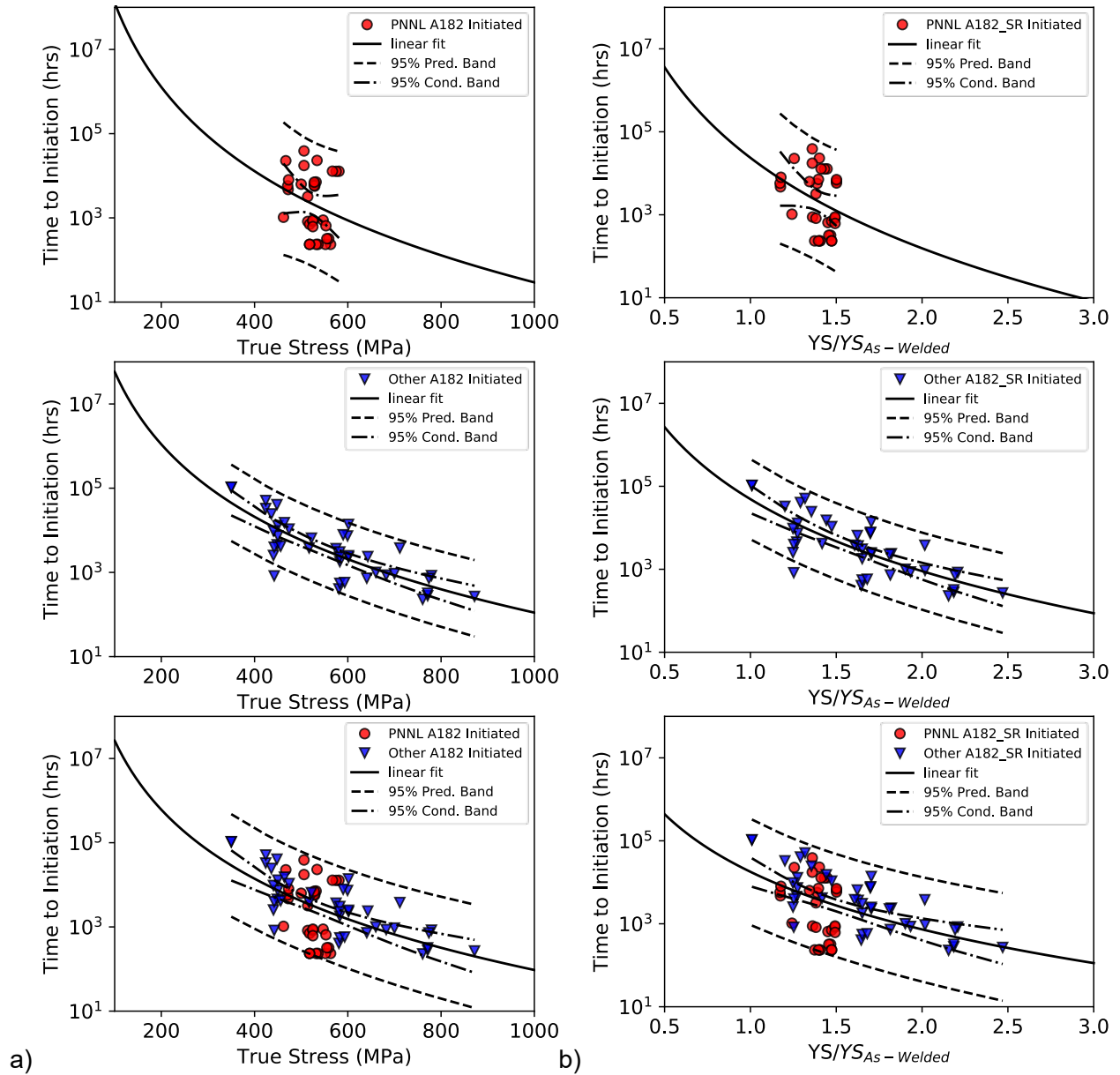


Figure 35. Same data and regression curves as in Figure 34 with additional information for prediction bands and confidence bands plotted.

Figure 36 shows plots of initiated and non-initiated data from PNNL and other labs' Alloy 182 tests. A summary of the fit values is provided in Table 13. Direct Model 1 was proposed to use only initiated data, but non-initiated data are included to explore their influence on the fit values. When considering only literature data or literature data combined with PNNL data, the estimated stress exponent is 4.3 and 5.5 regardless of whether its plotted versus true stress or stress ratio, while for PNNL-only data, the stress exponent is estimated to be 10.9 when plotted versus true stress and 11.8 when plotted versus stress ratio. The increased stress exponent for PNNL data is driven by the inclusion of non-initiated Alloy 182 data which did not exhibit SCC initiation when tested at lower stress. As further exposure time is accumulated on the PNNL specimens, the stress exponent will increase because nearly all the non-initiated specimens are at lower stresses.

For data from other labs, about half (51 out of 94) of the samples were not initiated, and among the 51 non-initiated samples, 21 appear to have been tested at stresses representative of the as-welded YS. When considering the data of other labs only, inclusion of their non-initiated data reduces the stress exponent slightly. The reason for this is that there are a large number of specimens at moderate YS that also did not initiate, and these deviate from the trend of the initiated data more than the non-initiated data at lower YS values, causing the curve to flatten slightly. PNNL believes that if these tests could be continued to the point of initiation, the stress exponent of the literature data would increase because the lower strength specimens would likely run longer to initiation than the remaining non-initiated, moderate stress specimens. It would likely not increase to the value of the PNNL-only stress exponent because the data from other labs has initiation times from very high stresses that would act to limit how much the stress exponent could increase, but it would nevertheless increase. While testing of the specimens at other labs is complete, tests being conducted by PNNL are continuing, and as exposure time increases on the PNNL data, the stress exponent from the combined data of PNNL and other labs will increase.

Another aspect of the data that becomes apparent is the relative degree of scatter between the PNNL data and the data of other labs. When viewing just the initiated data, the PNNL dataset has somewhat more scatter, but when including non-initiated data, the data of other labs has the same or even a greater degree of spread in the same stress range where the PNNL data has wide scatter, and if those tests were able to be continued, that spread would continue to grow.

Overall, this combination of qualitative and quantitative assessment of the PNNL data and data of other labs shows that the PNNL data are consistent with the data from other labs both in SCC initiation times and the relative degree of scatter. The analysis also provides a solid foundation for selecting a higher stress exponent than indicated by the data from other labs only. These conclusions are further emphasized by the histogram and Weibull analyses that are covered next.

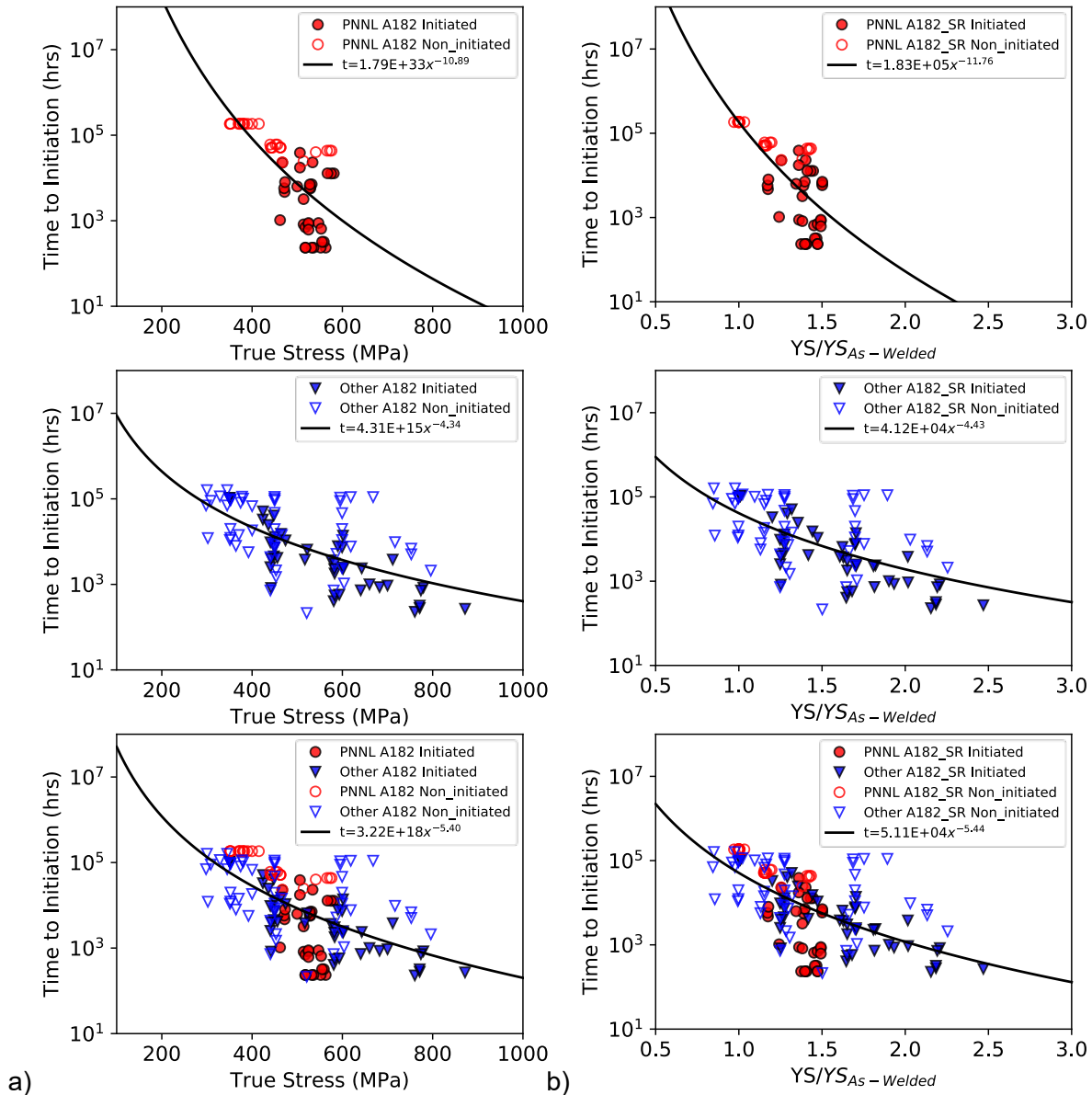


Figure 36. Test data for Alloy 182 samples with and without SCC initiation obtained at PNNL and other laboratories: a) initiation time vs. true stress; b) initiation time vs. stress ratio.

Table 13. Estimated pre-exponential factors and stress exponents for Direct Model 1 for Alloy 182 including non-initiated data. The pre-exponential factors are expressed with standard error inside the exponential term due to the log transformation.

Initiated and non-Initiated Data	Input Variable	Number of Data	Pre-exponential factor	Stress Exponent	R-squared
PNNL	True Stress	60	exp(76.6±9.2)	10.9±1.5	0.482
Others		93	exp(36.0±3.5)	4.3±0.6	0.388
PNNL+ Others		153	exp(42.6±3.6)	5.4±0.6	0.367
PNNL	Stress Ratio	60	exp(12.1±0.4)	11.8±1.4	0.572
Others		93	exp(10.6±0.3)	4.4±0.6	0.381
PNNL+ Others		153	exp(10.8±0.2)	5.4±0.6	0.377

Histograms of SCC initiation times are shown in Figure 37 plotted on the left as a linear function of time and on the right as a natural log function of time. For a linear time scale, the distribution of PNNL data and other labs data look very similar, both exhibiting a decreasing frequency of initiation with time. In the natural log scale histograms, the PNNL data continues to exhibit a decreasing initiation frequency as a function of time compared to a central peak in the data from other labs. For both datasets, the minimum initiation time is approximately the same. Because the data from other labs has a much wider range of test stresses, data from other labs was replotted using data covering stresses from 350-600 MPa. Using just this data does not change the data distribution other labs but does slightly raise the minimum SCC initiation time. Data bin size and scale range selection as a function of time will affect these qualitative comparisons.

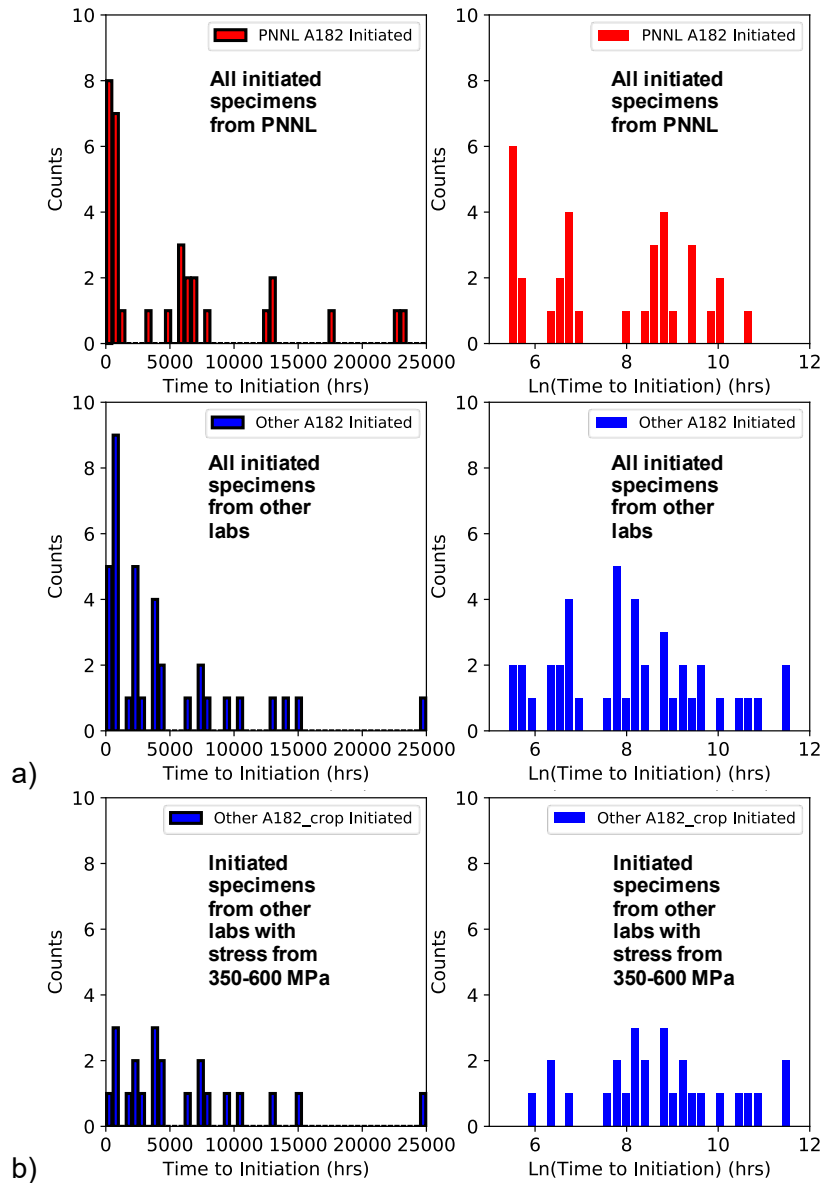


Figure 37. Histograms of SCC initiation time for a) PNNL’s test data and other labs’ data in linear and natural log scale; and b) other labs’ data with applied stress range from 350 to 600 MPa in tests. The stress range is selected to roughly match PNNL data and avoid counting low initiated time data at higher stress levels.

6.4.2 Analysis Using Weibull Models

Weibull analysis is widely used in failure analysis of materials, such as for lifetime forecasting and prediction [23, 24]. Figure 38 shows Weibull cumulative distribution plots for the SCC initiated Alloy 182 comparing PNNL data to other labs' data. Data from other labs was restricted to a stress range of 350 to 600 MPa to match the range of PNNL-initiated data. Using this approach, the estimated shape parameters, β , were found to be 0.68 for PNNL data and 0.62 for other labs' data. The scale parameter θ represents the time that ~63.2% of samples fail and is estimated to be 4,862 hours for PNNL's data, and 7,495 hours for other labs' data.

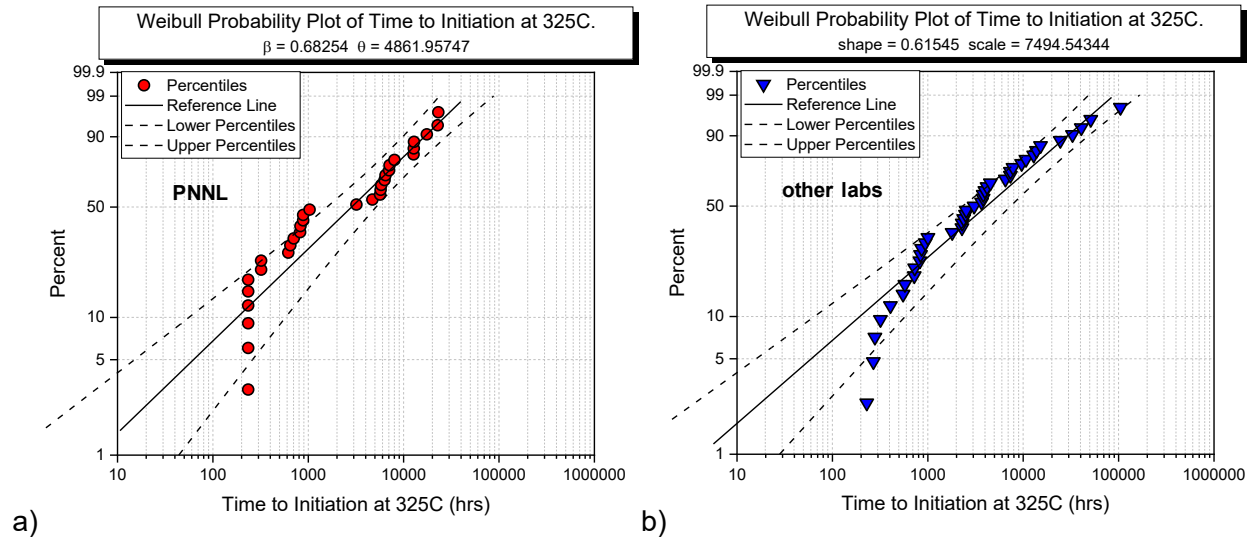


Figure 38. Two-parameter Weibull fittings to Alloy 182: a) tested at PNNL; b) tested at other labs. Note that only data with applied stress ranging within 350-600 MPa were included to match PNNL's testing condition.

For xLPR, a Weibull function is also employed to determine stress and temperature dependencies. A notable issue for Weibull analysis of initiation data from PNNL and other labs is the standard approach of only using initiated data. Weibull statistics, like the cumulative probability distribution from such analyses, undermine the fact that half of the specimens for the PNNL and non-PNNL datasets remain non-initiated at the end of testing. One way to bypass the issue is to calculate cumulative probability considering the remaining non-initiated samples [23]. A well-established approach to fully utilize censored data (in this case, non-initiated data) for Weibull analysis is through the MLE method for parameter estimation using a modified likelihood function, as described in Section 6.2.4. The results following this approach are shown in Figure 39. The curve fit lines for the plots that include non-initiated data sit near the high end the data range due to how the non-initiated data are treated in the MLE approach. The estimated parameters are listed in Table 14. For datasets containing only initiated data, the estimated shape parameter β is 0.70 for PNNL's data and is 1.16 for other labs' data. A β of 0.87 was found for the combined data. For datasets containing both initiated and non-initiated data, β is 0.56 for PNNL data, 0.56 for other labs, and 0.51 for combined data. This indicates that the data are more biased toward low initiation times than indicated by only initiated data. The estimated stress ratio exponent for initiated datasets is 5.6 for PNNL data, 6.2 for other labs, and 5.4 for combined data. For datasets containing both initiated and non-initiated data, the stress exponents increase to 19.9 for PNNL data, 7.1 for other labs, and 8.0 for combined data. For power law curve fit approach, the stress exponent of the PNNL-only and the

combined data both increased, but it decreased when using only data from other labs. As expected, the characteristic initiation time increased when including non-initiated data.

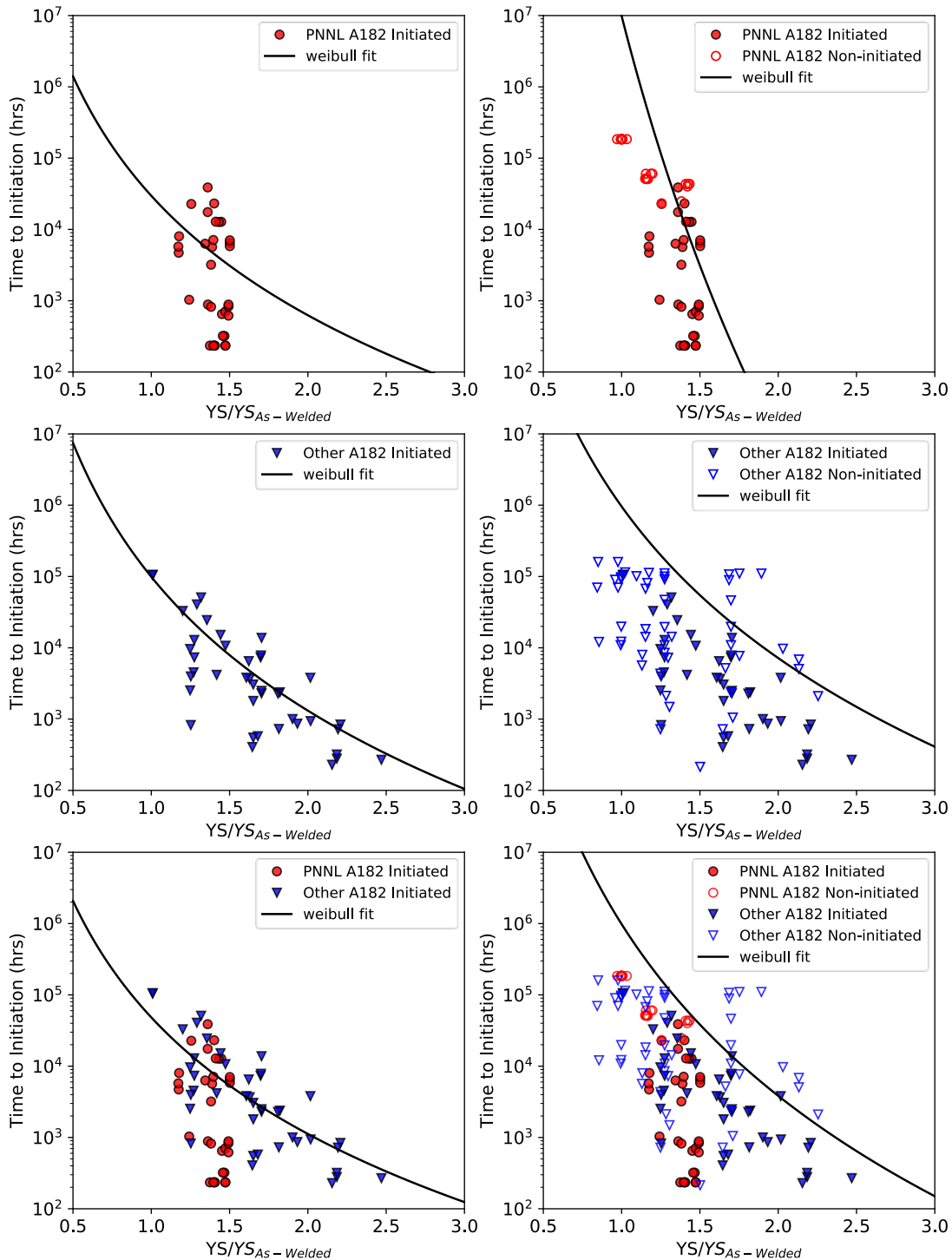


Figure 39. Weibull analysis on initiated datasets and right-censored datasets for PNNL’s test data, other labs’ data, and the combined of both. The solid lines are the characteristic time θ , as described by the Equation 8, which corresponds to the ~63.2% cumulative probability of SCC initiation at a giving stress ratio.

Table 14. Parameters for Weibull model analysis in Figure 39.

Dataset	Parameters	Estimated Values	
		Initiated	Initiated and Non-initiated
PNNL	β	0.70	0.56
	η_r	29,788	9,967,265
	n_r (stress exponent)	5.58	19.91
Other Labs	β	1.16	0.56
	η_r	99,023	959,731
	n_r (stress exponent)	6.23	7.06
PNNL + Other Labs	β	0.87	0.51
	η_r	48,353	982,174
	n_r (stress exponent)	5.43	8.00

6.5 Analysis of Alloy 600 Initiation Times

6.5.1 Analysis Using Direct Model 1

Alloy 600 SCC initiation data from PNNL adjusted to a 325°C test temperature testing are shown in Figure 40 both as a function of applied stress and as a function of stress ratio. In the absence of any curve fitting, the use of stress ratio (Figure 40b) visually results in a tighter grouping of the data. For either method of representing the test stress, it is apparent that the 15% CF specimens have much lower initiation time than non-CW specimens, and the 15% CF specimens have a very weak stress dependence.

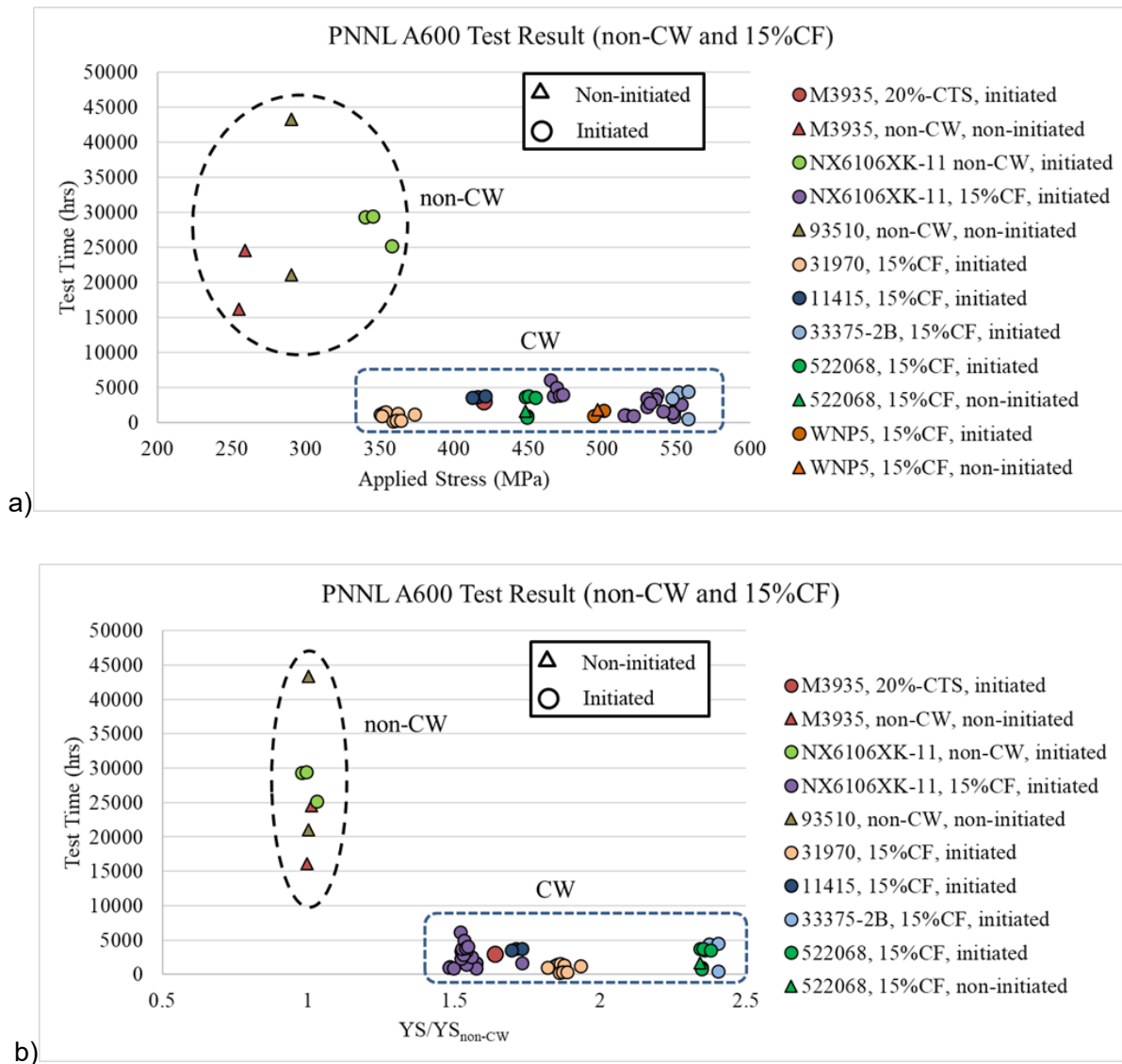


Figure 40. PNNL A600 initiation testing result plotted as test time against a) applied stress, and b) stress ratio between applied stress and yield strength of non-cold worked materials at the test temperature.

Regression analysis first focused on the 15% CF Alloy 600 with detectable SCC initiation at PNNL, and the result is shown in Figure 41. All cold worked samples were tested within a stress range of ~350 to ~600 MPa, and the corresponding stress ratios were around 1.4-2.5. The measured time to SCC initiation varied from ~10² to ~10⁴ hours. Solid lines are Direct Model 1 predicted initiation time-stress dependencies. Table 15 lists the parameters estimated in the regression analysis. The estimated stress exponent, *n*, is -2.6 and 0.5 for datasets using true stress and stress ratio, respectively. The negative stress exponent means initiation occurs faster at lower stress levels, which is physically unreasonable. This disconnect is due to the strong influence of the heat 31907 specimens that had a low yield stress and very low initiation times. The low YS of heat 31907 in the 15% CF condition stems from the fact that this heat has an as-fabricated YS of ~218 MPa, while most Alloy 600 has a YS of 300-320 MPa. In the stress ratio representation, the estimated stress exponent is positive. However, the stress exponent is below 1.0, indicating a very weak dependence of initiation time on the stress ratio.

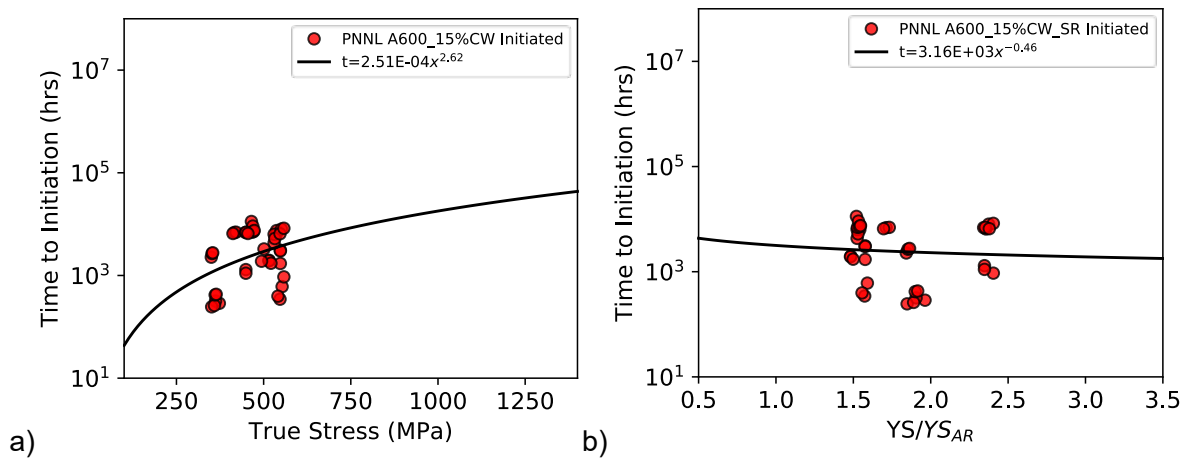


Figure 41. Test data for 15% CF, initiated PNNL Alloy 600 samples: a) PWSCC time to initiation vs. true stress; b) PWSCC time to initiation vs. stress ratio.

Table 15. Estimated parameters for Direct Model 1 for 15% CF Alloy 182.

Alloy 600	Input Variable	Number of Data	Pre-exponential factor	Stress Exponent	R-squared
PNNL 15%CW Initiated	True Stress	42	exp(-8.3±6.7)	-2.6±1.1	0.126
PNNL 15%CW Initiated	Stress Ratio	40	exp(8.1±0.7)	0.5±1.1	0.004
PNNL 15%CW Initiated, Excluding heat 31907	True Stress	33	exp(30.9±10.4)	3.7±1.7	0.134
PNNL 15%CW Initiated. Excluding heat 31907	Stress Ratio	31	exp(8.0±0.6)	-0.3±0.9	0.004

To illustrate the influence of heat 31907 samples, comparison graphs excluding that heat are plotted in Figure 42. For the true stress plot, the stress exponent rises to 3.7 from the previous value of -2.6. The estimated stress exponent for stress ratio plot is -0.3, which still indicates a weak or no dependence on stress ratio. The value of heat 31907 data is not diminished by this analysis (unless there are some intrinsic manufacturing issues that caused the lower yield strength or/and resulted in an out-of-specification microstructure); rather this analysis highlights that even a few data points greatly affect the analysis result.

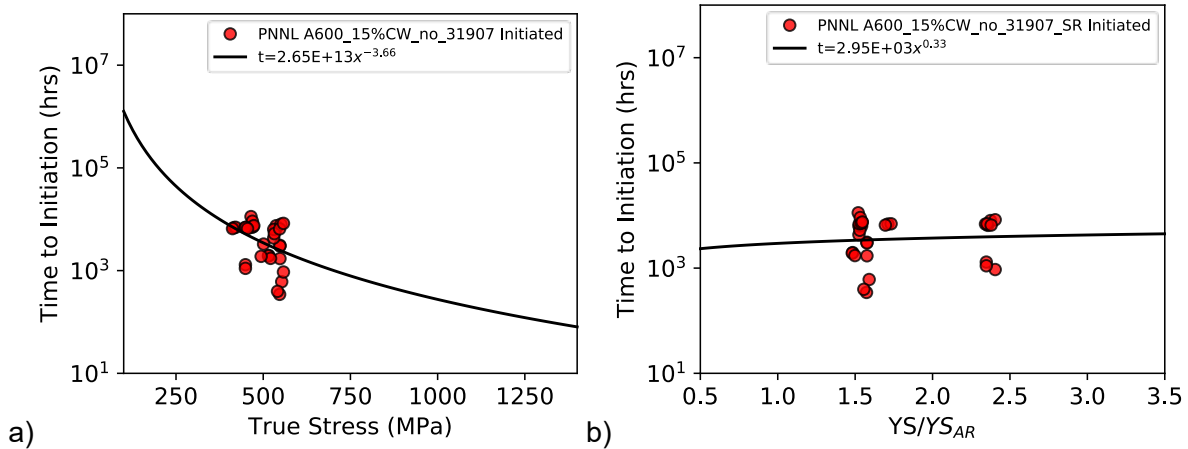


Figure 42. Test data for 15% CF, initiated PNNL Alloy 600 samples excluding heat 31907: a) PWSCC time to initiation vs. true stress; b) PWSCC time to initiation vs. stress ratio.

The analysis was then expanded to include all PNNL-tested Alloy 600 that exhibited SCC initiation. For this dataset, most samples were 15% CF/CW, some were 6%-20% CF/CW, and others were non-cold worked. For comparison purposes, PNNL data and other labs' data were curve fit separately, and then the combined data were curve fit. The results for the time to SCC initiation versus true stress and stress ratio are plotted in Figure 43. The curve fit parameters are listed in Table 16. For PNNL data, the stress exponent is -1.8 for using true stress and is 1.5 for using stress ratio, again showing the strong effect of the heat 31907 data. The stress exponents were estimated to be 2.0 and 1.4 based on other labs' data in true stress and stress ratio plots, respectively. Combining PNNL's data and other labs' data resulted in stress exponents estimated of -0.1 for true and 0.6 for stress ratio. The PNNL data have lower SCC initiation times than data from other labs, and since the PNNL data are at relatively low stress values, they bring down the stress exponent of the combined data.

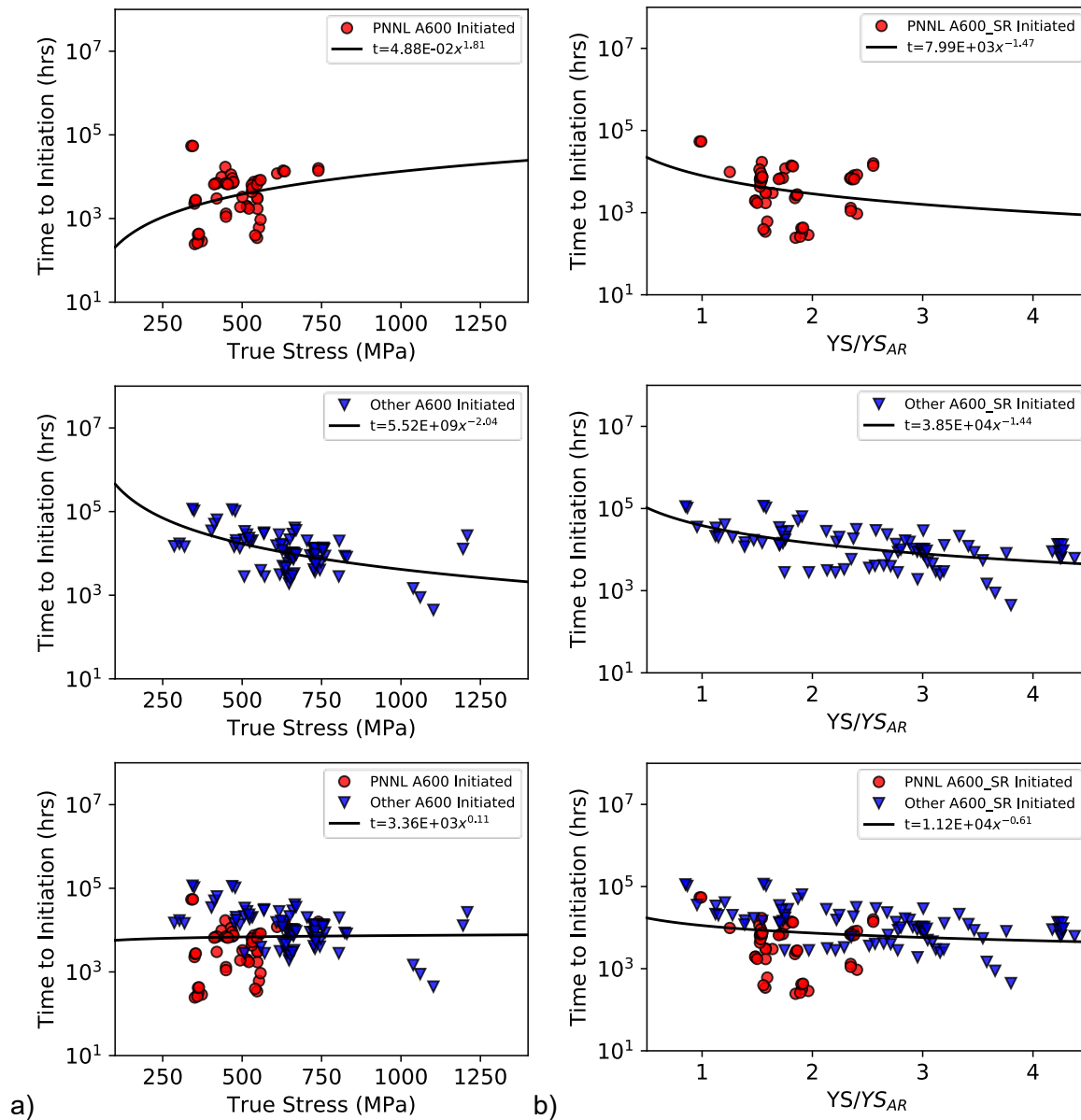


Figure 43. Test data for Alloy 600 samples that exhibited SCC initiation obtained at PNNL and other laboratories: a) initiation time vs. true stress; b) initiation time vs. stress ratio.

These stress exponent values are clearly lower than the value of 4 suggested by Amzallag et al. [15]. It is likely that the stress exponent of 4 was calculated with respect to engineering stress. In a recent study [25] and in our own re-examination of selected Alloy 600 SCC initiation literature data shown in Figure 44, the stress exponents for Alloy 600 are estimated to be in the range from 2 to 3 with respect to true stress. The data shows that PNNL's Alloy 600 samples initiated considerably earlier than Alloy 600 samples tested at other labs. The root cause of this difference is not certain, but it may be due to a more sensitive initiation detection technique used at PNNL compared to that used for previous studies.

Table 16. Power law fitting parameters for Alloy 600 SCC initiated data.

Alloy 600	Input Variable	Number of Data	Pre-exponential Factor	Stress Exponent	R-squared
PNNL Initiated	True Stress	52	$\exp(-3.0 \pm 5.8)$	-1.8 ± 0.9	0.070
Other Initiated		83	$\exp(22.4 \pm 2.3)$	2.0 ± 0.4	0.280
PNNL + Others Initiated		135	$\exp(8.1 \pm 2.5)$	-0.11 ± 0.40	0.001
PNNL Initiated	Stress Ratio	50	$\exp(9.0 \pm 0.5)$	1.5 ± 0.9	0.054
Other Initiated		83	$\exp(10.6 \pm 0.2)$	1.4 ± 0.2	0.315
PNNL + Others Initiated		133	$\exp(9.3 \pm 0.2)$	0.6 ± 0.3	0.032

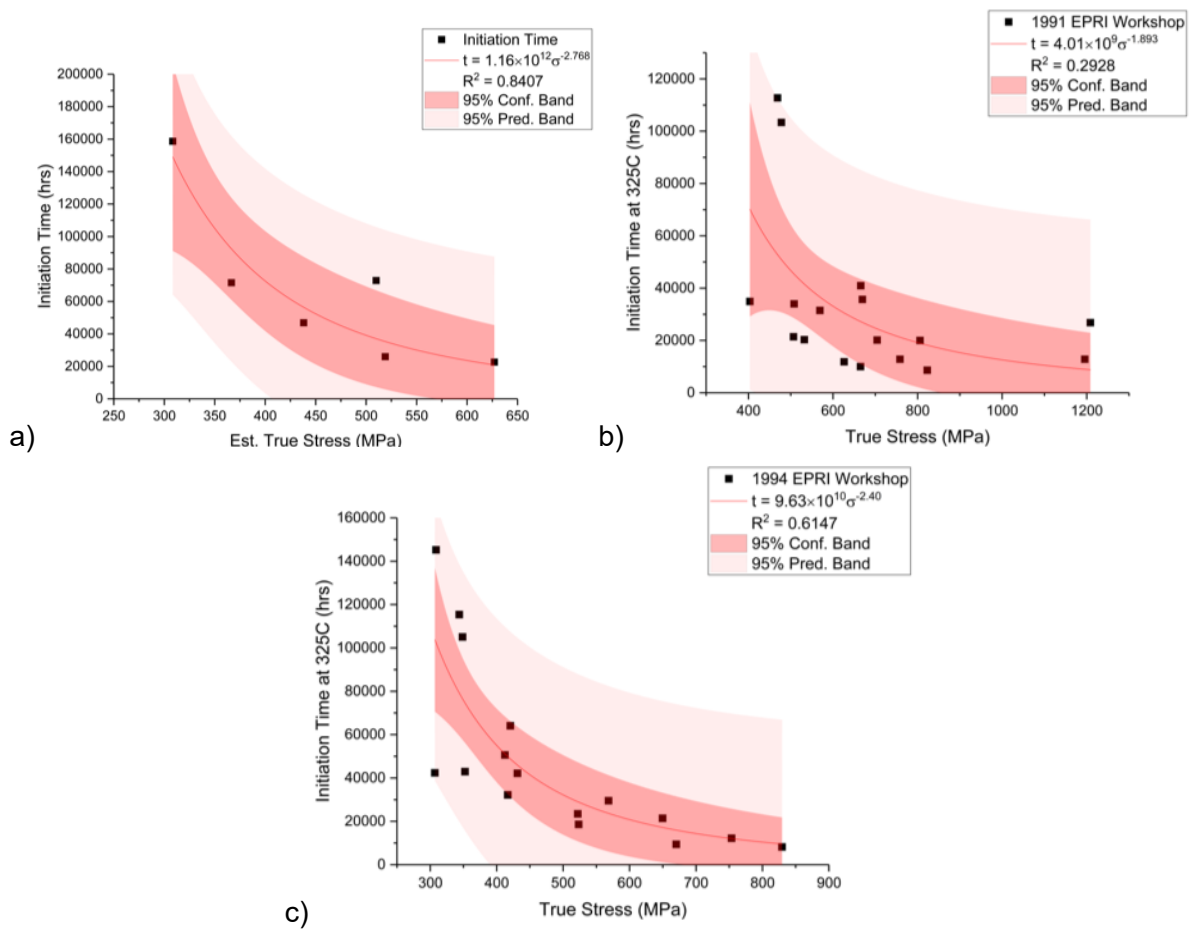


Figure 44. Re-analysis on several published Alloy 600 datasets using true stress: a) Bandy and van Rooyen 1983 [14], n=2.8; b) Yonezawa 1991 [22], n=1.9; c) Itoh 1994 [21], n=2.4.

Figure 45 shows 95% prediction bands and the 95% confidence bands plotted for datasets in Figure 43. The prediction band establishes the range within which new data is expected to fall given a fixed probability, and the confidence band indicates the confidence that the real regression line exists in the bounds. Both are based on the error assumptions for the regression, which is generally assumed to be normally distributed. For a power law fit as used here, the error term was assumed to be normally distributed in the log space. The uncertainties in parameter estimation are larger in PNNL's Alloy 600 test data than in other labs' test data.

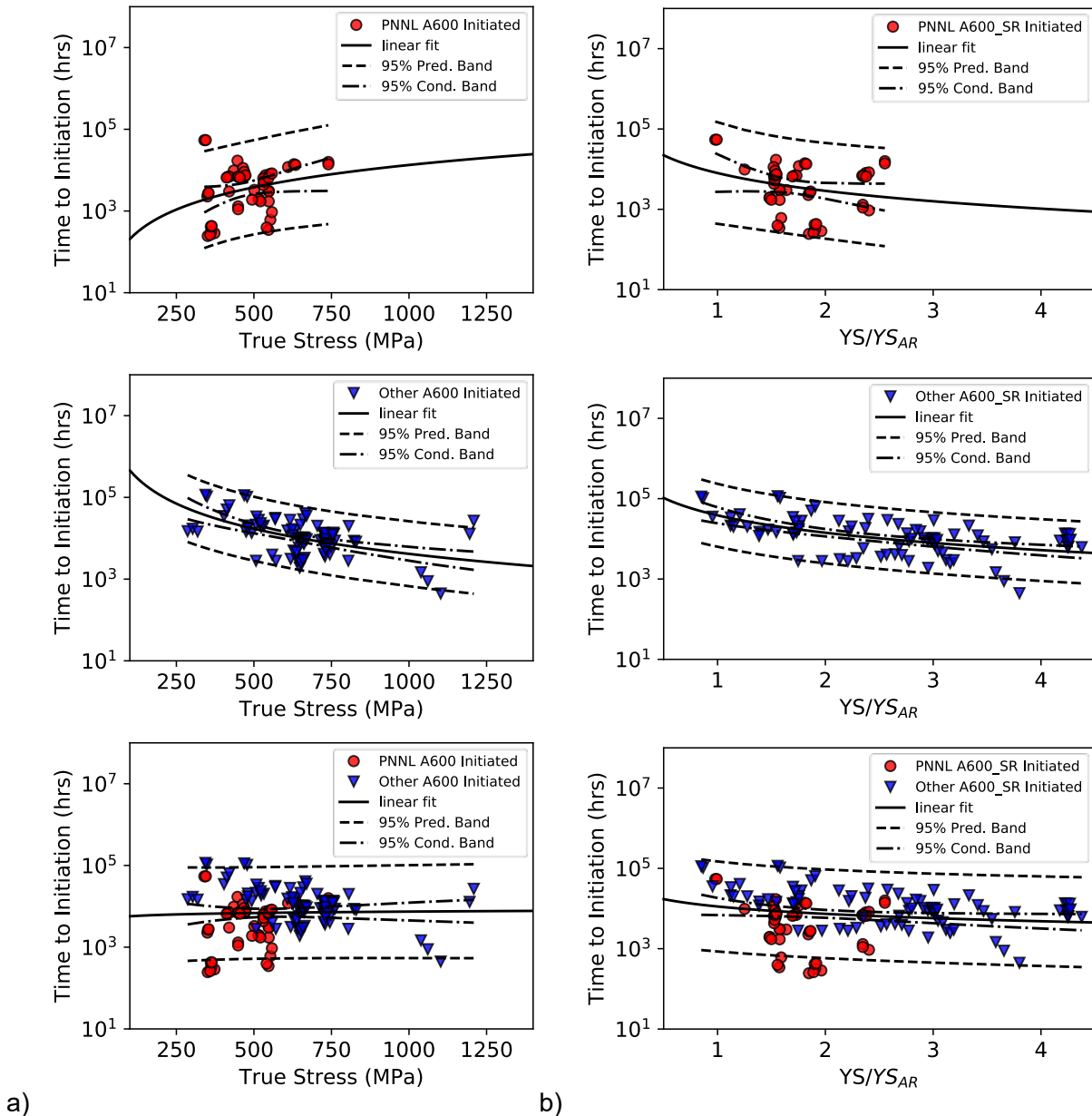


Figure 45. Same data and regression curves as in Figure 43 with additional information for prediction bands and confidence bands plotted.

Figure 46 shows initiated and non-initiated Alloy 600 samples from PNNL and from other labs. The estimated stress exponents are 0.9 (true stress) and 2.7 (stress ratio) for PNNL’s test data, 2.1 (true stress) and 1.5 (stress ratio) for other labs’ test data, and 0.7 (true stress) and 1.0 (stress ratio) for the combined data from PNNL and other labs. The PNNL data shows a significant difference in stress exponent between true stress and stress ratio plots. This difference appears to be caused by the inclusion of the heat 31907 that has lower yield strength. The non-initiated samples would exhibit SCC initiation at a higher testing time which would increase in the estimated stress exponent.

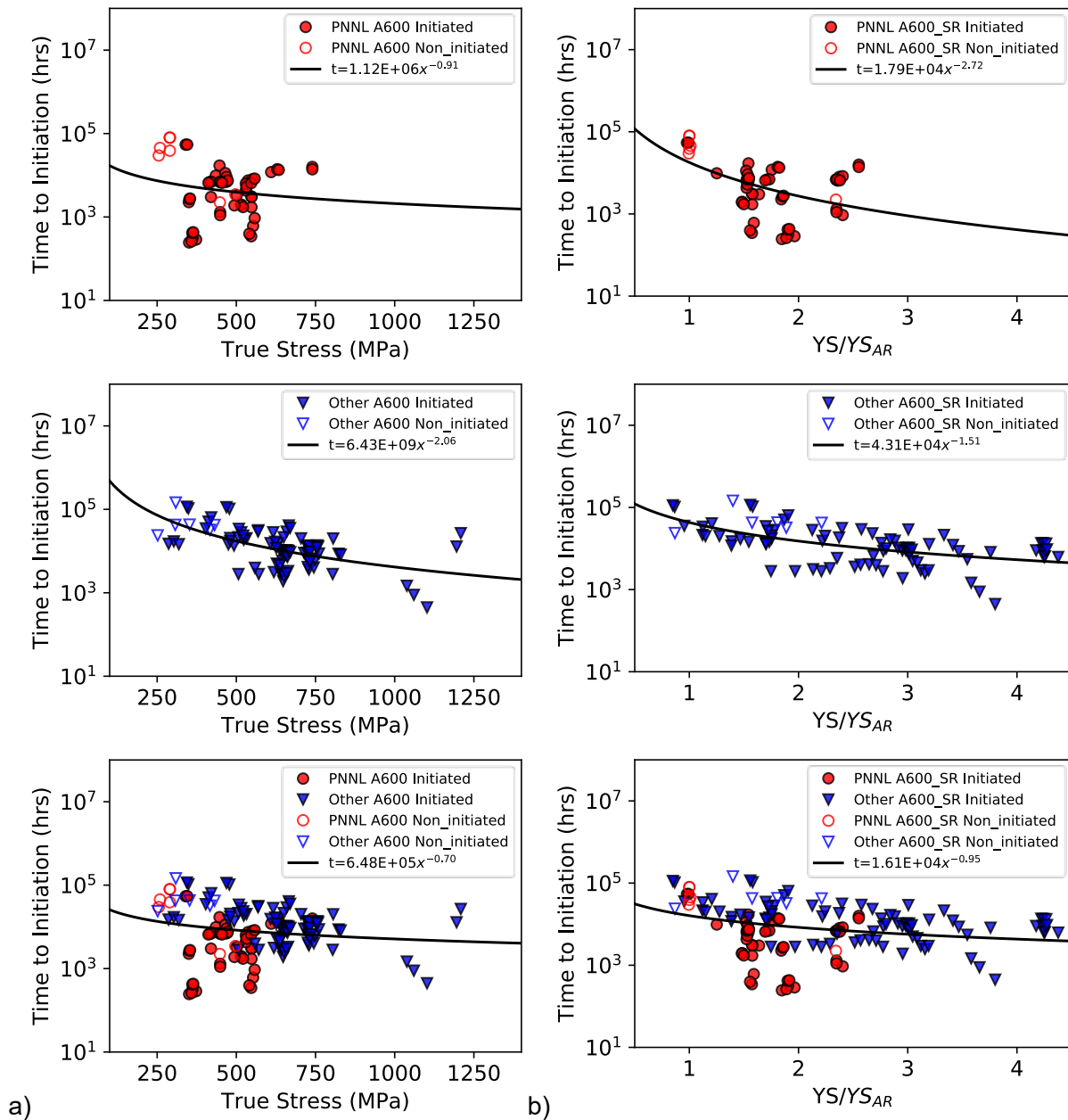


Figure 46. Test data for Alloy 600 samples with and without SCC initiation obtained at PNNL and other laboratories: a) initiation time vs. true stress; b) initiation time vs. stress ratio.

Table 17. Power law fitting parameters for Alloy 600 SCC initiated and non-initiated data.

Alloy 600 Initiated and Non-initiated Data	Input Variable	Number of Data	Pre-exponential Factor	Stress Exponent	R-squared
PNNL	True Stress	59	$\exp(13.9 \pm 5.0)$	0.9 ± 0.8	0.022
Others		89	$\exp(22.6 \pm 2.0)$	2.1 ± 0.3	0.345
PNNL + Others		148	$\exp(13.4 \pm 2.2)$	0.7 ± 0.3	0.030
PNNL	Stress Ratio	56	$\exp(9.8 \pm 0.4)$	2.7 ± 0.7	0.225
Others		89	$\exp(10.7 \pm 0.2)$	1.5 ± 0.2	0.336
PNNL + Others		145	$\exp(9.7 \pm 0.2)$	0.9 ± 0.3	0.079

Histograms of SCC initiation time are shown in Figure 47 in linear scale and log scale. Distributions of PNNL’s data and other labs’ data look similar, with a slightly higher proportion of low initiation time samples in the PNNL data group. Both initiation time histograms follow a log-normal type distribution rather than a normal distribution. This log-normal distribution of crack initiation times has also been observed in field service steam generator tube components in a page 4-4 of a commercial technical report [23].

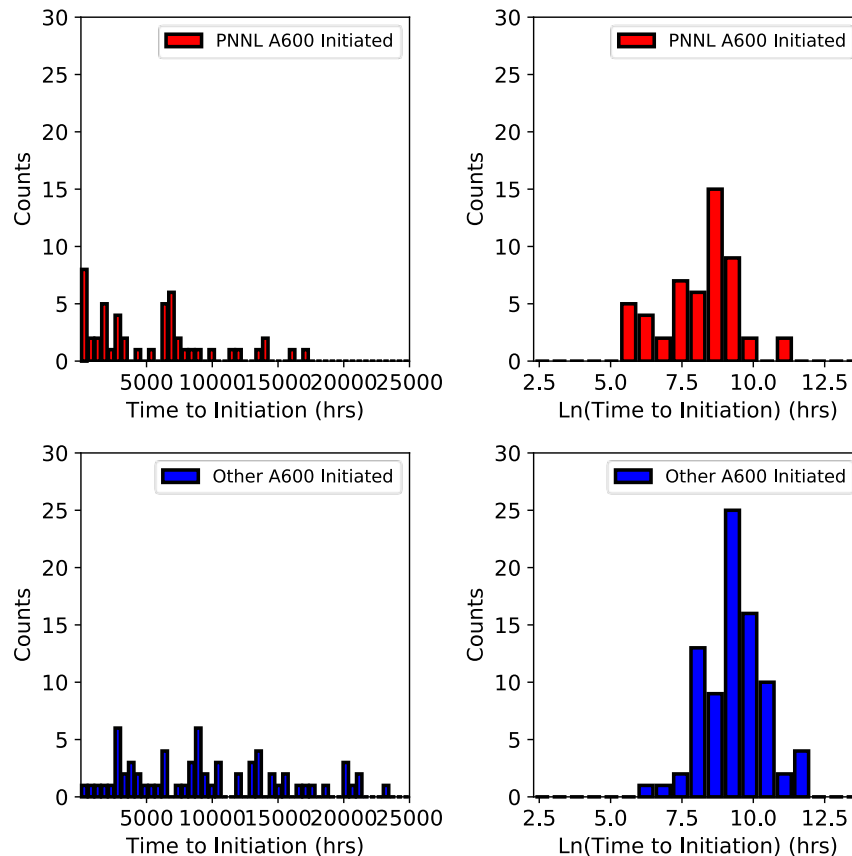


Figure 47. Histograms for SCC initiation time for PNNL’s Alloy 600 test data and other labs’ data in linear and natural log scale.

6.5.2 Analysis using Weibull Models

Figure 48 shows Weibull probability plots for initiated Alloy 600 samples using data for specimens loaded between 350-750 MPa which is the range of initiated PNNL data. The two-

parameter Weibull model (solid lines) fits both PNNL’s data and other labs’ data well. The estimated shape parameter β is found to be 0.84 for PNNL’s test data and ~ 1.0 for other labs’ test data. Shack et al. [26] suggested a shape parameter of 3 for Alloy 600. However, the value recommended by Shack could not be found in any of the cited reports written by Gorman et al. [23] and Staehle et al. [24]. In effect, the estimated β based on field data has a wide range from 0.4 to 4.8 (page 86 in [24]). The estimated shape parameter based on laboratory data from other labs suggests a nearly constant rate of initiation as a function to time while the PNNL value of 0.84 suggests a slightly decreasing rate of initiations as a function of time. The scale parameter θ represents that $\sim 63.2\%$ of samples fail until time t equals θ and is estimated to be 6,542 hours for PNNL’s data, and 19,579 hours for other labs’ data.

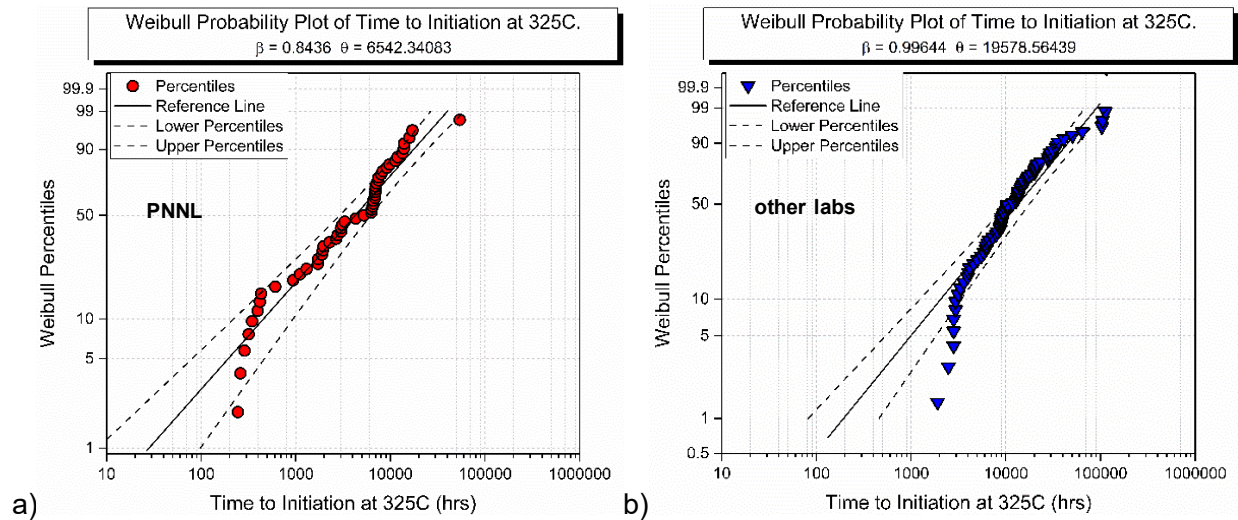


Figure 48. Two-parameter Weibull fit to a) Alloy 600 tested at PNNL, and b) Alloy 600 tested at other labs, note the applied stress range is limited to 350-750 MPa, which is the same range as PNNL testing, for comparison.

Unlike the Alloy 182 data where almost half of the test samples remain non-initiated, SCC initiation occurred in most of the tested Alloy 600 samples. Even though the non-initiated data is a small proportion of the entire Alloy 600 datasets, including both initiated and non-initiated data is still meaningful. To fully utilize censored data, the MLE method for parameter estimation using a modified likelihood function was used as described in Section 6.2.4.

The results following this approach are shown in Figure 49 for initiated data alone and for the combined initiated and non-initiated data. The estimated parameters are listed in Table 18. The scale parameter θ is calculated by Equation 8, and the corresponding characteristic initiation times at given stress ratios are plotted as solid lines. For all datasets with and without non-initiated data, the estimated shape parameters β are near unity, from 0.8 to 1.3, which are similar to the shape parameters estimated using the two-parameter Weibull probability approach. The estimated scale parameter θ increases by adding non-initiated data to the datasets. The stress exponent with respect to stress ratio is estimated to be around 2.7 to 1.5.

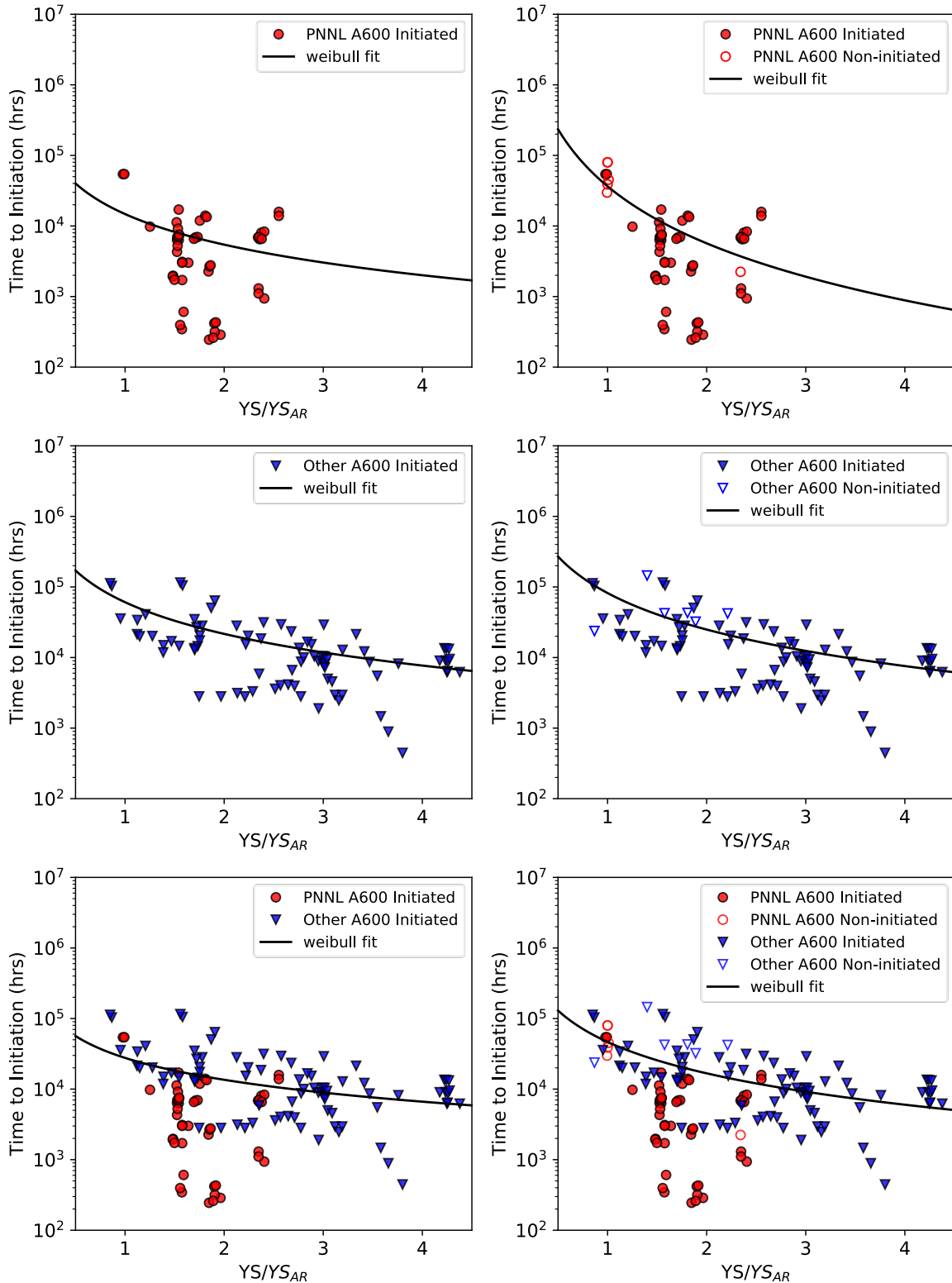


Figure 49. Weibull analysis on initiated datasets and right-censored datasets for PNNL’s test data, other labs’ data, and the combined of both. The solid lines are the characteristic time θ , as described by the Equation 8, which corresponds to the ~63.2% cumulative probability of SCC initiation at a giving stress ratio.

Table 18. Parameters for Weibull model analysis in Figure 49.

Dataset	Parameters	Estimated Values	
		Initiated	Initiated and Non-initiated
PNNL	β	0.94	0.86
	η_r	14,748	36,475
	n_r	1.44	2.68
Other Labs	β	1.34	1.27
	η_r	60,807	81,980
	n_r	1.49	1.72
PNNL + Other Labs	β	0.98	0.93
	η_r	27,681	46,565
	n_r	1.03	1.48

The primary purpose of the Alloy 600 analysis was to provide another point of comparison between PNNL-generated SCC initiation data and data in the literature. In this regard, the PNNL data match up well with the literature data, both for Alloy 600 and Alloy 182. When plotting PNNL data and the data of other labs together, the most obvious difference is that the PNNL data tends to have lower SCC initiation times which is likely due to the use of in-situ detection of initiation at PNNL.

A secondary outcome of this in-depth analysis is the determination that the stress exponent for Alloy 600 initiation behavior is clearly different than Alloy 182. Various SCC initiation analyses of Alloy 600 and Alloy 182 performed by different authors and labs have given the impression that the stress exponent for these two materials is very similar. However, the unified analysis presented here clearly shows the stress exponent for Alloy 600 is significantly below that for Alloy 182. In addition, the Weibull β parameter for Alloy 600 is much closer to one than for Alloy 182 indicating that Alloy 600 initiation has a more uniform SCC initiation frequency as a function of time while Alloy 182 tends to exhibit a decreasing frequency of SCC initiation with time.

6.6 Complexities in Regression Analysis

Although the functional forms of Direct Model 1 and Weibull models seem simple and straight forward, regression analysis can be approached in more than one way, and different results may be obtained. For example, in the analysis section it was discussed that calculating empirical probability using a standard approach (Equation 6) could lead to an incorrect cumulative probability function for censored data. Instead, employing a MLE approach with a modified likelihood function may suit the problem better.

For the power law function described in Direct Model 1, most previous investigations rely on applying linear regression on a log transformation of initiation data (the graphical method). Because a log transformation is non-linear, it may introduce unintended and unexpected bias in the weighting of data points [27, 28]. Application of a log transformation to the data acts to compress the initiation time values as viewed in log space. A non-linear regression approach constructs its error function directly on raw data so that a data transformation to a linear system is not required. An example of a comparison between linear regression and non-linear regression is shown in Figure 50. For consistency with previous studies, this study employed a least square error function type for the optimization process in both approaches. The corresponding residuals, which are the difference between the predicted value and measured

value, are shown in the plots on the right. For the linear regression applied to log-transformed data, the residuals for higher initiation time data are disproportionately positive. The log transformation introduces a bias whereby the influence of higher initiation times on the fitting constants is reduced. Although the non-linear regression appears to have a better balance of residuals, the fit line to the data is qualitatively more appealing for the linear regression applied to the log-transformed data. For either approach, the residuals of the long initiation time data dominate the fit. It is not the intention of this comparison to prove which approach is correct, but rather to illustrate the potential differences between them. The estimated exponent for other labs' data is 5.7 using linear regression and 7.8 using non-linear regression, respectively. This difference in stress exponent could non-trivially affect the lifetime prediction of components. Xiao, et al. [28, 29] examined these two methods on biology data using Monte Carlo simulations and concluded the preference of method should be based on the error type of data.

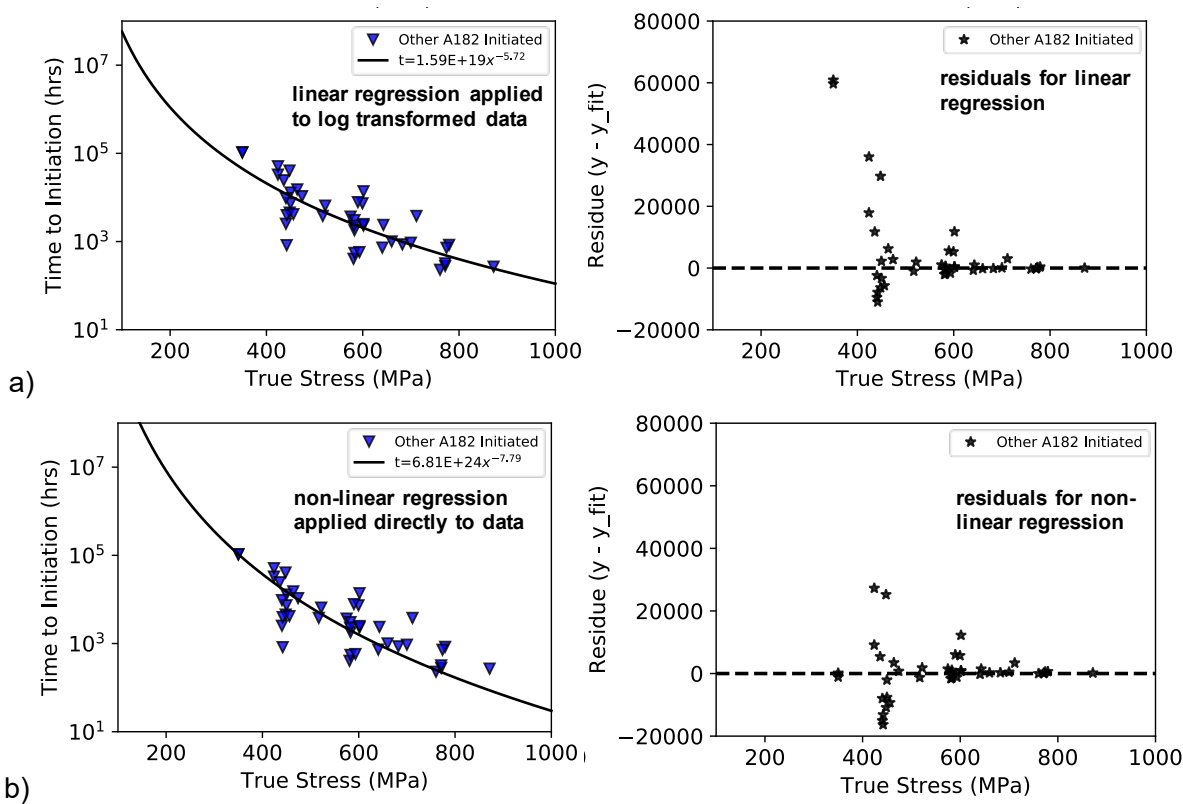


Figure 50. Power law fit to the other labs' Alloy 182 test data and associated residues: a) linear regression on log-transformed data; b) non-linear regression on raw data.

Besides the effect of linear versus non-linear regression, the optimization method could also play a role on the curve fit. Goldstein, et al. suggested that the MLE method is more reliable than the least squares approach [27]. The use of MLE for power law curve fitting was not examined in this report, but it may be beneficial to be evaluate in future studies. When applying a power law to empirical data, more caveats and traps need to be considered as described in numerous publications [30-32]. When applying regression analysis to SCC initiation data, it is important to acquire parameters for validation and verification of models. However, sometimes it is not as straight forward as it seems, especially for data with high variance, like the SCC initiation data. Employing multiple statistical methods and exploring data more extensively may help to interpret and understand the data.

7.0 SEM Examinations of Low Initiation Time Alloy 182 Specimens

7.1 Introduction

To better understand the cause of the very low initiation times in the 15% CF Alloy 182, detailed microstructural characterizations were performed on 16 specimens that initiated within 150 hours (highlighted in yellow in Table 19). The results are provided following an introduction to the techniques and methodologies used for the characterization. The DCPD response of these specimens are included to facilitate understanding the SCC initiation behavior.

Table 19. SCC initiation times for nine each of four 15% CF Alloy 182 welds tested at YS.

KAPL	YS (MPa)	t _{init} (h)	Studsvik	YS (MPa)	t _{init} (h)
IN166	563	≤30	IN169	541	>5,126*
IN167	552	≤30	IN170	536	30
IN168	547	113	IN171	534	2,957
IN194	581	1,635	IN191	553	83
IN195	575	1,625	IN192	559	41
IN196	567	1,642	IN193	555	41
IN279	572	>5,554*	IN233	532	≤30
IN280	566	>5,554	IN234	529	725
IN281	576	>5,554	IN235	532	910
Phase 2B	YS (MPa)	t _{init} (h)	Flawtech	YS (MPa)	t _{init} (h)
IN185	514	≤105	IN188	518	≤30
IN186	514	>3,173	IN189	518	≤30
IN187	514	409	IN190	518	90
IN197	500	806	IN200	528	825
IN198	506	4,964	IN201	528	746
IN199	506	2,238	IN202	528	900
IN216	462	132	IN221	525	106
IN217	467	>2,971	IN222	525	113
IN218	467	2,908	IN223	525	79

* The ">" indicates not yet initiated. Will expose further if possible.

7.2 Procedures for Microstructural Characterization

For the first several Alloy 182 SCC initiation tests, detailed pre-test examination of the gauge surface was not performed. This decision was based on PNNL's previous experience with Alloy 600 initiation specimens where SCC initiation generally did not occur for at least 1,000 hours in 15% CW material. However, after several very low SCC initiation times were observed during the initial Alloy 182 testing, it became apparent that it would be important to perform pre-test examinations of the specimens to try to understand the low initiation times. To facilitate the pre-test examinations, an additional light polish using colloidal silica was applied to the gauge surface of specimens with ID number starting at IN185. Pre-, mid- (if a test interruption took place) and post-test backscatter electron (BSE) SEM montage imaging was routinely conducted on the entire gauge and fillet surface of the specimens. This was achieved by attaining a multi-

image montage at each of four different views (90° to one another) of the gauge region of the specimens (Figure 51). These observations were made using a JEOL 7600 scanning electron microscope operated in backscattered electron (BSE) mode. A high acceleration voltage (30 kV) was used to increase the sampling depth of the beam so that features covered by thin surface oxides could be revealed. In general, 700-800 images were collected for each specimen and stitched together using automation features on the microscope. The montage was performed at a magnification of 200X with a resolution of 1024 x 1024 pixels for every image in the montage.

Previous experience with Alloy 600 and 690 had proved that this approach can sufficiently locate surface damage in a variety of forms, including nano-size cavities [6]. More detailed characterizations including higher magnification SEM secondary electron (SE), BSE imaging, and energy dispersive x-ray spectroscopy (EDS) were occasionally performed on selected pre-existing defects found prior to testing. Upon conclusion of a test, the pre-test and post-test morphologies were routinely compared with a focus on the relationship between pre-existing defects and nucleated cracks. Keep in mind that post-test examination times occurred slightly after the time of SCC initiation.

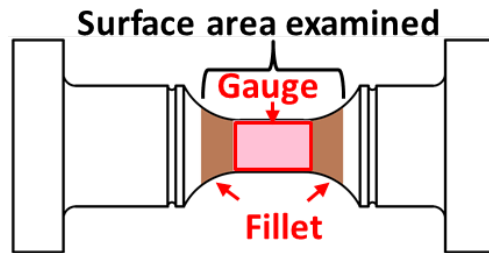


Figure 51. Schematic of the surface area of one rotation mapped in SEM for pre-, mid- and post-test examination. The gauge surface mapped in SEM is highlighted in pink and the surface in the fillet region mapped in SEM is highlighted in taupe.

A common practice developed at PNNL for examining cracking in Alloy 600 initiation specimens involves serial sectioning of the gauge section and measuring the depth of all cracks on the polished cross sections. Multiple cross sections allow determination of a crack depth profile. The main reason for this approach is that multiple large cracks of similar size were commonly observed in the surface of Alloy 600 specimens upon initiation, and it is difficult to know which one is the primary crack (largest, fastest growing crack) unless all were characterized to determine their depth. The serial polish maximizes the possibility for examining multiple cracks. As will be shown later, the Alloy 182 specimens usually only exhibited one or two major cracks when initiation was detected. While the number of large cracks was lower, the number of specimens involved in this program is quite high, making the serial sectioning approach both time and cost prohibitive. Therefore, the decision was made to air fatigue open selected specimens to exam the shape and morphology of the surface of the primary crack. Fatigue loading parameters were carefully chosen, and the process was closely watched to ensure fatigue crack extension from the primary SCC crack without substantial plastic strain. After a water bath to remove excessive boric acid residue, the fractured surface containing the revealed primary crack surface was montaged under both SEM SE and BSE modes. A high acceleration voltage (30 kV) was used for SE imaging to maximize the topological resolution while low acceleration voltage (5 kV) was used for BSE imaging to leverage the small interaction volume to better capture the contrast due to the difference in thickness of the oxide layer formed on crack wall, thus aiding in visualization of the crack nucleation area.

7.3 Observations

7.3.1 15% CF KAPL Alloy 182 Specimens IN166-168

The three 15% CF KAPL Alloy 182 initiation specimens IN166-168 were the first set of Alloy 182 specimens tested in this program. They were polished to a 1 μm finish on the gauge surface following the same routine preparation used for Alloy 600 initiation specimens, and SEM examination was not performed prior to the start of the test. The overall DCPD-referenced strain response of these three specimens is shown in Figure 52. IN166 and IN167 immediately exhibited a high strain rate with IN167 also showing an increasing strain rate that clearly signifies SCC initiation. While IN166 did not exhibit an increasing slope in this limited exposure, it was thought that the starting high strain rate was a strong indicator of SCC initiation, and thus it was assumed to be initiated. This test was stopped at 33 hours, and SEM examinations were performed on all three specimens to record the gauge surface morphology. After completion of these baseline SEM examinations, the non-initiated specimen IN168 specimen was put back into test. The specimen was reloaded back to its original load without indication of plastic strain, and the subsequent referenced strain response in Figure 52 shows initiation after 113 hours of total exposure.

Figure 53 summarizes the post-test surface morphology of the three specimens where cracks are highlighted in red. Cracking was found in all three specimens, the extent of which seems to scale with the increase in their DCPD response. For IN167 which showed the fastest and largest increase in DCPD-referenced strain, two large cracks both with a surface length >1 mm were found in the gauge center after 33 hours of exposure. IN166 also exhibited one crack >1 mm long near the fillet region after 33 hours. In comparison, only one short crack of ~ 50 μm long was found in IN168 after 33 hours of exposure. This crack grew into an ~ 850 μm long crack after an additional 100 hours of exposure and became the primary crack after 113 hours (Figure 54). Since no pre-test examination was done, it is not known with certainty whether the short crack observed at 33 hours was pre-existing or occurred during the initial exposure, but the smooth edges observed after only 33 hours of exposure strongly suggest that it was a pre-existing crack, and it is tentatively labeled as such.

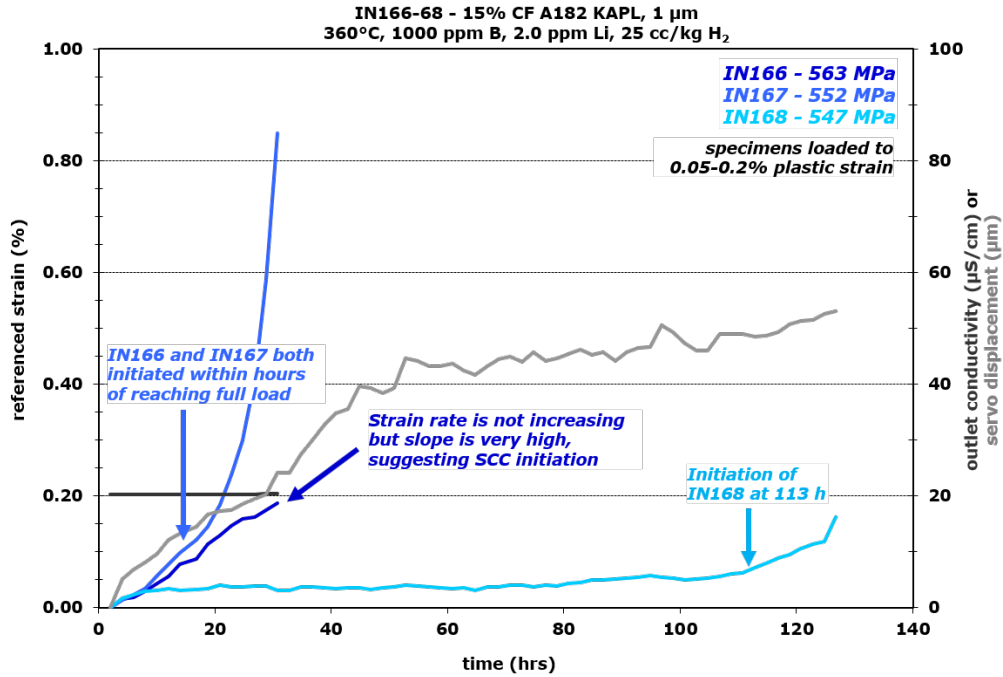


Figure 52. Referenced strain response for three 15% CF KAPL Alloy 182 specimens, IN166-68.

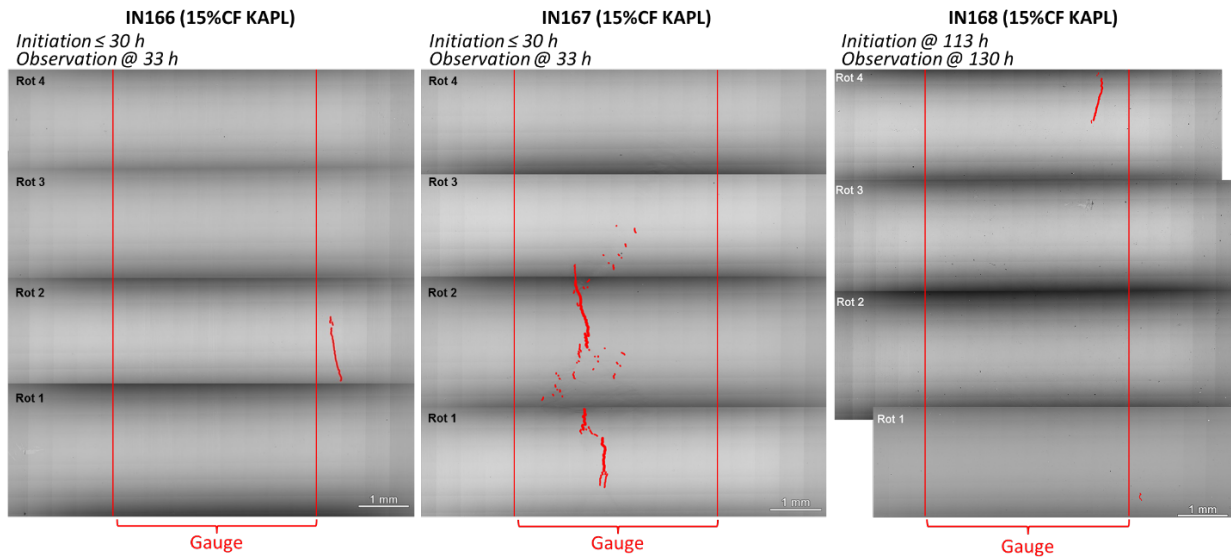


Figure 53. Post-test SEM-BSE montage imaging of the entire surface of the gauge and fillet region of the first set of 15%CF KAPL Alloy 182 weld specimens, IN166-168, after initiation was detected. The cracks are highlighted in red.

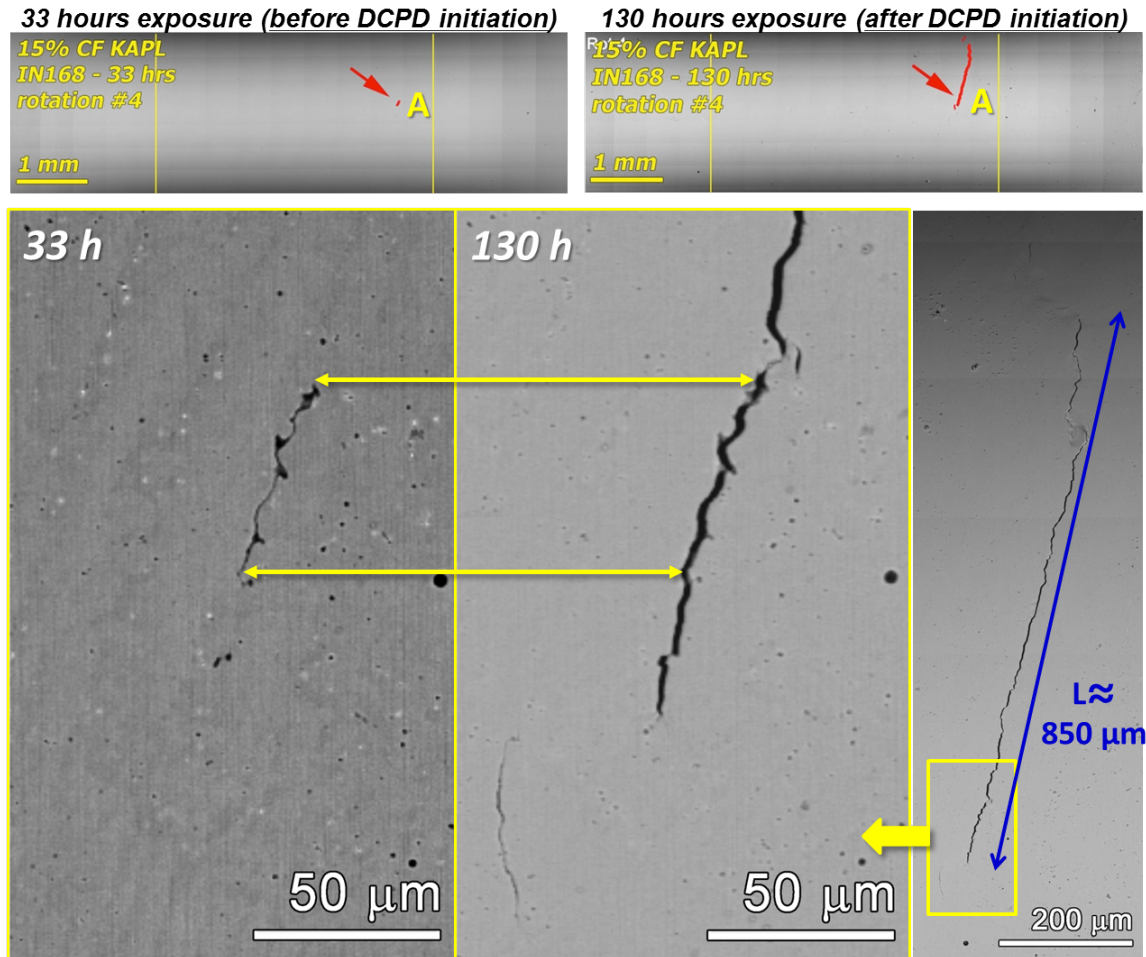


Figure 54. Crack evolution on the surface of the 15%CF KAPL Alloy 182 specimen IN168 with SCC initiation detected at 115 hours of exposure. The cracks are highlighted in red with zoom-in images showing the primary crack nucleated from a pre-existing defect on a solidification grain boundary.

To investigate the effect of crack shape and grain orientation on SCC initiation, IN168 was fatigued open, and detailed SEM examination was performed on the crack surface. As shown in Figure 56, the area of intergranular (IG) stress corrosion cracking on the fatigued-open specimen is outlined as an aid to visualize the shape of the primary crack by the time the test was stopped. Both yellow and orange outlines are present in the images. Orange denotes regions of lighter contrast while yellow denotes regions of darker contrast. The orange boundary represents the final stress corrosion IG growth. Very different from most cracks observed in Alloy 600 which appear to be semi-elliptical in shape, the primary crack in IN168 exhibited an irregular depth profile that likely followed the shape of the SGBs on which the cracks grew. The primary crack nucleated and grew along the short direction of the SGBs. This is known as a T-L cracking morphology relative to the weld grain structure. The possible cracking orientations relative to weld grain structure are provided in Figure 55.

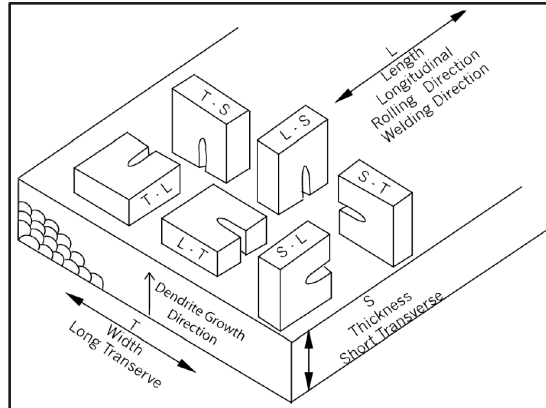


Figure 55. S-L-T nomenclature of cracking orientations relative to weld grain structure.

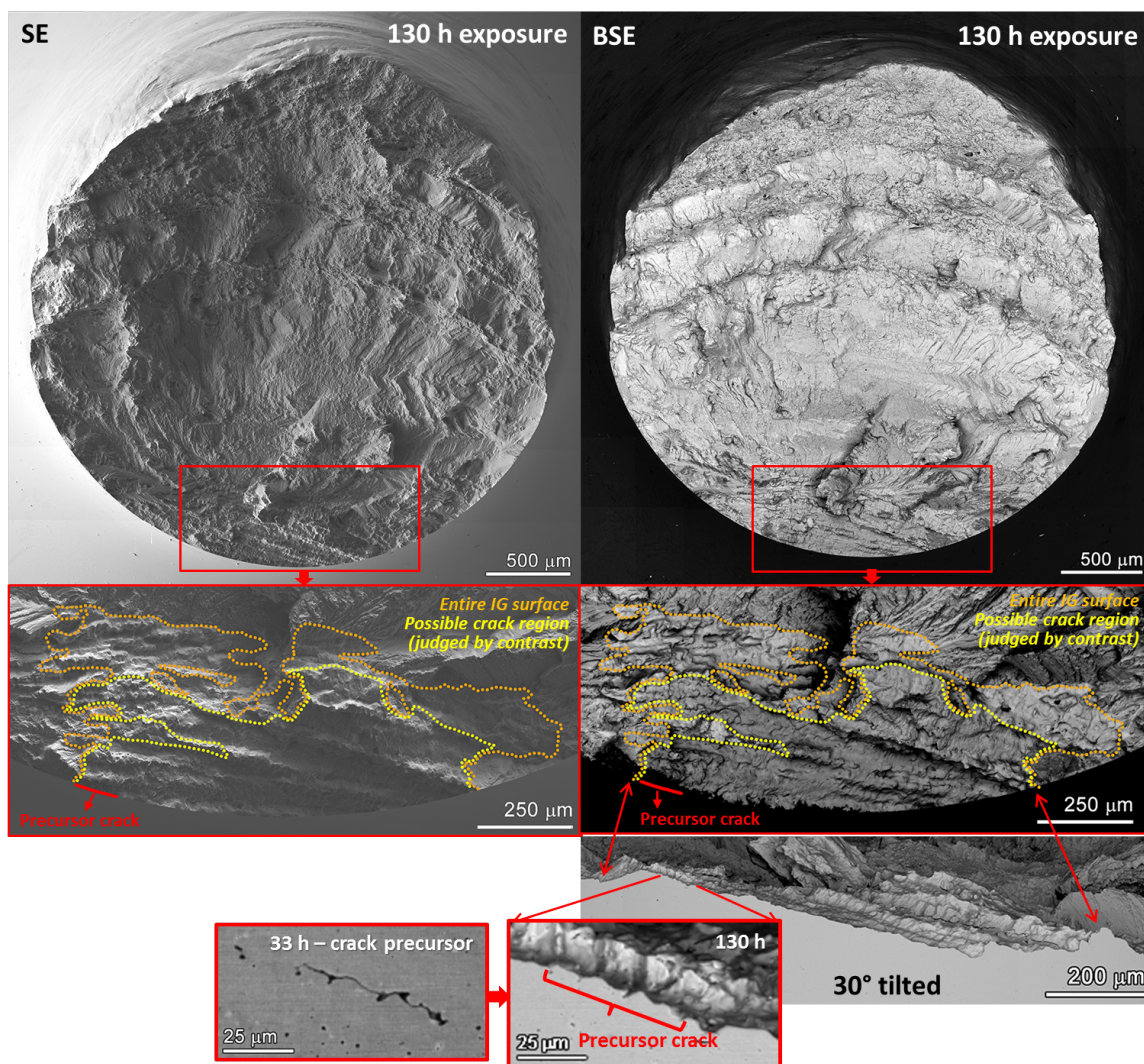


Figure 56. The SEM SE (left) and BSE (right) images of the fractured surface of the 15% CF KAPL Alloy 182 specimen with initiation detected at 113 hours. Orange and yellow outlines encompass IG cracking. The position of the precursor crack observed at 33 hours is marked in red along the perimeter of the specimen.

7.3.2 15% CF Studsvik Alloy 182 Specimens IN170, IN191-93, and IN233

Five of the nine 15% CF Studsvik Alloy 182 specimens exhibited initiation within 150 hours of exposure, as shown in Figure 57. Two specimens, IN191 and IN192 exhibited strain jumps followed by an immediate transition to an increasing slope representative of SCC initiation. Jumps such as these have been seen in Alloy 600 tests and are thought to be due to strain bursts triggered by loss of cross-sectional area, allowing for a momentary strain of the specimen in the region of the crack. Local hardening then prevents further plastic deformation. A unique aspect of this event is that rather than a continual plastic strain process occurring as cross-sectional area is lost due to cracking, the specimen is able to resist plastic strain until reaching some critical crack size. This may be due to dynamic strain aging.

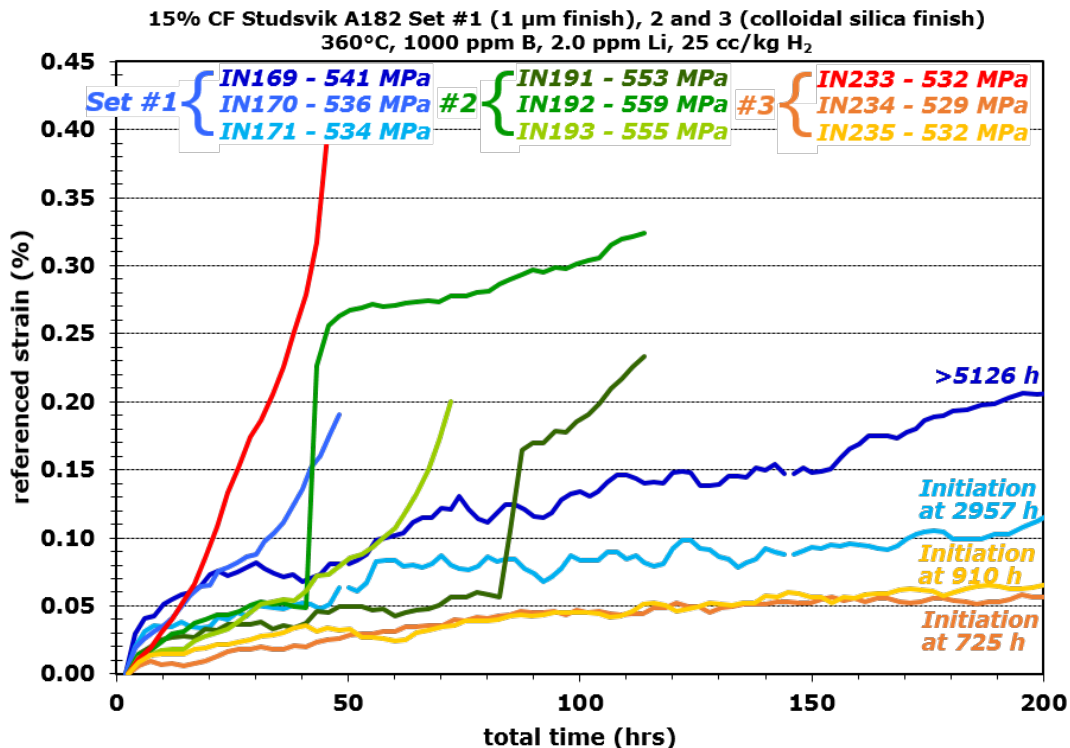


Figure 57. Referenced strain response during the first 200 hours of the constant load SCC initiation testing for the nine 15% CF Studsvik Alloy 182 specimens.

An overview of the post-test gauge surface morphology of the five low initiation time specimens is provided in Figures 58 and 59 in order of increasing SCC initiation time. Extensive cracking had already occurred by the time the test was stopped at 46 hours in IN233, the specimen that exhibited the most rapid SCC initiation. Several cracks reached a surface length of more than 1 mm long during this very short exposure time. In comparison, only a few cracks were observed by the time the test ended in the other four specimens, among which the largest ones were ~300-800 μm long. IN191 and 192, the specimens that underwent a strain jump, exhibited normal cracking morphology with a primary crack and a few other shorter cracks sporadically distributed in the specimen.

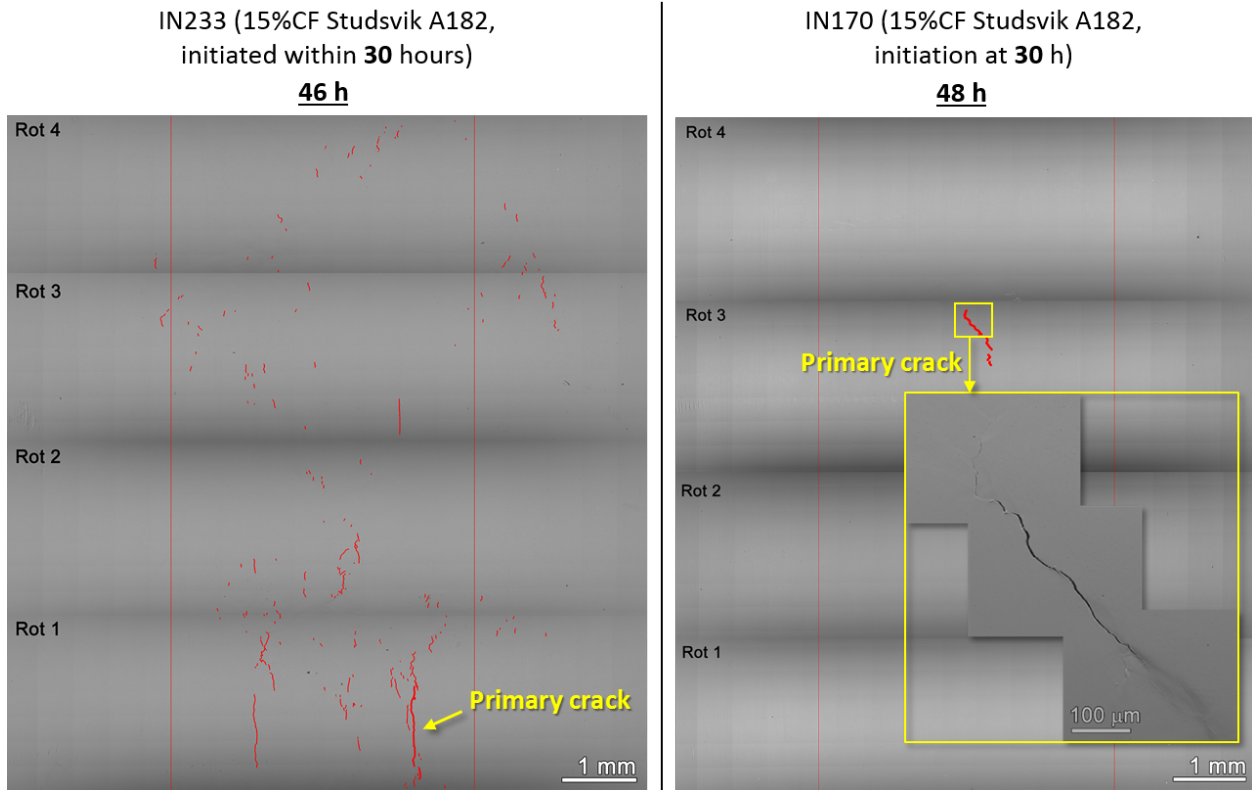


Figure 58. Post-test SEM examination of the surface of the 15% CF Studsvik Alloy 182 specimens IN233 and IN170 that initiated at around 30 hours of exposure. Obvious cracks are highlighted in red. The likely primary crack leading to DCPD detection of SCC initiation is also identified in each specimen.

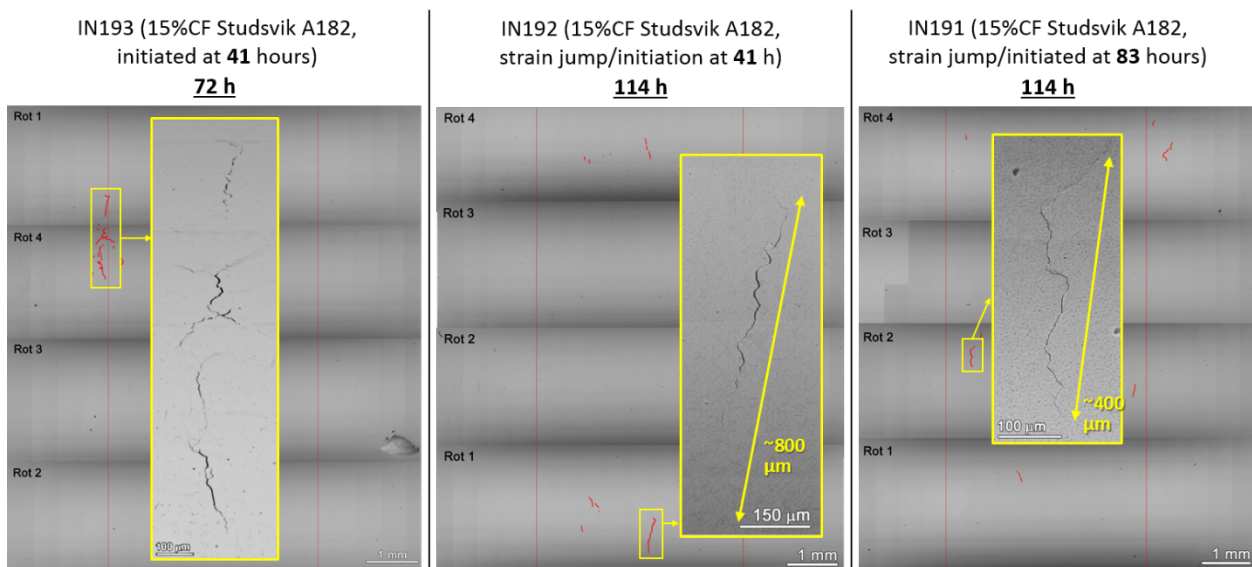


Figure 59. Post-test SEM examination of the surface of the 15% CF Studsvik Alloy 182 specimens IN191-193 that initiated at 41-83 hours of exposure at yield stress. Obvious cracks are highlighted in red. A zoom-in image was also shown on the primary crack leading to DCPD detection of SCC initiation in each specimen.

IN170 was among the second set of 15% CF Alloy 182 specimens tested in this program. It was prepared to a 1 μm finish, and a pre-test examination of the gauge surface to document defects on the gauge surface was not performed. However, the specimen was fatigued open after the test to investigate the effect of crack shape and grain orientation on SCC initiation in Alloy 182 welds with the result shown in Figure 60. IG cracking on the fracture surface is outlined as an aid to visualize the shape of the primary crack at the time the test was stopped. Quite different from what was observed on the fracture surface of the 15% CF KAPL Alloy 182 specimen IN168, for IN170 the primary crack nucleated on a grain boundary with the long axis roughly aligned to the radius of the specimen, and the IG extension protruded ~ 1 mm deep into the specimen. This cracking direction relative to the weld grain morphology is known as the T-S orientation. This suggests that very low SCC initiation times may not have a strong dependence on the grain orientation. Examination of additional specimens is planned to provide a greater base of data to better understand this aspect of Alloy 182 SCC initiation.

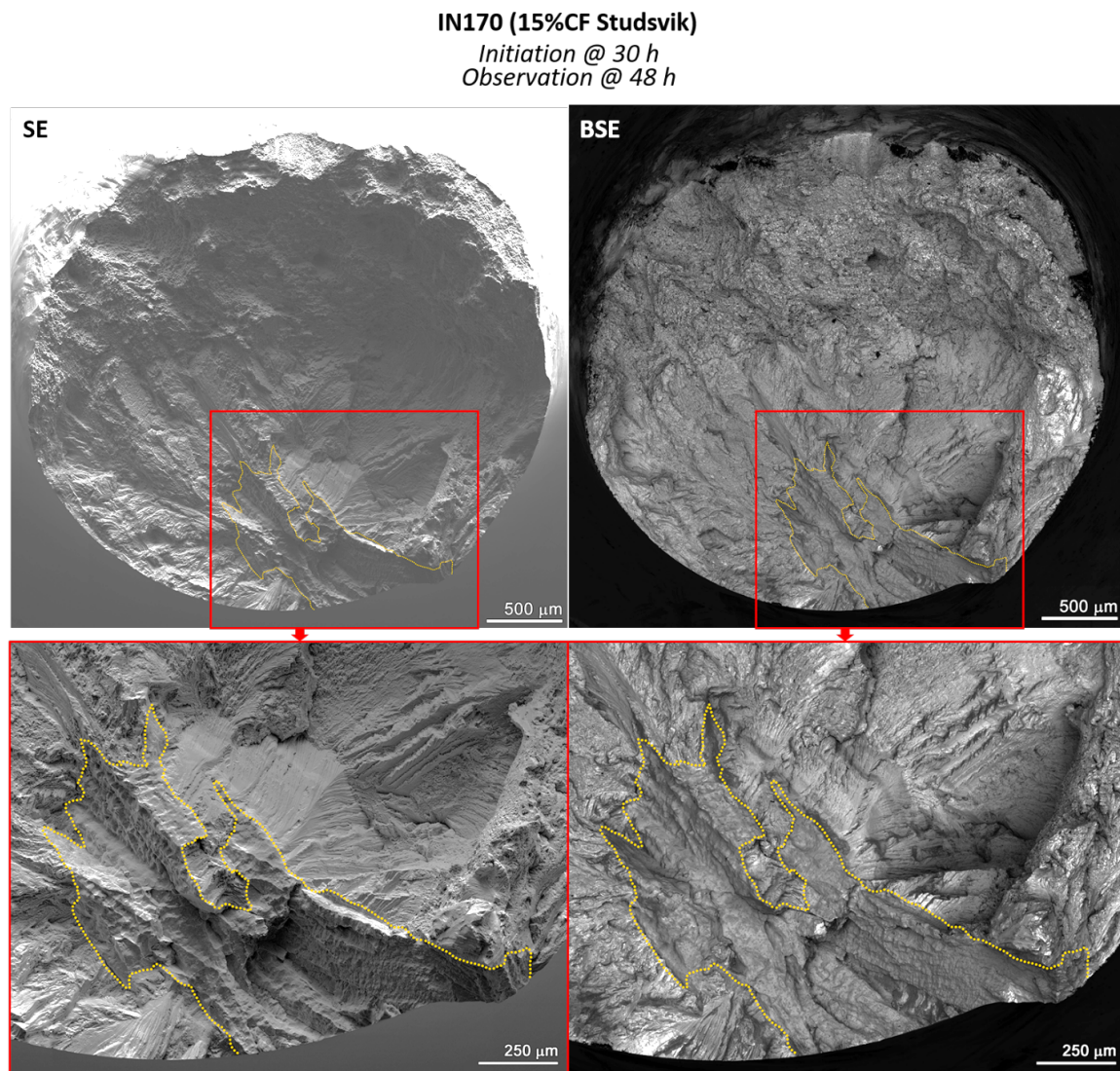


Figure 60. The SEM SE (left) and BSE (right) montage imaging of the fractured surface of the 15%CF Studsvik Alloy 182 specimen with initiation detected at 30 hours of exposure. The area of IG failure was highlighted in orange.

Detailed SEM examinations were performed on the other four specimens both before and after SCC initiation testing, as well as mid-test if a test interruption of these specimens took place. The evolution of crack morphology on the gauge surface and in part of the fillet region for these four specimens are presented in Figures 61-64 in the order of increasing SCC initiation time. Pre-existing defects with sizes ranging from a few micrometers to hundreds of micrometers were identified in several of the specimens, but none of the defects were associated with the very low SCC initiation times. As shown in Figures 62 and 63, large defects ranging from tens to hundreds of micrometers in the form of a dent and curled cracks were found prior to testing in the fillet region of IN192 and IN193. Yet these also did not undergo observable changes during exposure in high temperature water.

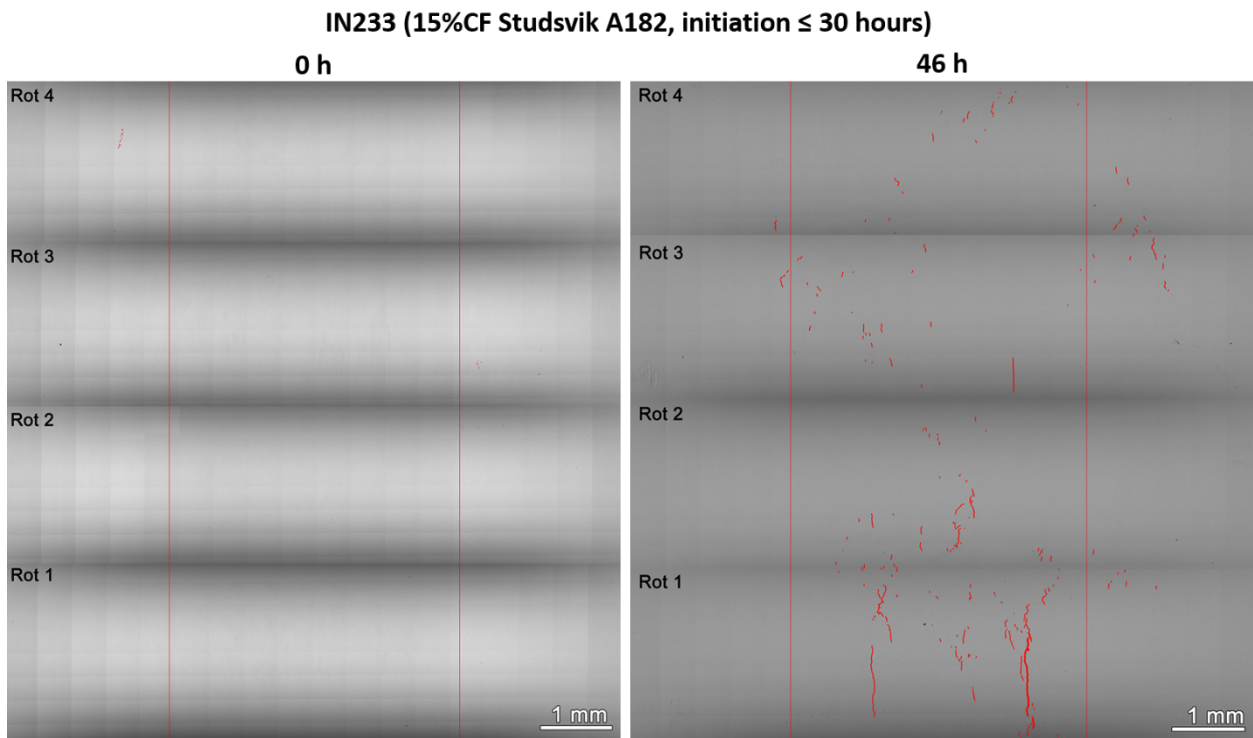


Figure 61. SEM montage images showing the evolution of the gauge surface of the 15% CF Studsvik Specimen IN233 that initiated within ~30 hours of testing in high temperature water at yield stress. Cracks are highlighted in red.

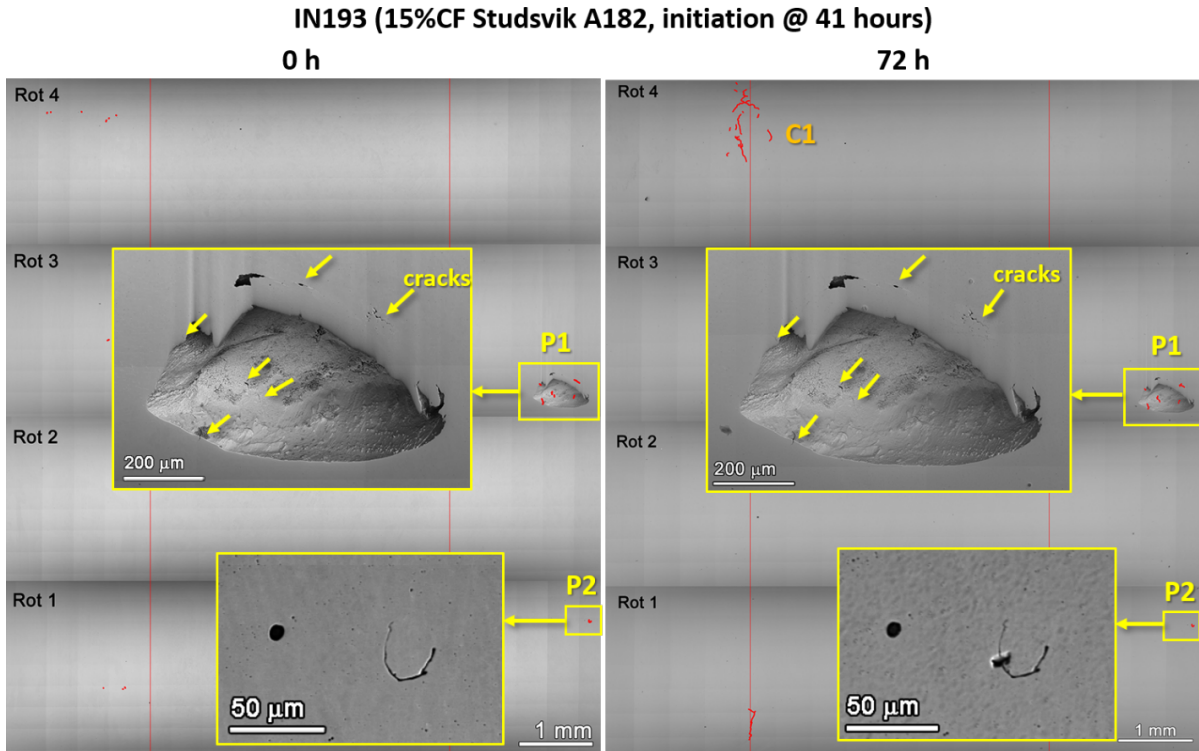


Figure 62. SEM montage images showing the evolution of the gauge surface of the 15% CF Studsvik Specimen IN193 that initiated at ~41 hours of testing in high temperature water at yield stress. Defects and cracks are highlighted in red. The zoom-in images of a large dent and a small crack in the fillet region are also presented showing no evolution during the short exposure time.

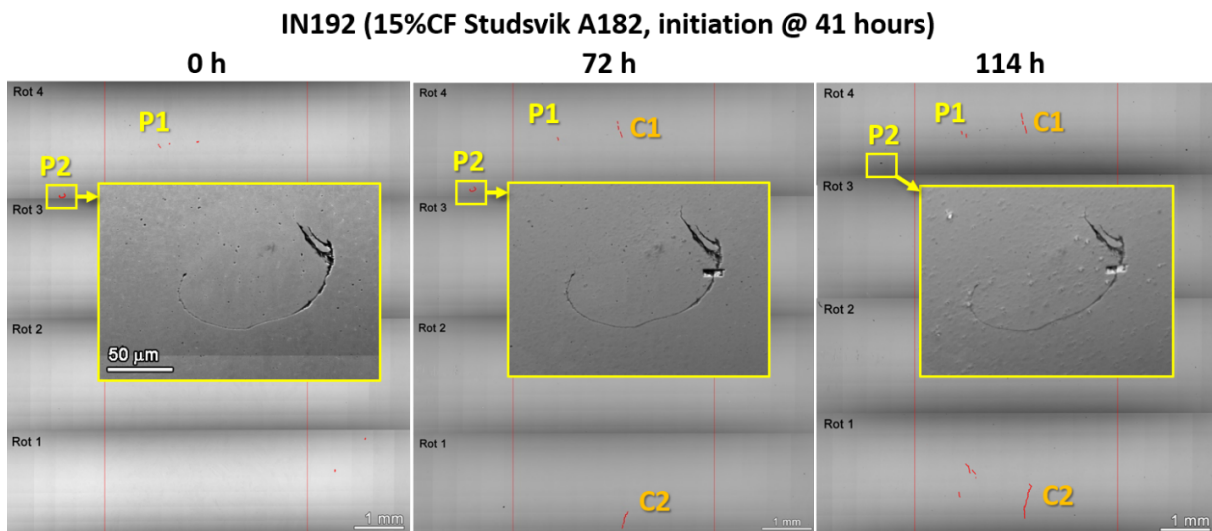


Figure 63. SEM montage images showing the evolution of the gauge surface of the 15% CF Studsvik Specimen IN192 that initiated at ~41 hours of testing in high temperature water at yield stress. Defects and cracks are highlighted in red. The zoom-in image of a small crack in the fillet region is also presented showing no evolution during the short exposure time.

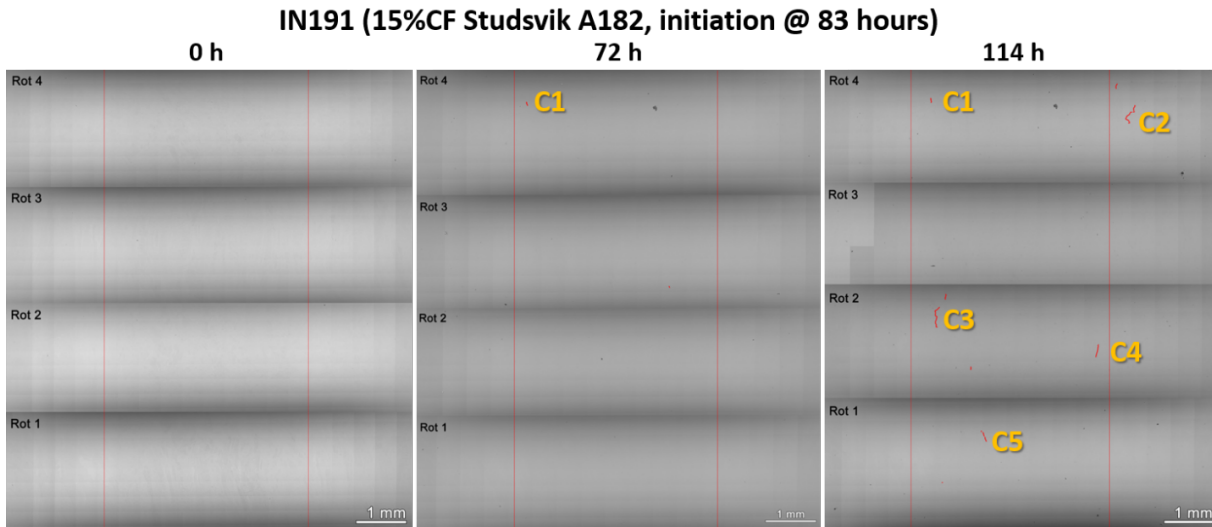


Figure 64. SEM montage images showing the evolution of the gauge surface of the 15% CF Studsvik Specimen IN191 that initiated at ~83 hours of testing in high temperature water at yield stress. No pre-existing defects were found prior to testing. Cracks are highlighted in red.

A few irregularly shaped dark features less than 10 μm in size were also identified in the montage image of the gauge section in IN192 (Figure 63 location P1). Higher magnification imaging was performed on these features prior to testing to record their morphology and chemical composition. As shown in Figure 65, two voids of $\sim 5 \mu\text{m}$ in size indicated by their brighter edge contrast in the SE image are located inside a grain at Site P1-a, while another similarly sized void exists at Site P1-b where it is linked to a narrower crack along a grain boundary. EDS analyses were conducted on these features and revealed that the voids are high in Ti, Cr, C and N content, suggesting that they are likely carbonitride particles that had fallen out during the polishing process. Meanwhile, the small defect at Site P1-b was found to be a crack-like feature as it does not exhibit enrichment of any element but only low Ni concentration.

These features were closely tracked in mid-test and post-test examinations since it is of interest to know if the small IG crack feature could evolve into a large crack. Interestingly, the characterization results showed no growth of these features during testing (Figure 67). Instead, a few short cracks nucleated at nearby SGBs where no defects were observed prior to testing. Similarly, detailed comparisons were made between pre-test and post-test SEM montage images at locations where large cracks were found in all of these specimens with examples shown in Figures 68-70. It is obvious that the areas where these cracks nucleated are free of observable pre-existing defects on the surface.

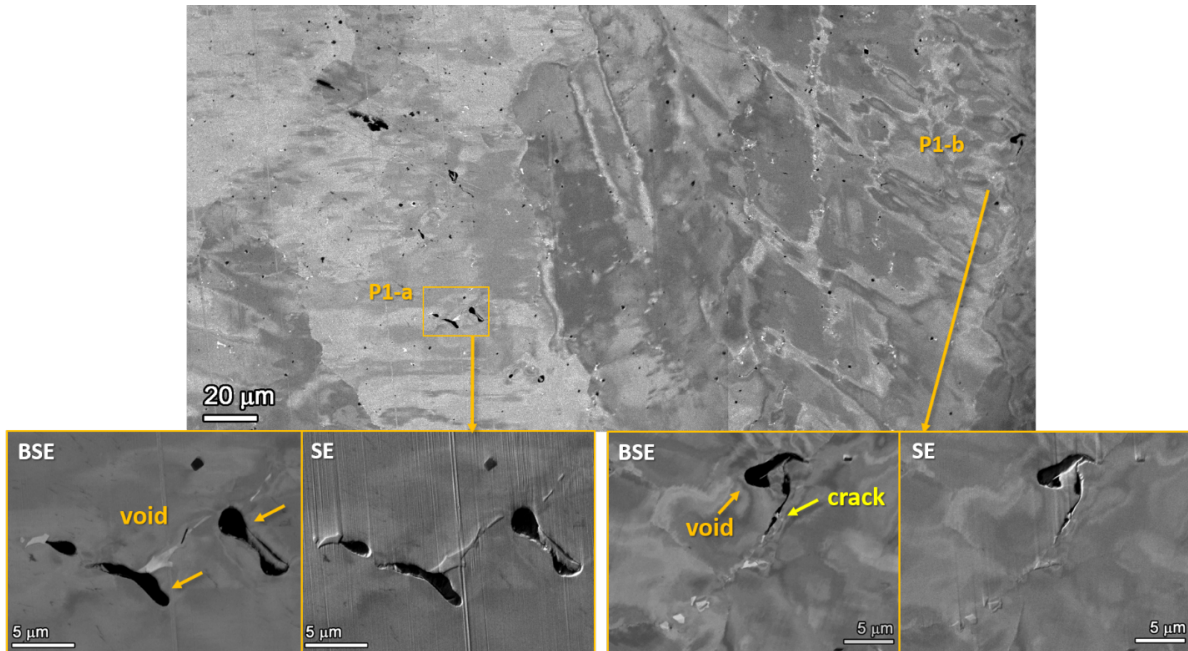


Figure 65. Higher magnification SEM-BSE (unless otherwise noted) images acquired prior to test on the pre-existing defects at Site P1 marked in IN192 in Figure 63.

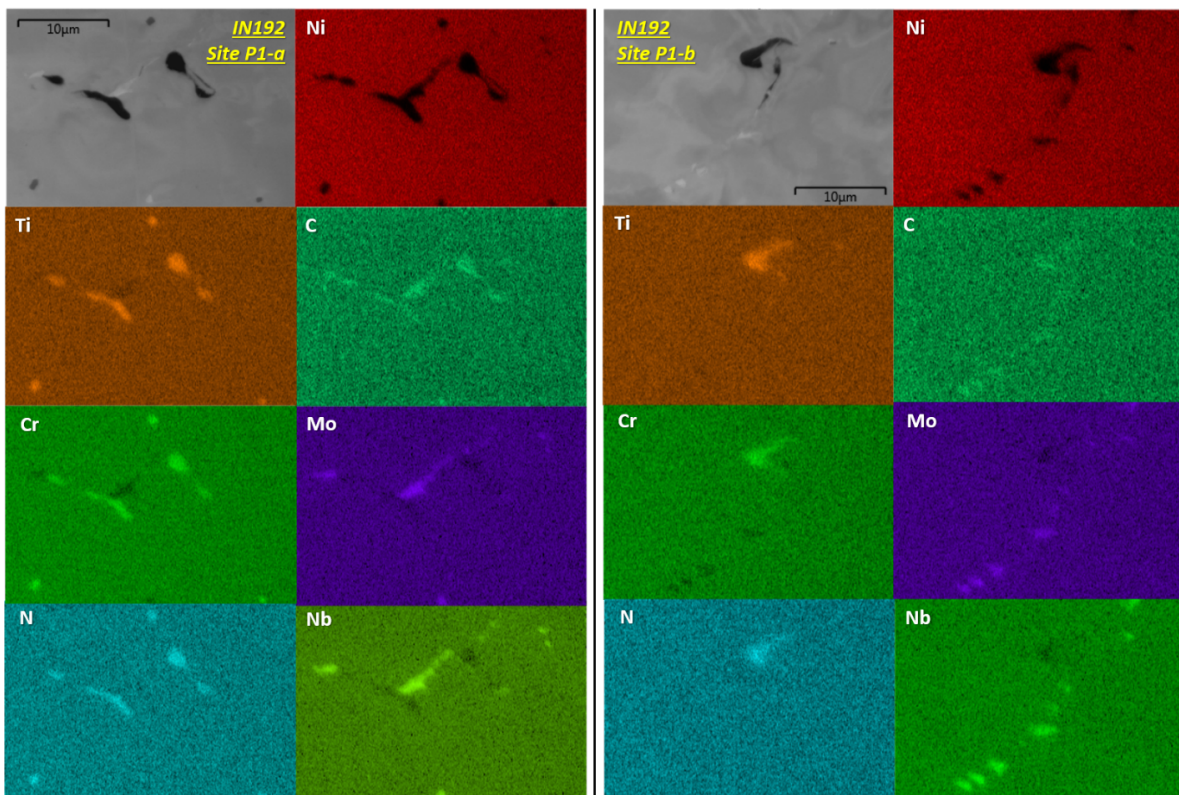


Figure 66. EDS composition maps of the sites P1-a and b identified in Figure 65. The EDS was conducted using low acceleration voltage (5 kV) for small interaction volume and better detectability of light elements, so that qualitative information of the chemical composition of sub-micrometer size precipitates on the surface can be obtained.

IN192 (15%CF Studsvik A182) - Site P1

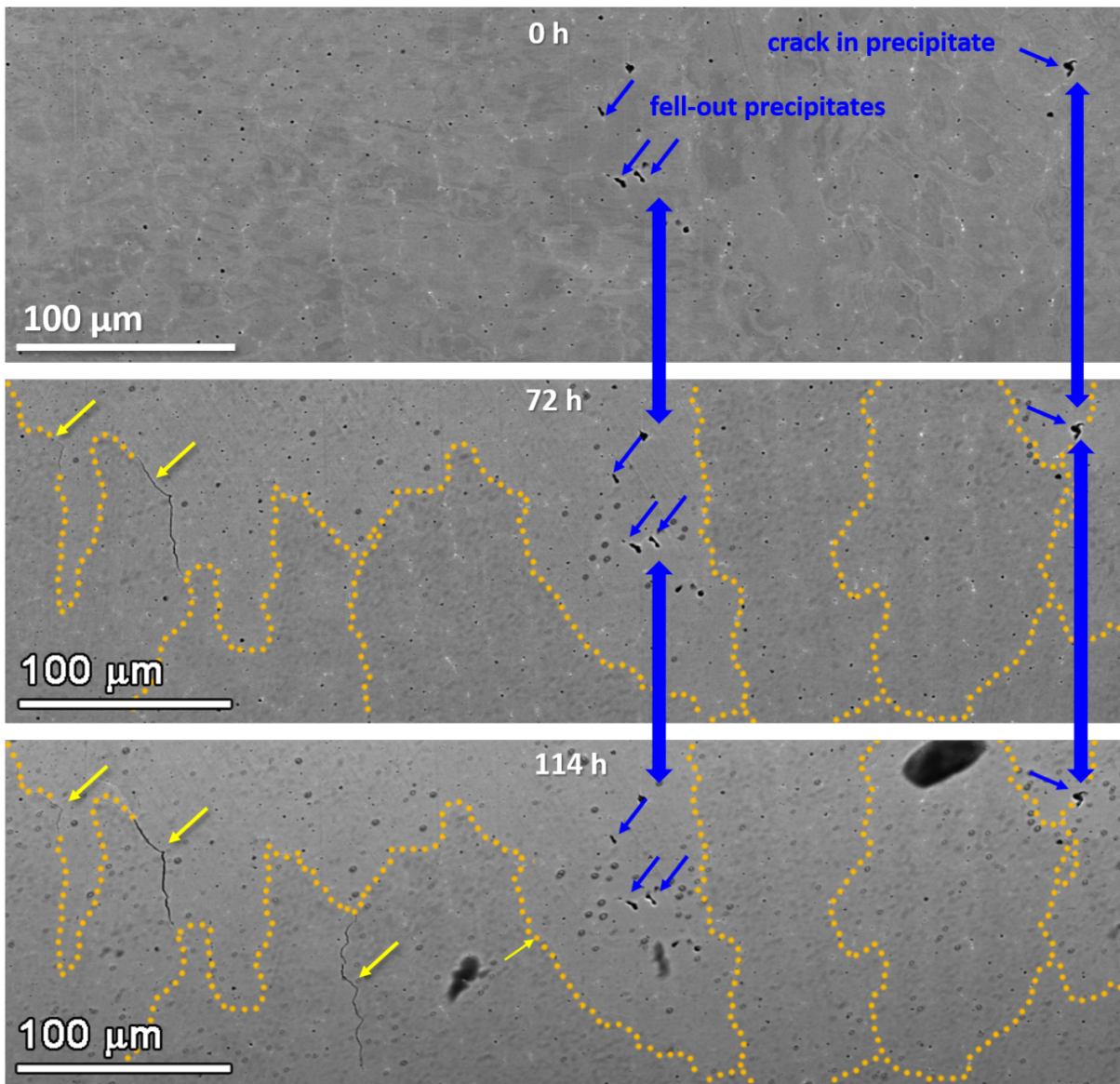


Figure 67. Crack evolution at Site P1 in Figures 63-66 on the surface of the 15%CF Studsvik Alloy 182 specimen IN192 with SCC initiation detected at 41 hours of exposure. The pre-existing defects are highlighted in blue while the cracks are highlighted in yellow and IG attack along grain boundaries are highlighted in orange. No observable change occurred in the pre-existing defects and new cracks were nucleate at grain boundaries that appear clean of defects.

IN193 (15%CF Studsvik A182) - Site C1

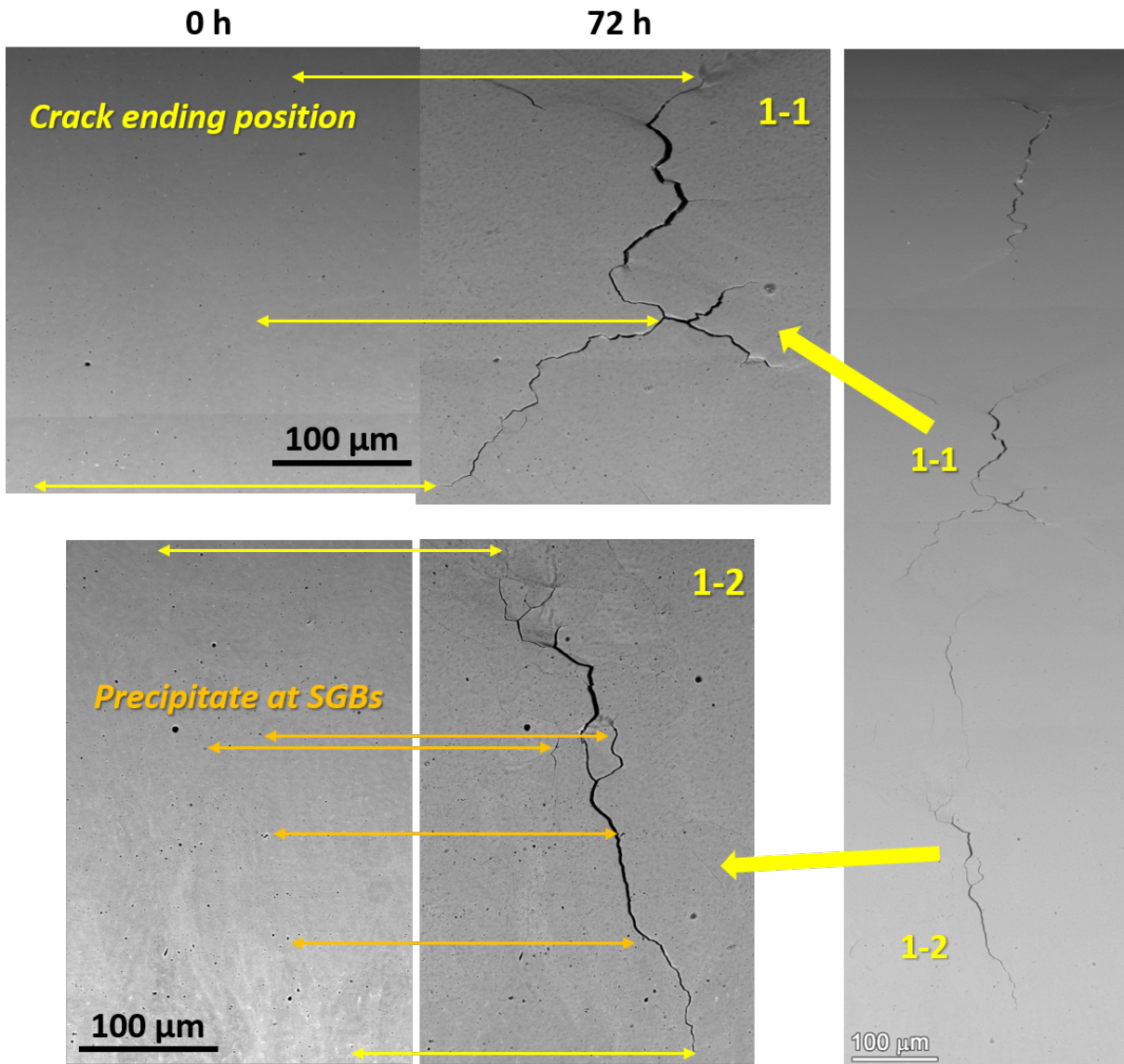


Figure 68. SEM examination of the primary crack marked at Site C1 in Figure 62 before and after testing on the surface of the 15% CF Studsvik Specimen IN193 that initiated at ~41 hours of testing in high temperature water at its yield stress.

IN192 (15%CF Studsvik A182) - Site C1

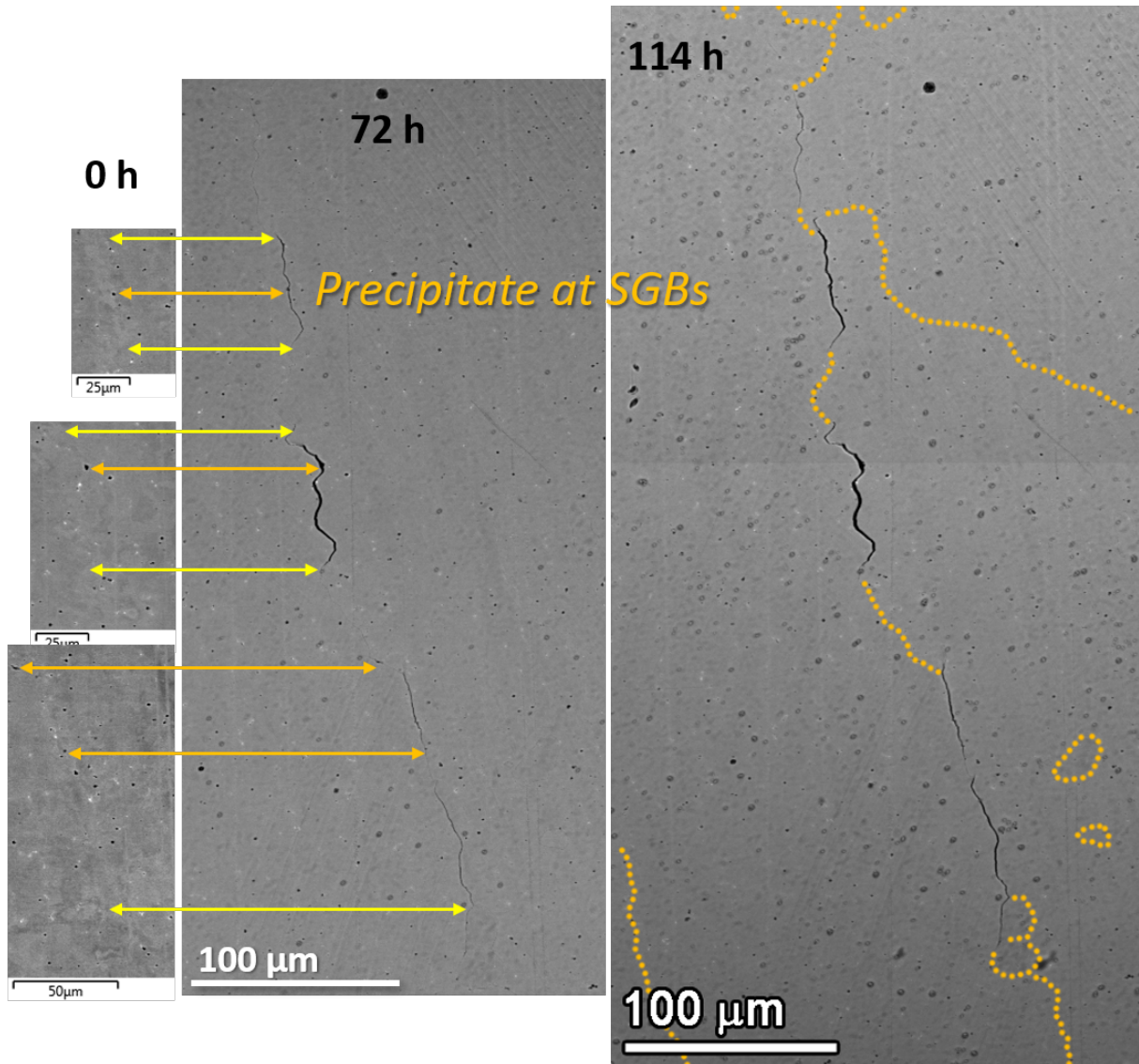


Figure 69. SEM examination of the crack marked at Site C1 in Figure 63 before and after testing on the surface of the 15% CF Studsvik Specimen IN192 that initiated at ~41 hours of testing in high temperature water at its yield stress.

IN192 (15%CF Studsvik A182) - Site C2

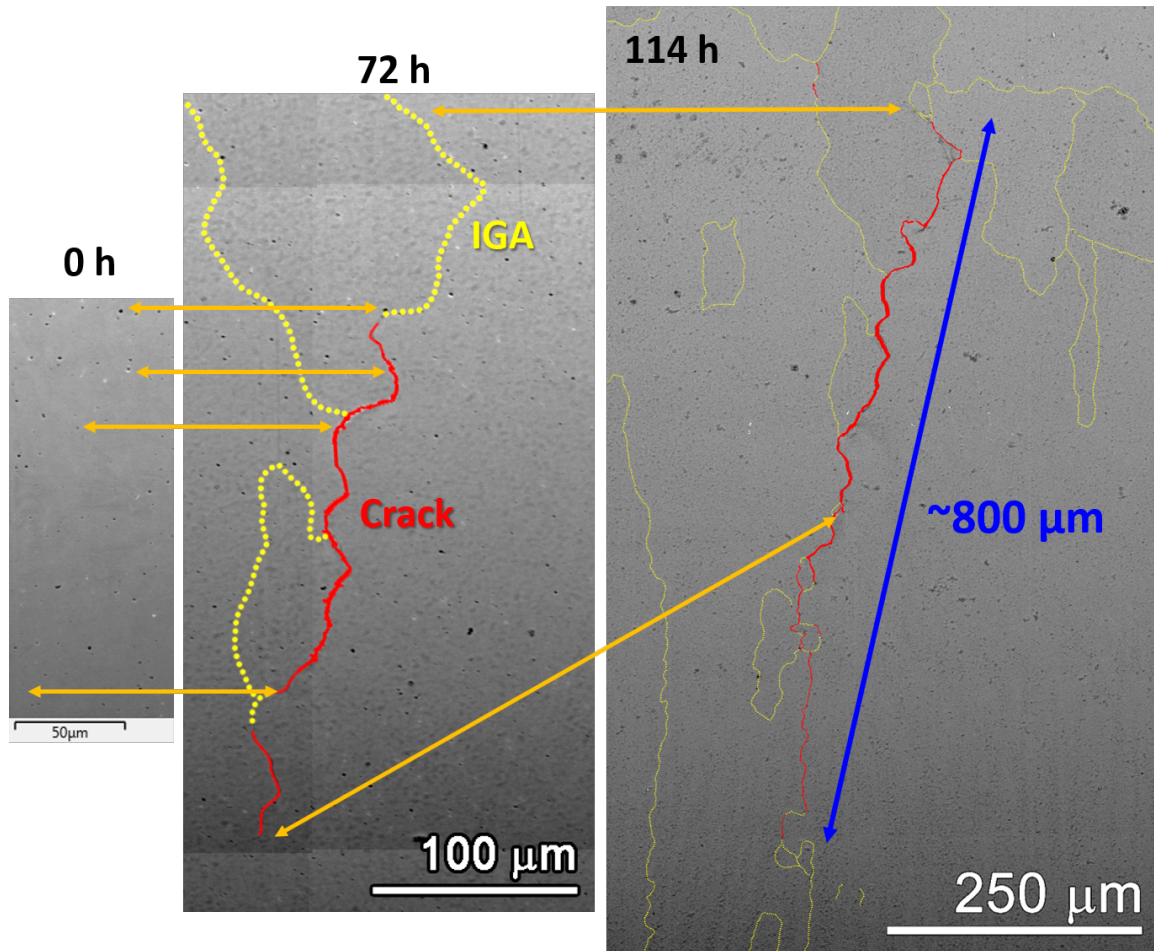


Figure 70. SEM examination of the primary crack marked at Site C2 in Figure 63 before and after testing on the surface of the 15% CF Studsvik Specimen IN192 that initiated at ~41 hours of testing in high temperature water at its yield stress.

7.3.3 15% CF Phase 2B Alloy 182 Specimens IN185 and IN216

Only two out of the nine 15% CF Phase 2B specimens initiated within 150 hours. Their DCPD-referenced strain response is shown in Figure 71. IN185 exhibited a much higher strain rate right after being loaded to the yield stress, but the trend slowed down starting at ~35 hours of exposure before increasing again at ~105 hours. IN216 exhibited a much lower strain rate similar to the specimens with much higher SCC initiation times before it started to increase gradually after ~130 hours of exposure. The difference in the change of magnitude in strain response of these two specimens is also reflected in their post-test crack morphologies. As shown in Figure 72, two large, wide open cracks of ~1 mm long on the surface were found on IN185 with a number of shorter cracks in the gauge and the fillet region. For IN216, only one tight but long crack with a surface length of ~1 mm was found near the fillet in Rotation #4. As shown in Figure 73, this crack was likely formed due to coalescence of two cracks (one with a surface length of ~750 μm and the other ~350 μm) where apparent plastic deformation is apparent in the vicinity of where the ends of these two cracks approach each other. The cracks in these two specimens initiated at locations that appear to be free of pre-existing defects.

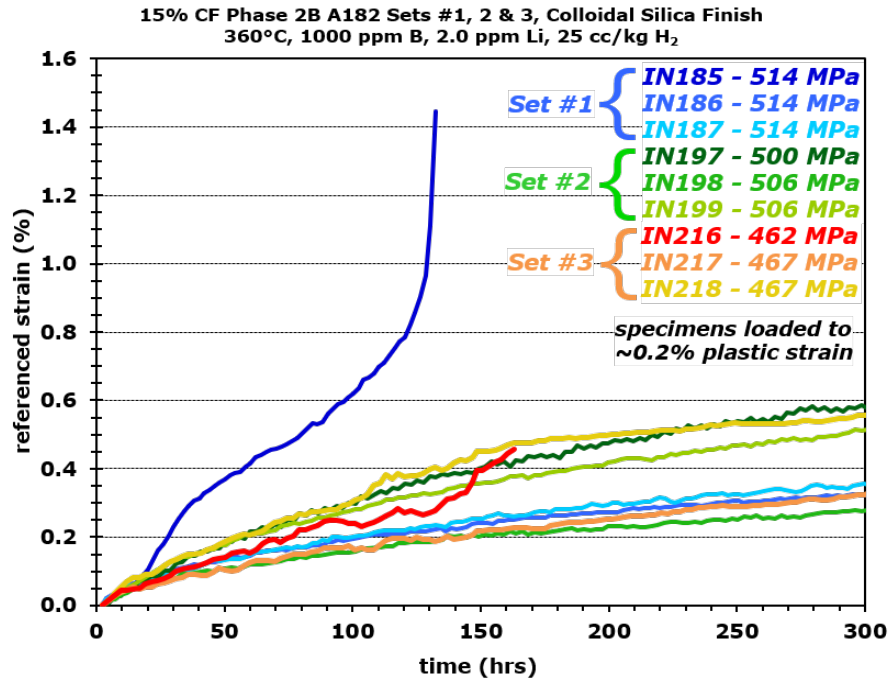


Figure 71. Referenced strain response during the first 300 hours of the constant load SCC initiation testing for the nine 15% CF Phase 2B Alloy 182 specimens.

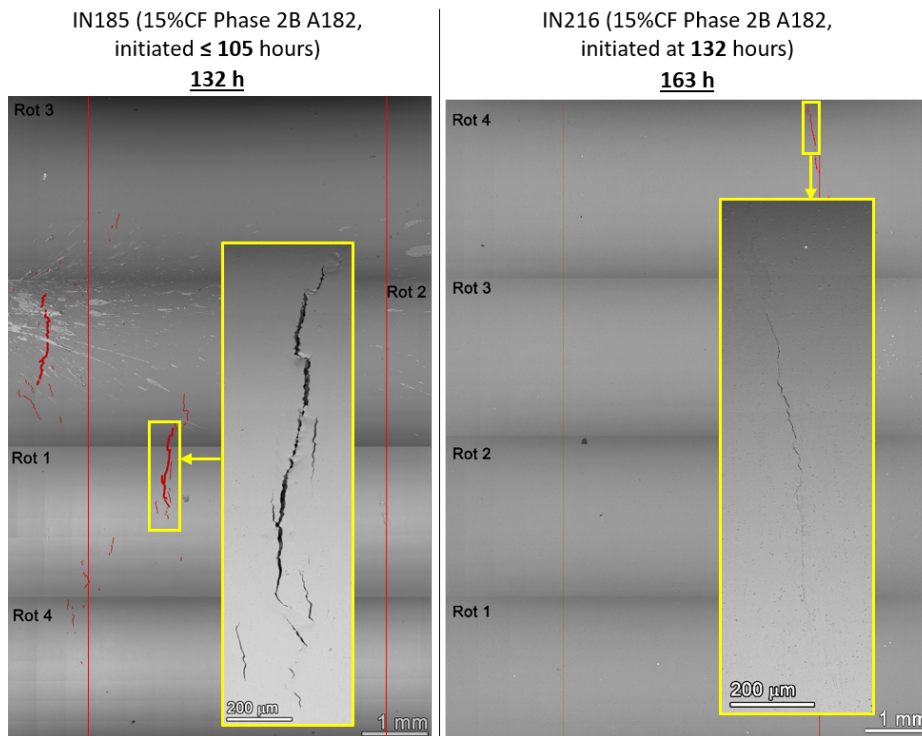


Figure 72. Post-test SEM examination of the surface of the 15% CF Phase 2B Alloy 182 specimens IN185 and IN216 that initiated within 150 hours of exposure at yield stress. Obvious cracks are highlighted in red. The primary crack leading to DCPD detection of SCC initiation in each specimen is also shown in a zoom-in image.

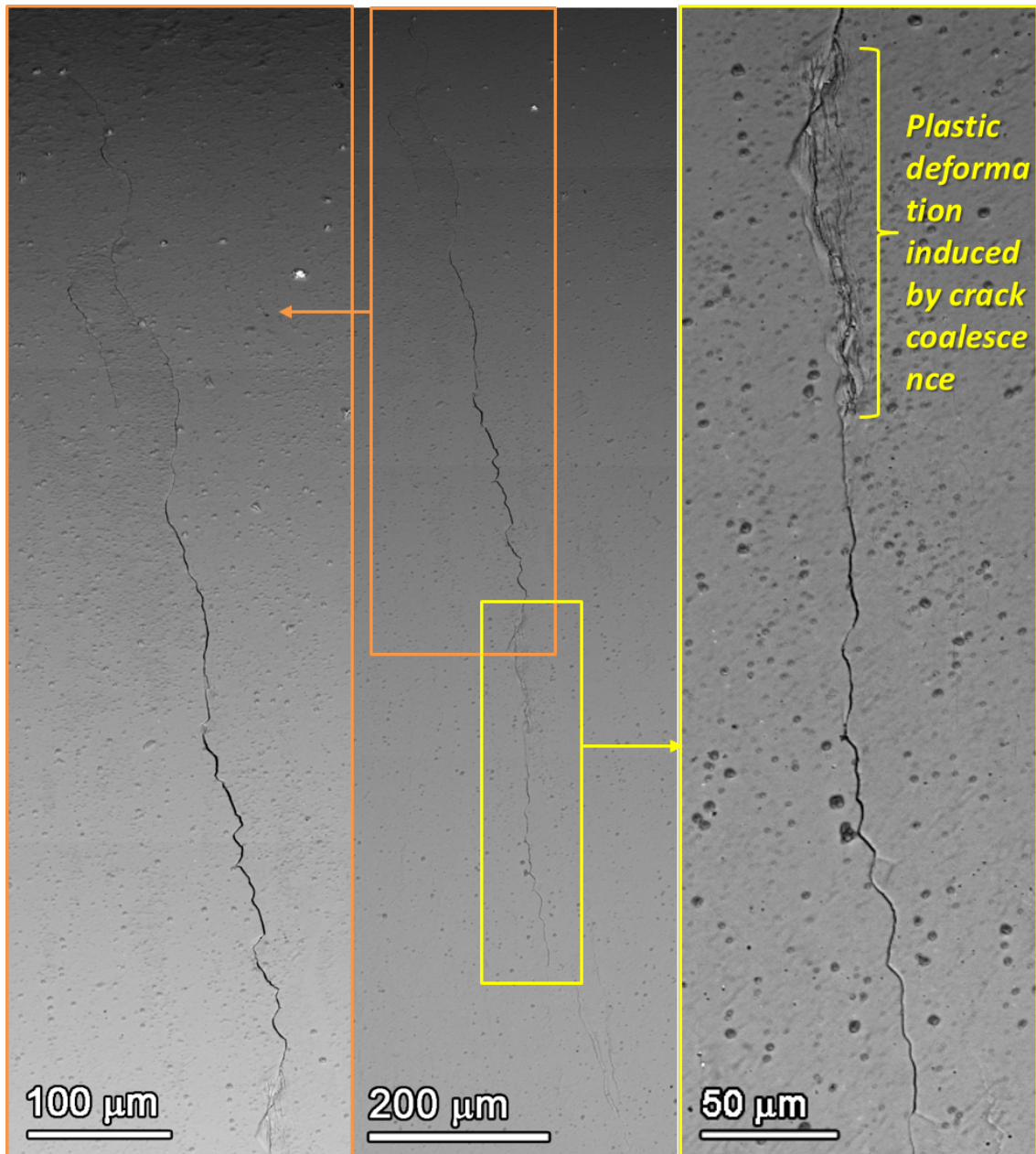


Figure 73. Post-test SEM examination of the primary crack of the 15% CF Phase 2B Alloy 182 specimen IN216 initiated at 132 hours.

7.3.4 15% CF Flawtech Alloy 182 Specimens IN188-190 and IN221-223

Six out of the nine 15% CF Flawtech specimens initiated within 150 hours. Their DCPD-referenced strain response is shown in Figure 74. Two of the specimens initiated essentially upon reaching full load, just as for some of the KAPL and Studsvik specimens. In the following, the pre- and post-test surface morphology of the six low initiation time specimens are summarized and compared to see if insights can be gained.

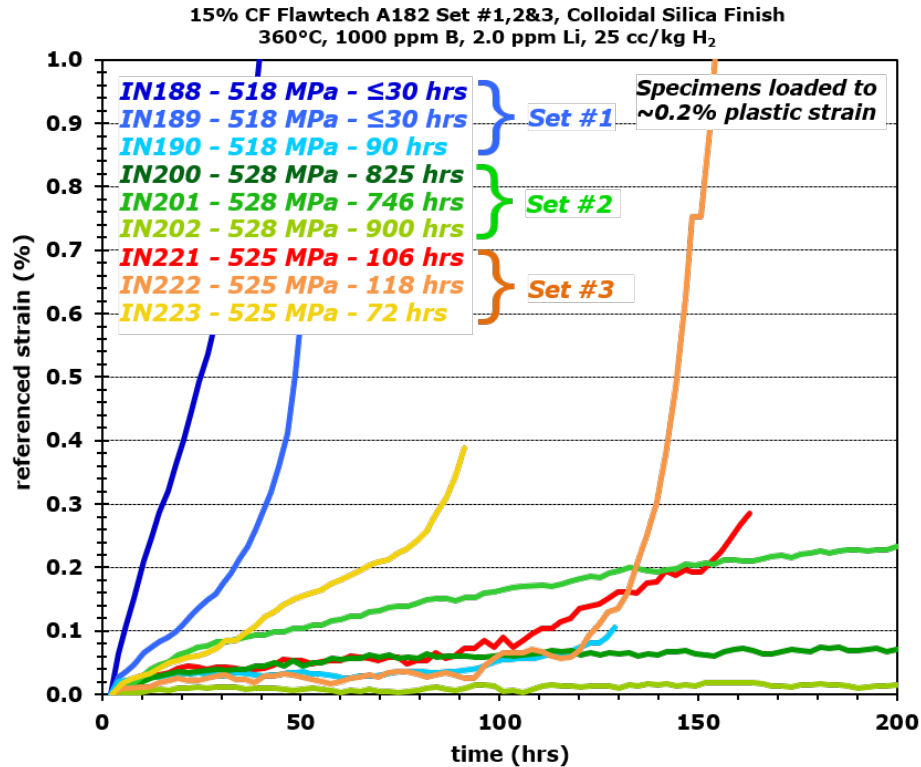


Figure 74. Referenced strain response during constant load SCC initiation testing for the nine 15% CF Flawtech Alloy 182 specimens.

Pre- and post-test surface morphology of the six specimens IN188-190 and IN221-223 are presented in Figures 75-77. The specimens are shown in order of increasing SCC initiation time. Before the start of an SCC initiation test, SEM examinations were carried out to document defects that may affect SCC initiation in these specimens. The onset of cracking in IN189 that had the lowest initiation time of ≤30 hours can be correlated to pre-existing IG cracks found at Site #3 (Figure 78). However, the primary cracks in the other four specimens that initiated shortly afterwards were formed at locations appearing to be free of pre-existing cracks, such as shown in Figure 79. IN188, with a very low SCC initiation time of ≤30 hours, had a large pre-existing crack well into the fillet region, but the post-initiation appearance of the specimen (Figure 75) shows that many large cracks rapidly formed on this specimen including in the gauge region, making the presence of the pre-existing crack less significant with respect to the DCPD response.

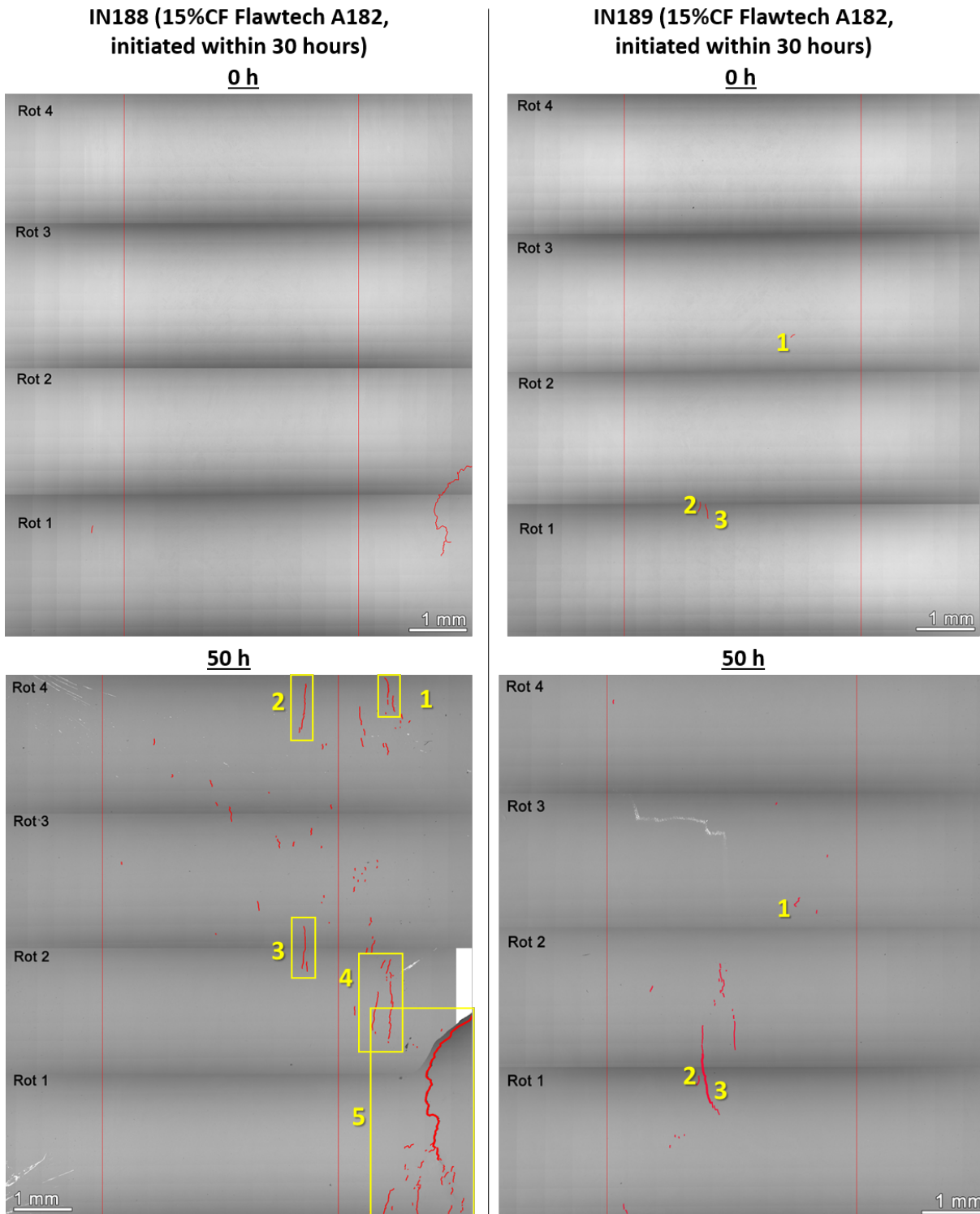


Figure 75. SEM examination of the surface before and after testing of 15% CF Flawtech Alloy 182 specimens IN188 and IN189 that initiated within 30 hours of exposure. The pre-existing cracks were observed in these two specimens and are highlighted in the pre-test SEM montage images.

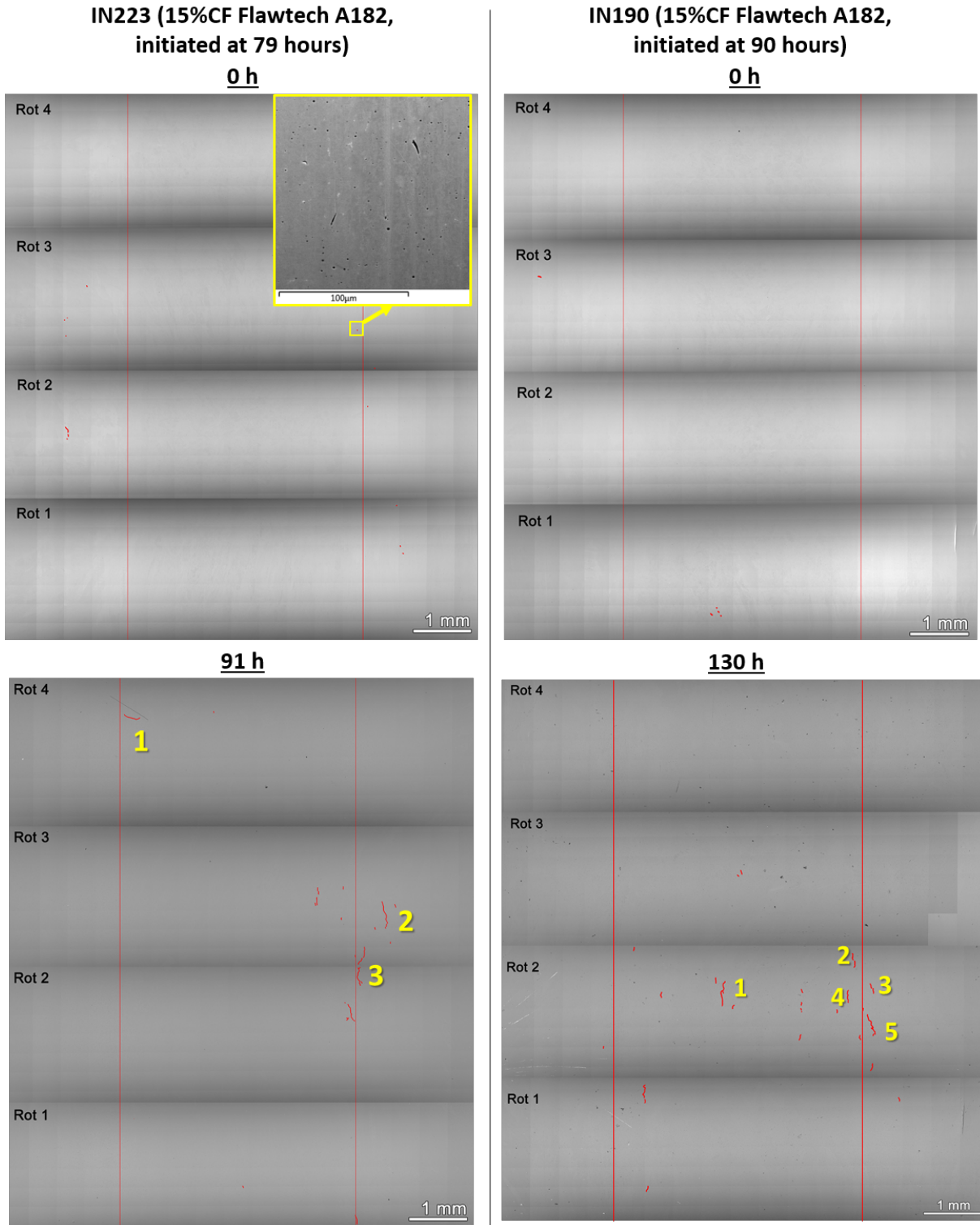


Figure 76. SEM examination of the surface before and after testing of 15% CF Flawtech Alloy 182 specimens IN223 and IN190 that initiated at ~80-90 hours of exposure. No pre-existing defects are related to the cracks that formed later during exposure.

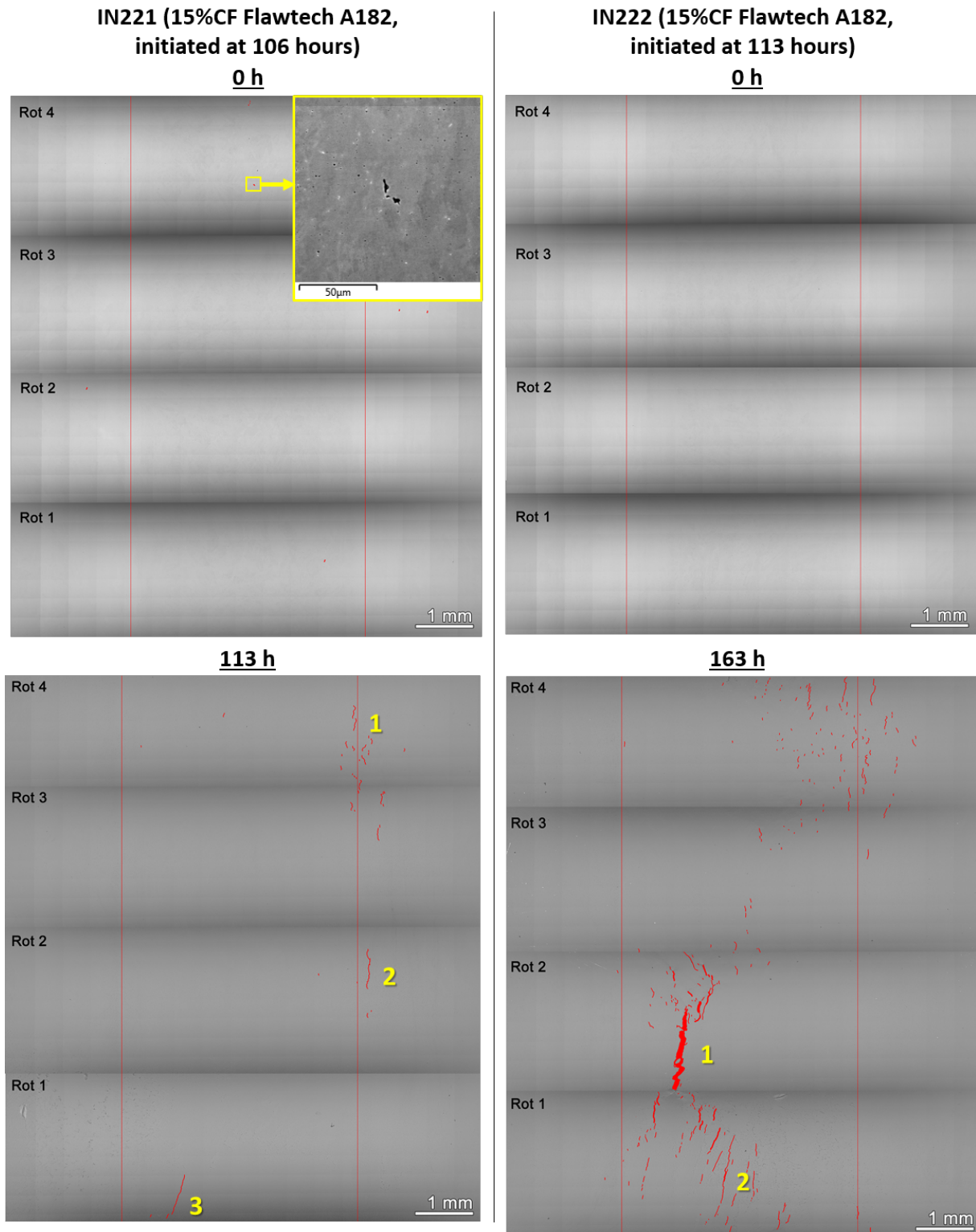


Figure 77. SEM examination of the surface before and after testing of 15% CF Flawtech Alloy 182 specimens IN221 and IN222 that initiated at ~100-160 hours of exposure. No pre-existing defects are related to the cracks that formed later during exposure.

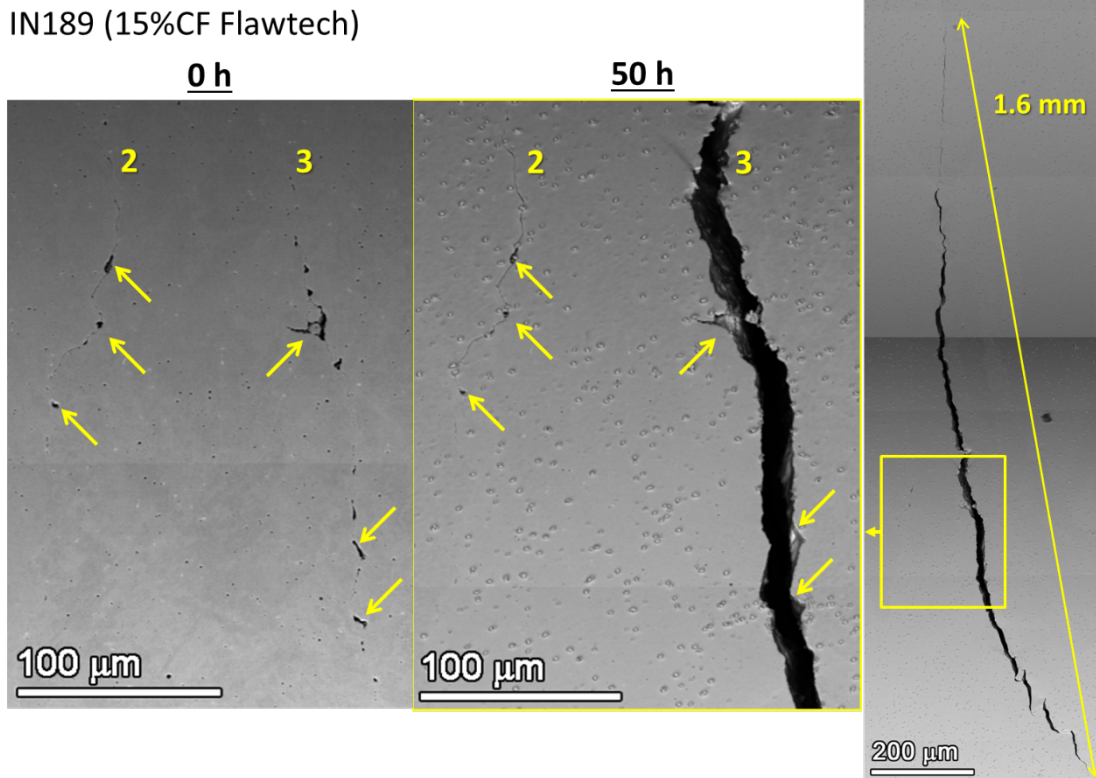


Figure 78. SEM examination of Sites 2 and 3 in Figure 58 before and after SCC initiation testing of the 15% CF Flawtech specimen IN189 that initiated at ≤ 30 hours of testing in high temperature water at its yield stress.

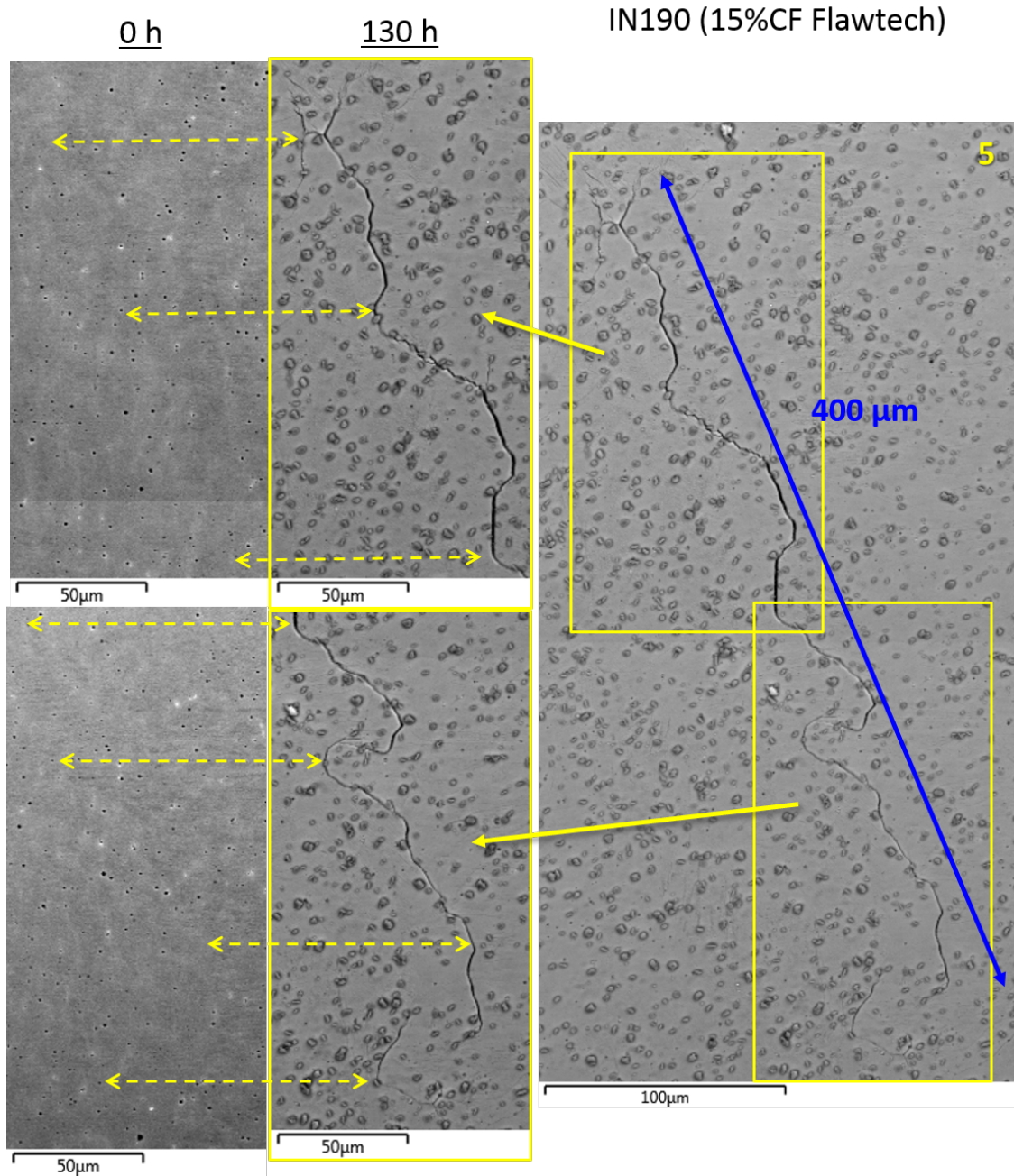


Figure 79. SEM examination of Site 5 in Figure 76 after SCC initiation testing of the 15% CF Flawtech specimen IN190 that initiated at ~90 hours in high temperature water at its yield stress.

8.0 Detailed Microstructural Comparisons Between a Low and a High Initiation Time Specimen

8.1 Overview

As discussed previously, a wide range of SCC initiation responses have been detected by DCPD for specimens fabricated from each weld. Among the nine specimens tested so far for each weld, very low SCC initiation times (<130 hours) were detected in 16 of the 36 specimens, whereas the remaining specimens have exhibited initiation times that are as much as two orders of magnitude higher. In a few cases, SCC initiation was not detected after more than ~3,000 hours of exposure. Routine pre- and post-test SEM surface examinations did not reveal a consistent difference between the specimens with very short and long initiation times. To better investigate possible microstructural origins of the differences in the initiation times, a more detailed study was carried out on selected specimens utilizing high resolution, analytical electron microscopy techniques including SEM, FIB milling, electron backscattered diffraction (EBSD), transmission electron microscopy (TEM), EDS, and scanning transmission electron microscopy (STEM).

Two specimens, IN169 and IN233, from the 15% CF Studsvik Alloy 182 weld were selected for this study. IN169 went 5,126 hours without DCPD-indicated SCC initiation while IN233 initiated at 46 hours. They were tested in the first and the third set of Studsvik samples and had yield strengths of 541 and 532 MPa, respectively. In the image of IN169 after 5,126 hours shown in Figure 80, some cracking is present around a dent well into the fillet region in Rotation 4, and two cracks of 350-500 μm long were observed in the gauge of Rotation 1. These cracks were all present after ~3,000 hours of exposure but did not grow further during the exposure to 5,126 hours.

In contrast, IN233 exhibited very rapid SCC initiation with several cracks reaching a surface length of >1 mm long during a total exposure of 46 hours in 360°C simulated PWR primary water. The two specimens were cross sectioned along their axis (shown by the yellow line for each specimen in Figure 80) to intersect major cracks in both specimens. Cross-section SEM examinations were performed to probe the morphology and composition of weld defects, bulk spinels, intergranular attack (IGA) and cracks in detail. EBSD analyses were performed in the region where major cracks were present to investigate possible effects of grain orientation and local strain distribution on crack initiation and growth. In addition, a few TEM samples were lifted out from the gauge surface in both specimens to evaluate whether any local microchemical inhomogeneity was involved in triggering the low SCC initiation time in IN233. In the following section, results of each of these characterization activities will be presented, and the difference between the two samples will be discussed to attempt to understand the cause of very low SCC initiation times in Alloy 182.

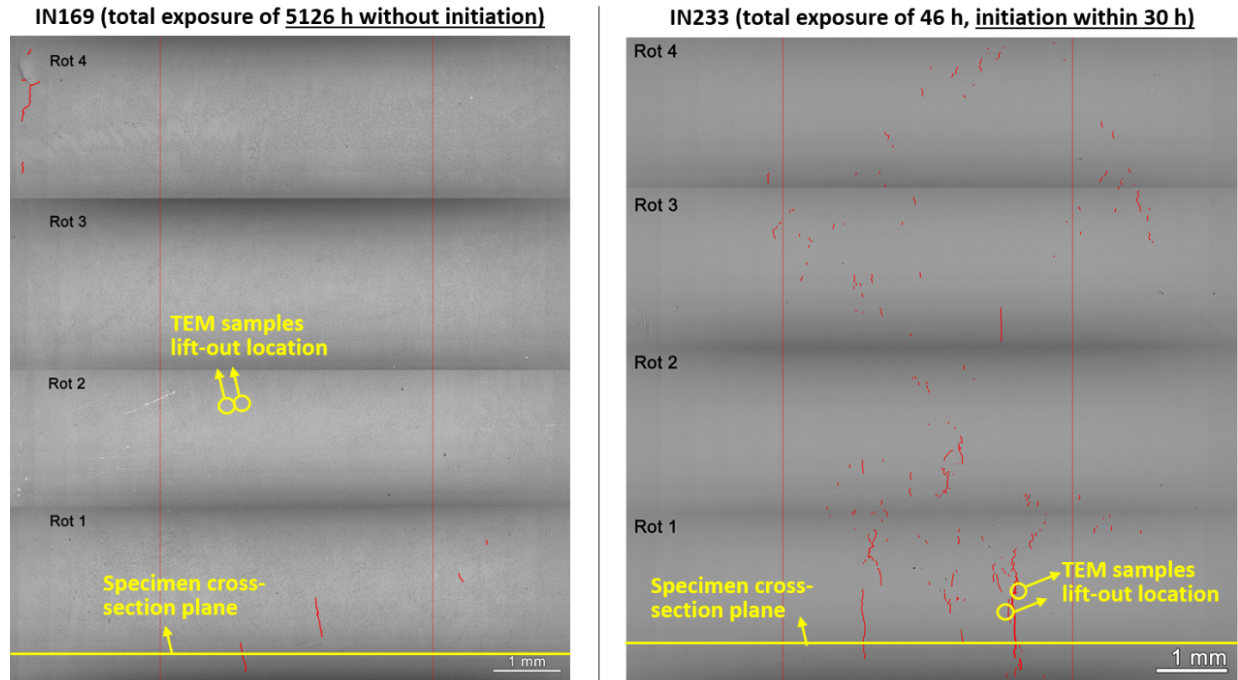


Figure 80. Post-test SEM backscatter electron (BSE) montage images of the two 15%CF Studsvik Alloy 182 specimens IN169 (left) and IN233 (right) with obvious cracks highlighted in red. The locations for cross-sectioning and TEM sampling in each specimen are marked in yellow.

8.2 SEM Cross-Sectional Analysis

8.2.1 Weld Defects in IN233 and IN169

Six regions that were randomly selected in different portions of one cross section of IN233 were examined, and weld defects with different size and morphologies were observed in three of them, ranging from small, IG discontinuities to larger lack-of-fusion (LOF) defects (Figures 81-85). All defects are assumed to be pre-existing prior to the start of the high temperature water exposure.

Small IG weld defects with widths on the order of hundreds of nanometers and semi-continuous lengths as long as 20 μm were documented within one $\sim 1 \times 1 \text{ mm}^2$ region within the cross section near the center (both length and width) of the gauge section of IN233 (Figures 81-85). Due to the size and morphology of the defects, they are unlikely to be a result of IG precipitate fallout during polishing of the cross section, but EDS needs to be performed to confirm this assumption. In Figure 82, it is demonstrated that this type of defect can exist in series, forming semi-continuous crack-like features as long as $\sim 20 \mu\text{m}$. Strain fields were observed around some of the defects, suggesting that local deformation occurred during cold forging of this material.

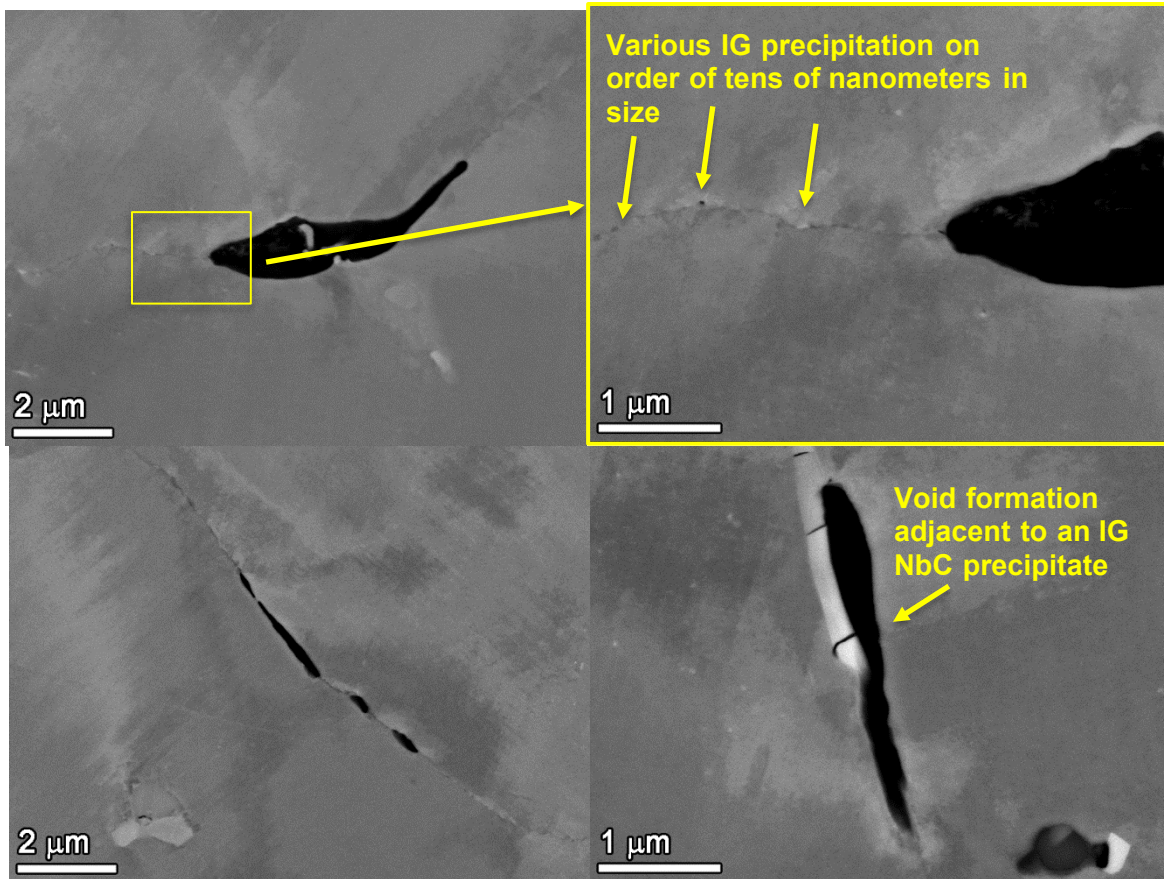


Figure 81. SEM(BSE) of small (micrometers), IG weld defects observed in a cross section of IN233.

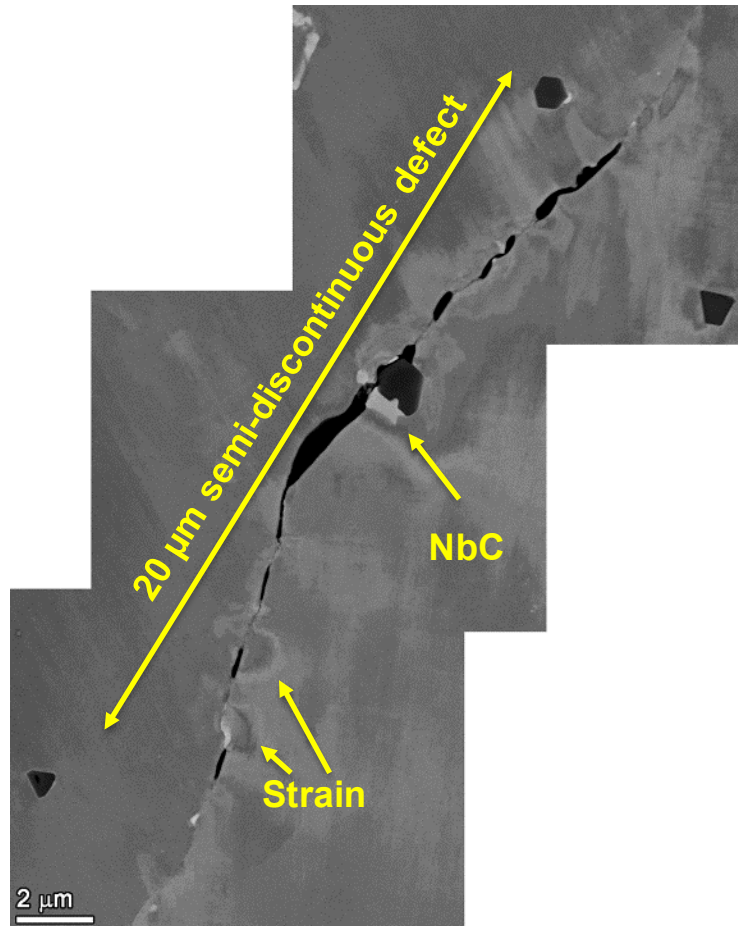


Figure 82. SEM(BSE) of small (micrometers), IG weld defects observed in IN233 that have joined up to form a 20 μm long defect.

Two large defects, likely LOF, were found in the cross section of the fillet region as shown in Figure 83 and Figure 84. The larger defect shown in the upper-left image in Figure 83 was on the order of 0.3 mm x 1 mm in size as viewed in this cross section and appeared to have small IG cracks emanating from its perimeter. EDS analysis of these IGA cracks did not exhibit a strong O-K signal, and thus were not believed to have been caused by exposure to high temperature water. Interestingly, semi-continuous voids on the order of tens of nanometers in size appeared at the leading front of one of the IG cracks.

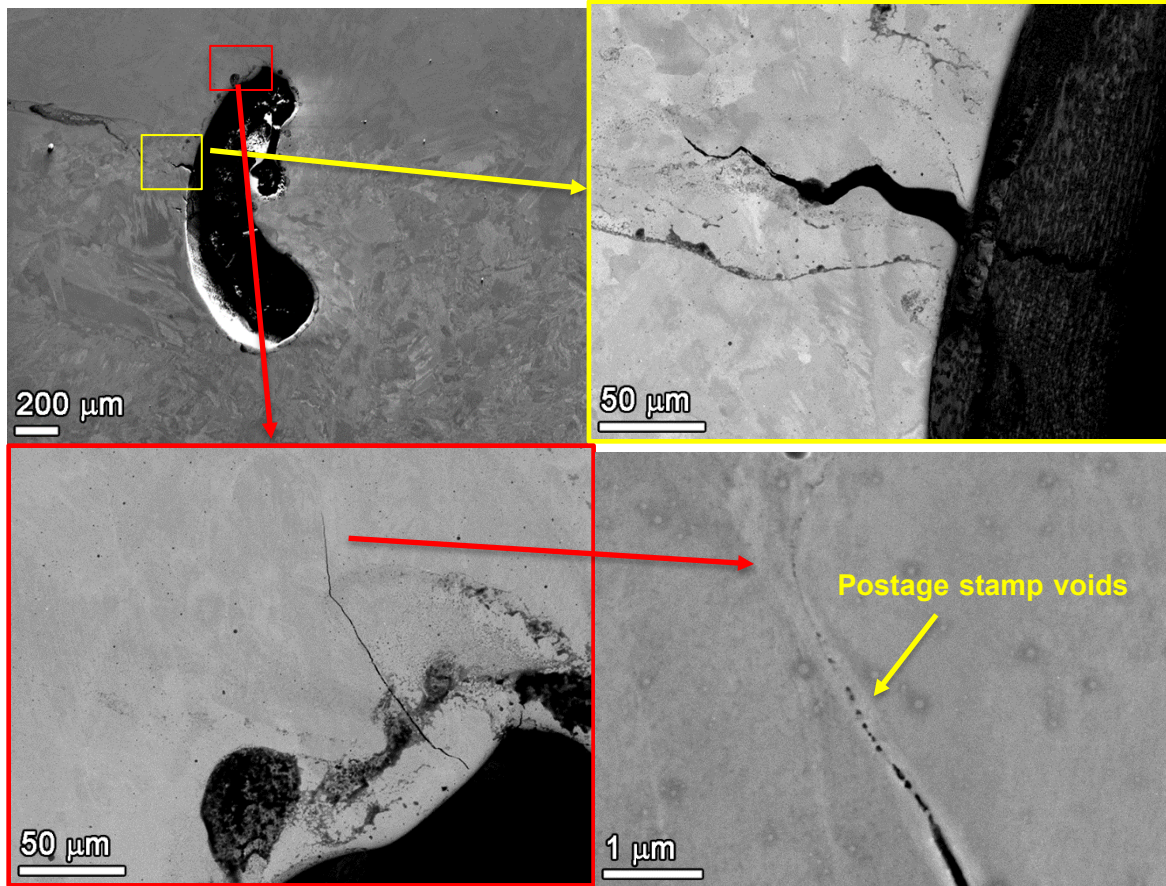


Figure 83. SEM(BSE) of larger (tens to hundreds of micrometers) TG weld defects observed in IN233. Smaller, tight cracks were observed to emanate from these sub-surface defects.

The second LOF defect (Figure 84) was found during FIB trenching to remove a TEM specimen. The grain boundary could be traced from the surface of the identified IGA along the entire face of the wall, even appearing to pass through a discontinuity. EDS elemental analysis (Figure 85) of the FIB trench wall shows no oxide within the discontinuity walls and has a composition qualitatively resembling that of the surrounding weld metal.

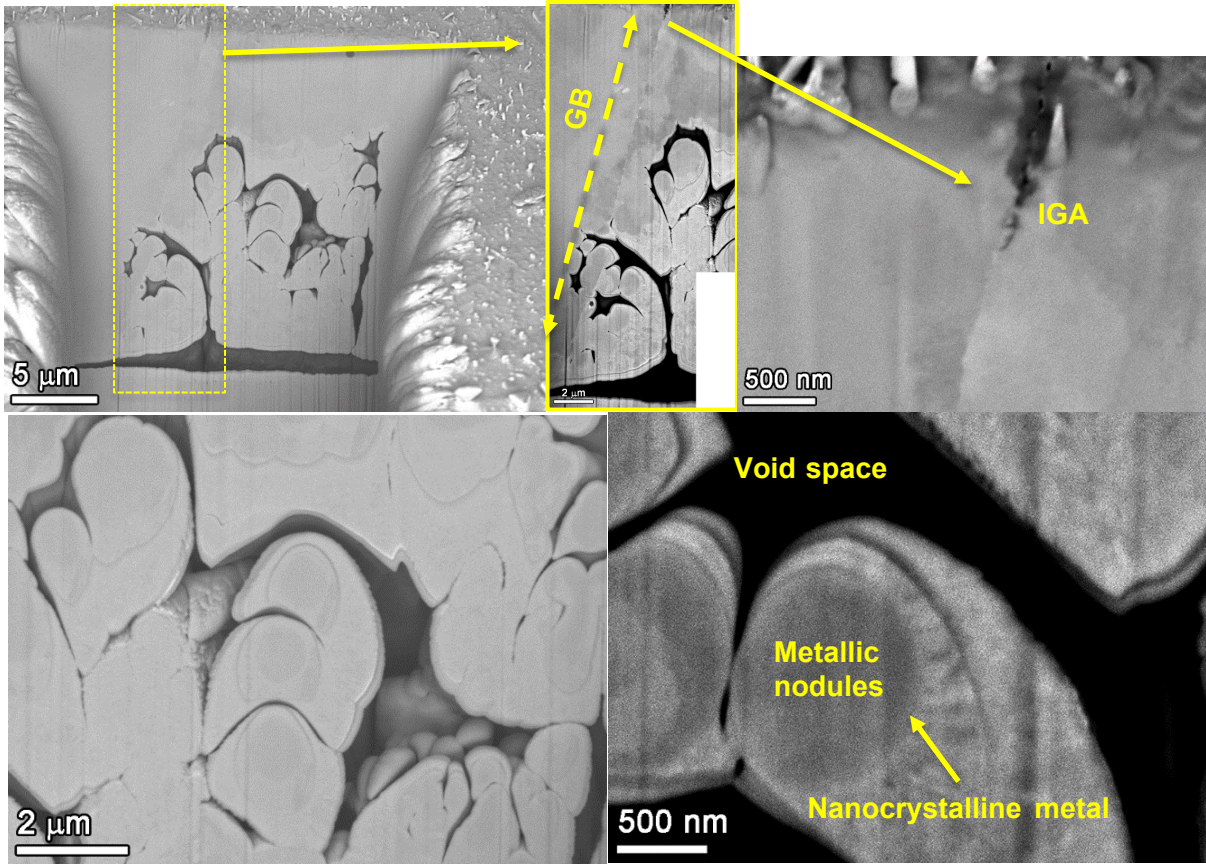


Figure 84. SEM(BSE) images detailing the void space sub-surface discovered during FIB milling of a TEM lamella from IN233. The TEM lamella was aimed at capturing the identified IGA observed in the trench wall.

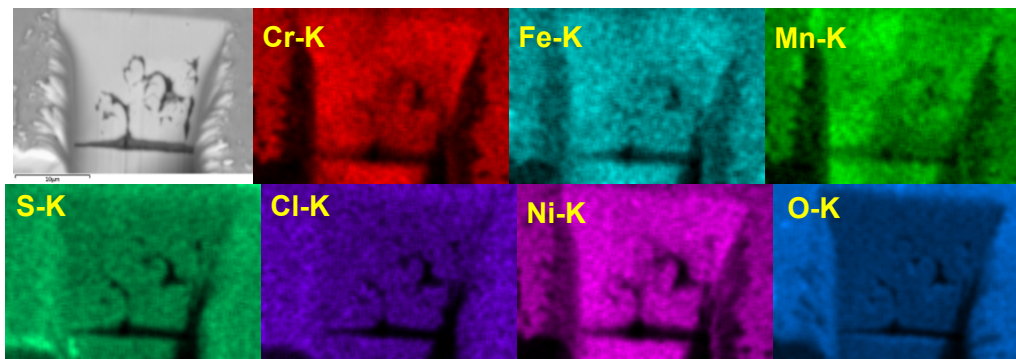


Figure 85. SEM(SE) and EDS elemental maps of the FIB lamella trench showing sub-surface void space.

Similarly, five $\sim 1 \times 1 \text{ mm}^2$ randomly selected regions were examined in IN169 and only one region near the center of the gauge section exhibited a few small IG weld defects with similar morphology as those observed in Figures 81 and 82 in IN233. However, they only appear in isolated form with a much shorter length of $\sim 5 \text{ }\mu\text{m}$ (Figure 86).

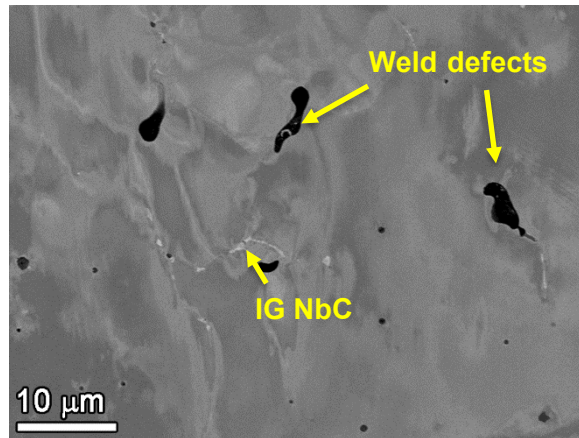


Figure 86. SEM(BSE) of micrometer size IG weld defects observed in IN169.

8.2.2 Bulk Oxide Inclusions in IN233 and IN169

Bulk dark-contrasted phases (both IG and TG), often decorated with brighter NbC phases were occasionally observed in the cross section of IN233. Closer examination (Figures 87 and 88) of these features suggest that they are oxides rich in Cr, Ti, Al and Mn (Figure 88). Figure 87 shows both a buried oxide (upper) and an oxide intersecting the surface (lower), which had subsequently formed a large Fe-rich spinel on the surface. The size and shape of the oxides presented are representative of those observed in this weld. The majority of the observed oxides were TG, but instances of random IG oxides were noted as well. The bright contrast on the oxide perimeter was confirmed to be Nb-rich carbides, which suggests that these oxides were present in the melt prior to the nucleation of NbC. For the oxide particle in Figure 87c, the transition to darker contrast in the portion of the oxide particle embedded in the specimen is due to Al enrichment as shown in Figure 88. Because these oxides are not typically observed in welds, their origin is uncertain but likely due to contamination during the welding process.

Examination of the cross section of IN169 confirms the presence of these oxide phases in this weld as well. Representative examples are shown in Figure 89 with three buried oxides that are hundreds of nanometers in size. EDS mapping again suggest these oxides are rich in Cr, Ti, Al and Mn (Figure 90). The majority of these were observed as TG, but instances of IG oxides were noted as well. Brightly contrasted Nb-rich carbides were seen wrapping around the darker oxide spinels, again indicating these oxides were present in the melt prior to the nucleation of NbC. It is interesting to note that as shown in the left image of Figure 89, one of these Nb-rich carbide/oxide structures was close enough to the surface to be in contact with penetrative oxidation. However, it appears to be unaffected by high temperature water even after extended exposure of 5,126 hours. Based on this observation and the fact that most of these spinel oxides are TG (whereas SCC initiation is IG), it is believed that they are not related to the very low SCC initiation time for IN233.

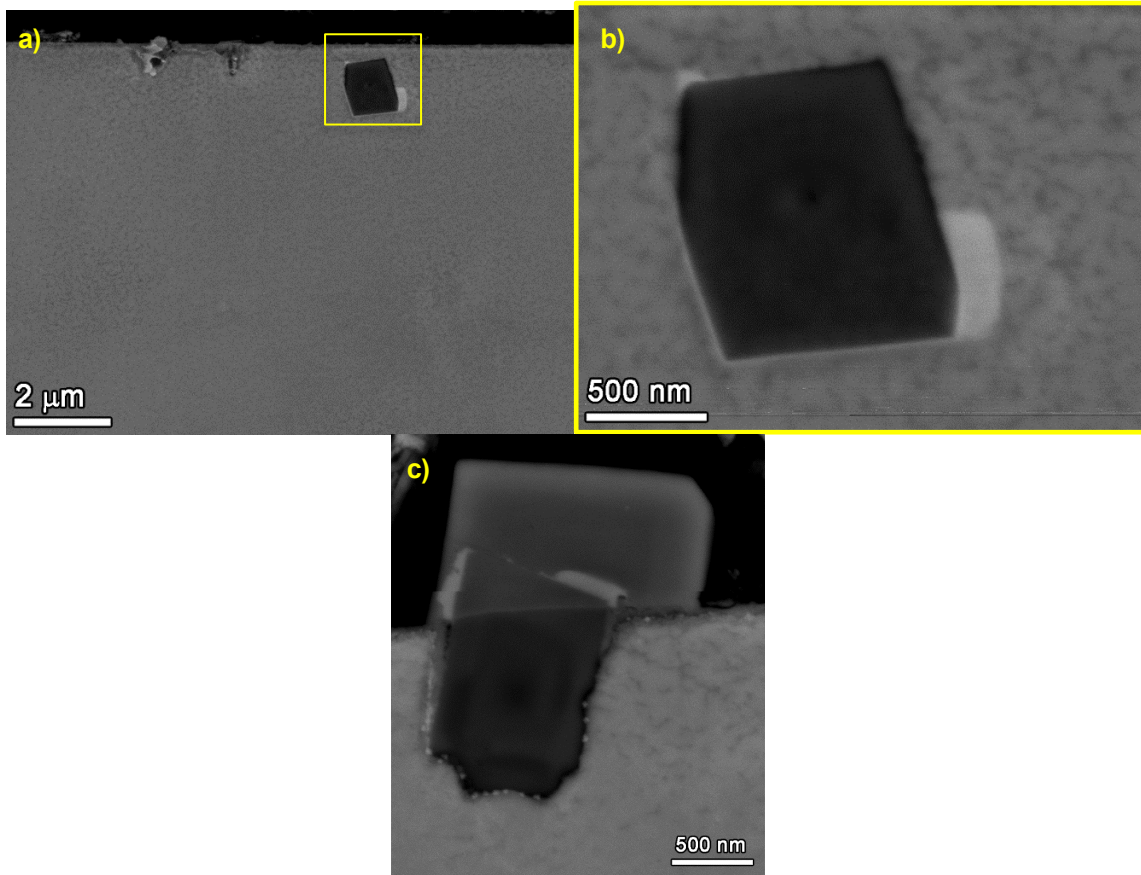


Figure 87. SEM(BSE) of micrometer, cuboidal oxides observed TG in the sample. Brighter Nb-rich phases were noted to form on the surface. When this oxide intersects the surface, the high temperature water appears to form spinel on top of the matrix oxide.

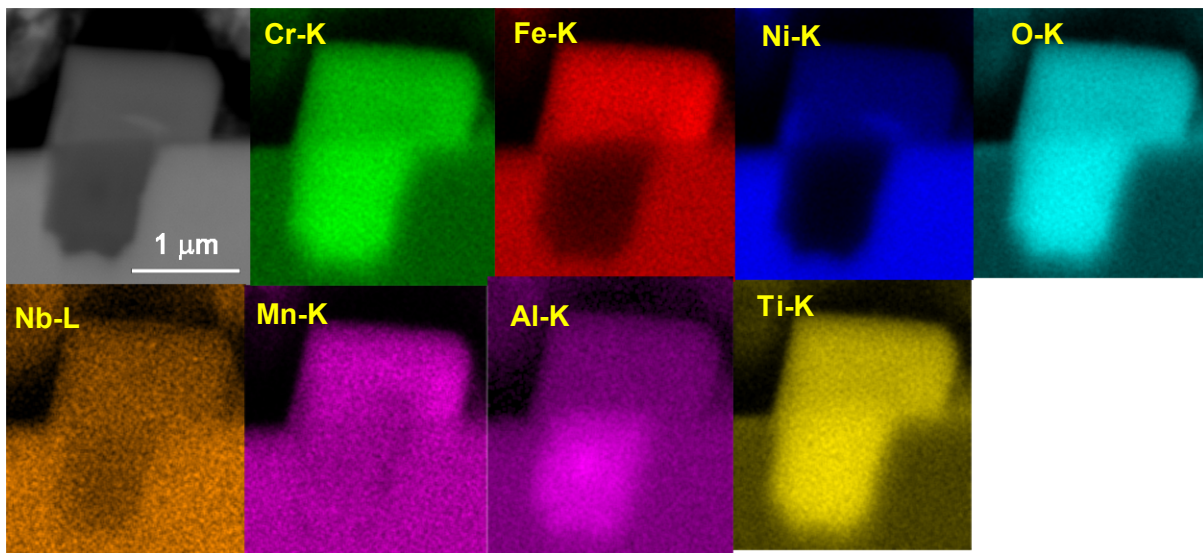


Figure 88. SEM(BSE) and EDS of the Cr-, Ti-, Al-, and Mn-rich oxides observed both IG and TG within the bulk of the sample. NbC can be observed nucleating from these larger oxide crystals.

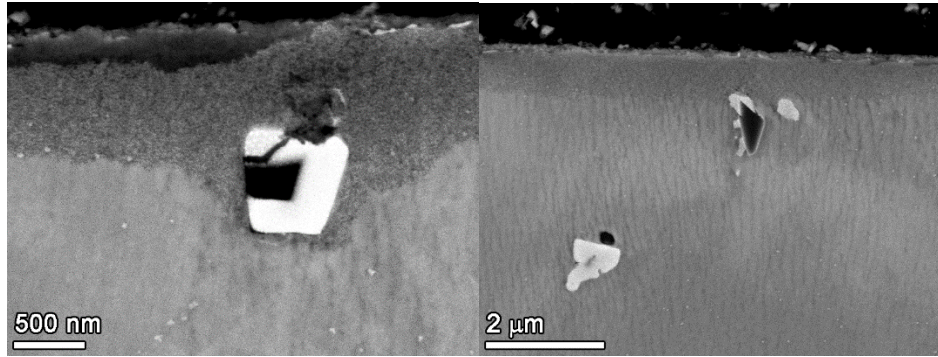


Figure 89. SEM(BSE) of micrometer, cuboidal oxides observed at TG locations in the sample. Brighter Nb-rich phases were noted to form on the surface.

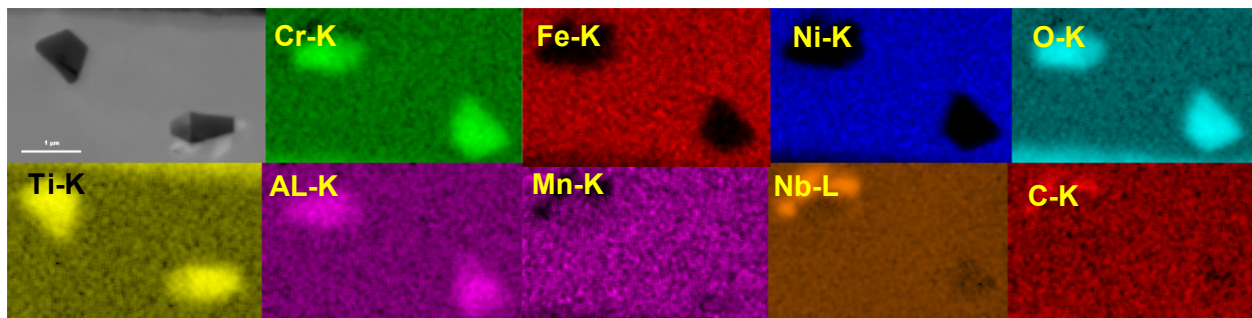


Figure 90. SEM(BSE) and EDS of the Cr-, Ti-, Al-, and Mn-rich oxides observed both IG and TG within the bulk of the sample. NbC can be observed nucleating from these larger spinel crystals.

8.2.3 IGA in IN233 and IN169

The polished cross sections were used to examine the IGA starting from the surface of the specimens. Five IGA examples in IN233 are shown in Figure 91 with BSE images at both low (left column) and high (column) magnifications. The depth of IGA consistently ranges from a few hundreds of nanometers up to one micrometer. Near the surface there is a slightly wider, dark contrast which is consistent with Cr- and Fe-rich oxides. Toward the leading front there always appears to be a tighter, darker oxide contrast which is indicative of a Cr-rich oxide. The appearance of bright contrast adjacent to the IGA can either be the onset of diffusion-induced grain boundary migration (DIGM) or small NbC precipitates on the boundaries, which are difficult to discern by SEM at these length scales. The apparent differences in width of the Fe- and Cr-rich oxides near the surface is a function of the orientation of the boundaries to the surface, with some being more on edge than others. Since the tight, IG corrosion at the leading IGA front is typically on the order of a few tens of nanometers, the projection factor is not as pronounced. EDS elemental maps (Figure 92) were collected from an instance of shallow IGA from which the various elemental compositions of not only the IGA but also DIGM are apparent. Chlorine (Cl) mapping was performed because Cl was observed in TEM examinations conducted in tandem with the SEM examinations. No Cl was observed in the SEM mapping, likely due to insufficient detection resolution at the magnification levels used.

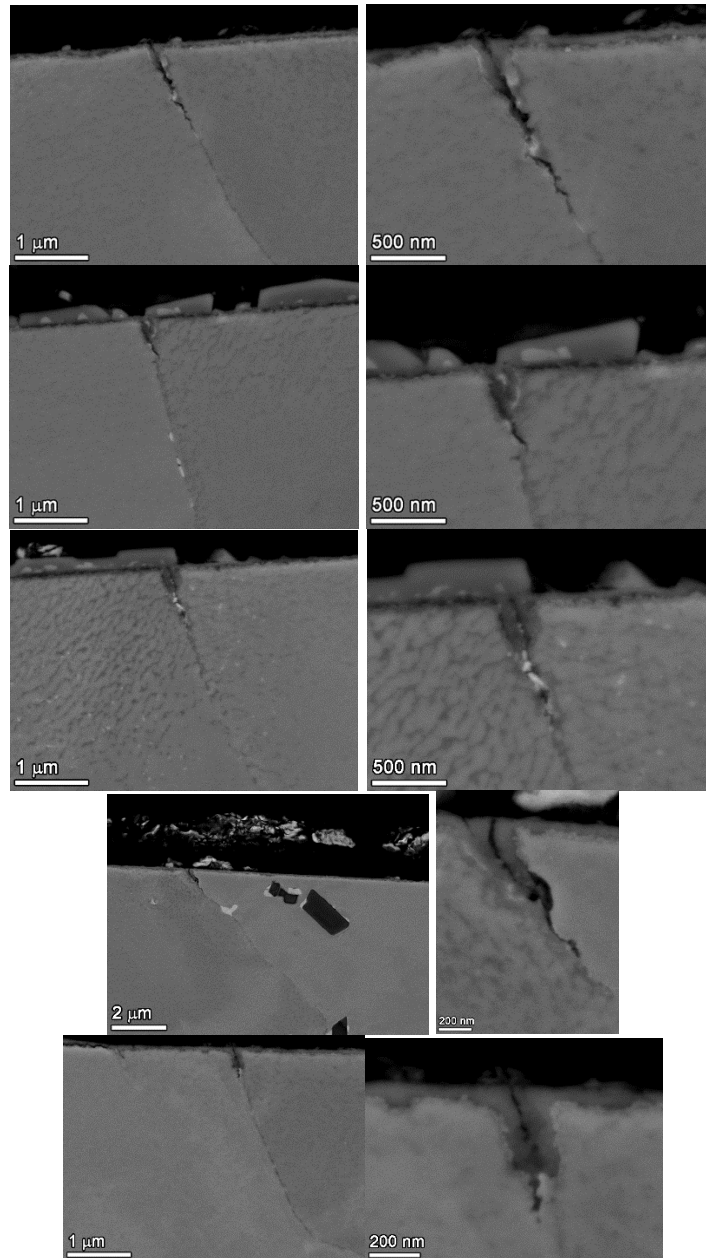


Figure 91. SEM(BSE) of a number of representative instances of IGA in IN233. The images in the right-hand column are higher magnification conjugates of the lower magnification regions in the left-hand column. The IGA depths were all on the order of hundreds of nanometers.

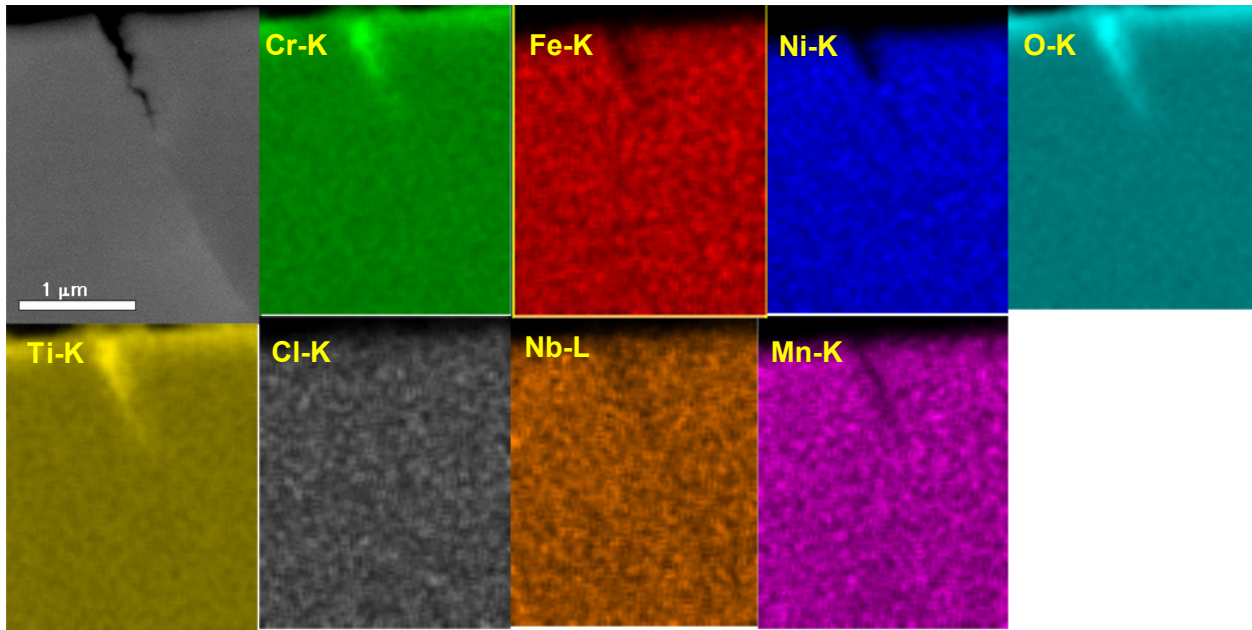


Figure 92. SEM(BSE) and representative EDS of IGA in IN233.

Six representative examples of IGA in IN169 are shown in Figure 93, where the majority exhibited a depth on the order of a micrometer, but one was as long as 2 μm . Along nearly the entire length of each IGA ingress, tight, darker contrast is visible and is consistent with a Cr-rich oxide. The appearance of bright contrast adjacent to the IGA is strongly indicative of DIGM, which was confirmed via EDS elemental mapping (Figure 94). There was no strong indication of Cl anywhere in the IGA, although SEM EDS analysis most likely would not be able to detect Cl at these levels even if it were present. Cr-rich penetrative oxidation (darker contrast) was noted on either side of the IGA, and it should be pointed out that in regions where DIGM has occurred, there was no penetrative oxidation because the alloy had become highly Ni enriched.

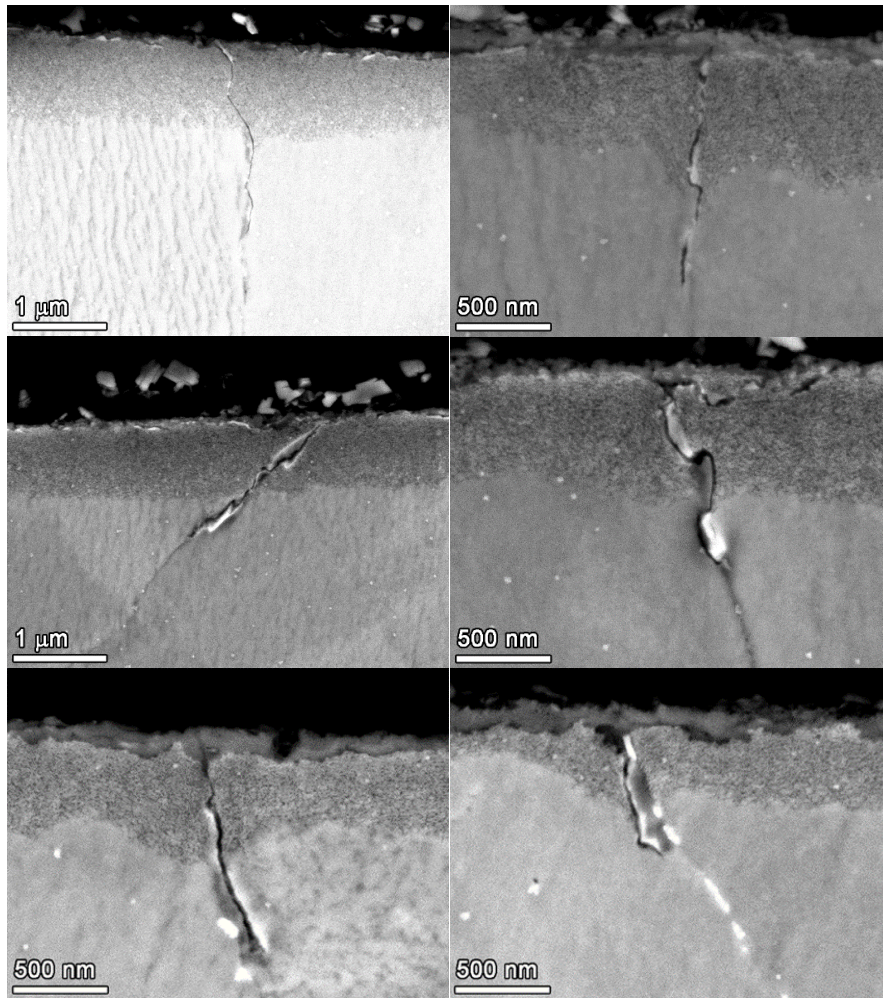


Figure 93. SEM(BSE) of a number of representative instances of IGA in IN169. The IGA depths were all greater than 0.5 μm with the longest noted at $\sim 2 \mu\text{m}$.

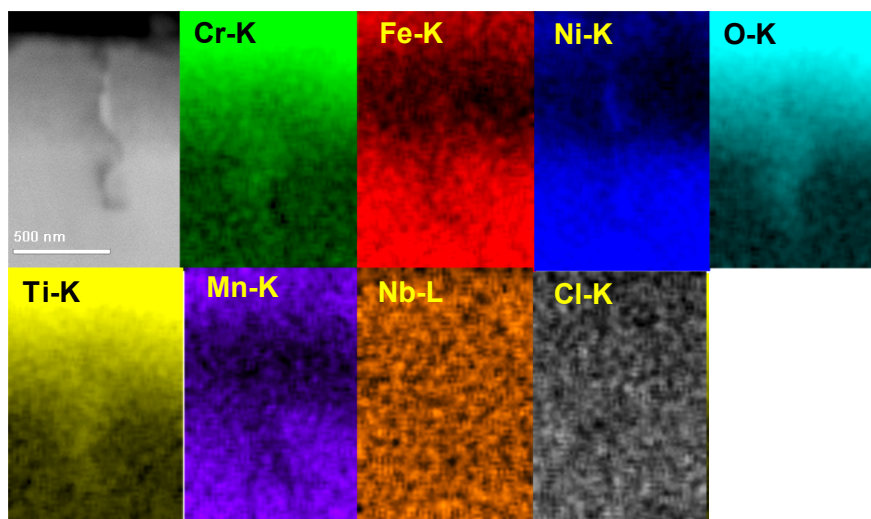


Figure 94. SEM(BSE) and representative EDS of IGA in IN169. Note the Ni-rich regions adjacent to the IGA which are indicative of DIGM.

8.2.4 SCC Crack Initiation in IN233

Sample IN233 exhibited rapid SCC initiation, and Figure 95 highlights the cross section of one of the SCC cracks on the order of 50 μm long. The morphology of the crack indicates that it is IG, and high magnification imaging of the leading crack tip illustrates that it is blunted but does have minor IGA immediately ahead. The presence of IG precipitation ahead of the leading crack tip was observed as small (tens of nanometers), semi-continuous precipitates with varying contrast suggesting both Nb- and Cr-rich carbides. A larger (micrometer scale) Nb-rich carbide was noted approximately 1 μm behind the leading crack tip, although the majority of the carbide is TG. EDS elemental mapping (Figure 96) confirms the backscatter contrast in Figure 95. There was no strongly segregated Cl signal in the oxide or on the boundary, but it was detected in the NbC which is possibly due the proximity of Nb and Cl energies and hence could be assigned as an artifact from EDS analysis. The EDS Nb-L map clearly indicates the size and density of IG NbC within this region.

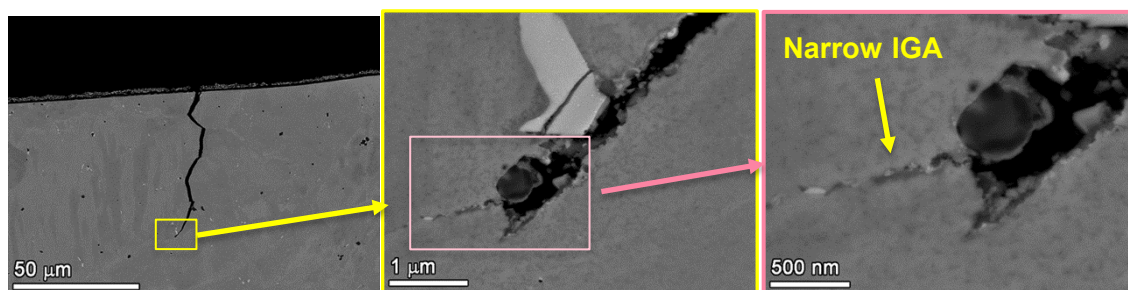


Figure 95. SEM(BSE) of one IGSCC crack ($\sim 40 \mu\text{m}$ long) at various magnifications. In this IN233 cross section this was the only crack observed.

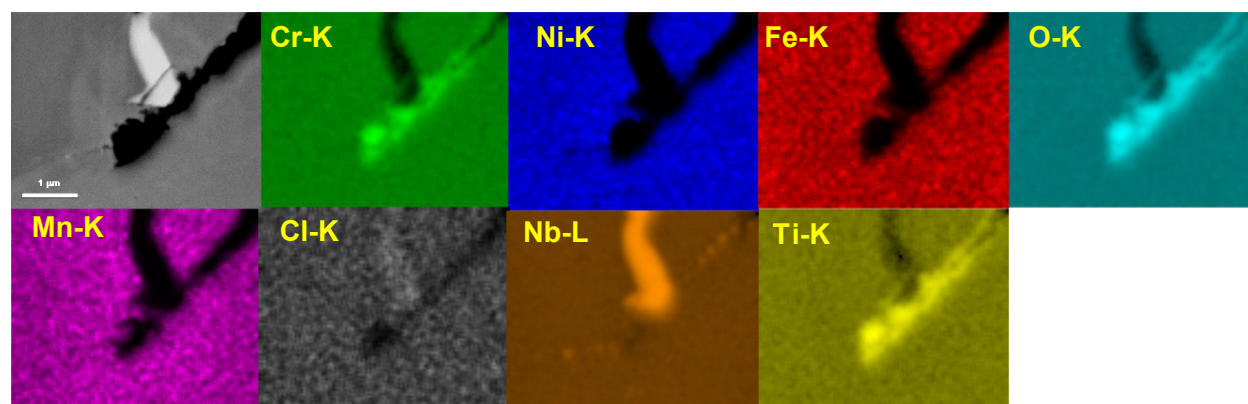


Figure 96. SEM(BSE) and representative EDS mapping of the leading SCC crack tip in IN233.

8.3 EBSD Cross-Sectional Analysis

EBSD analysis was carried out in the cross section of both IN233 and IN169. As shown in Figure 80, the sectioning plane in these two specimens was carefully chosen to intersect large cracks that were found on the surface without affecting the regions where TEM samples were taken. The cross-section morphology of these cracks is shown in the SE maps in Figures 97a and 98a, respectively. It is evident that the depth of these cracks is commensurate with their surface length and opening width. Interestingly, the crack observed in IN169 is already ~ 340

μm deep in the cross section, a depth that is usually considered to be able to result in DCPD detection of SCC initiation. Nevertheless, no indication of SCC initiation was indicated by DCPD after 5,126 hours of exposure, and the surface morphology of this crack remain unchanged between $\sim 3,000$ hours (observed at a test interruption) and when the test was concluded at 5,126 hours. To better understand the difference in SCC initiation and growth behavior, the EBSD analyses were focused on obtaining local orientation information of near-surface grain boundaries with and without cracks in IN169 as well as grain boundaries with SCC cracks in IN233. Mapping near the stalled crack in IN169 was also performed.

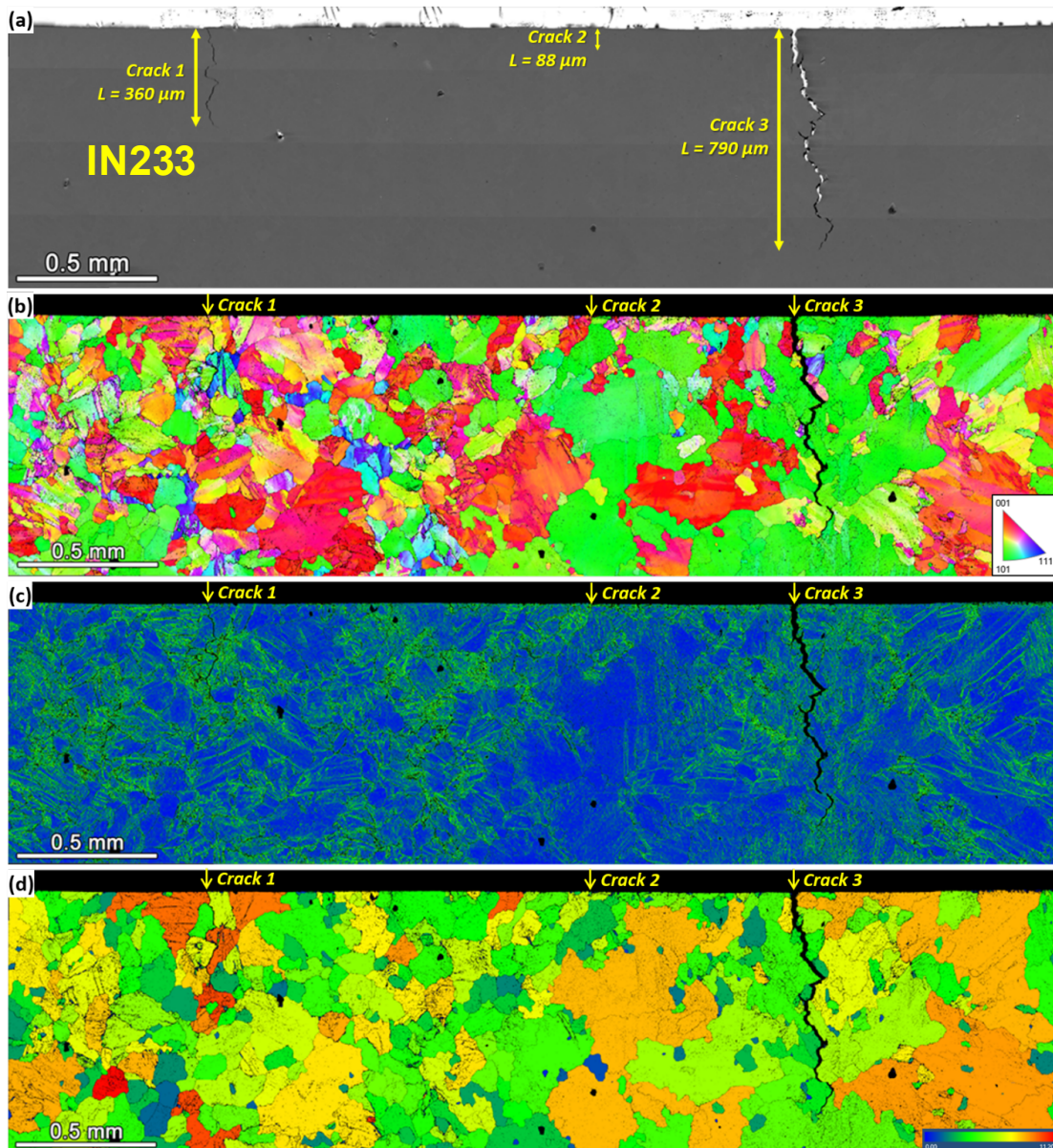


Figure 97. (a) SE, (b) IPF-X, (c) KAM, and (d) GOS maps of the cross-sectional region in IN233 intersecting the primary crack (Crack 3) and two other cracks found on the surface as shown in Figure 80.

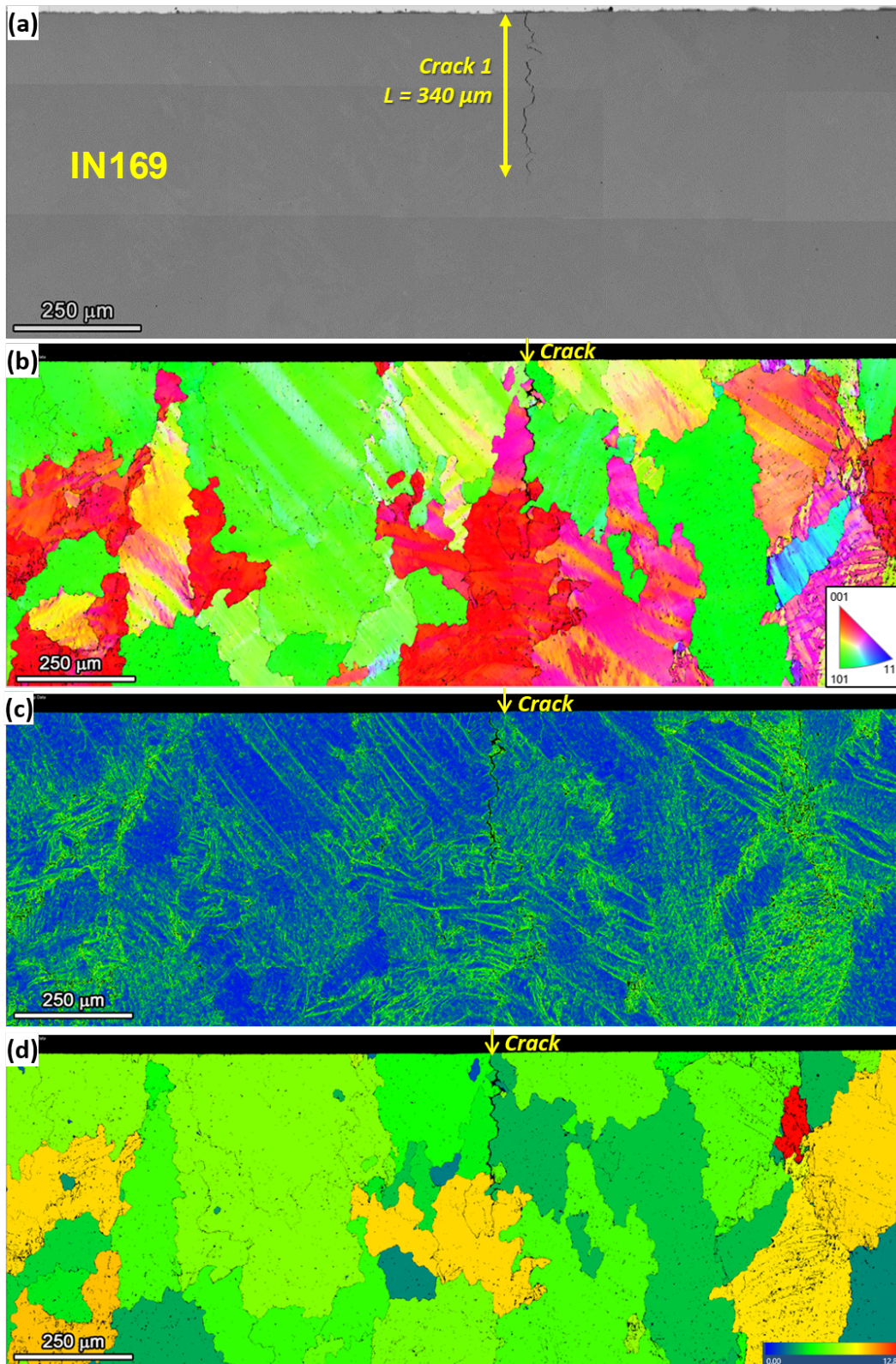


Figure 98. (a) SE, (b) IPF-X, (c) KAM, and (d) GOS maps of the cross-sectional region in IN169 intersecting a large, halted crack found on the surface as shown in Figure 80.

Inverse pole figure (IPF) maps were constructed with respect to the X-axis (i.e., the specimen loading direction) and are shown in Figure 97b and Figure 98b, respectively for IN233 and IN169. The maps define the texture using out-of-plane crystallographic orientation. It is shown that among the three cracks in IN233 and the one crack in IN169, three of them nucleated next to grains that have a [101] direction (assigned with the color of green) parallel to the loading axis. In addition, the primary crack in IN233 (Crack 3) and the crack in IN169 propagated mostly next to grains with the same direction parallel to the loading axis. Because the [101] orientation (as defined here) is the most prevalent orientation in these images, it's unclear if there is any true correlation between this alignment and higher susceptibility to cracking. Note that the magnification for the images of IN169 in Figure 98 is about 2x higher than the images of IN233 in Figure 97, giving the appearance of much smaller grains in IN233 that has a low initiation time. The grains in IN233 are indeed smaller, but not as small as suggested by a comparison of images. Furthermore, the grains observed in the IPF maps of both specimens appear to be equiaxed in general. This is different from the typical elongated shape of solidification grains with a lamellar structure, suggesting the propagation of cracks in these two specimens favor the short axis along multiple solidification grains rather than going along the long axis of the solidification grains.

Figures 97c and 98c show the Kernel Average Misorientation (KAM) maps for IN233 and IN169, respectively. Here local misorientations are presented on a 0-5° misorientation scale as the color changes from blue to red. While mildly elevated misorientations are seen in close vicinity of all the identified cracks, the degree is similar among all cracks and among the two specimens.

The last map constructed for both specimens is the grain orientation spread (GOS) map (Figures 97d and 98d), which visualizes the average value of the orientation spread for each grain with a scale showing increasing GOS from 0 to ~ 12° (blue to red) in both specimens. GOS is a method to describe the degree of strain within a grain. The GOS value is determined by summing the misorientation of each pixel within a grain relative to the average orientation of the grain and then dividing that sum by the total number of pixels in the grain. Higher GOS values represent greater amounts of strain within that grain. This strain can either be a result of elastic or plastic strains. Values higher than one degree are due primarily to plastic strain. In general, IN233 appears to exhibit a higher degree of GOS in comparison to IN169, indicating more strain in the vicinity of the cracks in IN233. The two larger cracks in IN233 are seen to emanate next to grains with an elevated GOS, while the other small crack in the same specimen and the one crack in IN169 did not. While this may suggest that local deformation can promote crack formation, the evidence is insufficient to attribute the very fast SCC initiation of IN233 purely to mechanical properties. Therefore, detailed TEM analyses were performed with a focus on probing local chemistry near the surface of the specimens. The results are presented in Section 8.4.

8.4 TEM/STEM Analysis

As mentioned earlier, the purpose of the TEM/STEM analysis is to evaluate whether any local microchemical or microstructural inhomogeneity is involved in triggering the very low SCC initiation time for IN233. To achieve this, the TEM sampling sites were carefully chosen in both IN169 (long initiation time) and IN233 (short initiation time). As shown in Figure 80, three TEM samples were collected from IN169 on random SGBs far away from the existing cracks. IGA is commonly seen on these SGBs but none exhibited cracking after 5,126 hours of exposure. Thus, it is believed that these SGBs should have a local microchemistry/microstructure with low susceptibility to SCC initiation. In comparison, TEM samples from IN233 were collected from

the end of two smaller cracks in regions adjacent to the primary crack (Figure 99). These regions feature a high density of cracks formed within 50 hours of exposure, thus possibly representing a large number of SGBs with high susceptibility to cracking.

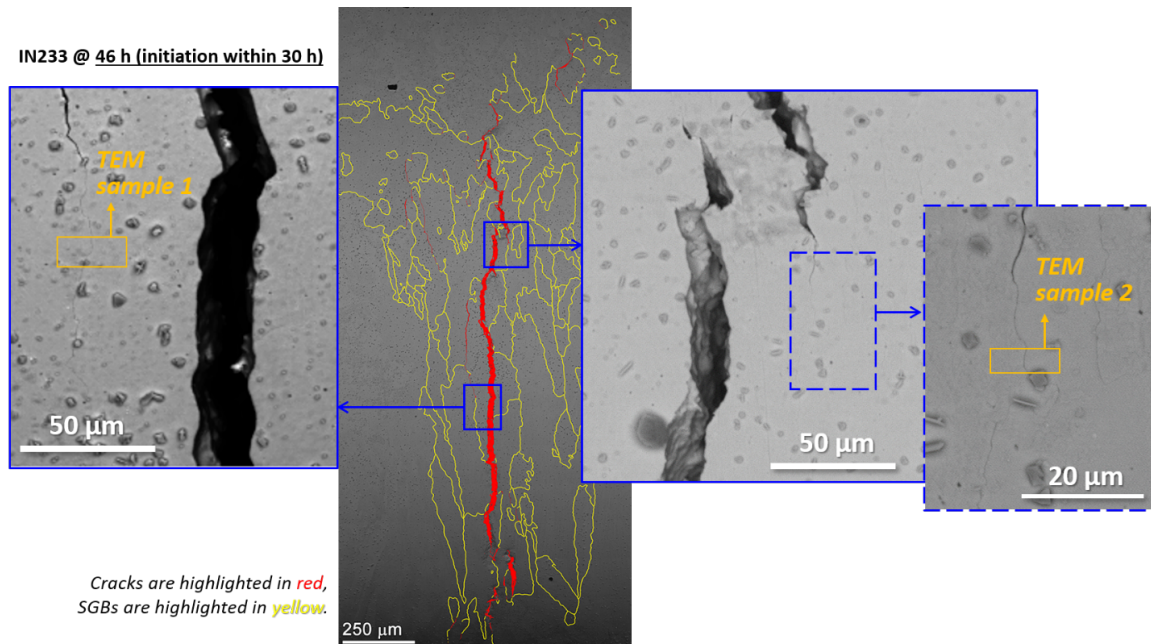


Figure 99. A closer look at the TEM lift-out sampling location in IN233. In the second image to the left, the cracks are highlighted red while SGBs with IGA are highlighted in yellow.

8.4.1 TEM/STEM Analysis of IN233

Sample #1

Figure 100 presents the STEM annular darkfield (ADF) and bright field (BF) low-magnification images of the cross section of an IGA selected from the end of a short crack shown in Figure 99. This FIB foil is from the same location as the data collected in Figure 84. These STEM images show similar IGA depths (~500 nm) as observed in the SEM image from the FIB trench (Figure 84). The analysis of this sample was focused only on the IGA and the grain boundary immediately ahead of the IGA. The roughness at the surface of the sample in Figure 100 does not represent the actual surface as seen in Figure 84. The uneven topography is a result of the FIB preferentially milling past the Pt capping layer. The leading IGA was kept intact, and hence the uneven milling was not considered to be detrimental.

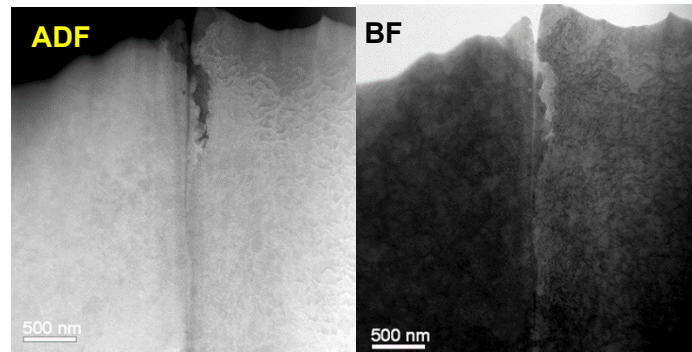


Figure 100. STEM ADF and BF FIB cross section of IN233 showing IGA.

EDS elemental mapping (Figures 101-103) collected at various magnifications of this sample from IN233 indicate the IGA is comprised of discrete Cr-rich oxides as well as continuous Fe-rich oxide. At lower magnification (Figure 101) the top 200 nm of the continuous oxide appears to have traces of Cl and Ti, and closer to the leading IGA of the crack there appears to be Cr carbides as well as Mn sulfides on the order of tens of nanometers. Higher magnification maps (Figures 102-103) provide more detail of the oxidation near the surface as well as the leading IGA. The S signal appears to be consistently observed in the penetrative oxidation of the matrix grains, whereas the Cl and Ti signal are present in the oxide along the center of the IGA. The IGA shows up as a mixture of discontinuous Cr-rich oxide (chromia) and Fe-rich oxide (mostly spinel). Substantial Cr depletion is noted adjacent to the IGA, which is indicative of DIGM but appears to end ~50-75 nm ahead of the leading IGA. The grain boundary itself was noted to be depleted in Cr as seen in Figure 101 where only Cr is depleted along the boundary as opposed to Mn and Fe being slightly depleted in the DIGM region. The absence of Nb-rich precipitates within this grain boundary is interesting considering Alloy 182 should contain 1-2.5 wt.% Nb.

Small (10-25 nm), rounded Cr carbides and MnS are present along the boundary ahead of the IGA as well as near the leading IGA. The dissolution of these MnS precipitates is most likely the cause of the large S signal in the penetrative oxidation near the surface. The Ti signal in the center of the IGA being concentrated near the surface is most likely a function of Ti incorporation from the water (via a titanium preheater in the autoclave loop) and has been observed in almost all SCC tests conducted at PNNL. The presence of the Cl signal, which appears in a similar region to the Ti is not typical. To verify the Cl signal, a local summation of the spectra in the Cl-rich region was performed (Figure 104). The appearance of the Cl K alpha and beta lines confirms that the oxide is enriched in Cl to ~2.9 at.%. With no Cl-rich impurities present within the material, its origin is unknown.

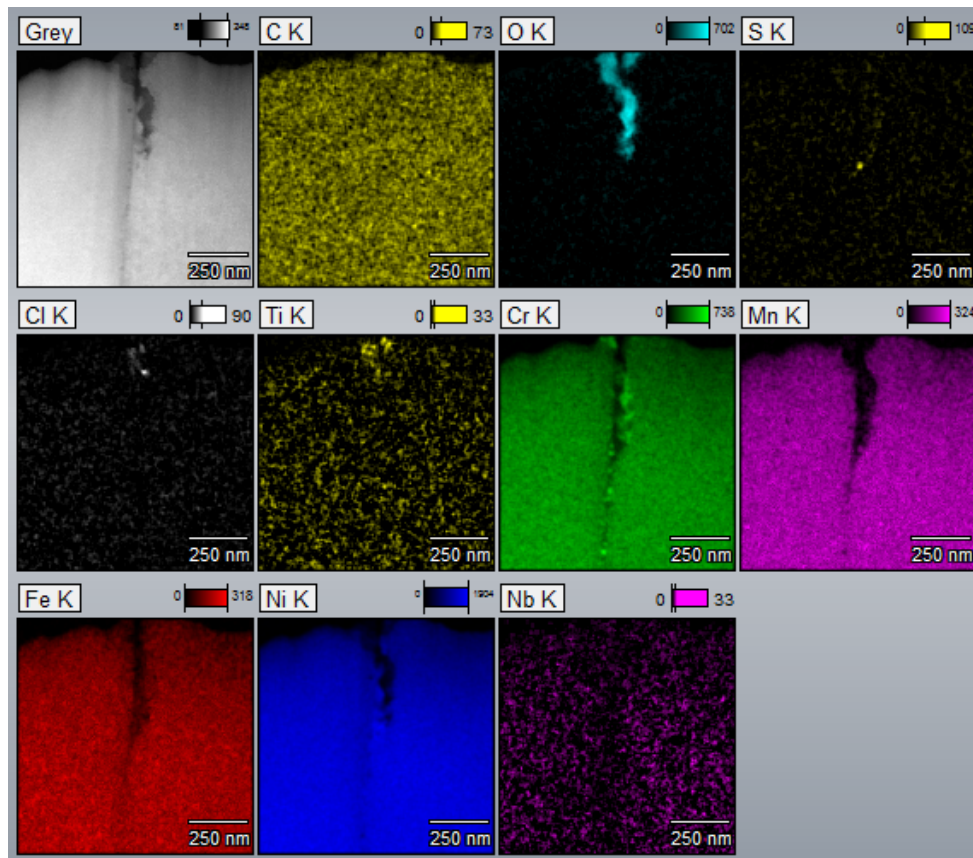


Figure 101. STEM ADF and EDS elemental maps of the near-surface IGA of IN233.

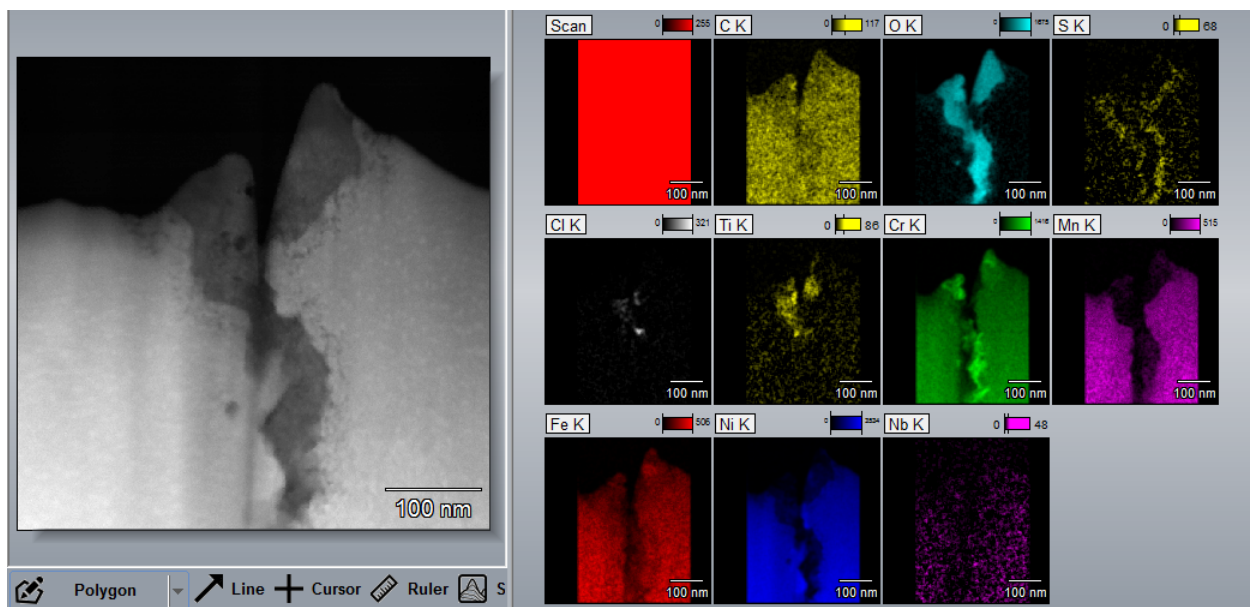


Figure 102. Higher magnification STEM ADF and EDS elemental images of the near-surface IGA in IN233. The Fe and Cr-rich IGA appears to have increased concentrations of Cl, Ti and S.

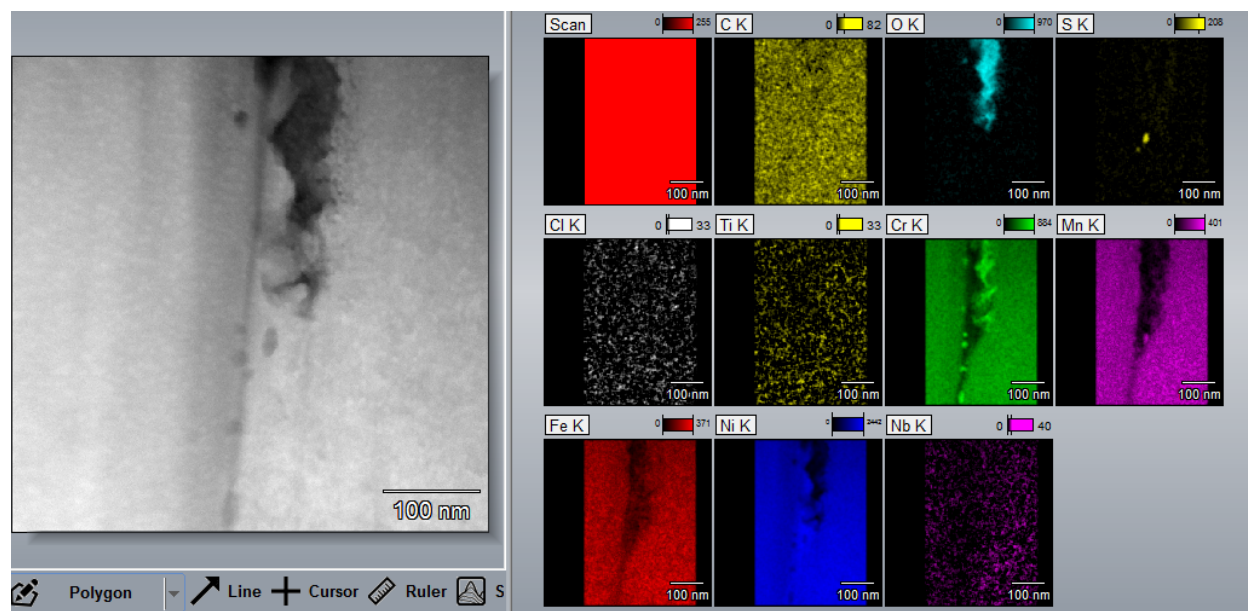


Figure 103. Higher magnification STEM ADF and EDS elemental maps of the leading IGA of IN233 showing the grain boundary is decorated with Cr carbides and manganese sulfides on the order of tens of nanometers.

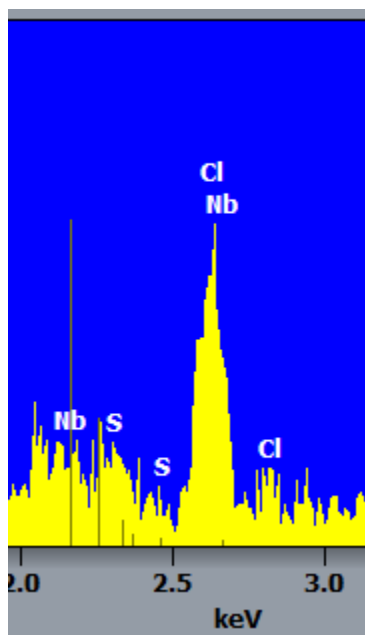


Figure 104. Subset of the EDS spectrum from a summed region containing Cl signal illustrating that the Cl-K edge is not an artifact. The series of vertical gray lines are the theoretical positions of the Nb-L edge, and hence the identification of the Nb at the Cl-K alpha line is a function of the EDS software labeling and does not indicate Nb (i.e., the Nb line at that energy does not follow the theoretical trend).

Sample #2

The second TEM sample in IN233 was prepared from the IGA portion in the immediate vicinity of a large, wide open crack along an SGB (Figure 99) with the cross-section morphology shown in Figure 105. The STEM ADF and BF images show an IGA depth (~300 nm) and a larger, cuboidal feature under the surface not apparently connected to the surface IGA. The high dislocation density is apparent and is commensurate with the level of cold work imparted into these weld materials.

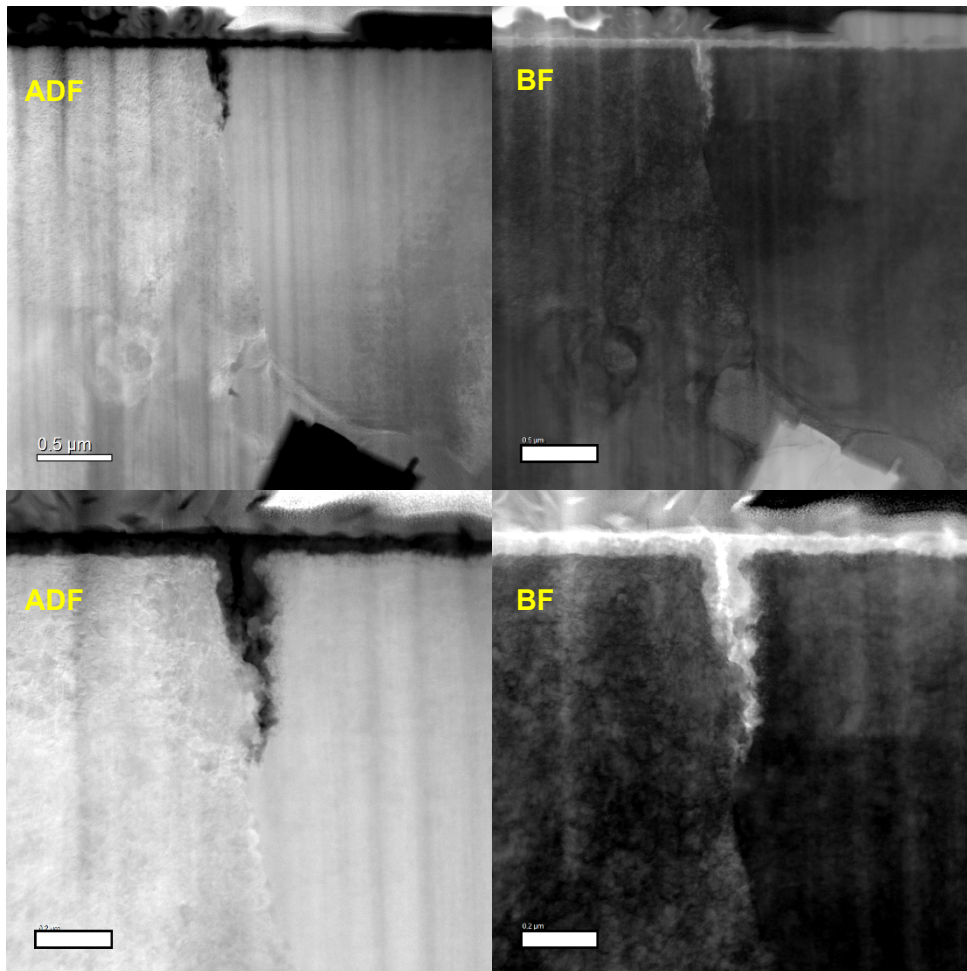


Figure 105. STEM ADF and BF of the cross section of the second FIB lift-out from IN233 showing IGA as well as a large oxide inclusion micrometers from the surface.

EDS elemental mapping (Figures 106-110) provides a compositional overview of the entire FIB lift-out. At lower magnification (Figure 106), the extent of the IGA matches the STEM images shown in Figure 105, and it also identifies the large ($1 \mu\text{m}^2$) cuboidal sub-surface feature as Cr/Ti/Mn/Al-rich oxide with a core shell appearance that is not connected by an oxide path to the surface IGA. This larger oxide appears to have MnS and NbC residue on top (Figure 106), but also appears to connect to the same grain boundary on which the IGA was observed.

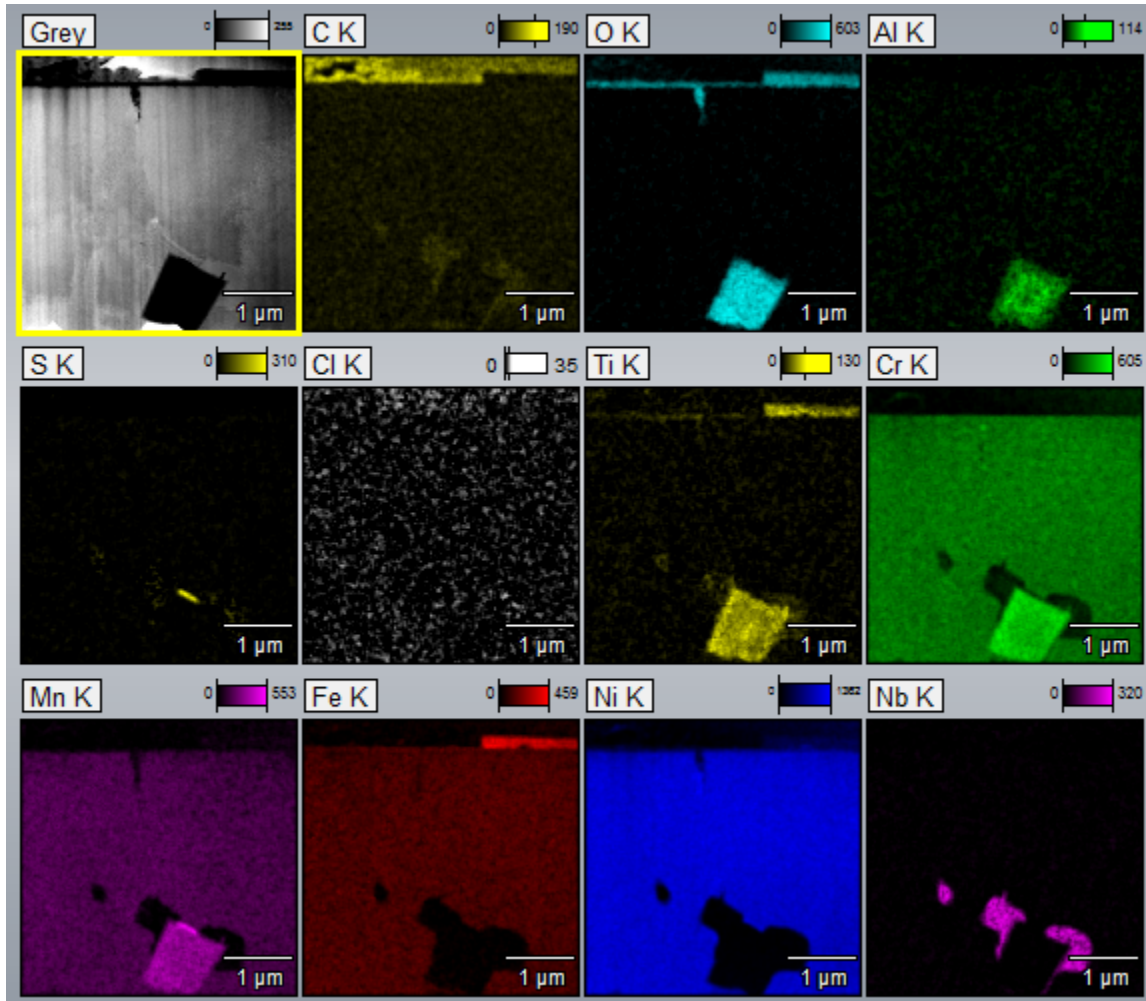


Figure 106. STEM ADF and EDS elemental maps of the near-surface IGA of IN233.

Higher magnification maps (Figure 107) provide more detail into the IGA, indicating the presence of Cl, Ti and S impurities within the IGA. The majority of the S signal was observed within the penetrative oxidation, and Cl and Ti were noted in the central portion of the IGA. The Ti was detected only partially through the IGA, whereas the Cl was noted in the middle. A 40 nm Ni-rich nodule of metal was found within the center of the IGA surrounded by discrete Cr-rich oxide and continuous Fe-rich oxide. Very little concentrated Nb signal was observed at this resolution. A small amount of DIGM was noted just ahead of the IGA.

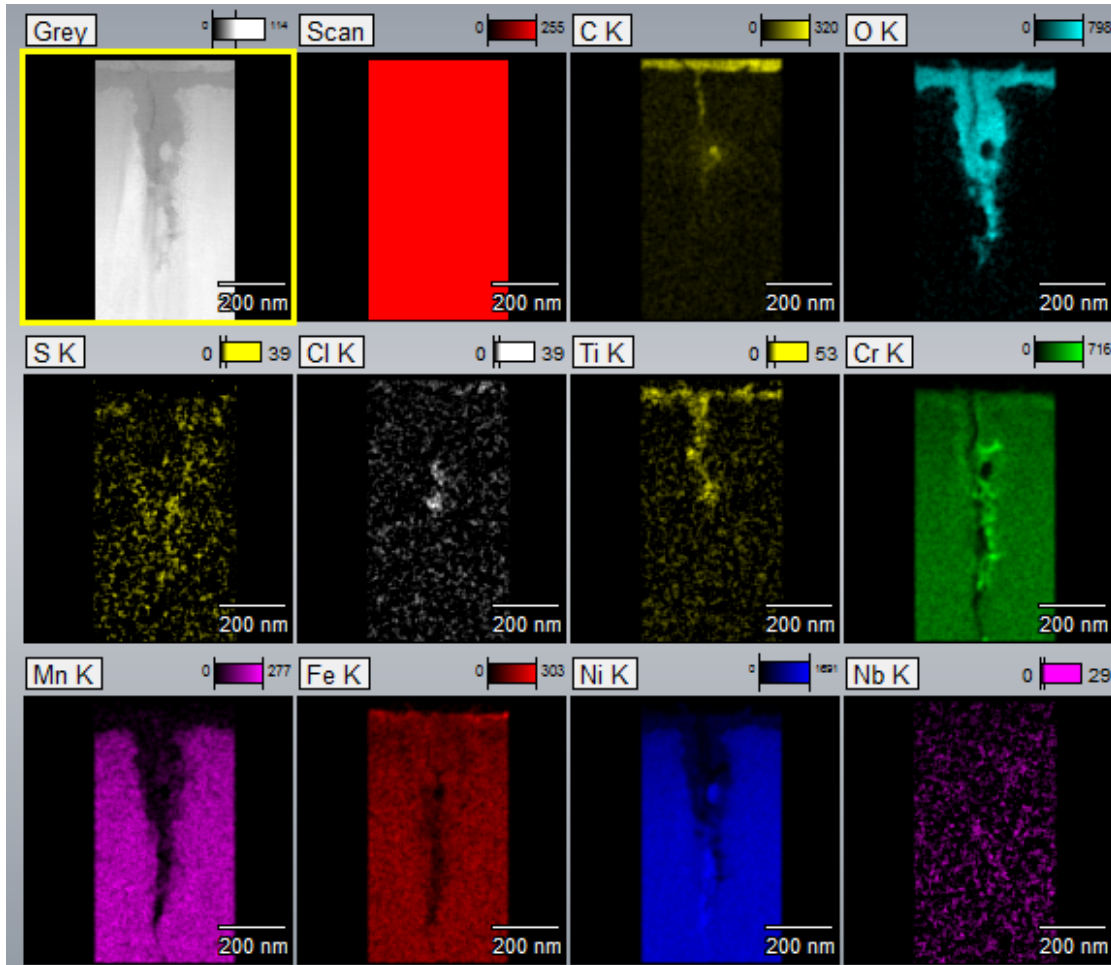


Figure 107. STEM ADF and EDS elemental images of the near-surface IGA in IN233. The Fe- and Cr-rich IGA appears to have increased concentrations of Cl, Ti and S.

Increasingly higher magnification mapping of the central region of the IGA (Figure 108) and the leading IGA (Figure 110) provide more clarity regarding the position of each of the oxides as well as the impurities. The Ni nodule in the middle of the IGA appears to be comprised completely of Ni metal which was confirmed by electron energy loss spectroscopy (EELS) (Figure 109) and atomic column imaging which indicated that the orientation matched the adjacent grain. The nodule was accented by Cl, Ti and S, and as provided in the inset, the Cl was shown to be a real phenomenon. While not observed at lower magnifications, small (5-10 nm) Nb-rich particles were observed within the IGA. These are most likely a function of small, intergranular NbC being dissolved during oxidation. The Cl and the Ti signals appear to end at

the same location within the oxide, suggesting that they both came in through the water and did not originate from this grain boundary.

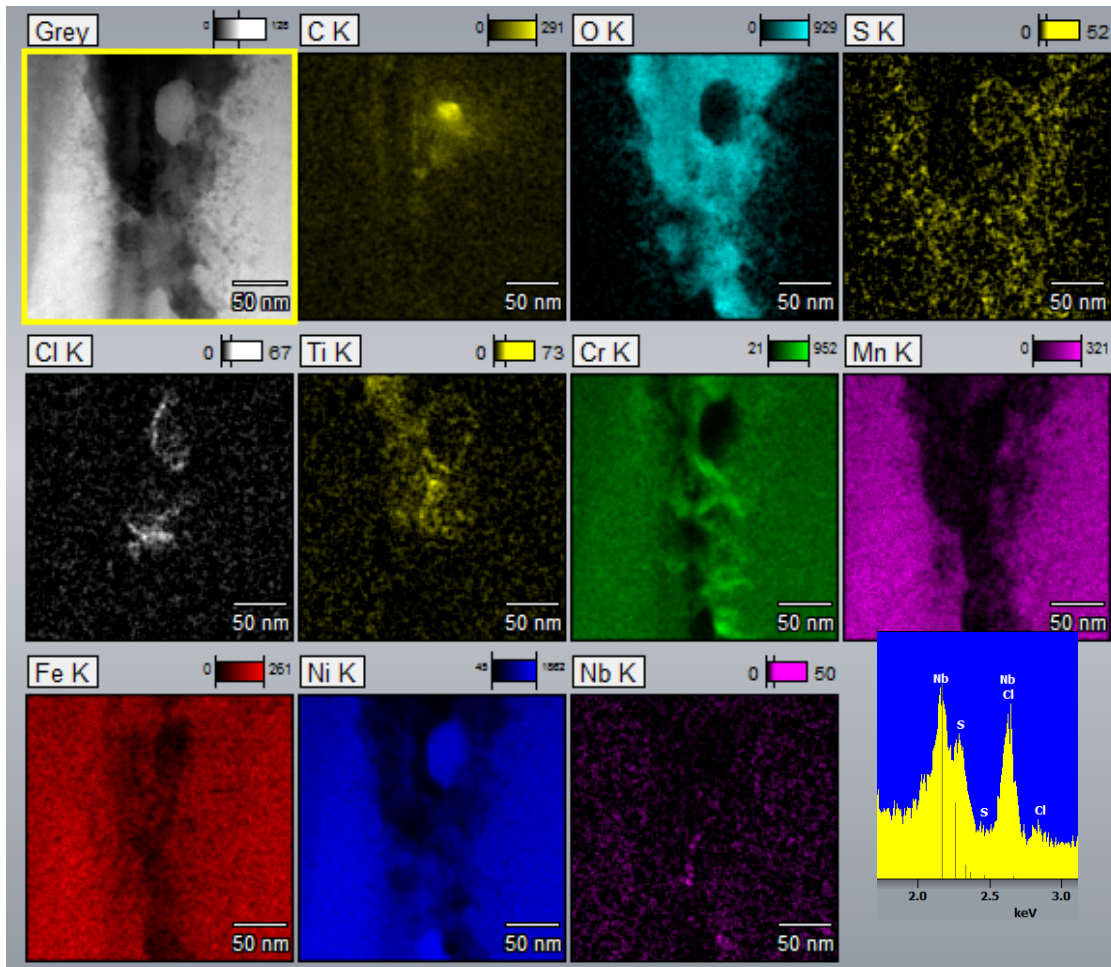


Figure 108. STEM ADF and EDS elemental maps of the middle of the IGA of IN233 showing the distribution of the Fe/Cr oxides as well as Ti, Cl and S impurities. A spectrum of the Cl-K edge summed from the region of high Cl is also provided.

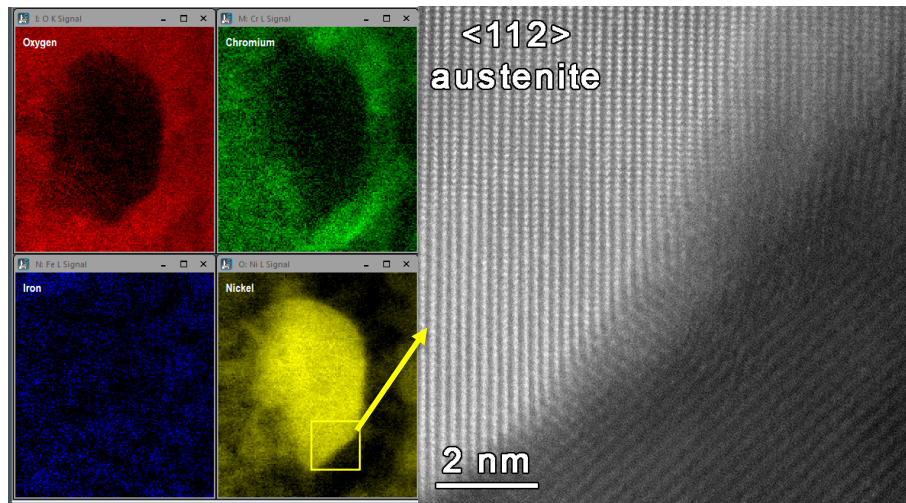


Figure 109. EELS mapping and atomic column imaging of the Ni-rich nodule observed in the middle of the IGA. The atomic column image is flipped from the EELS orientation.

Examination of the leading IGA and the grain boundary ahead (Figure 110) shows a minimal extent of DIGM just ahead of the leading IGA. This is noted by the Cr and Mn depletion in the EDS sum linescan 1. Semi-continuous Cr-rich carbides on the order to 10-20 nm were noted along the grain boundary, although there were no small NbC observed on the boundary. Very small, 1-5 nm, S-rich signals in the form of small precipitates were noted along the grain boundary and are most likely MnS. Sensitization of the grain boundaries was observed as Cr depletion in the absence of the depression of the Mn signal as noted in sum linescan 2. To better understand any possible changes in the local water chemistry, the surface oxidation was examined (Figure 111). Cr-rich penetrative oxidation is noted just below the inner Cr/Fe-rich oxide layer. As in the IGA, S was noted enriched in the penetrative oxidation, but no enrichment of Cl could be detected.

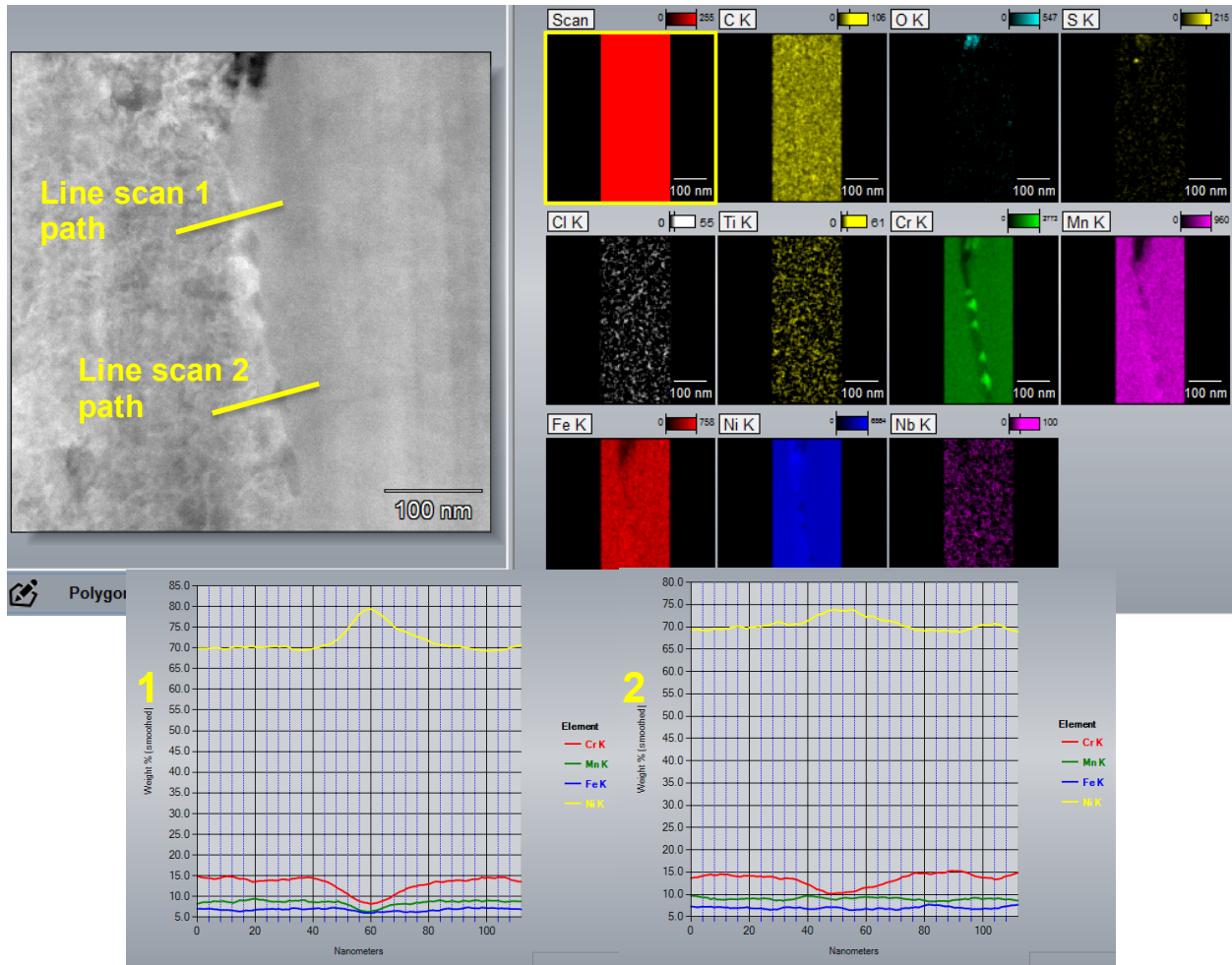


Figure 110. Higher magnification STEM ADF and EDS elemental maps of the leading IGA of IN233 showing the grain boundary is decorated with Cr carbides and manganese sulfides on the order of tens of nanometers. Two line scans were performed across the grain boundary at locations indicated by the arrows in the upper-left figure and the composition variation is shown in the two figures at the bottom.

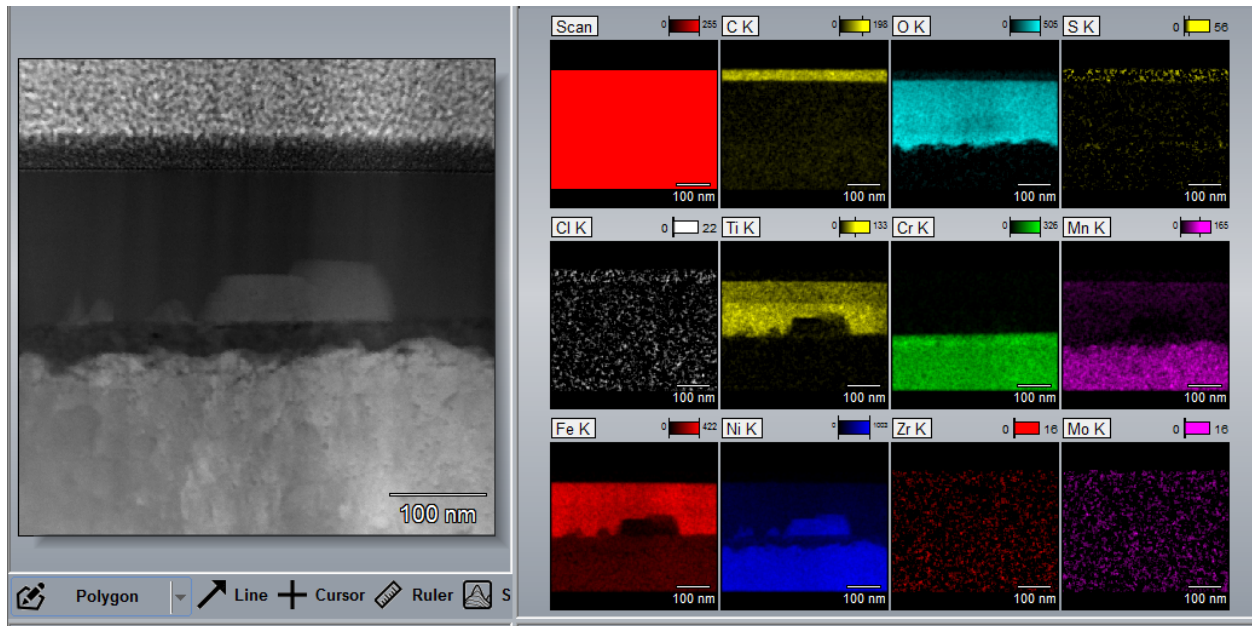


Figure 111. STEM ADF and EDS elemental maps of the surface oxide indicating the presence of S within the penetrative oxidation and the lack of any Cl signal.

Higher magnification analysis of the large, buried oxide was performed to help determine whether it was part of the initial weld microstructure or if it was a product of corrosion (Figures 112-114). As shown in lower magnification EDS maps, the large oxide is rich in Cr, Ti, Mn, and Al with varying Al concentration throughout the oxide. High angle annular darkfield imaging of the oxide confirmed that it had a spinel type structure (with the {001} and {114} poles provided). A thin (50-75 nm) MnS phase was observed deposited directly onto the oxide as well as two larger (micrometer scale) NbC phases which also appeared to envelop the spinel crystal as if they were nucleated on the spinel. Diffraction (Figure 114) from the spinel, the spinel/NbC, and the spinel/NbC/MnS confirms that the MnS and the NbC phases have a cube/cube orientation to the spinel. The absence of any IGA path to this oxide, the size of the oxide, and the fact that phases (MnS and NbC) which are known to be common in this alloy deposited onto the spinel it suggests that this was already in the weld material before testing.

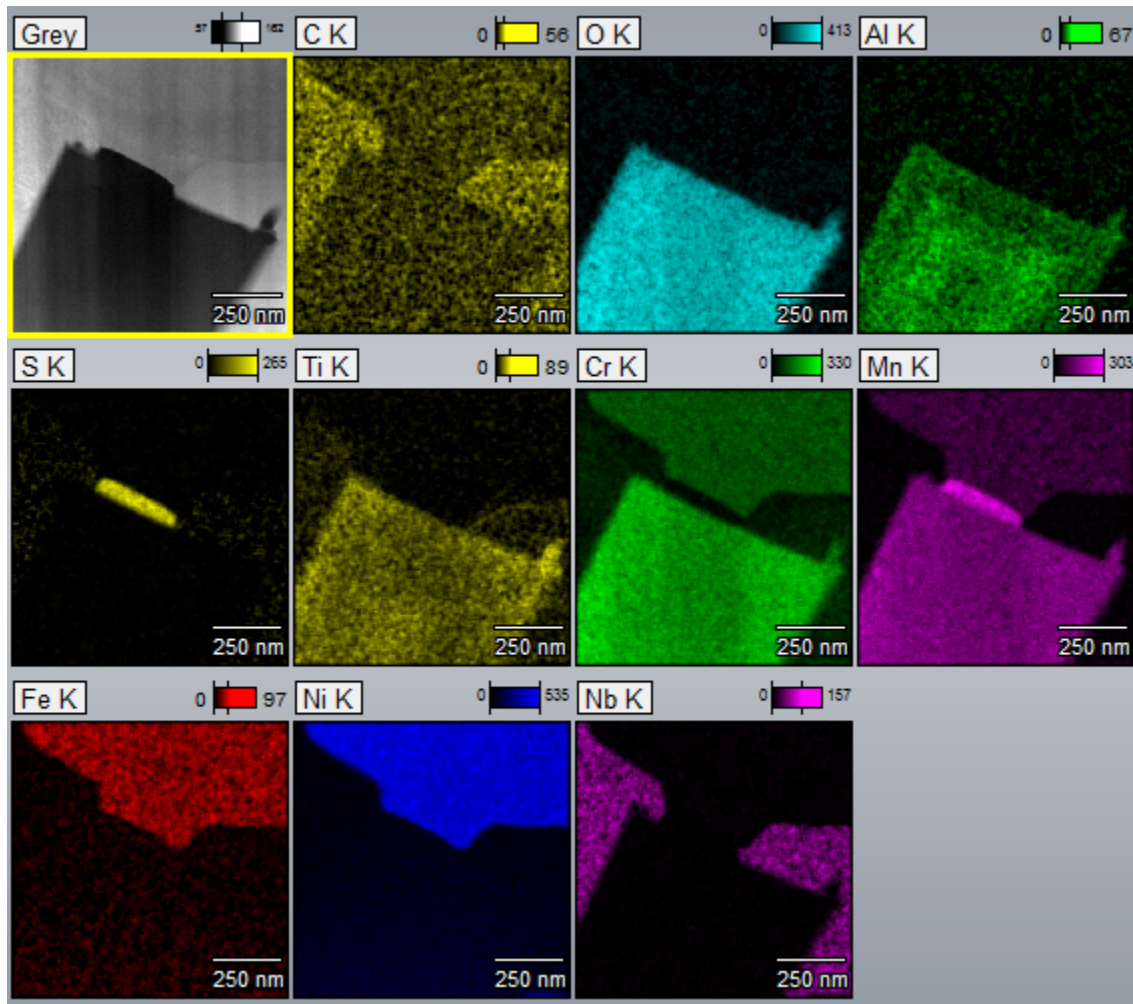


Figure 112. STEM ADF and EDS elemental maps of the sub-surface cuboidal oxide indicating it is rich in Cr, Ti, Mn and Al. MnS and NbC were observed directly adjacent to this large oxide particle.

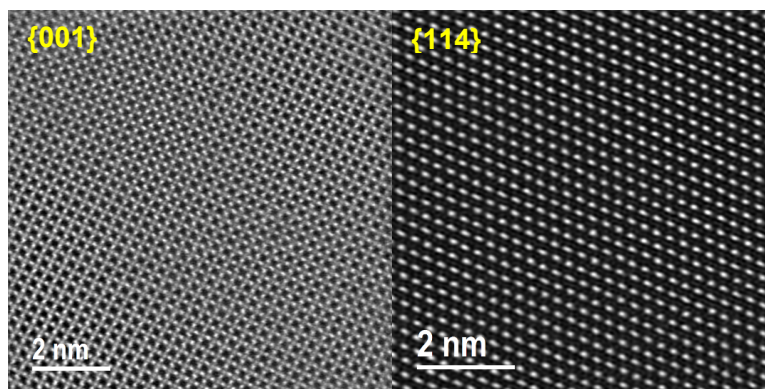


Figure 113. Large, buried oxide in the [001] and [114] orientations (spinel type structure). EDS shows it has a core shell of Al-rich oxide. The small Nb-rich and MnS particles around it are oriented to the oxide suggesting that it was in the melt before solidification. It does not have an orientation relationship to either metal grain.

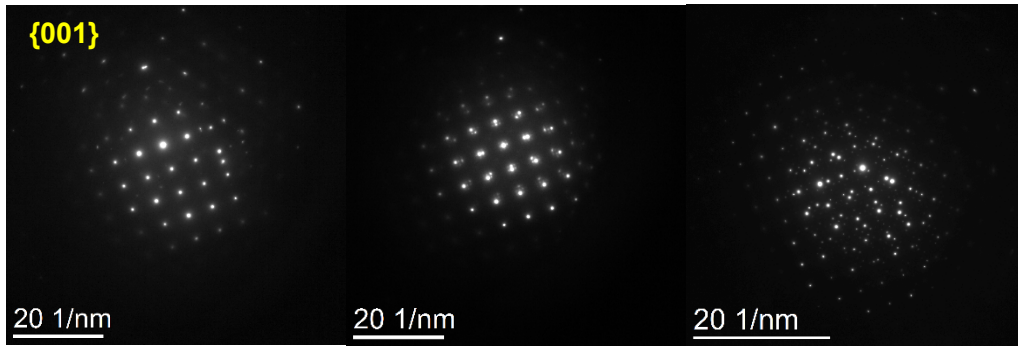


Figure 114. SAD patterns collected from the {001} orientation of the spinel, spinel plus NbC and spinel/NbC/MnS showing that the NbC and MnS are oriented to the spinel.

8.4.2 TEM/STEM Analysis of IN169

Sample #1

The cross-section capture in the first IGA TEM sample (Figure 115) highlights the IGA depth to ~500 nm from the surface. Penetrative oxidation has nearly enveloped the entire IGA except for the last 25-50 nm. The IGA appears to expand 50 nm to either side of the original boundary, suggesting DIGM has occurred. The extremely high dislocation density in the lower grain corresponds to the cold work imparted in these samples before testing.

Elemental mapping of the IGA (Figures 116 and 117) confirms the presence of DIGM. Ni enrichment/Cr depletion adjacent to the intergranular Cr-rich oxide is a hallmark of DIGM. Additionally, the Cr-rich penetrative oxidation occurring across the top layer of the sample and adjacent to the IGA was not observed in the Ni-rich DIGM regions. This is a result of these migrated regions having a much higher Ni content (~18-20 wt.% higher than the bulk), and thus not being susceptible to penetrative oxidation.

The boundaries ahead of the leading IGA (Figure 117) were decorated with elongated Cr and Nb carbides on the order of 50-100 nm long and ~10-20 nm wide. While the IGA dissolves these carbides during growth, a faint Nb signal was observed along the Cr-rich IGA suggesting that Nb is incorporated into the oxide after the carbide is dissolved. There were no other minor impurities (such as Cl) detected through the oxide or along the grain boundary ahead of the oxide.

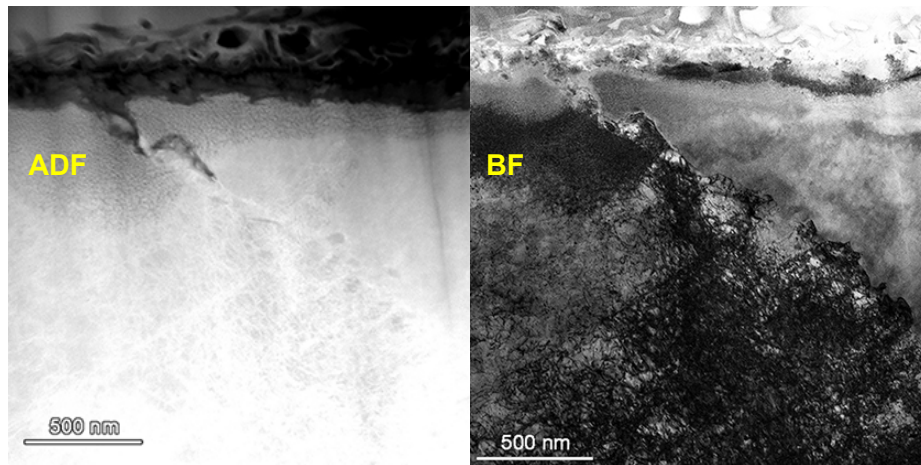


Figure 115. STEM ADF and BF of the 1st FIB cross section of IN169 showing IGA of ~500 nm deep from the surface. The IGA is surrounded by penetrative oxidation until last 50 nm of the IGA.

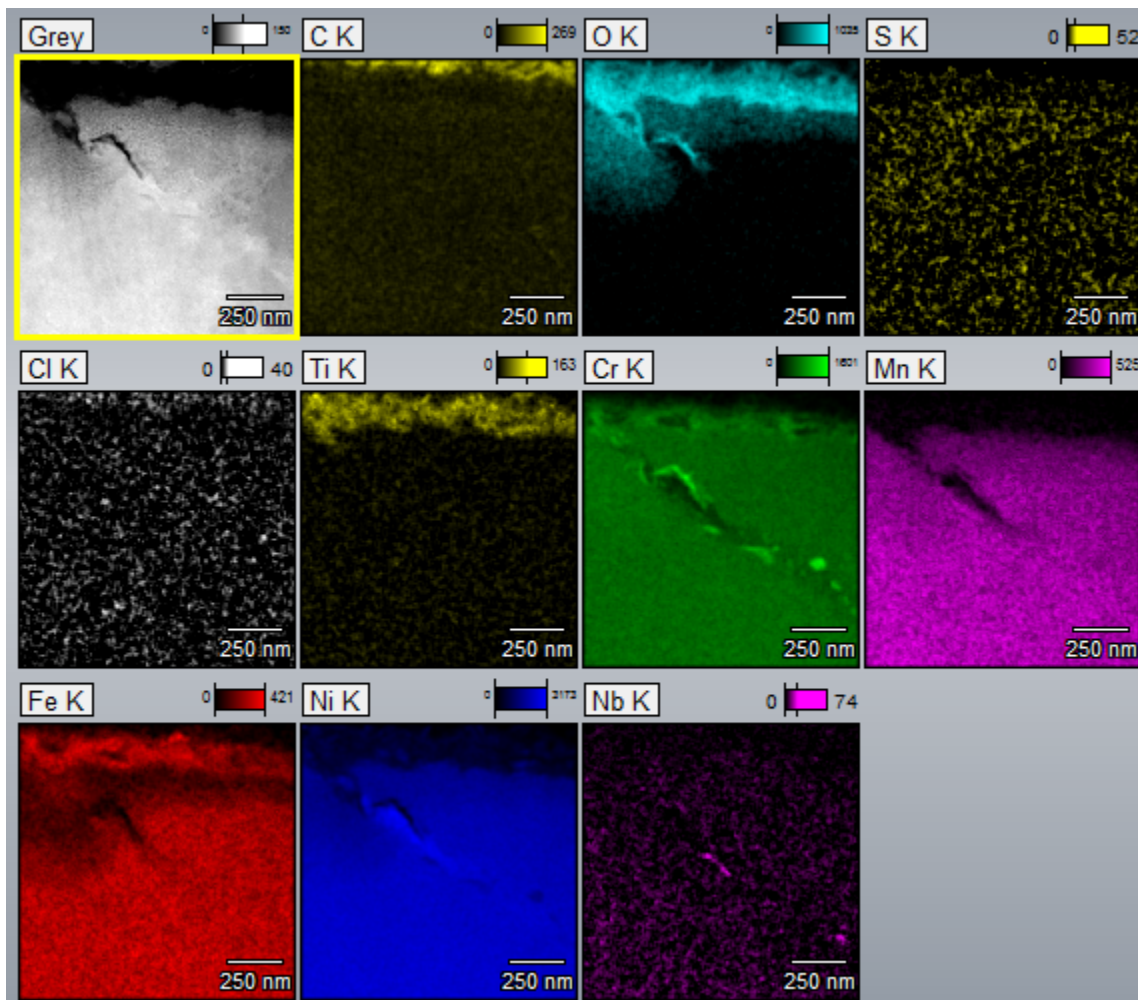


Figure 116. STEM ADF and EDS elemental maps of the near-surface IGA of IN169.

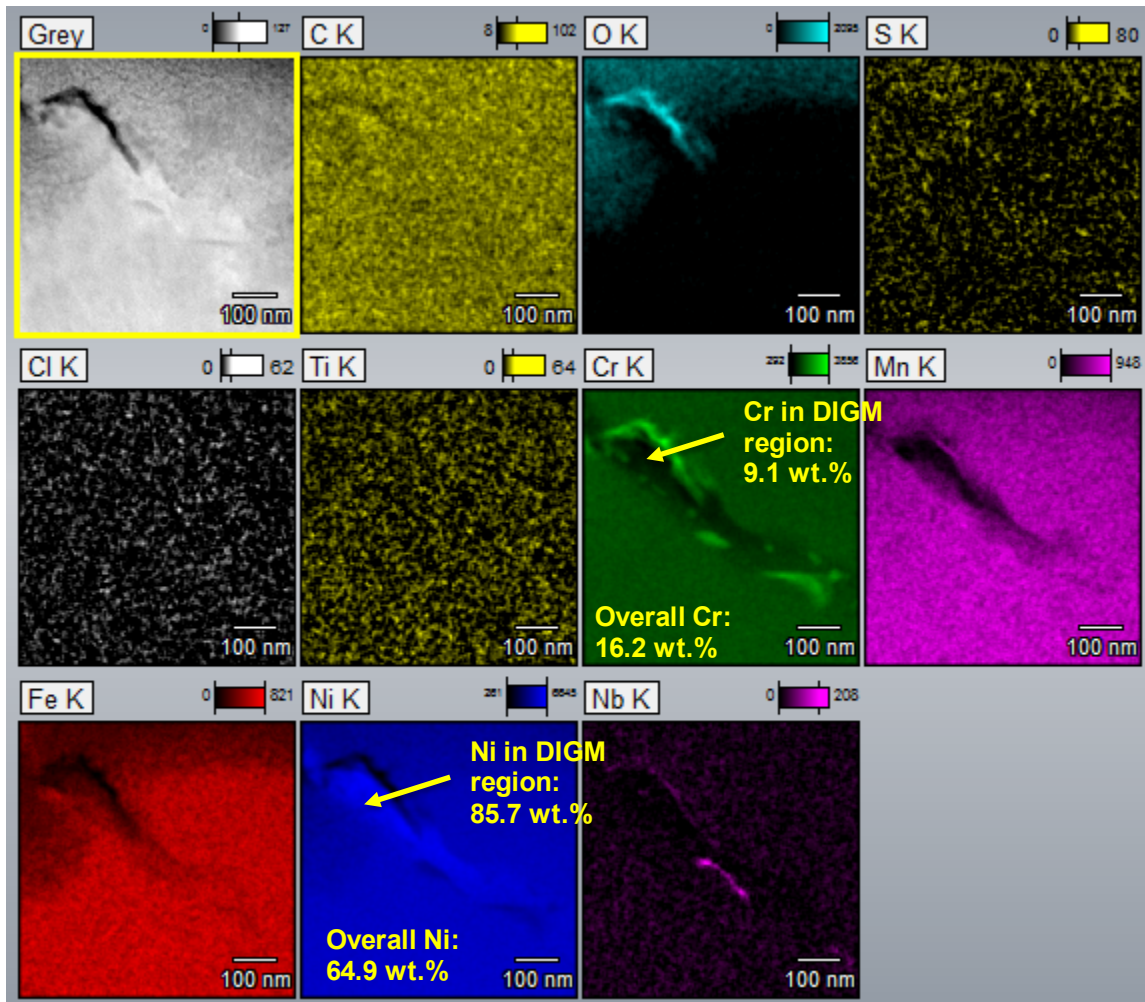


Figure 117. Higher magnification STEM ADF and EDS elemental maps of the near-surface IGA of IN169. Arrows point to regions of DIGM.

Grain boundary analysis micrometers ahead of the leading IGA (Figures 118 and 119) illustrate representative boundary microstructures for the Alloy 182 weld metal in IN169. The boundary is decorated with small (~50 nm in size), semi-continuous chromium carbides and larger (~100 nm in size), discrete NbC. In Figure 118 the boundary is observed off edge as noted by the width of the NbC as compared to the thin, elongated NbC in Figure 117. When the boundary was tilted on edge (Figure 119) a region of grain boundary without Cr carbides was observed, and the level of sensitization could be measured. The Cr content appears to drop from 15-16 wt.% in the bulk down to ~9 wt.% in this region.

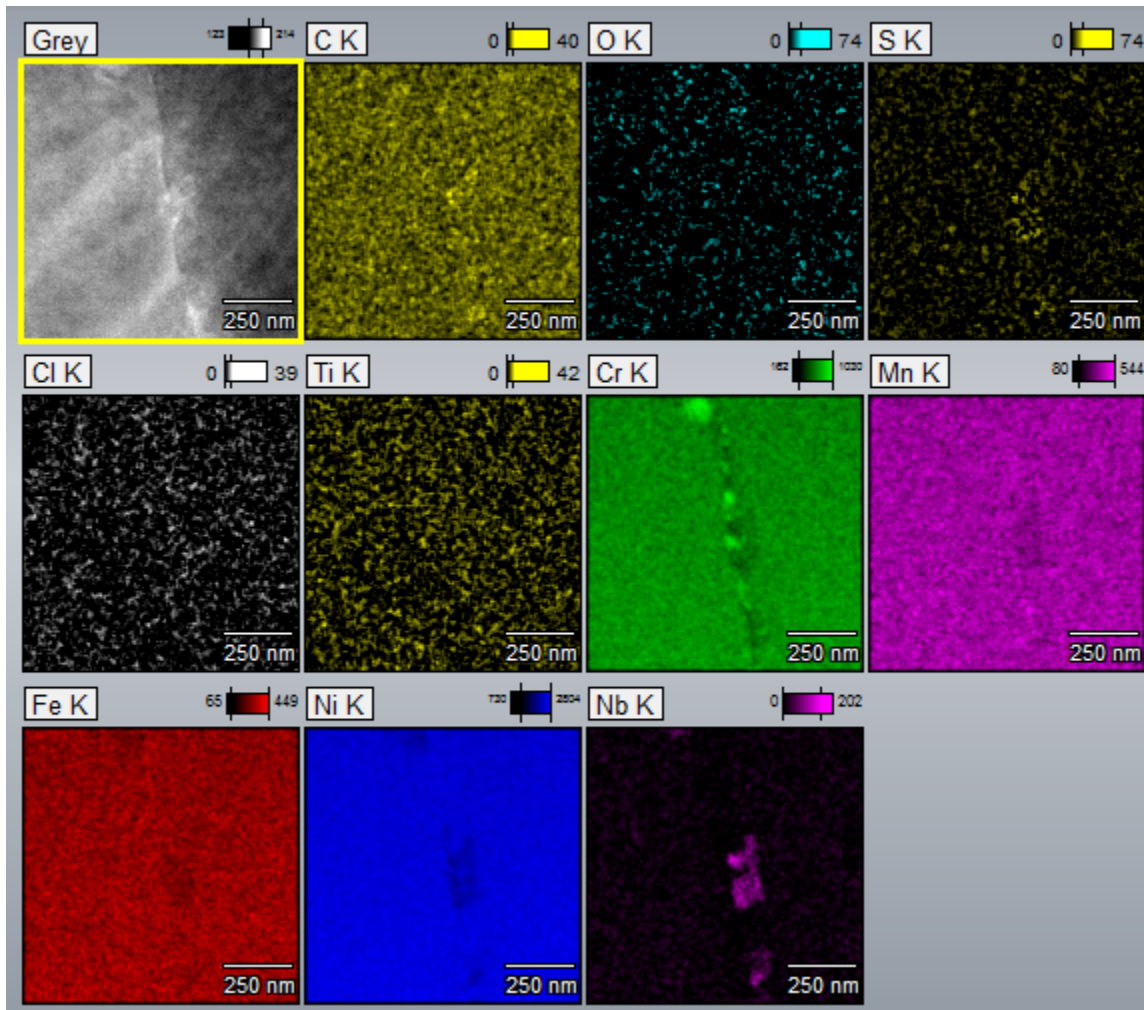


Figure 118. STEM ADF and EDS elemental maps of the grain boundary ~1-2 μm ahead of the leading IGA showing minor Cr depletion, Cr and Nb carbides, and no apparent segregation of impurities such as Cl.

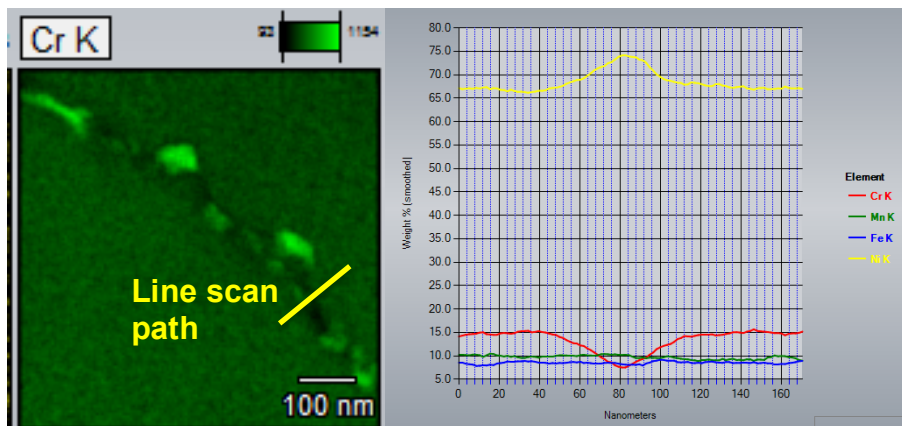


Figure 119. Cr-K elemental map of a representative grain boundary micrometers ahead of the IGA showing sensitization.

Sample #2

A second FIB lift-out of IGA identified on the surface of IN169 was extracted from the specimen, and Figure 120 highlights this IGA depth to ~600-700 nm from the surface, of which penetrative oxidation has nearly enveloped the entire IGA except for the last 200 nm. The IGA appears to migrate 100 nm to either side of the original boundary, suggesting grain boundary migration has occurred. The extremely high dislocation density in the lower grain corresponds to the cold work imparted in these samples before testing. EDS elemental mapping (Figures 121 and 122) of the entire grain boundary as well as near the leading IGA, respectively, illustrates the grain boundary carbides and the grain boundary migration due to diffusion of Cr to the surface. No Cl, Ti or S were detected in the oxide or along the boundary. The spurious S signal from the NbC in Figure 121 is a function of the sample thickness in this region as the Nb and S overlap. While DIGM was observed in this sample, it can be seen in Figure 122 that the carbide arrested further migration.

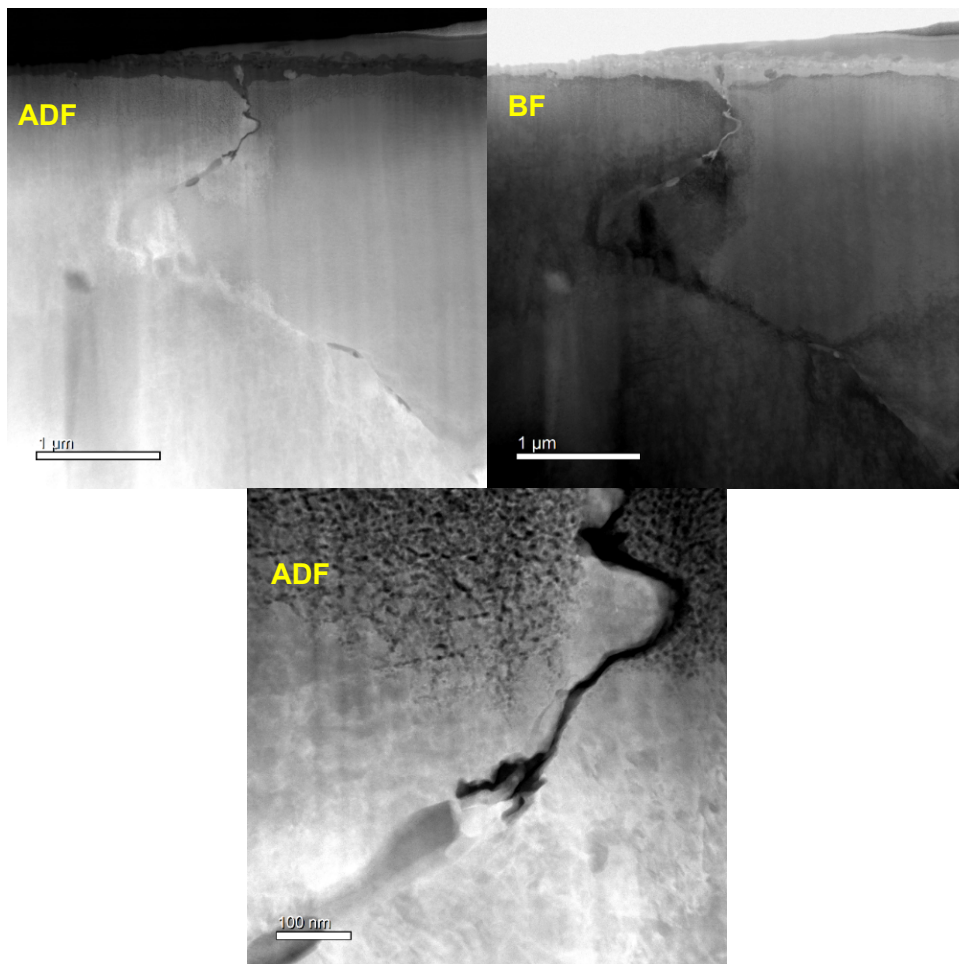


Figure 120. STEM ADF and BF of the 2nd FIB cross section of IN169 showing IGA of ~600-700 nm deep from the surface. The IGA is surrounded by penetrative oxidation until last 200 nm of the IGA.

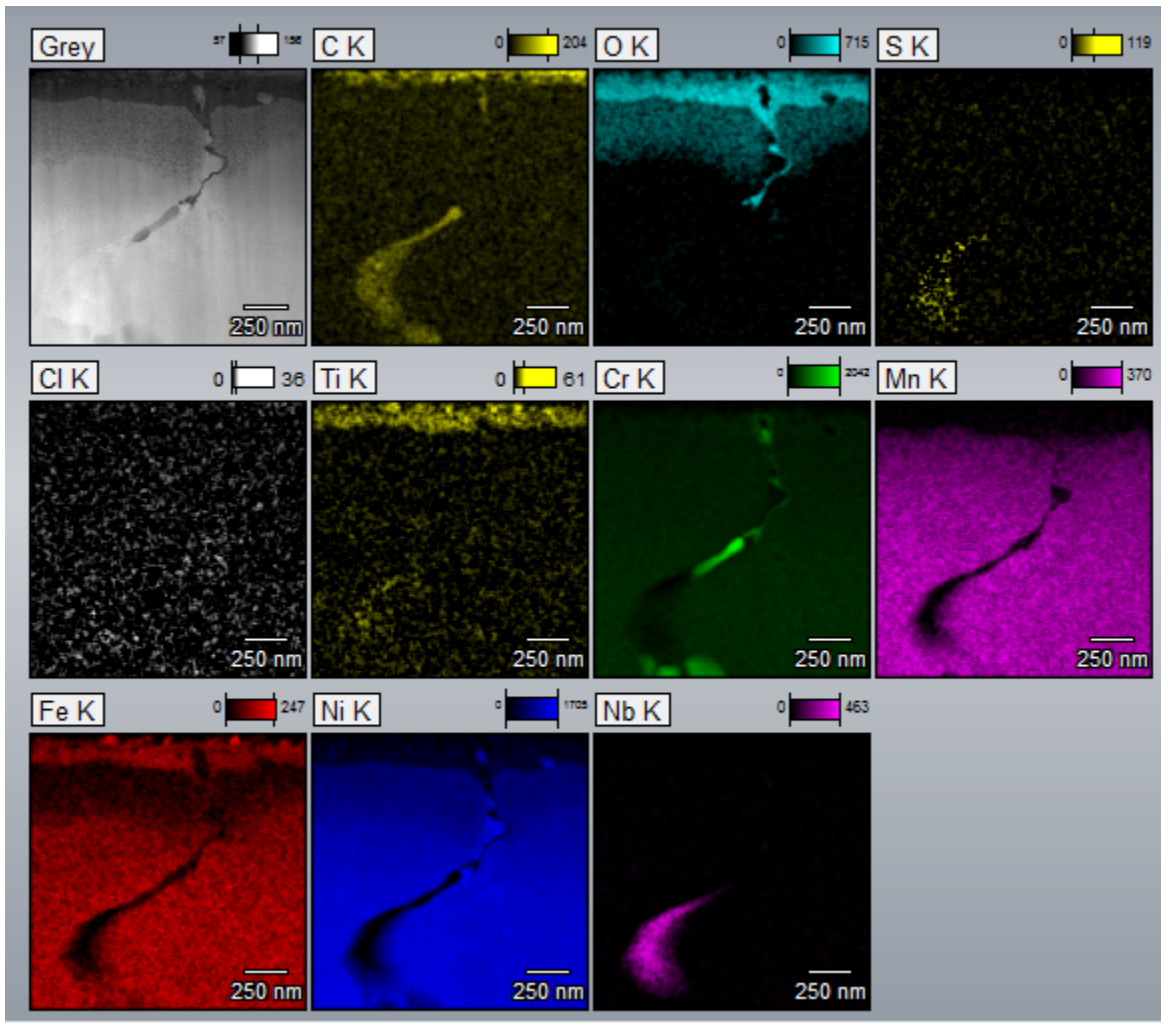


Figure 121. STEM ADF and EDS elemental maps of the near-surface IGA of IN169.

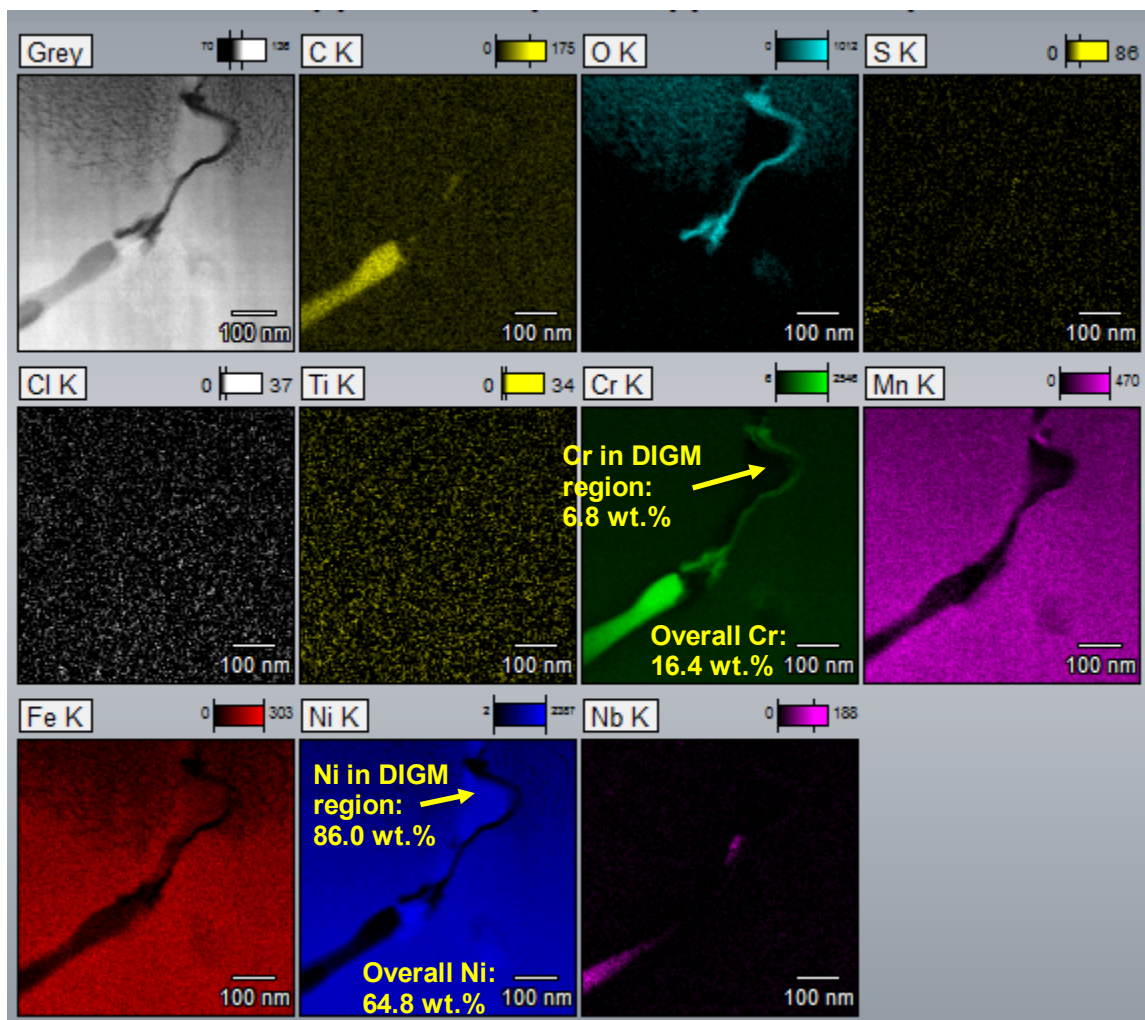


Figure 122. Higher magnification STEM ADF and EDS elemental maps of the near-surface IGA of IN169 showing the leading IGA front ending near a Cr carbide.

Sample #3

The third FIB lift-out of IGA identified on the surface of IN169 was performed. Figure 123 highlights the IGA depth to ~600 nm from the surface, of which penetrative oxidation has nearly enveloped the entire IGA except for the last 200 nm. The IGA appears to extend 75 nm to either side of the original boundary, suggesting grain boundary migration has occurred with the IGA following it. It should be noted that in all three samples from IN169, the IGA is slightly deeper than that observed in the two samples from IN233 (300-500 nm in IN233 vs. 500-700 nm in IN169), likely due to the much longer exposure of IN169 in high temperature water. In addition, the penetrative oxidation in IN169 was located nearly as deep as the IGA. This suggests that the IGA has slowed down significantly, if not stopped, during the exposure, which allowed the penetrative oxidation to reach similar depths. EDS elemental mapping (Figure 124) of the entire grain boundary as well as near the leading IGA illustrates the grain boundary carbides and the grain boundary migration due to diffusion of Cr to the surface. No Cl, Ti or S were detected in the oxide or in along the boundary. While DIGM was observed in this sample, it can be seen in Figure 124 that while Cr, Mn and Fe depletion are present ahead of the leading IGA, the carbide arrested any further migration.

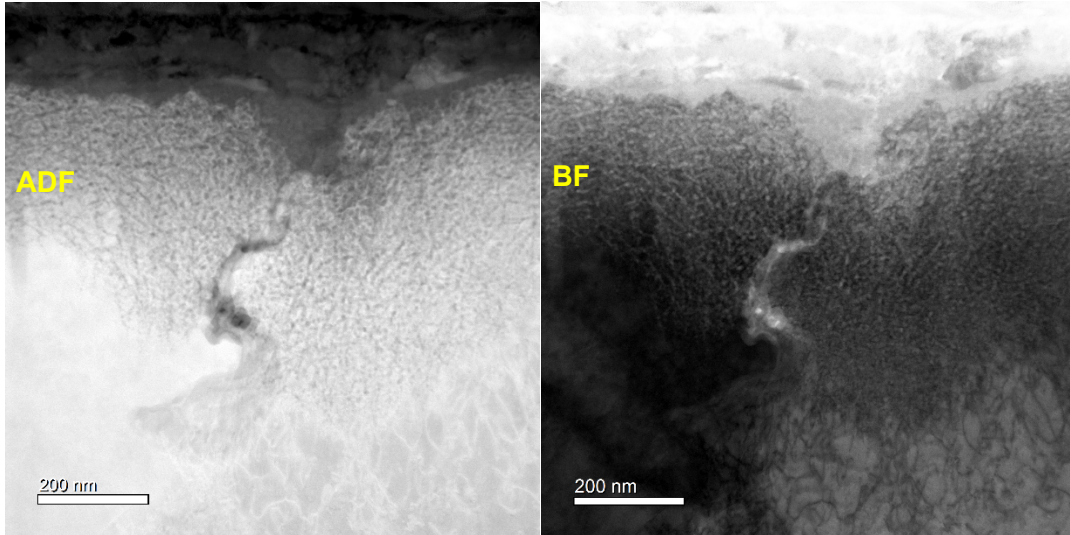


Figure 123. STEM ADF and BF of the 3rd FIB cross section of IN169 showing IGA of ~600 nm deep from the surface. The IGA is surrounded by penetrative oxidation until last 200 nm of the IGA.

In addition, a secondary TG inclusion that is micrometers away from the IGA was noted (Figure 125). This inclusion was shown to be polycrystalline with small, dark features within the metal matrix. Oxidation appearing as dark contrast adjacent to the inclusion was also noted. EDS mapping of this inclusion is shown in Figures 126 and 127. The data shows that while the metal is almost entirely comprised of Ni, at higher resolution the dark spot observed in the ADF images show that these are small (10-20 nm) Cr/Mn/Ti-rich oxides. The Cr-rich oxide cap surrounding the Ni-rich metal region is a chromia film. There does not appear to be a grain boundary below the Ni-rich region, and with the presence of small, spinel-like oxides within the Ni-rich region, it suggests this may have been a foreign inclusion near the surface during the production of the weld.

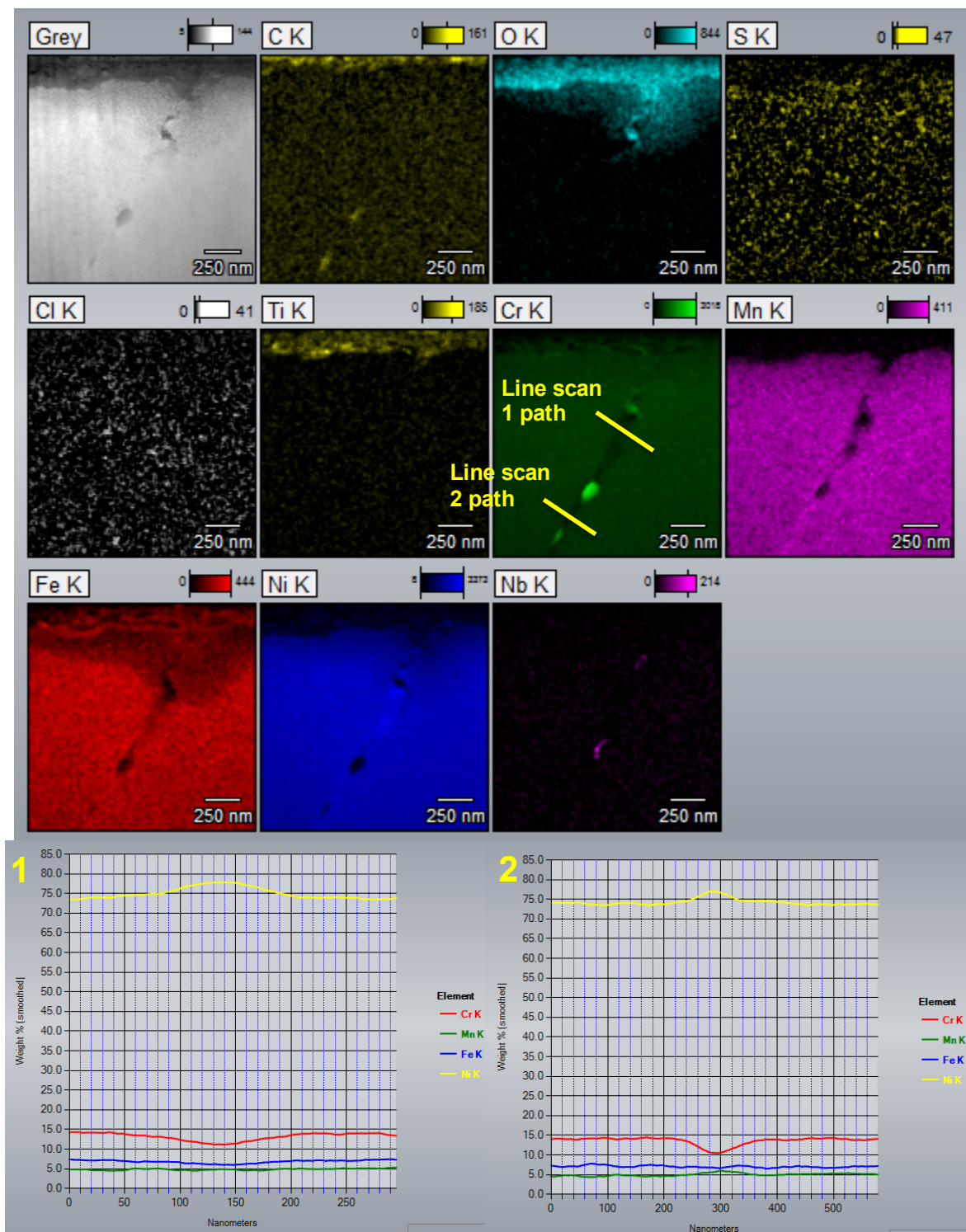


Figure 124. STEM ADF and EDS elemental maps and line scans of the near-surface IGA of IN169.

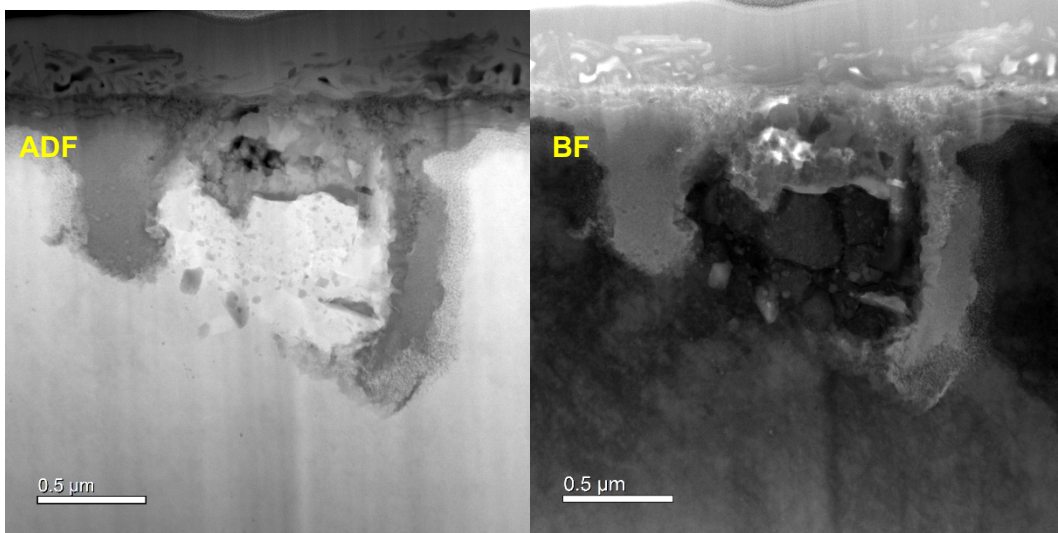


Figure 125. STEM ADF and BF of a TG inclusion near the IGA intersecting the surface.

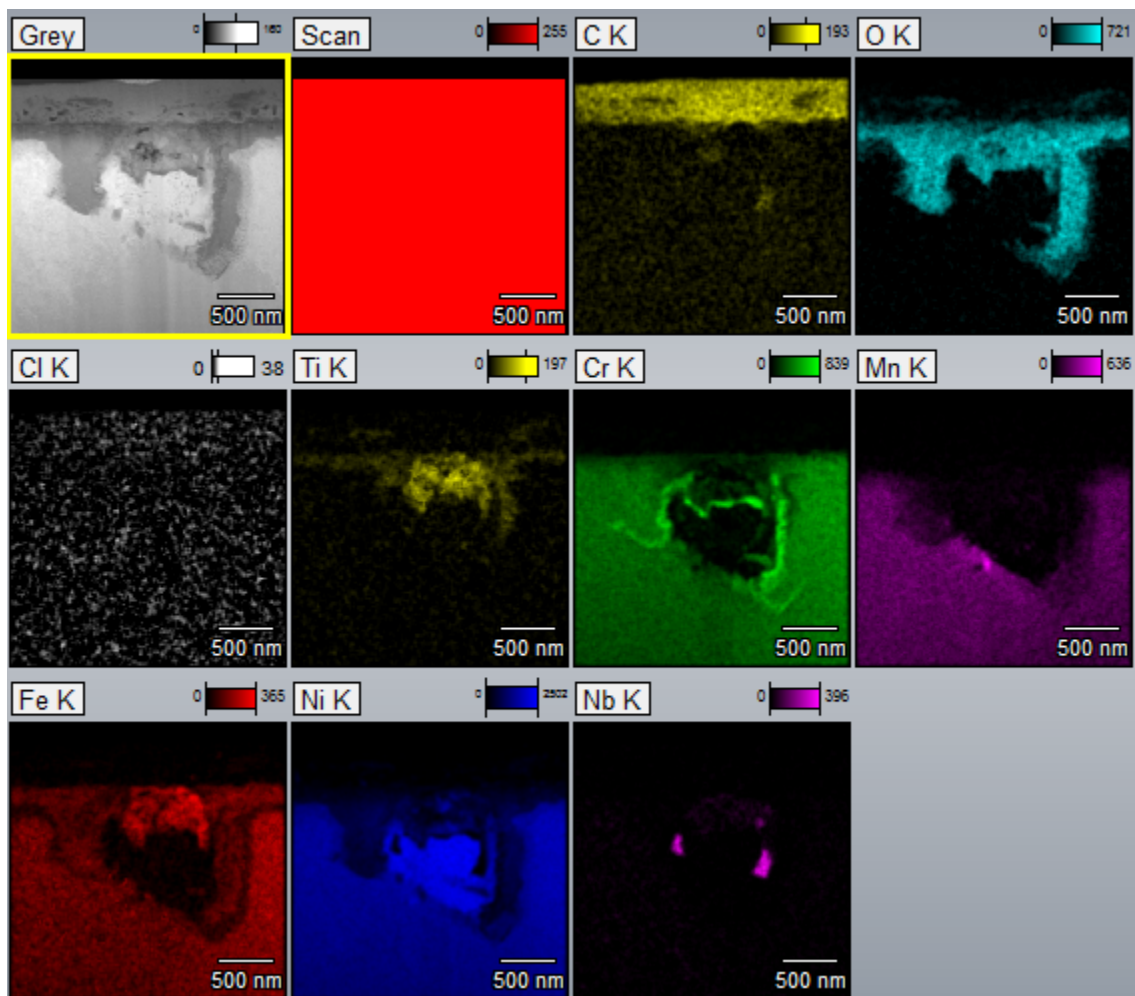


Figure 126. STEM ADF and EDS elemental maps of the TG inclusion near the surface IGA of IN169.

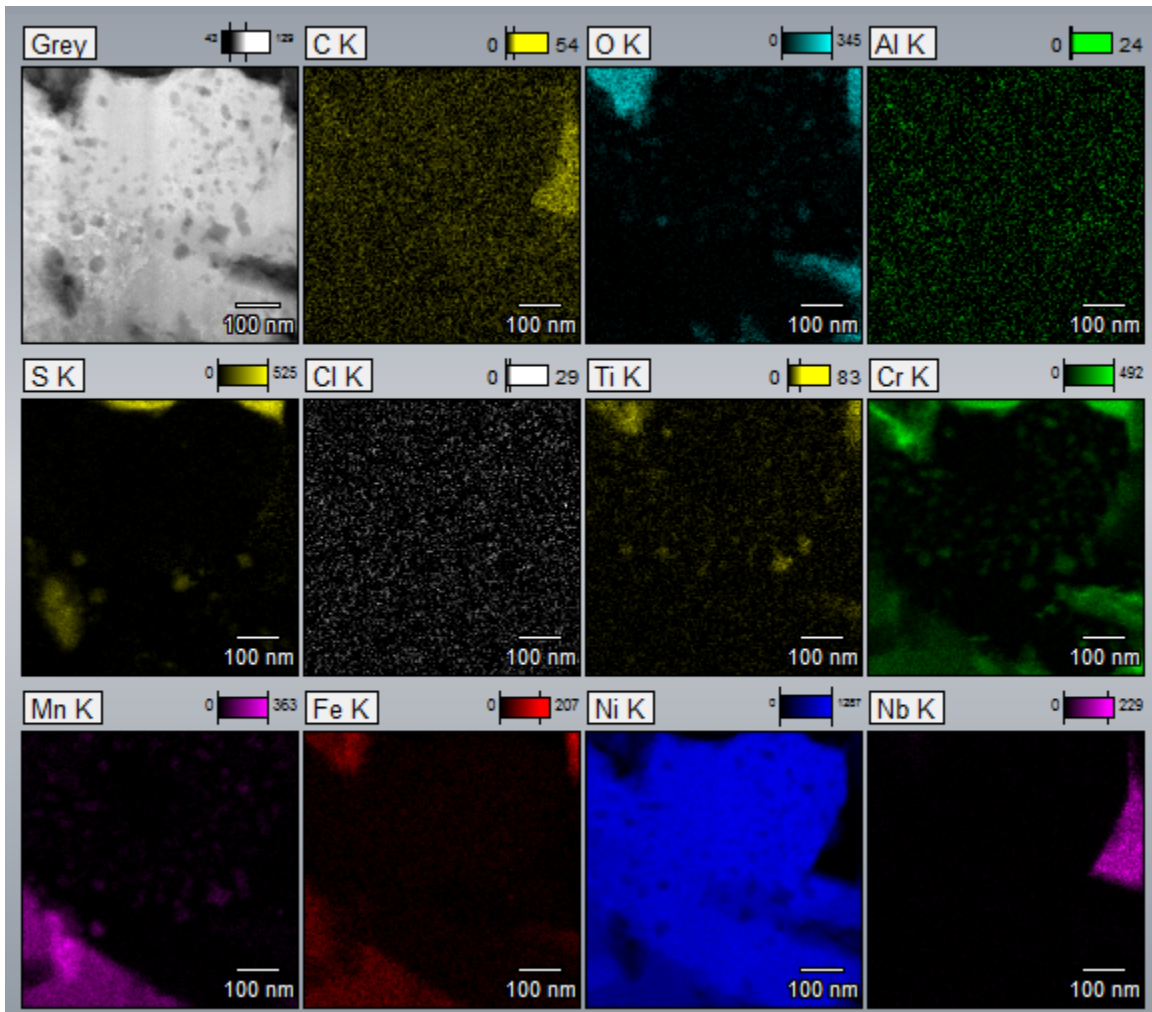


Figure 127. Higher magnification of the Ni-rich portion of the STEM ADF and EDS elemental maps of the TG inclusion near the surface IGA of IN169.

8.5 Summary of Comparisons

In summary, a preliminary study has been carried out on two 15% CF Studsvik Alloy 182 specimens IN233 (initiated within 30 hours) and IN169 (no DCPD-indicated SCC initiation after 5,126 hours of exposure) to investigate the cause of low SCC initiation times in Alloy 182. SEM and TEM analyses were performed in multiple regions of each sample. Cross-section examinations were carried out in the SEM to document weld defect morphology and distribution and to investigate grain orientation and deformation via EBSD. Regions of IGA either near the primary crack in IN233 or random areas far away from existing cracks in IN169 were selected for site-specific FIB cross-sectional lift-out for TEM analysis. The major differences between IN233 and IN169 are as follows:

- A slightly higher density of pre-existing weld defects seems to exist in IN233. In at least a few locations in the cross section of IN233, sub-surface voids were detected. Both TG and IG voids appeared to have formed during weld solidification. Voids were observed to be on the order of millimeters in size. IG defects were smaller (tens of micrometers in scale) and existed as isolated features and in series, resulting in a postage stamp appearance that

linked up to 20 μm in one case. When present on the surface, this latter type of defect has been associated with SCC initiation based on previous experience and should be readily observable by SEM surface examination prior to the start of the test. However, no such pre-existing defects were observed in the pre-test SEM surface examination of IN233, thus reducing the likelihood of a pre-existing weld defect being the root cause of the very low SCC initiation time.

- A slightly higher degree of local deformation was observed in IN233, especially in the grains adjacent to larger primary cracks.
- Cr/Ti/Mn-rich, cuboidal oxides that exhibiting a spinel crystal structure were observed in both IN233 and IN169. They are believed to be pre-existing in the bulk prior to exposure to high temperature water. In the case of IN233, the buried spinel crystal was on the order of 1 μm in each observable dimension and was found to have NbC and MnS nucleated from its surface. Smaller, tens of nanometer scale spinel crystals were found in a sub-surface, Ni-rich region of IN169. These findings suggest that these oxides were not inherent to the weld material but were folded into the weld most likely during brushing or fabrication. However, there is no evidence showing that they have an important impact on SCC initiation.
- Both TEM samples from IN233 exhibit a unique presence of chlorine in the IGA whereas there was no chlorine detected in the IGA of all three TEM samples from IN169. The Cl in IN233 was always associated with Ti in the center of Fe-rich IGA. Ti incorporation in the Fe-rich oxide is typically a result of Ti from the high temperature water, which suggests Cl is also coming from the water. This is likely due to localized dissolution of some impurity in the weld material and not from the water source. If Cl originated from the water, then it should have been detectable through the entire IGA. Although Cl in Ni-base alloys is not believed to be as detrimental to SCC resistance as in stainless steels, further investigation is needed to clarify whether Cl plays a key role in the very low SCC initiation time for IN233.

9.0 Summary

9.1 Alloy 182 SCC Initiation Behavior

Alloy 182 in the 15% CF condition exhibited a skewed distribution of initiation times with nearly half of a set of 36 specimens fabricated from four different welds undergoing SCC initiation in less than 150 hours with the remaining specimen initiations tailing out to more than 5,000 hours. This distribution of initiation times is consistent with research conducted by EdF on Alloy 182, but because this initiation behavior is different than what has been observed for Alloy 600, several microstructural investigations have been performed on the 15% CF specimens to try to determine the cause of the wide range of SCC initiation times with an emphasis on understanding the very low SCC initiation times. Comparison of short and long initiation time specimens revealed some differences in microstructure, but at this point, nothing that conclusively explains the short initiation times. The most unexpected aspect of these observations was the presence of chlorine in the grain boundary oxide of two cracks in the short initiation time specimen. In high purity water, chlorine would very likely affect SCC initiation behavior, but in water that is pH buffered with boric acid and lithium hydroxide, it is unclear whether chlorine could have a significant effect on SCC initiation behavior.

Alloy 182 in the 7.5% CF condition and in the as-welded condition are exhibiting much higher SCC initiation times than the 15% CF material. Of the 12 specimens being tested in the 7.5% CF condition, only three have initiated while the remaining 9 specimens have reached at least 6,500 hours of exposure without initiation. None of the 12 specimens from as-welded Alloy 182 have initiated after nearly 28,000 hours (3.2 years). In comparison, Alloy 600 with 7.5 % cold work tested at PNNL for other programs has exhibited only slightly higher SCC initiation times than Alloy 600 with 15% cold work. In the as-received condition, it initiated at 5,000 to 10,000+ hours. Microstructural examinations have yet to be performed on any of the 7.5% CF and as-welded Alloy 182 specimens, primarily because nearly all of these specimens are still in-test.

The stress exponent for the PNNL Alloy 182 tested at its YS was analyzed in substantial detail and compared to the Alloy 182 stress exponent from available literature data. Most tests at PNNL on the 7.5% CF and as-welded Alloy 182 are still in-progress, leaving only the 15% CF Alloy 182 data available for stress exponent analysis when considering only initiated data. A regression analysis on these specimens following the same approach used by other researchers of Alloy 182 gives a stress exponent close to the literature values, and the range of initiation times of these specimens matches well with literature observations. However, the relatively narrow spread of YS values for these specimens along with the wide range of SCC initiation times results in a stress exponent with a large degree of uncertainty. When non-initiated data was also included in the analysis, the degree of uncertainty goes down and the stress exponent increases. This stress exponent is significantly higher than the stress exponent based on initiated and non-initiated data from the literature. This is because the average exposure time of non-initiated PNNL Alloy 182 tests significantly exceeds the exposure time of non-initiated data published in the literature. A Weibull-based analysis of the PNNL data and literature data result in stress exponents similar to that obtained by curve fitting an exponential dependence. The unique information provided by the Weibull analysis is that when considering initiated and non-initiated data together, the β value is substantially below one for PNNL data and for literature data, indicating a skew in the data toward lower initiation times.

Sub-yield strength testing of 15% CF Alloy 182 at 90% YS has been completed on 12 specimens. Unique never-before-used techniques were applied to precisely bring the

specimens to 90% YS. One specimen initiated at 500 hours while the remainder initiated at 9,200 hours or longer. Considering that these specimens were loaded to only 10% below the YS, and the specimens all exhibited small amounts of plastic strain to reach 90% YS, this was a surprising observation. However, further consideration suggests that this behavior at sub-YS may be linked to the ability for some 15% CF Alloy 182 specimens to reach very long SCC initiation times. To further explore and better understand this behavior, the NRC has recently funded PNNL to perform sub-YS SCC initiation tests on 15% CF Alloy 600.

9.2 Alloy 600 SCC Initiation Behavior

The four heats of 15% CF Alloy 600 tested for this program have all exhibited roughly similar initiation times. There is some uncertainty in the initiation times for six NX6106XK-11 specimens and two 33375-2B specimens that were tested as part of a shakedown run on the NRC12 SCC test system. Additional initiation tests will be performed to replace these suspect data points.

A curve fit of initiation time as a function of applied stress for these specimens and other specimens that were tested under the DOE LWRS program at PNNL indicates a stress exponent of less than 2 when considering only initiated data and a stress exponent of between 2 and 3 when including non-initiated data. A reevaluation of the stress exponent based on literature data for Alloy 600 SCC initiation gives a similar result. These values are somewhat lower than the stress exponent of ~ 4 published in the literature. The lower value obtained by PNNL is likely due to more careful pre-treatment of the data to ensure that true stress is used rather than engineering stress. A Weibull analysis of the PNNL data and literature data both give a β value close to 1, which indicates a roughly uniform rate of SCC initiation, i.e., the number of initiations is not biased to short or long times within the spread of initiations. The observed stress exponent and β value for Alloy 600 are distinctly different from Alloy 182, indicating a fundamental difference in SCC initiation behavior for the two materials.

9.3 Alloy 690/152 SCC Initiation Behavior

Testing of 12 Alloy 690 specimens and 24 Alloy 152(M)/52(M) specimens has reached the 4-year mark with no SCC initiations as expected based on SCC initiation behavior of more highly cold worked Alloy 690 being tested at PNNL for the DOE LWRS program. Examinations of the gauge surface of selected specimens after 2.4 years of exposure have revealed minor surface-only void formation along grain boundaries in some Alloy 690 and Alloy 152(M)/52(M) specimens. However, FIB-trench cross sections revealed that there were no sub-surface creep cavities like what was observed in more highly cold worked Alloy 690 initiation tested at PNNL under the DOE LWRS program. Cracks with length no greater than 20 μm were observed on the surface of the Alloy 152M specimen that was examined (IN128), but FIB trenching revealed these cracks to have a depth of no greater than 1 μm and no indication of active SCC. The test on these specimens was recently at the 4-year mark, and examinations of the same set of specimens are underway. Initial observations show no significant changes in any of the specimens.

These specimens are expected to easily make it to 5 years or more without SCC initiation. The current FOI for Alloy 690 compared to Alloy 600 is 41x when considering the average initiation time of the Alloy 600 and 67x when considering the median initiation time. Assuming that the remaining Alloy 600 initiation tests to be conducted do not substantially change the Alloy 600 initiation time statistics, reaching 5 years of exposure on the Alloy 690 without initiation will give

FOIs of 51x and 83x for average and median times, respectively. For Alloy 152(M)/52(M), the current FOIs are 24x and 48x for average and median times, respectively, compared to Alloy 182 initiation times. These will increase to 30x and 60x if no Alloy 152(M)/52(M) initiations occur before five years.

10.0 Future Testing and Analysis Recommendations

10.1 NRC-Expanded Test Matrix

In February 2017, a revised test matrix as listed in Figure 1 and reproduced here in Figure 128, was identified during a meeting between PNNL, NRC, EPRI, Dominion Engineering, and xLPR participants. The matrix includes an increased number of replicate specimens for tests in the 2015 test matrix, and it includes several additional tests to better identify the effect of temperature, strength, and applied stress on SCC initiation times for Alloy 182 in support of xLPR. In early 2020, the NRC identified several specific tests that they would like to have conducted, resulting in an expanded test matrix as shown in Figure 129. Completed tests are indicated by light gray lettering. Multiple SCC test systems are being utilized to accomplish the expanded program objectives, including several systems being provided by the NRC from other programs that ran at PNNL.

Additional tests on Alloy 182 in a 15% tensile strain condition have been requested by the NRC to better evaluate the effect of the type of deformation on Alloy 182 initiation. The intent is to provide a means to better link the PNNL results on 15% CF data to the useful literature data that were primarily obtained through tensile straining to achieve target stresses. A second area of expansion is to conduct sub-YS SCC initiation tests on 15% CF Alloy 600 to provide information that can be used to better understand the long SCC initiation times of 15% CF Alloy 182 when tested at 90% of its YS. These Alloy 600 tests are already underway, but it is too early to provide any results. In the 2017 test matrix, a place holder was set aside to allow for SCC initiation testing of interface regions, weld defects, and heat affected zones of Alloys 600/182/690/152(M)/52(M). The NRC-expanded test matrix defines those tests more fully.

	2016	2017	2018	2019	2020	2021
36-Specimen System #1	<i>Alloy 690/52/152 at 100% YS</i> 6 each of 4 welds @ 15% CF + 3 each of four base metals @ 15% CF (F1, F2)					
36-Specimen System #2		15% CF A600 6 each of 2 heats (F1)	AW A182 6 each of 4 welds (X3)	15%CF A182 @ 345°C 12 each of 2 welds (X4)	15% CF A182 @ 330°C 12 each of 2 welds (X4)	
3-Spec. System #1		15% CF A182 9 each of 4 welds (X1, F2)		7.5% CF A182 @ YS 6 each of 2 welds (X3)	15% CF A600 6 each of 2 heats (F1)	15% CF A182 vs Dissolved Hydrogen (X6)
3-Spec. System #2						15% CF A182 vs Surface Condition (X7)
6-Spec. System			15% CF A182 @ 0.93YS - 6 each of 2 welds (X2)	15% CF A182 @ 0.85YS 6 each of 2 welds (X2)	7.5% CF A182 @ 0.93YS - 6 each of 2 welds (X3)	Other Materials (Interfaces, weld defects)

Figure 128. Expanded SCC initiation test matrix selected in 2017.

	CY2016	2017	2018	2019	2020	2021	2022	2023
Large System #1	Alloy 690/52/152 @ YS 4 welds 6 each @ 15% CF, 4 base metals / 3 each @ 15% CF (F1, F2)						15% CF A182 @ 0.82YS 2 welds / 6 each (X2)	
Large System #2	15% CF A600 4 heats / 9 each (F1)	AW A182 4 welds / 3 each (X3) [no initiations as of 02/2020]				15% CF A182 @ 330°C 2 welds / 12 each (X4)		
3-Spec. System #1		15% CF A182 4 welds / 9 each (X1, F2)		7.5% CF A182 @ YS 2 welds / 6 each (X3) [50% complete]		15% CF A182 EW 1 weld / 9 each (X1, F2)	15% TS A182 2 welds / 6 each (X3)	15% CF A600 HAZ 2 heats / 12 each Groups #1, #2
3-Spec. System #2							7.5% TS A182 2 welds / 6 each (X3)	
6-Spec. System #1				15% CF A600 4 heats / 9 each (F1) (cont.)				
6-Spec. System #2			15% CF A182 @ 0.90YS 2 welds / 6 each (X2)					
Large System #3					15% CF A600 @ 0.50YS 2 heats / 12 each (X2)	15% CF A182 @ 345°C 2 welds / 12 each (X4)	15% CF Defected A152/52 12 specimens	
Large System #4						15% CF A182 @ high H2 2 welds / 6 each (X6)	15% CF A690 HAZ 2 heats / 6 each	
Large System #5					15% CF A600 4 heats / 9 each (F1) (cont.)	15% CF A182 @ low H2 2 welds / 6 each (X6)	7.5% CF A182 @ 0.90YS 2 welds / 6 each (X3)	
3-Spec. Sys. #3, #4						15% CF A182 vs Surface Condition 2 welds / 6 each (X7)		15% CF A600 HAZ 2 heats / 12 each Groups #3, #4

Figure 129. NRC-expanded SCC initiation test matrix selected in 2019.

10.2 Alloy 182 SCC Initiation Evaluation by Dominion Engineering

In 2019, EPRI contracted Dominion Engineering to evaluate the data being obtained by the NRC/EPRI SCC initiation program. A draft version of the resulting whitepaper provided to PNNL states some concern about the applicability of the Alloy 182 SCC initiation data being obtained by PNNL. One concern has been the testing approach. Since the onset of the program in 2015, Dominion Engineering has noted that initiations in plant components have occurred in regions where a surface cold work layer exists on an otherwise as-fabricated Alloy 182 weld, and because of this, laboratory tests should attempt to replicate this system. The approach accepted by EPRI and the NRC at the onset of the program was to test materials with uniform deformation levels. PNNL proposed this because of potential substantial complications and unknowns with devising a test method that could effectively evaluate SCC initiation of an as-fabricated material with a surface cold work layer.

This concern about a plant-specific test methodology was partially driven by PNNL’s experience with SCC initiation testing of as-received Alloy 600 with a surface cold work layer [3]. Tests on such specimens consistently showed a tendency for specimens with a cold work surface layer to initiate later than specimens with a polished surface that exposes GBs to the water. An example of this difference in initiation time is provided in Figure 130. The higher initiation times for laboratory specimens with surface cold work is opposite to the experience with plant components where a cold work surface layer accelerates SCC initiation. These contrasting results indicate that effectively simulating a plant component is a complicated topic that may require significant research and design to create a representative specimen and test method. It was also unclear how such a test specimen geometry could be used to determine the stress exponent for SCC initiation that is incorporated into the various SCC initiation models utilized by xLPR.

Because Dominion Engineering continues to express concern for this test approach, EPRI, NRC, Dominion Engineering, and PNNL have been engaging in ongoing discussions on how to resolve this concern. Several testing strategies have been proposed by PNNL and are being discussed. If a viable approach is determined, it will be implemented and used to provide supplemental information for this program.

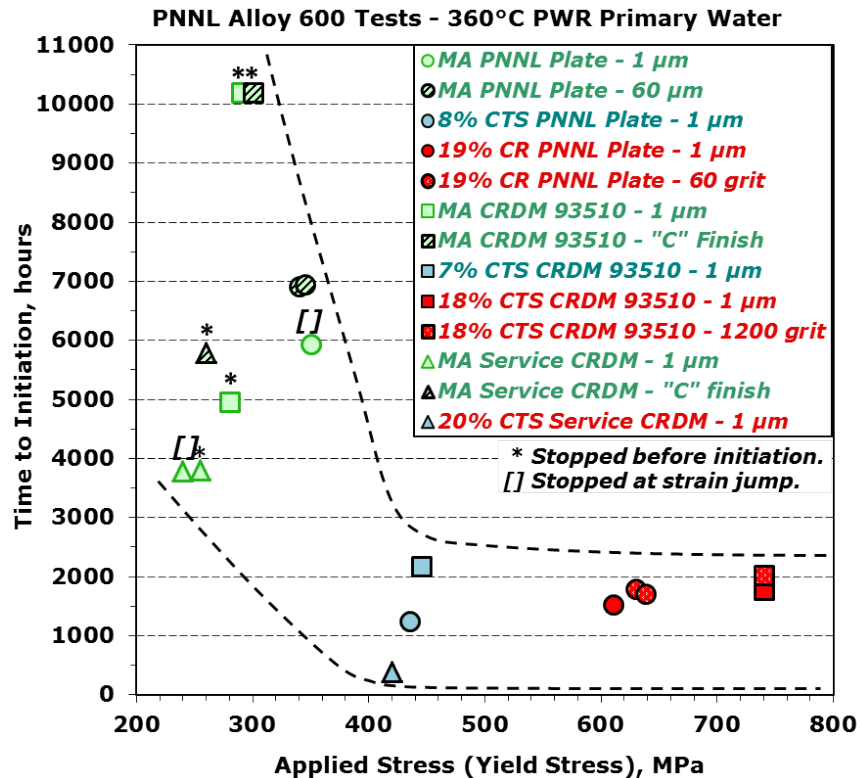


Figure 130. SCC initiation behavior of Alloy 600 tested for the DOE LWRS program [3].

Another item covered in the Dominion Engineering white paper is an expressed interest in further evaluating sub-YS SCC initiation response. The NRC-expanded matrix that includes sub-YS Alloy 600 SCC initiation testing is a first step toward meeting that desire, but depending on the outcome of discussions on a test method that can effectively simulate susceptible plant component conditions, this testing can be expanded as needed to include such specimens.

A third area of interest by Dominion Engineering has been to undertake temperature effects testing on the Alloy 182 as soon as possible because of its relevance to the xLPR SCC initiation models. Temperature effects tests are planned to begin just after the start of CY21.

The white paper also discusses several other interests in SCC initiation testing, but discussions on these topics have not taken place at this time. These topics such as evaluating the effect of stress relaxation and plant load cycles on SCC initiation, need to be discussed further by the program participants.

11.0 References

- [1] Materials Reliability Program: Stress Corrosion Crack (SCC) Initiation Testing of Ni-Base Alloys for PWR Applications - Part 1 (MRP-426), EPRI Product #3002010761, 2017.
- [2] C. Amzallag, J.-M. Boursier, C. Pages, C. Gimond, Stress corrosion life assessment of 182 and 82 welds used in PWR components, Proc. of the 10th International Symposium on Environmental Degradation of Materials in Nuclear Power Systems-Water Reactors, 2001.
- [3] M.B. Toloczko, M.J. Olszta, Z. Zhai, S.M. Bruemmer, "Stress Corrosion Crack Initiation Measurements of Alloy 600 in PWR Primary Water", Proc. 17th Int. Conf. Environmental Degradation of Materials in Nuclear Power Systems – Water Reactors, Ottawa, Ontario, Canada, Canadian Nuclear Society, 2015.
- [4] P. Scott, M. Foucault, B. Brugier, J. Hickling, A. McIlree, Examination of stress corrosion cracks in Alloy 182 weld metal after exposure to PWR primary water, Proceedings of the 12th International Conference on Environmental Degradation of Materials in Nuclear Power System–Water Reactors– Edited by TR Allen, PJ King, and L. Nelson TMS (The Minerals, Metals & Materials Society), 2005, pp. 497-509.
- [5] S.A. Attanasio, J.S. Fish, D.S. Morton, P.M. Rosencrans, G.S. Was, Y. Yi, "Measurement of the fundamental parameters for the film-rupture/oxidation mechanism", KAPL Atomic Power Laboratory: Schenectady, NY, 1999 (KAPL-P-000215).
- [6] Z. Zhai, M. Olszta, M. Toloczko, S. Bruemmer, "Crack Initiation Behavior of Cold-Worked Alloy 690 in Simulated PWR Primary Water - Role of Starting Microstructure, Applied Stress, and Cold Work on Precursor Damage Evolution", Proceeding 19th International Conference on Environmental Degradation of Materials in Nuclear Power Systems - Water Reactor, August 2019, American Nuclear Society, 2020.
- [7] K. Arioka, T. Yamada, T. Miyamoto, T. Terachi, "Dependence of Stress Corrosion Cracking of Alloy 690 on Temperature, Cold Work, and Carbide Precipitation—Role of Diffusion of Vacancies at Crack Tips", Corrosion, Vol. 67, 2011, p. 1252.
- [8] K. Arioka, R. Staehle, T. Yamada, T. Miyamoto, T. Terachi, "Degradation of Alloy 690 After Relatively Short Times", Corrosion, Vol. 72, 2016.
- [9] F. Vaillant, J.-M. Boursier, C. Amzallag, C. Bibollet, S. Pons, Environmental behaviour and weldability of Ni-base weld metals in PWRs, Revue Générale Nucléaire (6) (2007) 62-71.
- [10] T. Couvant, F. Vaillant, Initiation of PWSCC of weld Alloy 182, Proceedings of the 15th International Conference on Environmental Degradation of Materials in Nuclear Power Systems—Water Reactors, Springer, 2011, pp. 1141-1154.
- [11] J.P. Park, C. Park, Y.-J. Oh, J.H. Kim, C.B. Bahn, Statistical analysis of parameter estimation of a probabilistic crack initiation model for Alloy 182 weld considering right-censored data and the covariate effect, Nuclear Engineering and Technology 50(1) (2018) 107-115.
- [12] G. Troyer, S. Fyfe, K. Schmitt, G. White, C. Harrington, Dissimilar metal weld PWSCC initiation model refinement for xLPR part I: a survey of alloy 82/182/132 crack initiation literature, Proceedings of the 17th International Conference on Environmental Degradation of Materials in Nuclear Power Systems—Water Reactors, Ottawa, ON, Canada, 2015, pp. 9-13.
- [13] M. Erickson, Models and Inputs Developed for Use in the xLPR Pilot Study (MRP-302), Electrical Power Research Institute, 2011, p. 226.
- [14] R. Bandy, D.V. Rooyen, Stress Corrosion Cracking of Inconel Alloy 600 in High Temperature Water—An Update, CORROSION 40(8) (1984) 425-430.
- [15] C. Amzallag, S. Le Hong, C. Pagès, A. Gelpi, Stress Corrosion Life Assessment of Alloy 600 PWR Components, Ninth International Symposium on Environmental Degradation of Materials in Nuclear Power Systems—Water Reactors (1999).
- [16] Y. Garud, Stress Corrosion Cracking Initiation Model for Stainless Steel and Nickel Alloys, Electric Power Research Institute (EPRI): Palo Alto, CA, USA (2009).

- [17] Y. Garud, Validation of Stress Corrosion Cracking Initiation Model for Stainless Steel and Nickel Alloys, Electric Power Research Institute, 2012, p. 76.
- [18] D. Rudland, C. Harington, xLPR Version 1.0 Report, U.S. NRC and EPRI, 2011.
- [19] J. Boursier, D. Desjardins, F. Vaillant, The influence of the strain-rate on the stress corrosion cracking of alloy 600 in high temperature primary water, *Corrosion science* 37(3) (1995) 493-508.
- [20] E. Richey, D.S. Morton, R.A. Etien, G.A. Young, R.B. Bucinell, SCC Initiation in Alloy 600 Heat Affected Zones Exposed to High Temperature Water, Knolls Atomic Power Laboratory (KAPL), Niskayuna, NY, 2006.
- [21] H. Itoh, E. Otsuka, T. Yonezawa, K. Sakai, Effect of Pipe Making Proess on SCC Resistance of Alloy 600, Proceedings: 1994 EPRI Workshop on PWSCC of Alloy 600 in PWRs, Electric Power Research Institute, 1995.
- [22] T. Yonezawa, K. Onimura, H. Itoh, I. Saito, H. Takamatsu, T. Fujitani, Effect of cold working and applied stress on the stress corrosion cracking resistance of nickel-chromium-iron alloys, United States, 1992, pp. E11-E19.
- [23] J.A. Gorman, R.W. Staehle, K.D. Stavropoulos, Statistical Analysis of Steam Generator Tube Degradation, Dominion Engineering, INC., 1991, p. 240.
- [24] R. Staehle, Bases for predicting the earliest penetrations due to SCC for Alloy 600 on the secondary side of PWR steam generators, Argonne National Laboratory, 2001, NUREG/CR-6737, ANL-01/20 RWS 151, Argonne, Illinois, 2001.
- [25] J. Daret, Initiation of SCC in Alloy 600 Wrought Materials: A Laboratory and Statistical Evaluation, Proceedings of the 12th International Conference on Environmental Degradation of Materials in Nuclear Power System—Water Reactors, Salt Lake City, UT, USA, 2005, pp. 14-18.
- [26] W.J. Shack, O.K. Chopra, Statistical Initiation and Crack Growth Models for Stress Corrosion Cracking, ASME 2007 Pressure Vessels and Piping Conference, 2007, pp. 337-344.
- [27] M.L. Goldstein, S.A. Morris, G.G. Yen, Problems with fitting to the power-law distribution, *The European Physical Journal B-Condensed Matter and Complex Systems* 41(2) (2004) 255-258.
- [28] X. Xiao, E.P. White, M.B. Hooten, S.L. Durham, On the use of log-transformation vs. nonlinear regression for analyzing biological power laws, *Ecology* 92(10) (2011) 1887-1894.
- [29] G.C. Packard, On the use of log-transformation versus nonlinear regression for analyzing biological power laws, *Biological journal of the Linnean Society* 113(4) (2014) 1167-1178.
- [30] A. Clauset, C.R. Shalizi, M.E. Newman, Power-law distributions in empirical data, *SIAM review* 51(4) (2009) 661-703.
- [31] Y. Virkar, A. Clauset, Power-law distributions in binned empirical data, *The Annals of Applied Statistics* 8(1) (2014) 89-119.
- [32] R. Hanel, B. Corominas-Murtra, B. Liu, S. Thurner, Fitting power-laws in empirical data with estimators that work for all exponents, *PLOS ONE* 12(2) (2017) e0170920.

Pacific Northwest National Laboratory

902 Battelle Boulevard
P.O. Box 999
Richland, WA 99354
1-888-375-PNNL (7665)

www.pnnl.gov